


Конденсированные среды и межфазные границы

РЕЦЕНЗИРУЕМЫЙ НАУЧНЫЙ ЖУРНАЛ

Condensed Matter and Interphases

PEER-REVIEWED SCIENTIFIC JOURNAL

Том
Vol. 24, No. 2
2022

<p>Co 27 58.933</p>  <p>Cobalt</p>	<p>Ni 28 58.693</p>  <p>Nickel</p>	<p>Cu 29 63.546</p>  <p>Copper</p>
<p>Rh 45 102.91</p>  <p>Rhodium</p>	<p>Pd 46 106.42</p>  <p>Palladium</p>	<p>Ag 47 107.87</p>  <p>Silver</p>
<p>Ir 77 192.22</p>  <p>Iridium</p>	<p>Pt 78 195.08</p>  <p>Platinum</p>	<p>Au 79 196.97</p>  <p>Gold</p>

Condensed Matter and Interphases

Kondensirovannye sredy i mezhfaznye granitsy

Peer-reviewed scientific journal

Published since January 1999

Periodicity: Quarterly

Volume 24, No. 2, 2022

Full-text version is available in the Russian language on the website: <https://journals.vsu.ru/kcmf>

Condensed Matter and Interphases (Kondensirovannye Sredy i Mezhfaznye Granitsy) publishes articles in Russian and English dedicated to key issues of condensed matter and physicochemical processes at interfaces and in volumes.

The mission of the journal is to provide open access to the results of original research (theoretical and experimental) at the intersection of contemporary condensed matter physics and chemistry, material science and nanoindustry, solid state chemistry, inorganic chemistry, and physical chemistry, and to share scientific data in the **following sections**: atomic, electron, and cluster structure of solids, liquids, and interphase boundaries; phase equilibria and defect formation processes; structure and physical and chemical properties of interphases; laser thermochemistry and photostimulated processes on solid surfaces; physics and chemistry of surface, thin films and heterostructures; kinetics and mechanism of formation of film structures; electrophysical processes in interphase boundaries; chemistry of surface phenomena in sorbents; devices and new research methods.

The journal accepts for publication: reviews, original articles, short communications by leading Russian scientists, foreign researchers, lecturers, postgraduate and undergraduate students.

FOUNDER AND PUBLISHER:

Voronezh State University

The journal is registered by the Russian Federal Service for Supervision of Communications, Information Technology and Mass Media, Certificate of Registration ПИ № ФС77-78771 date 20.07.2020

The journal is included in the List of peer reviewed scientific journals published by the Higher Attestation Commission in which major research results from the dissertations of Candidates of Sciences (PhD) and Doctor of Science (DSc) degrees are to be published. Scientific specialties of dissertations and their respective branches of science are as follows: 1.4.1. – Inorganic Chemistry (Chemical, Physical sciences); 1.4.4. – Physical Chemistry (Chemical, Physical, Technical sciences); 1.4.6. – Electrochemistry (Chemical, Physical, Technical sciences); 1.4.15. – Solid State Chemistry (Chemical, Technical, Physical sciences); 1.3.8. – Condensed Matter Physics (Physical, Technical sciences).

The journal is indexed and archived in: Russian Scientific Index Citations, Scopus, Chemical Abstract, EBSCO, DOAJ, CrossRef

Editorial Board and Publisher Office:
1 Universitetskaya pl., Voronezh 394018

Phone: +7 (432) 2208445

<https://journals.vsu.ru/kcmf>

E-mail: kcmf@main.vsu.ru

Signed for printing 24.06.2022

Price – not fixed

Subscription index
in the Catalogue «Russian Post»
is IИH134

When reprinting the materials, a reference to the Condensed Matter and Interphases must be cited

The journal's materials are available under the Creative Commons "Attribution" 4.0 Global License



© Voronezh State University, 2022

EDITOR-IN-CHIEF:

Victor N. Semenov, Dr. Sci. (Chem.), Full Professor, Voronezh State University, (Voronezh, Russian Federation)

VICE EDITORS-IN-CHIEF:

Evelina P. Domashevskaya, Dr. Sci. (Phys.–Math.), Full Professor, Voronezh State University, (Voronezh, Russian Federation)

Polina M. Volovitch, Ph.D. (Chem.), Associate Professor, Institut de Recherche de Chimie (Paris, France)

EDITORIAL BOARD:

Nikolay N. Afonin, Dr. Sci. (Chem.), Voronezh State Pedagogical University (Voronezh, Russian Federation)

Vera I. Vasil'eva, DSc in Chemistry, Associate Professor, Voronezh State University, (Voronezh, Russian Federation)

Aleksandr V. Vvedenskii, Dr. Sci. (Chem.), Full Professor, Voronezh State University, (Voronezh, Russian Federation)

Victor V. Gusarov, Dr. Sci. (Chem.), Associate Member of the RAS, Ioffe Physical-Technical Institute RAS (St. Petersburg, Russian Federation)

Vladimir E. Guterman, Dr. Sci. (Chem.), Full Professor, Southern Federal University (Rostov-on-Don, Russian Federation)

Boris M. Darinskii, Dr. Sci. (Phys.–Math.), Full Professor, Voronezh State University, (Voronezh, Russian Federation)

Vladimir P. Zlomanov, Dr. Sci. (Chem.), Full Professor, Moscow State University, (Moscow, Russian Federation)

Valentin M. Ievlev, Dr. Sci. (Phys.–Math.), Full Member of the RAS, Moscow State University, (Moscow, Russian Federation)

Aleksandr D. Izotov, Dr. Sci. (Chem.), Associate Member of the RAS, Kurnakov Institute of General and Inorganic Chemistry RAS (Moscow, Russian Federation)

Oleg A. Kozaderov, Dr. Sci. (Chem.), Associate Professor, Voronezh State University, (Voronezh, Russian Federation)

Andrey I. Marshakov, Dr. Sci. (Chem.), Full Professor, Frumkin Institute of Physical Chemistry and Electrochemistry RAS (Moscow, Russian Federation)

Irina Ya. Mittova, Dr. Sci. (Chem.), Full Professor, Voronezh State University, (Voronezh, Russian Federation)

Victor V. Nikonenko, Dr. Sci. (Chem.), Full Professor, Kuban State University (Krasnodar, Russian Federation)

Oleg V. Ovchinnikov, Dr. Sci. (Phys.–Math.), Full Professor, Voronezh State University, (Voronezh, Russian Federation)

Sergey N. Saltykov, Dr. Sci. (Chem.), Associate Professor, Novolipetsk Steel (Lipetsk, Russian Federation)

Vladimir F. Selemenev, Dr. Sci. (Chem.), Full Professor, Voronezh State University, (Voronezh, Russian Federation)

Vladimir A. Terekhov, Dr. Sci. (Phys.–Math.), Full Professor, Voronezh State University, (Voronezh, Russian Federation)

Evgeny A. Tutov, Dr. Sci. (Chem.), Associate Professor, Voronezh State Technical University (Voronezh, Russian Federation)

Pavel P. Fedorov, Dr. Sci. (Chem.), Full Professor, Prokhorov General Physics Institute RAS (Moscow, Russian Federation)

Vitaly A. Khonik, Dr. Sci. (Phys.–Math.), Full Professor, Voronezh State Pedagogical University (Voronezh, Russian Federation)

Vladimir A. Shaposhnik, Dr. Sci. (Chem.), Full Professor, Voronezh State University (Voronezh, Russian Federation)

Andrey B. Yaroslavl'tsev, Dr. Sci. (Chem.), Associate Member of the RAS, Kurnakov Institute of General and Inorganic Chemistry RAS (Moscow, Russian Federation)

INTERNATIONAL MEMBERS OF THE EDITORIAL BOARD:

Mahammad Babanly, Dr. Sci. (Chem.), Associate Member of the ANAS, Institute of Catalysis and Inorganic Chemistry ANAS (Baku, Azerbaijan)

Tiziano Bellezze, Dr. Sci. (Chem.), Marche Polytechnic University (Ancona, Italy)

Mane Rahul Maruti, Ph.D. (Chem.), Shivaji University (Kolhapur, India)

Nguyen Anh Tien, Ph.D. (Chem.), Associate Professor, University of Pedagogy (Ho Chi Minh City, Vietnam)

Vladimir V. Pankov, Dr. Sci. (Chem.), Full Professor, Belarusian State University (Minsk, Belarus)

Fritz Scholz, Dr. Sci., Professor, Institut für Biochemie Analytische Chemie und Umweltchemie (Greifswald, Germany)

Mathias S. Wickleder, Dr. Sci., Professor, University of Cologne (Koln, Germany)

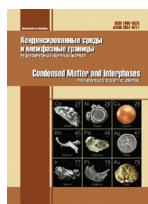
Vladimir Sivakov, Dr. rer. nat., Leibniz Institute of Photonic Technology (Jena, Germany)

EXECUTIVE SECRETARY:

Vera A. Logacheva, Cand. Sci. (Chem.), Voronezh State University, (Voronezh, Russian Federation)

CONTENTS

Review			
<i>Belov D. V., Belyaev S. N.</i>			
The decisive role of biological factors in the corrosion of the D16T alloy. Review	155	<i>Mamand D. M., Rasul H. H., Omer P. K., Qadr H. M.</i>	
		Theoretical and experimental investigation on ADT organic semiconductor in different solvents	227
Original articles			
<i>Abdullaeva Sh. S., Bakhtiyarly I. B., Kurbanova R. J., Mukhtarova Z. M.</i>		<i>Iman A. Mahdy, El Sheikh S. M., Hosny A. Omar, Seredin P. V., Manal A. Mahdy</i>	
The quasi-binary $\text{Cu}_3\text{In}_5\text{S}_9 - \text{FeIn}_2\text{S}_4$ section	182	Preparation and characterization of Ge-Ni-Te nanocomposite	243
<i>Bayramova U. R., Poladova A. N., Mashadiyeva L. F., Babanly M. B.</i>		<i>Tien Dai Nguyen, Kim J. O., Lee S. J.</i>	
Calorimetric determination of phase transitions of Ag_8BX_6 (B = Ge, Sn; X = S, Se) compounds	187	Growth of InGaAsSb/GaSb compound for infrared optoelectronic devices	250
<i>Deineka V. I., Salasina Ya. Yu., Deineka L. A.</i>		<i>Panteleeva V. V., Simonov G. A., Shein A. B., Miloserdov P. A., Gorshkov V. A.</i>	
Sorption of 3-glucosides of six common natural anthocyanidins on anatase	196	Kinetics of the cathodic evolution of hydrogen on alloys of the $\text{Mo}_x\text{W}_{1-x}\text{Si}_2$ system in an alkaline electrolyte	256
<i>Zabolotnykh S. A., Solovyev A. D., Sofronov A. S., Shcherban M. G.</i>		<i>Parinova E. V., Antipov S. S., Belikov E. A., Chuvenkova O. A., Kakuliia I. S., Koyuda D. A., Trebunskikh S. Yu., Skorobogatov M. S., Chumakov R. G., Lebedev A. M., Sinelnikov A. A., Artyukhov V. G., Ovchinnikov O. V., Smirnov M. S., Turishchev S. Yu.</i>	
Surface-active and chemical properties of alkylbenzenesulfonic acid – nitric acid – water composites	204	TEM and XPS studies of bio-nanohybrid material based on bacterial ferritin-like protein Dps	265
<i>Zlomanov V. P., Kazin P. E., Yatsenko A. V.</i>		<i>Suntsov Yu. K., Kharchenko G. Yu., Suntsova N. S.</i>	
Substances and the transformations they undergo: basic concepts	211	Liquid-vapour phase equilibria of three-component systems formed by <i>n</i> -propanol, <i>n</i> -butanol, and <i>n</i> -alkylethanoates	273
<i>Kasach A. A., Kharytonau D. S., Zharskii I. M., Kurilo I. I.</i>			
Electrocrystallisation of Cu-Sn-TiO ₂ composite coatings in sulphuric acid electrolytes	220		



Review

Review article

<https://doi.org/10.17308/kcmf.2022.24/9256>

The decisive role of biological factors in the corrosion of the D16T alloy. Review

D. V. Belov✉, S. N. Belyaev

*Federal Research Centre Institute of Applied Physics of the Russian Academy of Sciences,
46 Ulyanova str., Nizhny Novgorod 603950, Russian Federation*

Abstract

The biocorrosion of duralumin grade D16T has been studied and a mechanism has been proposed according to which the initiators of initial corrosion damage are reactive oxygen species (ROS) produced by micromycetes. An assumption was made about the participation of hydrogen peroxide in the mycological corrosion of the D16T alloy, which is formed both during the life of micromycetes and during the activation of oxygen by zero-valent aluminium (ZVAL). The mechanisms of intergranular, pitting and pitting corrosion of duralumin under the influence of microscopic fungi are proposed. Purpose: determination of the main biological factor initiating biocorrosion of the D16T alloy; assessment of the biological impact of the association of microscopic fungi on the alloy in order to develop scientifically grounded and effective methods of protecting aluminium and its alloys from biocorrosion by micromycetes.

The object of the study was an aluminium alloy D16T in accordance with state standard (GOST) 4784–2019 after hardening and natural ageing, which is widely used for the manufacture of load-bearing elements of structures and equipment of fuel systems of aircraft, car bodies, parts of various machines and assemblies operating at low temperatures, and in the food and pharmaceutical industries. The stages of initiation and development of biocorrosion of the D16T alloy under the influence of a consortium of moulds have been studied using a scanning electron microscope. The phase composition of the D16T corrosion products has been studied.

In the process of vital activity of microscopic fungi, reactive oxygen species are formed, initiating the biocorrosion of the D16T alloy. The initial stage of biocorrosion is caused by hydrolysis of the protective passive aluminium film. At the stage of intense biocorrosion, oxygen-containing aluminium compounds are formed in the form of a water-saturated gel. Further, as this corrosion product accumulates, its water permeability decreases. The gel undergoes “ageing” and turns into crystalline products. Conidia and hyphae of microscopic fungi adhere, are mechanically fixed on the metal surface and penetrate into the surface layers and deep into the metal, causing its corrosive destruction in the form of pitting, ulcers, and cavities. It is possible that the initiation of metal biocorrosion is a consequence of the hyperproduction of reactive oxygen species by the cells of micromycetes as a result of oxidative stress. This may be their defensive strategy aimed at destroying xenobiotic material.

The development of intergranular and pitting corrosion of the D16T alloy under the action of micromycetes occurs at the sites of contact with the exudate, which, due to a cascade of reactions with the participation of ROS, is locally enriched in hydroxide ions. The origin and development of pitting on the duralumin surface occurs in defects of the passive oxide film due to the displacement of oxygen-containing surface aluminium compounds and their interaction with corrosive OH⁻ and ROS anions. Hydrogen peroxide, as an intermediate product of the metabolism of micromycetes, on the surface of the D16T alloy can participate in the Fenton process or decompose heterogeneously, also provoking the development of aluminium biocorrosion.

Keywords: Biocorrosion, Mycological corrosion, Duralumin, D16T, Zero-valent aluminium, ZVAL, Micromycetes, Microscopic fungi, Reactive oxygen species, ROS, Superoxide anion radical, Hydrogen peroxide, Intergranular corrosion, Pitting corrosion

Acknowledgements: The authors express their gratitude to G. A. Gevorgyan and M. V. Maksimov for help in performing macro- and microstructural analysis and studies on an electron microscope (JSC Central Research Institute Burevestnik, Nizhny Novgorod 603950, Sormovskoe shosse, 1a).

✉ Denis. V. Belov, belov.denbel2013@yandex.ru

© Belov D. V., Belyaev S. N., 2022



The content is available under Creative Commons Attribution 4.0 License.

For citation: Belov D. V., Belyaev S. N. The decisive role of biological factors in the corrosion of the D16T alloy. Review. *Condensed Matter and Interphases*. 2022;24(2): 155–181. <https://doi.org/10.17308/kcmf.2022.24/9256>

Для цитирования: Белов Д. В., Беляев С. Н. Об определяющей роли биологических факторов в коррозии сплава Д16Т. Обзор. *Конденсированные среды и межфазные границы*. *Конденсированные среды и межфазные границы*. 2022;24(2): 155–181. <https://doi.org/10.17308/kcmf.2022.24/9256>

1. Introduction

The most active biological agents ubiquitous in soil, water, and air are mould or microscopic fungi (micromycetes). Often they prevail over other microorganisms and have the greatest potential for impact on almost all infrastructure and human industrial and household activities. Micromycetes are active agents initiating microbiological corrosion of most metals and alloys. The species diversity of microscopic fungi, their high adaptability to living conditions, and powerful enzymatic apparatus lead to significant amounts of damage to metal materials by them. The microbiological corrosion (biocorrosion) of metals is the destruction caused by the direct or indirect action of microorganisms. The biocorrosion of metals by micromycetes in atmospheric and soil conditions, for example, in well-ventilated places with favourable temperature and humidity characteristics, with the presence of contaminants on the metal surface is especially characteristic [1].

The microbial corrosion of metals is a serious environmental and economic problem. In most cases, the corrosion of metals occurs in an oxygen-containing environment. Among the microorganisms involved in the corrosion of metals, the most active ones are aerobic. However, among anaerobic microorganisms, there are those that are capable of initiating and accelerating the oxidation of metals. Some of these microbes can consume molecular hydrogen, abiotically formed during the oxidation of metals. Due to the occurrence of coupled reactions, the anaerobic oxidation of metals becomes thermodynamically favourable. Additionally, extracellular enzymes, such as hydrogenases, accelerate the oxidation of metals. Organic electron carriers such as flavins, phenazines, humic substances can replace molecular hydrogen as an electron carrier between metal and living cells. Direct electron transfer without intermediaries from oxidising metal to microbial cells is also possible [2–5].

The role of biofilms in the corrosion of metals. First discovered in 1978, the existence of a specific form of bacteria in the form of biofilms [6] was recognised as the predominant form of microbial life on our planet. Biofilms are defined as a special form of organisation of microorganisms formed at the interface between two phases, intensively exchanging genetic information and capable of coordinating their behaviour through the secretion of molecular signals – *Quorum Sensing*. The study of biofilms has many practical applications, for example, in medicine, in the ecology of natural and industrial waters, and in hydrometallurgy. The practical significance of the study of planktonic and biofilm forms of habitation of corrosive microorganisms in aquatic environments is due to the relevance of increasing the efficiency of biocidal protection of buildings and structures.

The issue of the decisive role of bacterial biofilms in the corrosion of metals is widely discussed in the literature [7–12]. However, the issue of the effect of biofilms of microscopic fungi has been little studied. In our opinion, biofilms of micromycetes are one of the determining factors in the corrosion processes of metals.

A bacterial biofilm is a collection of surface-associated microbial cells enclosed in a matrix of an extracellular polymeric substance, predominantly a polysaccharide material. In [13], the decisive role of the adhesion of bacteria *Pseudomonas fluorescens* and *Desulfovibrio desulfuricans* to metal surfaces in their corrosion was reported. The authors provided evidence that the substance involved in the primary adhesion of bacteria to the surface of mild steel is of a polysaccharide nature. This substance is present in the outer membrane of bacterial cells in the form of lipopolysaccharide [14].

Mycelial fungi can organise multicellular, highly structured consortia known as fungal biofilms that form stable communities on a variety of biotic and abiotic surfaces. Most of the research is focused on the study of planktonic

forms of micromycetes. The analysis of the literature data showed that filamentous fungi are ubiquitous in various aquatic environments, including drinking water distribution systems. Within such closed water supply systems, consortiums of microscopic fungi, which form biofilms, develop. According to [15], the biofilm isolated from the drinking water distribution system included the following micromycetes: *Aspergillus* sp., *Alternaria* sp., *Botrytis* sp., *Cladosporium* sp., *Penicillium* sp.

The typical morphology of a biofilm of microscopic fungi is described as a complex three-dimensional structure of heterogeneous surface-associated colonies consisting of filamentous hyphae (chains of elongated cells), pseudohyphal cells, yeast-like cells, and various forms of extracellular matrix (Fig. 1) [16]. For example, micromycete *Aspergillus fumigatus* produces *in vitro* an extracellular hydrophobic matrix with typical characteristics of a biofilm, consisting of galactomannan, α -1,3-glucans, monosaccharides,

polyols, melanin, and proteins (antigens and hydrophobins) [17, 18].

During the initial stages of biofilm growth and development, the formation of a layer of substances surrounding the fungus is observed. This layer is involved in the binding of cells to each other (cohesion) and in their interaction with the surface of the substrate (adhesion). These substances provide the structural basis of the forming microfilm. Each microscopic fungus has its own pattern of biofilm development.

Microorganisms have now been shown to be able to adhere to virtually any surface. Surface-associated micromycetes, which form biofilms, have a special phenotype that differs from planktonic organisms. They have specific mechanisms of attachment to the surface, which are regulated by various characteristics of the nutrient medium, substrate, and cell surface [19].

In nature, adhesion is a widespread phenomenon inherent in many microorganisms, which allows them to colonise their habitats. The

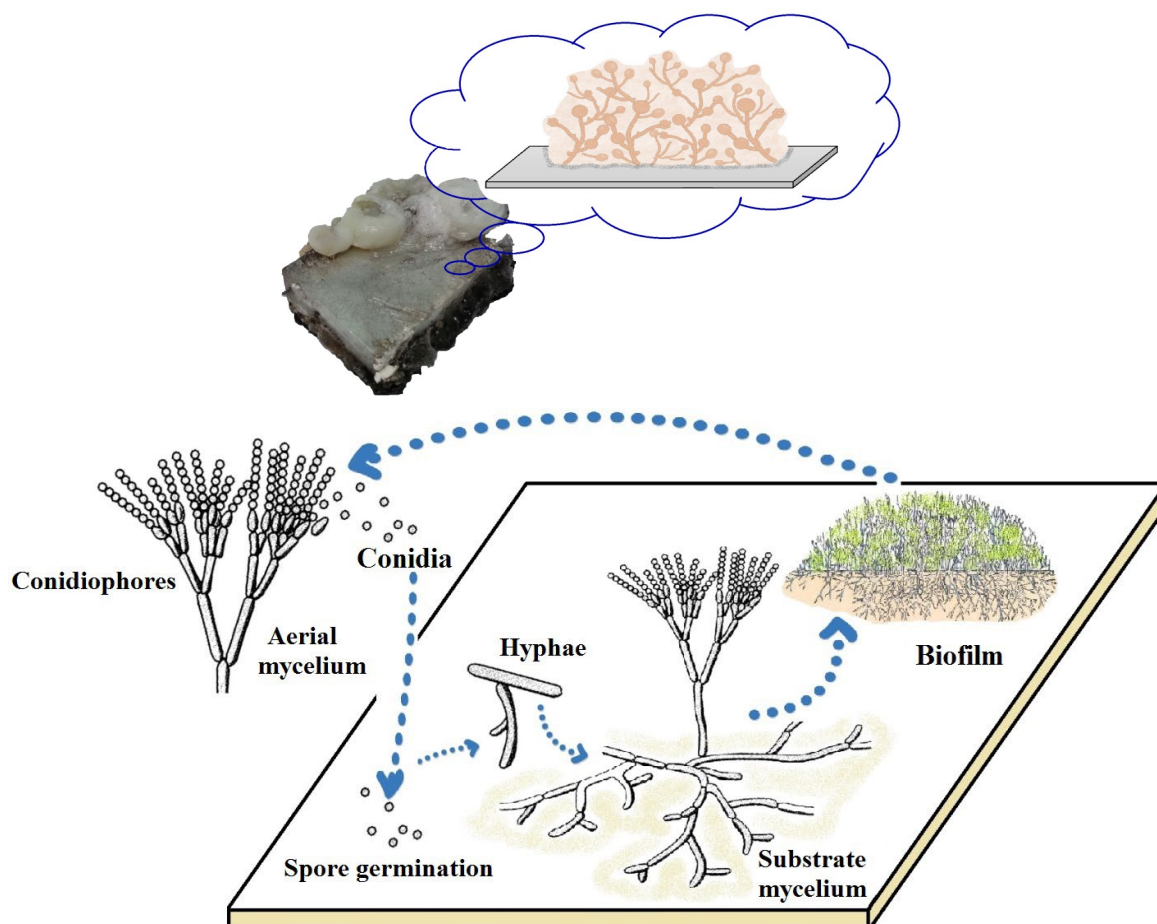


Fig. 1. Scheme of the formation of a biofilm of micromycetes on the surface of a metal

adhesive ability of micromycetes determines their further colonisation of the metal surface. The stage of attack of micromycetes on the metal surface following the primary adsorption is characterised by the invasive (from lat. *invasio* – invasion, attack) growth of a microorganism. Proteolytic, lipolytic enzymes of fungi (proteases, hyaluronidase, phospholipase, lipase, etc.) are involved in the destruction of the surface structural elements of the protective film on the metal surface and enable its further colonisation and penetration (from lat. *penetratio* – penetrate). The pathogenicity factors of microscopic fungi include adhesins. Adhesins are areas of the fungi surface (proteins, carbohydrate parts of cell wall mannoproteins, etc.) that ensure the attachment of a microorganism to a solid substrate. Adhesins of micromycetes differ by specificity and allow them to adhere to different solid substrates. [20]. The study [21] reports that the adhesion of microorganisms is the initial stage of the biofouling of materials, including metals, in air and water environments. The authors studied the adhesion of the conidia of a microscopic fungus, *Trichoderma viride*, to the surface of metals differing in oxidising potentials, and determined the quantitative kinetic parameters characterising the stage of adhesion of the conidia of micromycetes.

Now, scanning electron microscopy is widely used to visualise micromycete biofilms [22]. In the study [23], the stages of biofilm formation

of the *Aspergillus fumigatus* micromycete were studied using confocal laser scanning microscopy. The authors of the study [24] carried out a structural analysis of the biofilms of the *Aspergillus niger* micromycete using the same method.

In our studies, we observed the biofilm formation of microscopic fungi on all surfaces of corroding metals. Biofilms of microscopic fungi on the surface of the D16T alloy are shown in Figs. 2 and 3.

Recent advances in molecular techniques and confocal microscopy have shown that biofilm formation is a natural and preferred form of fungal growth and a major cause of persistent infections in humans. The study [25] presents microscopic, spectroscopic, and microsensor methods for studying biofilms. Analytical methods for studying extracellular polymeric substances, in particular, polysaccharides and proteins, are generalised.

The presence of microorganisms on the surface of a material can significantly affect its performance. Surface-mediated microbial growth and the formation of a biofilm on a solid substrate provokes its further biofouling. The presence of biofilms can promote interfacial physicochemical reactions, which are undesirable under abiotic conditions. Therefore, the generally accepted concept of biocorrosion is expanding. The existing definition of biocorrosion can be extended by noting that these are changes in

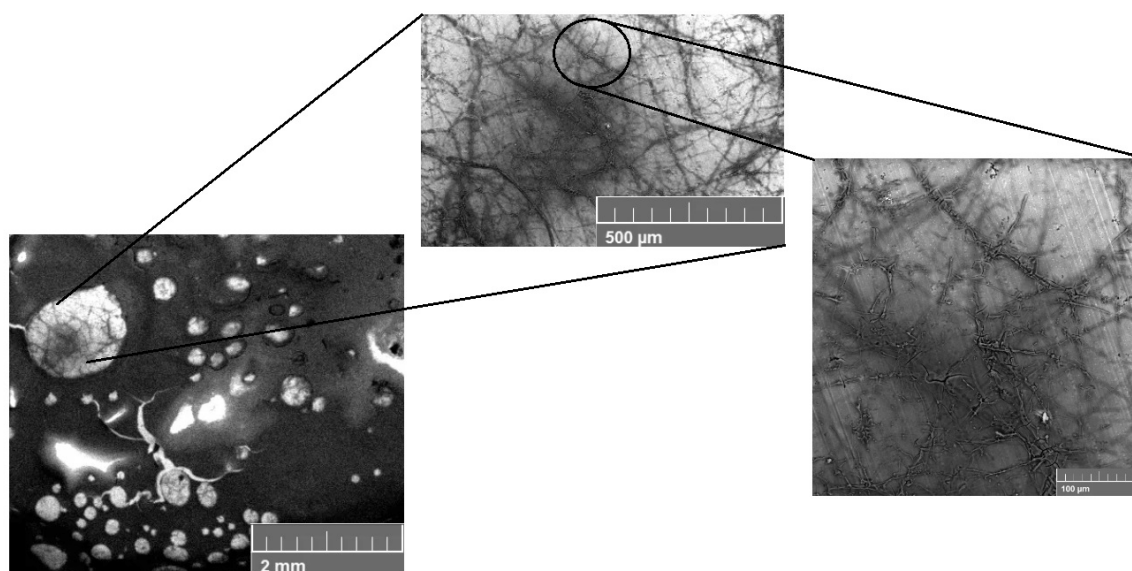


Fig. 2. Formation of a biofilm of a consortium of microscopic fungi on the surface of the D16T alloy

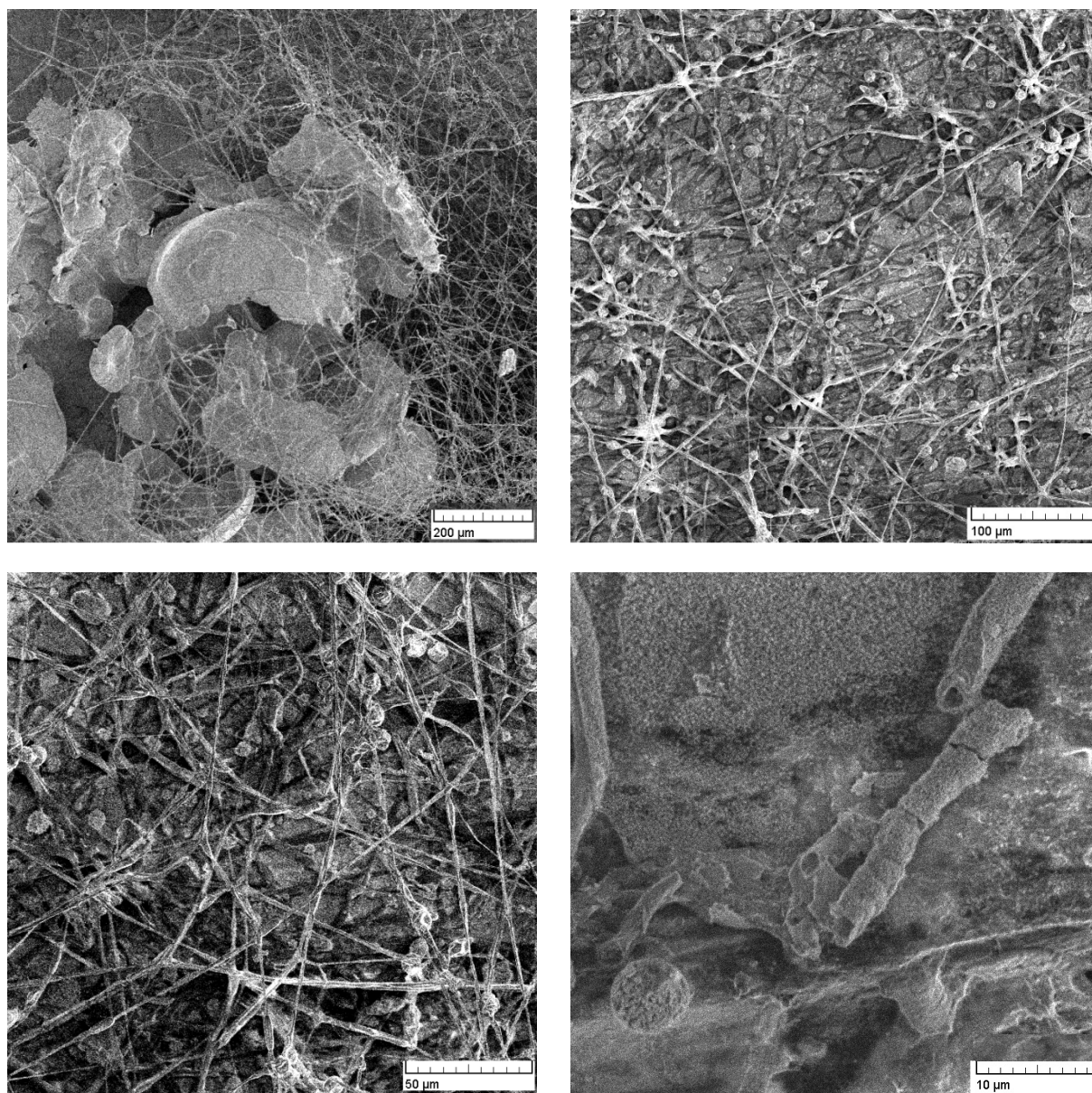


Fig. 3. Photographs of a biofilm of a consortium of microscopic fungi on the surface of the D16T alloy

the properties of metallic materials caused by the formation of a biofilm or biofouling layer. The biocorrosion of metals can be considered a consequence of coupled biological and abiotic reactions of electron transfer from metals to microbial cells [26].

The detailed mechanisms of biocorrosion are still poorly understood. Thus, in the article [27], the main attention of researchers was focused on studying the effect of biomineralisation processes occurring on metal surfaces, on the biocorrosion of metals, and the effect of extracellular enzymes active in the biofilm matrix on electrochemical reactions at the biofilm–metal interface.

It is generally accepted that the biocorrosion of metals under the influence of microscopic fungi is indirect and occurs when exposed to aggressive media formed as a result of their vital activity. However, we have shown in experiments that micromycetes are directly involved in the destruction of the surface of metals.

The role of reactive oxygen species (ROS) in the biocorrosion of metals. The production of ROS, including the superoxide anion radical ($O_2^{\cdot-}$), hydrogen peroxide (H_2O_2) and hydroxyl radicals (HO^{\cdot}), is a characteristic phenomenon of all living organisms, including mould fungi. ROS play various roles in cellular defence and

in the transmission of signals that control the differentiation, development, and pathogenesis of micromycete cells [28]. ROS regulate the germination, development, and intercellular interactions in microscopic fungi. The study [29] points out that ROS are formed in microscopic fungi over the course of metabolic activity. The formation of ROS increases under the influence of various stress factors, including starvation, light, mechanical damage, and interaction with other living objects. The regulation of ROS content is the most important aspect in the development of a fungal organism. The review considers the sources of ROS in fungal cells, sensors, and pathways of ROS signal transduction. A detailed description of antioxidant protection in different classes of microscopic fungi is provided.

Active oxygen metabolites - hydrogen peroxide H_2O_2 and the superoxide anion radical $O_2^{\cdot-}$ are always present in cells in low concentrations, participating, among other things, in intra- and intercellular signalling [30]. Hydrogen peroxide is considered to be a marker of oxidative stress [31]. Hydrogen peroxide is a by-product in various cellular processes and the end product of many metabolic reactions.

In the physiological range of concentrations (from 1 nM to 0.1–0.5 μM), H_2O_2 acts as a signalling molecule, takes part in the processes of cell differentiation, migration, and proliferation [32, 33]. With an increase in concentration to 1–10 μM , H_2O_2 causes the arrest of the cell cycle, which is usually restored and even accelerated in the case of a successful adaptation to oxidative stress. At high concentrations ($\geq 10 \mu M$ H_2O_2) oxidative stress prevails, adaptation does not occur, and apoptosis starts. The boundaries of these reactions are relative and strongly depend on the cell type, cultivation conditions, and heterogeneous distribution of H_2O_2 in the cell, which makes the concept of the average intracellular concentration of H_2O_2 unacceptable [34].

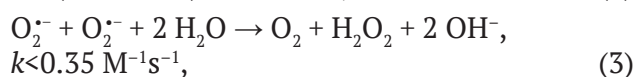
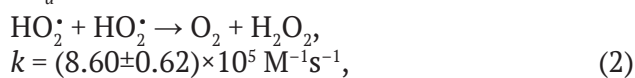
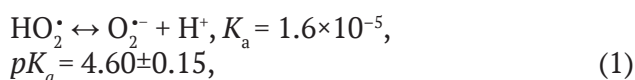
The ability of soil micromycetes to synthesise and release hydrogen peroxide into the environment is widely known [35]. The study [36] reports on the ability of a microscopic fungus, *Trichoderma guizhouense*, to synthesise and accumulate significant amounts of hydrogen

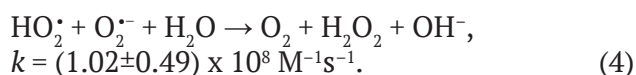
peroxide. The formation of H_2O_2 by fungi can occur through two main metabolic reactions: as a by-product of oxidation by FAD-dependent oxidases such as glucose oxidase or amino acid oxidases [37–40], and by dismutation of the superoxide anion radical $O_2^{\cdot-}$ by superoxide dismutases (SOD) [41].

In [42], it was reported that the key role in the development of the phytopathogenic fungus *Fusarium graminearum* depends on the balanced dynamics of the formation of reactive oxygen species, in particular hydrogen peroxide. In [43], 50 strains of fungi belonging to different types of basidiomycetes were tested for the ability to synthesise and release H_2O_2 . A comparative evaluation on the ability of microorganisms to decolorise synthetic dyes was carried out. Hydrogen peroxide is involved in the decomposition of lignin and cellulose by white and brown rot fungi as a co-substrate [44, 45]. In addition, it was shown that H_2O_2 plays a key role in the degradation of lignocellulose [46].

The study [47] proved the ability of mycelial fungus *Stilbella aciculosa* to produce an extracellular superoxide anion radical during cell differentiation. In [48–50], detailed descriptions of the chemical and biochemical properties of $O_2^{\cdot-}$ were presented.

Superoxide anion radicals during initiation of biocorrosion of metals. In our own previous studies [51, 52] it was shown that $O_2^{\cdot-}$, formed during the life of microscopic fungi, can pass into the pericellular environment and act as an initiator of physicochemical processes leading to deep destruction of metals. It is known that $O_2^{\cdot-}$ in an aqueous solution exists in the form of an equilibrium mixture of a base and a conjugated acid - a hydroperoxide radical. At $pH > 7$, the equilibrium is shifted towards $O_2^{\cdot-}$, the radicals of an equilibrium mixture in aqueous solutions rapidly transform into stable products as a result of parallel reactions [53, 54] in accordance with reaction schemes (1)–(4):





As a result of the cascade of these reactions, corrosive agents accumulate in the medium, initiating metal corrosion.

The participation of hydrogen peroxide in the corrosion of metals. In a number of literary sources, the issue of the effect of hydrogen peroxide on metal corrosion and its participation in the initiation and stimulation of metal corrosion is considered [55, 56].

For example, the authors of [57, 58] studied the effect of hydrogen peroxide on the corrosion of stainless steel. The study presents the characteristics of oxide films formed on stainless steel when exposed to H_2O_2 and O_2 in water. In [59], the corrosion of various stainless steels in chloride-containing alkaline solutions of hydrogen peroxide was studied by electrochemical methods. The authors concluded that alkaline solutions of hydrogen peroxide cause the corrosion of stainless steels to varying degrees, regardless of the content of chloride ions, and their corrosion activity increases with an increasing content of H_2O_2 .

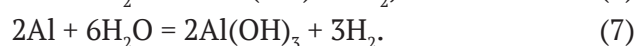
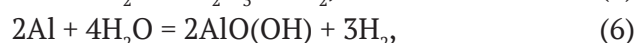
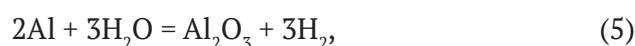
Titanium, currently widely used in dental implantology and orthopaedics due to its excellent corrosion resistance and mechanical properties, has proven to be unstable in environments containing H_2O_2 [60–62]. The corrosion of titanium in a hydrogen peroxide solution in an alkaline medium was investigated in [63]. The authors proposed a reaction mechanism based on the interaction of titanium oxide with perhydroxyl ion ($\text{HO}_2^{\cdot-}$).

The mechanism of aluminium dissolution in alkaline media. From a thermodynamic point of view, aluminium is an active metal, which is determined by the negative value of its equilibrium electrode potentials (-1.662 V , $\text{Al} - 3\text{e} = \text{Al}^{3+}$; -2.35 V , $\text{Al} + 4\text{OH}^- - 3\text{e} = [\text{Al}(\text{OH})_4]^-$) [64].

The high corrosion resistance of aluminium under natural conditions is due to the presence of a multilayer passive film on its surface. In air, pure aluminium is covered with a strong oxide film 5–10 nm thick, which protects it from further oxidation [65]. It is formed as a result of oxidation of the surface layer of a pure metal by air and water oxygen molecules and reaches a thickness

that ensures it is impervious to gases. To date, a lot of information about its structure has been accumulated. According to some data [66], under natural conditions at a temperature of 20–90 °C it consists of three layers: an amorphous oxide or hydroxide several nm thick located directly on the aluminium surface; a layer of pseudo-boehmite $\text{Al}_2\text{O}_3 \cdot 1.3\text{H}_2\text{O}$ located in between; and a layer of bayerite $\text{Al}_2\text{O}_3 \cdot 3\text{H}_2\text{O}$, a few microns thick on the top of it. According to other data [67–69], the protective film is a thin barrier layer of monohydrate orthorhombic boehmite $\gamma\text{-AlO}(\text{OH})$ adjacent to the metal surface and a thicker outer layer of crystalline oxide consisting of bayerite or hydrargillite $\text{Al}_2\text{O}_3 \cdot 3\text{H}_2\text{O}$. Some authors noted that under normal conditions, a protective X-ray amorphous oxide layer with a thickness of 4–10 nm was formed on the surface of the aluminium, which may include bayerite $\text{Al}(\text{OH})_3$ and boehmite $\text{AlO}(\text{OH})$ [70–72]. The determining influence on the biocorrosion of the D16T alloy is exerted by the composition and state of the passivating layer on its surface [73–76].

Metallic aluminium actively reacts with various oxidising agents, including O_2 and H_2O . For example, the reaction products of aluminium with water are hydrogen and solid oxidation products formed according to schemes (5)–(7):



The mechanism of aluminium oxidation has been studied in detail by a number of authors in [77–80]. The electrochemical dissolution of aluminium, according to the authors of [81, 82], includes at least two conjugated processes: the formation of a protective passive oxide film ($\text{Al} + 3\text{OH}^- - 3\text{e} = \text{AlO}(\text{OH}) + \text{H}_2\text{O}$) and its chemical dissolution with the formation of soluble aluminates. The authors of [83] believe that in solutions with $\text{pH} < 12$, the rate of formation of a passive film is higher than the rate of its dissolution. Therefore, the rate of aluminium corrosion is controlled by the stage of removing hydroxide films from the metal surface, the dissolution of which is determined by the diffusion of $[\text{Al}(\text{OH})_4]^-$ and OH^- . It was pointed out in [84] that the corrosion of pure aluminium

in an alkaline solution can be explained by the operation of a short-circuited corrosion cell and includes the stages of formation and dissolution of a natural oxide film with simultaneous reduction of water molecules.

The development of modern methods for a reliable assessment of the biodamage of materials, the prediction of the effect of biocorrosion on the mechanical characteristics of products and the safety of their further operation are important and urgent tasks. Therefore, the study of the problem of microbiological corrosion of metals is of great importance for the development of ways to increase the durability of metal materials and products and structures based on them. Aluminium and its alloys are used as the main structural material for the manufacture of equipment for the food industry, aircraft, and spacecraft [85].

Now, the mechanism of metal biocorrosion under the influence of microscopic fungi has not been fully studied, and the existing methods of protection against it are ineffective [86, 87]. The biocorrosion of aluminium and alloys based on it is still a poorly studied issue and causes a lot of controversy in the scientific world.

Purpose: determination of the main biological factor initiating biocorrosion of the D16T alloy; assessment of the biological impact of the association of microscopic fungi on the alloy in order to develop scientifically grounded and effective methods of protecting aluminium and its alloys from biocorrosion by micromycetes.

The focus of the study was the aluminium alloy D16T in accordance with state standard (GOST) 4784-2019 after hardening and natural ageing, which is widely used for the manufacture of load-bearing elements of structures and equipment of fuel systems of aircraft, car bodies, parts of various machines and assemblies operating at low temperatures, in the food and pharmaceutical industries. In our previous study, we investigated the biocorrosion of AD0 grade aluminium and aluminium-based alloys: B65, D16, AMg6 [88, 89].

Using a scanning electron microscope, the stages of initiation and development of biocorrosion of the D16T alloy under the influence of a consortium of mould fungi were studied. The

phase composition of D16T corrosion products has been studied.

2. Experimental

In the experiments, a consortium of natural strains of microscopic fungi was used, the spores of which were isolated from the air of industrial premises and from washings from the working surfaces of equipment. The surface of Czapek–Dox solid nutrient medium with sucrose, poured into Petri dishes, was inoculated with micromycete spores. Petri dishes with a dense nutrient medium were open in the working areas of production facilities for several hours, after they were placed in a thermostat for the development of lawn of micromycetes. According to the second method, swabbings of equipment surfaces were applied to the surface of a dense nutrient medium in the form of a suspension of micromycete spores in physiological solution (0.9% NaCl), obtained by wiping the surfaces with a cotton swab. Next, the prepared metal samples were placed on the lawns of micromycete consortiums. The experiment lasted at least 10 months at a temperature of (27 ± 2) °C in a biological thermostat. A comparison was performed with control samples placed on sterile nutrient media. The experimental technique is described in detail in [51, 52, 90].

The identification of micromycetes from the surface of metal samples was carried out based on their morphological and cultural features, using an identification guide [91, 92].

The results of the research showed that the mycobiota of aluminium alloys was mainly represented by the following genera of micromycetes: *Alternata*, *Aspergillus* *Mucor* and *Penicillium*.

Preparation of samples and the assessment of biocorrosive damage. Metal samples in the form of 30x20x15 mm and 20x20x15 mm bars were ground to obtain a smooth surface and polished to a mirror finish. Then they were washed with water, the surface was degreased with carbon tetrachloride, ethyl alcohol, and dried.

Corrosion products after exposure were removed mechanically with a brush with polymer bristles. Corrosion products strongly adhering to the surface was removed by ultrasonic cleaning with an ultrasonic frequency of 20–30 kHz. The

medium was distilled water with a temperature of (20 ± 2) °C. For the identification of the most severe biodamage, the samples were analysed visually. To reveal the microstructure of the surface, the samples were etched in a Keller solution of the following composition: HF (48 %) 1.0 ml; HCl ($\rho = 1.19 \text{ g/cm}^3$) 1.5 ml; HNO_3 ($\rho = 1.42 \text{ g/cm}^3$) 2.5 ml; H_2O 95.0 ml.

The macroscopic study of the surface of the samples was carried out using an MBS-2 light microscope. Microstructural studies in the cross section of corroded samples were carried using an optical microscope MT 753F. The fine structure of the corroded samples was analysed using TESCAN VEGA 3 XMH scanning electron microscope with a lanthanum hexaboride LaB_6 cathode. Qualitative and semi-quantitative analysis of chemical elements present in the composition of corrosion products after exposing the samples to the lawns of micromycete consortiums was carried out using energy dispersive X-ray spectroscopy (EDS-analysis). The equipment for EDS analysis was an energy-dispersive spectrometer based on a semiconductor silicon-drift detector with nitrogen-free cooling, mounted on a scanning electron microscope column with a range of detected elements from Be(4) to Pu(94).

X-ray phase analysis of sample biocorrosion products was carried out by the standard method using a Dron-3M diffractometer with monochromatised CuK_α -radiation in a Bragg-Brentano geometry. The identification of crystalline phases was carried out by comparison of the obtained experimental values of interplanar distances and relative intensities with the reference ones.

Identification of ROS. For the registration of the extracellular superoxide anion radical O_2^- ; nitro blue tetrazolium chloride dye (NBT^{2+}) 2Cl^- was used. This dye is widely used for these purposes in various chemical and biochemical studies [93, 94], it is reduced to mono- and diformazans characterised by absorption maxima at 525 nm ($\epsilon_{525} = 23400 \text{ M}^{-1}\text{cm}^{-1}$ in ethanol) and 605 nm ($\epsilon_{605} = 40200 \text{ M}^{-1}\text{cm}^{-1}$ in a mixture of ethanol – chloroform), respectively [95]. Formazan was eluted from the aqueous extract using a dimethyl sulfoxide – chloroform mixture in a 2:1 volume ratio. The concentration of coloured formazan

in the analysed samples was determined using a UV-3600i Plus spectrophotometer (Shimadzu, Japan). As a control, a dye solution with the addition of superoxide dismutase (SOD, 15 Units) was used, which at $\text{pH} = 7$ and a temperature of $(20-25)$ °C with a rate constant of $k = (1.8 - 2.3) \times 10^9 \text{ M}^{-1}\text{s}^{-1}$ with absolute specificity, catalyses the reaction of dismutation of the superoxide anion radical into H_2O_2 and O_2 [96–98]. The research methodology is described in detail in [52, 90, 99].

Also, the formation of O_2^- was confirmed by the spectrophotometric method using adrenaline [100]. For experiments, we used a pharmacopoeial preparation of epinephrine hydrochloride (1 mM, $\text{pH} = 7$, treatment time 15 min), which in the presence of O_2^- turns into adrenochrome [101]. Adrenochrome formation was monitored spectrophotometrically using a UV-3600i Plus (Shimadzu, Japan) at $\lambda_{\text{max}} = 347 \text{ nm}$. The reaction constant of the superoxide anion radical with adrenaline is $(4.0-5.6) \times 10^4 \text{ M}^{-1}\text{s}^{-1}$ [102, 103]. The superoxide specificity of the adrenaline-adrenochrome system was confirmed by a significant (up to 75 %) inhibition of the detection of the superoxide anion radical in the presence of superoxide dismutase (SOD, 15 Units). 200 μl of 0.1 % aqueous solution of epinephrine hydrochloride was added to 2 ml of liquid exudate freed from micromycete cells. After 15-mins of incubation, spectrophotometric measurement was performed.

For the determination of hydrogen peroxide in the liquid exudate formed during aluminium biocorrosion, the so-called FOX method was used. The FOX-method is based on the change in colour of the xylenol orange dye ($\lambda_{\text{max}} = 540 \text{ nm}$, $\epsilon_{540} = 26800 \text{ M}^{-1}\text{cm}^{-1}$). The reaction reagent included: 500 μM iron ammonium sulphate; 50 mM sulphuric acid; 100 mM sorbitol; 250 μM xylenol orange [104]. The measurements were carried out using a UV-3600i Plus spectrophotometer (Shimadzu, Japan) at a wavelength of 540 nm. The amount of hydrogen peroxide was calculated using calibration curves.

The concentration of H_2O_2 was measured by the titanium method [105, 106].

3. Results and discussion

Interactions in the “metal - micromycetes” system at the stage of initiation of biocorrosion

should be considered as a set of physicochemical, chemical, and biochemical processes occurring at the interfaces between surface oxygen compounds of aluminium, forming its protective passive film, and an aqueous solution of exudate formed during the life of cells microscopic fungi, with the involvement of environmental components - oxygen and water.

The first stage mycological corrosion of metal is characterised by the development of colonies of micromycetes. For some period of time (3-5 days) they adapt, grow and develop, then exometabolites appear and locally accumulate, initiating the primary processes of destruction of the metal surface. Biocorrosion begins from the ends and on the side surfaces of the samples with the appearance of exometabolites or the so-called exudate in the form of a transparent mobile liquid. Where there is a local concentration of exometabolites, they interact with the components of the passive protective metal film. This is possible only with the participation of water, the film of which can appear on the metal surface due to capillary condensation. This will be facilitated by the mycelium of microscopic fungi fixed on the surface of the metal. Due to the energy inhomogeneity of the metal surface, its various parts will interact with living cells and electrolytes with different intensities [107]. This leads to the uneven formation of corrosion centres. Following this, electrochemical processes on the metal surface take part in the general mechanism and cathodic and anodic depolarisations occur. When the surface structures protecting the base metal are loosened, hyphae and conidia of microscopic fungi penetrate deep into the metal and interact with the components of the corrosive medium.

In these experiments, we simulated conditions close to the real operating conditions of metals and alloys, using artificially prepared nutrient media for cultivating micromycetes.

We have assessed corrosion damage during all stages of biocorrosion with a detailed analysis of the stages of the process, the appearance of samples, the area and depth of corrosion damage:

- the appearance of exudate in the form of a transparent liquid from the ends and on the side surfaces of the samples and the initiation of biocorrosion;
- fouling of the sample surface with mycelium

followed by the introduction of hyphae into the loose surface structures of the metal;

- transformation of a transparent exudate into a mobile gel, easily removed from the metal surface;

- the transformation of the gel into jelly;

- ageing and crystallisation of jelly with the formation of amorphous corrosion products;

- the formation of solid crystalline corrosion products that firmly adhere to the surface of the sample.

In the case of electrochemical corrosion of aluminium, a similar sequence of processes is not observed. We will consider these stages in more detail.

The initial stage of biocorrosion is the local appearance on the surface of a micromycete consortium lawn in contact with the metal, an exudate in the form of a transparent and highly mobile liquid with a pH of 8–9 (Fig. 4). The formation of an exudate was also noticed in the study of aluminium biocorrosion under the influence of individual strains of micromycetes on it [90]. Similarities can also be traced in the

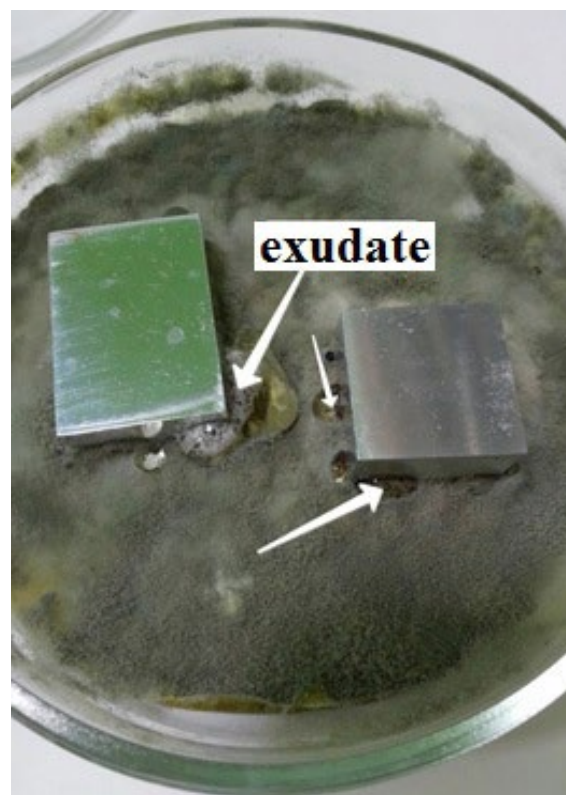


Fig. 4. Drops of exudate on the lateral surfaces of corrosive samples (shown by arrows)

staging of the process and general observations.

Within two to three days from the beginning of the experiment, the consistency of the exudate becomes gel-like (Fig. 5). A transparent gel eventually turns into a jelly, undergoes ageing and its structural changes occur: compaction, turbidity and crystallisation, and the pH value gradually shifts to neutral.

The study of the surface morphology of the samples at the initial stage of biocorrosion showed that the mycelium of micromycetes is fixed on the surface of the samples (Fig. 6) and then penetrates through the protective film deep into the metal (Fig. 7).

After adsorption and fixation of hyphae of micromycetes on certain energetically favourable areas of the alloy surface, hyphae and conidia of micromycetes are introduced into the loose and defective sites of the surface layers of the metal. In these sites, pittings and ulcers are subsequently found (Fig. 8).

Biocorrosion mechanism of the aluminium.

The biocorrosion of aluminium is a complex phenomenon that includes at least three processes [89]: 1) the interaction of the components of the protective passive film and pure metal with reactive oxygen species released during the life of microscopic fungi; 2) electrochemical corrosion

of the alloy due to the operation of short-circuited galvanic cells; 3) reductive activation of oxygen with the participation of zero-valent aluminium ZVAL with the formation of hydrogen peroxide, which is involved in the direct destruction of the metal and in the cascade of ROS reactions, as well as heterogeneous decomposition of hydrogen peroxide by a mechanism similar to the Fenton reaction.

Intense corrosion damage to the surface of the D16T alloy at the initial stages of exposure to microscopic fungi suggests that the corrosive

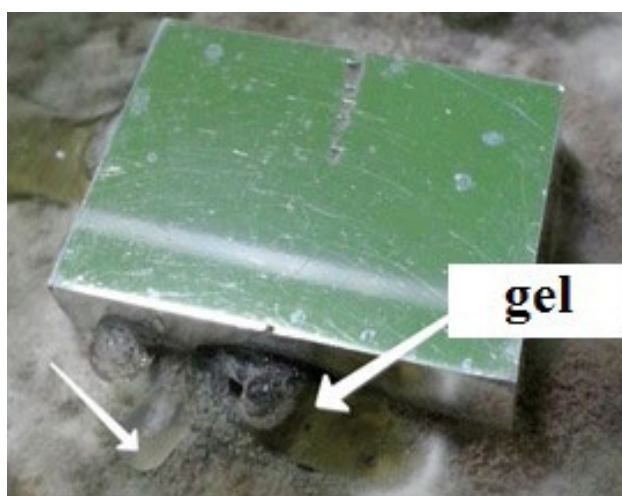


Fig. 5. Translucent gel at the sites of exudate formation (shown by arrows)

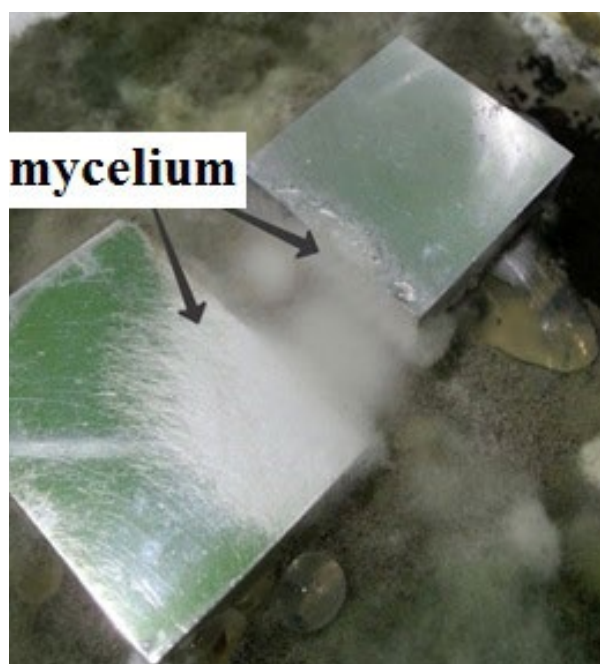


Fig. 6. Adhesion of mycelium of micromycetes on the surface of the samples and their gradual overgrowth (shown by arrows)

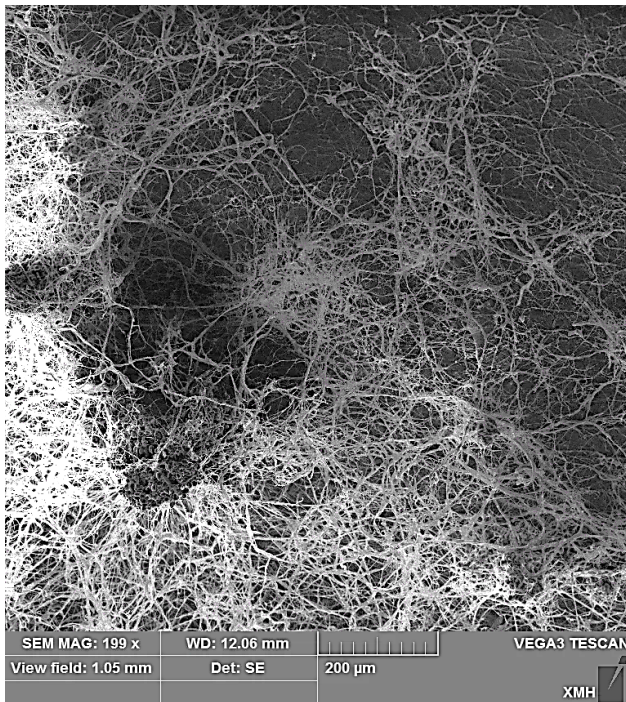


Fig. 7. Micrograph of the sample surface with mycelium filaments (hyphae) of micromycetes

agents are, first of all, OH^- and H_2O_2 . The cascade of reduction reactions involving water molecules that proceed according to the electrochemical mechanism on the microcathode areas of the surface of the corroding aluminium alloy can serve as the source of OH^- -ions, while oxidative dissolution of aluminium alloy occurs on the microanode areas. It is difficult to explain the continuous accumulation of OH^- ions during the initial stages of biocorrosion using only the electrochemical mechanism of corrosion. During this period, no obvious corrosion damage is observed, however, exudate drops in direct contact with the surfaces of the samples grow in volume and, at the same time, their pH value increases (up to 10–11). Upon exposure to microscopic fungi OH^- ions constantly accumulate in the liquid exudate in sites of direct contact with the metal, which is possible only as a result of the occurrence of respiratory and metabolic processes in the cells of microscopic fungi with the participation of oxygen and water.

Interaction of aluminium with ROS produced by micromycetes. The surface charge of a protective aluminium oxide film plays an important role in its interaction with charged particles. We believe that the surface of aluminium in an aqueous

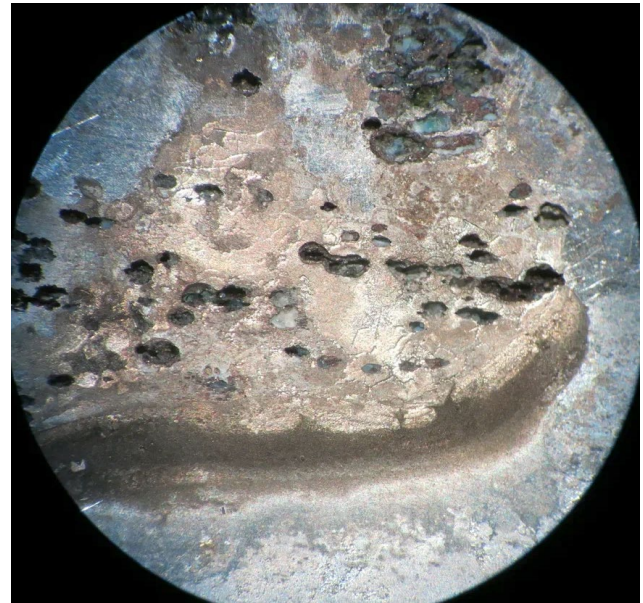
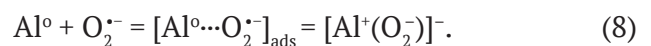


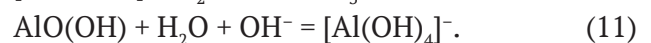
Fig. 8. Surface of the sample after exposure to a consortium of micromycetes for 60 days. Pitting is visible. Some pits merge into ulcers and cavities

solution containing hydroxide ions is negatively charged. This promotes the adsorption of electron acceptor molecules, including oxygen molecules, on the surface of a passive aluminium film, which are rapidly reduced on it.

If we assume that due to a local increase in pH, the protective passive film was dissolved and its clean surface was exposed, then aluminium will react rapidly with the ROS produced by micromycete cells. For example, it becomes possible for aluminium to interact with the superoxide anion radical released during the life of microscopic fungi, which can be represented by the scheme (8):



The resulting surface adsorption complex undergoes hydrolysis with the formation of an OH^- ion and $\text{Al}(\text{OH})_3$ by reactions (9)–(11):



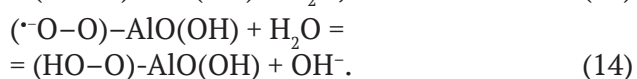
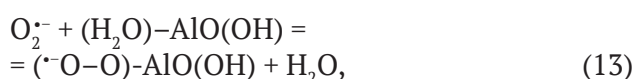
After dissolution of the protective film of aluminium with the formation of tetrahydroxoaluminate ions, they diffuse into the volume of a drop of liquid exudate, where

its further transformations are possible in close proximity to the mycelium of micromycetes.

Hydroxide ions and water molecules are able to penetrate and move in films of surface oxygen compounds of aluminium [107]. Studies [108, 109] have shown a significant effect on the rate of dissolution of aluminium in an alkaline medium of the diffusion factor - the delivery of OH^- ions to corroding metal. We believe that the development of pitting corrosion of aluminium in an aqueous medium with $\text{pH} > 7$ is initiated due to the local enrichment of the surface with hydroxide ions. The nucleation and development of pitting on the aluminium surface proceeds primarily in defects in the passive oxide film due to the displacement of oxygen-containing aluminium compounds by aggressive OH^- anions followed by the interaction of the metal with ROS. The adsorption/chemisorption of the superoxide anion radical on the hole centres of the passive aluminium film components is possible. For example, the ability of the $\gamma\text{-AlO}(\text{OH})$ boehmite surface to stabilise ROS has been proven [110]. The superoxide anion radical $\text{O}_2^{\cdot-}$ stabilises on the defect-free boehmite surface, then, with the participation of water, the surface hydroperoxide (perhydroxyl) radical HO_2^{\cdot} is formed according to reactions (12)–(14):



or



During the life of microscopic fungi, as well as under the conditions of oxidative stress of micromycete cells, a certain amount of endogenous hydrogen peroxide in concentrations of 10^{-4} – 10^{-6} M metabolically accumulates in the environment. In this case, its interaction with aluminium can occur according to the Fenton reaction. The formation of hydroxyl radicals (HO^{\cdot}) will be initiated through electron transfer from Al^0 to H_2O_2 according to schemes (15)–(17) [111]:

$$\text{Al}^0 + 3\text{H}_2\text{O}_2 = \text{Al}^{3+} + 3[\text{H}_2\text{O}_2]^{\cdot-}, \quad (15)$$

$$3[\text{H}_2\text{O}_2]^{\cdot-} = 3\text{OH}^- + 3\text{OH}^{\cdot}, \quad (16)$$

$$\text{Al}^{3+} + 3\text{OH}^- = \text{Al}(\text{OH})_3. \quad (17)$$

Our experiments confirmed that the decomposition of hydrogen peroxide begins after some time, during which the natural oxide layer dissolves. Thus, under the considered conditions, hydrogen peroxide is an intermediate product of oxygen activation reactions and undergoes heterogeneous decomposition, electrochemical transformation (conjugated oxidation and reduction reactions), or enzymatic decomposition. In an alkaline environment H_2O_2 turns into HO_2^- and then reduced to OH^- according to schemes (18)–(20):



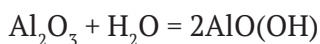
in total:



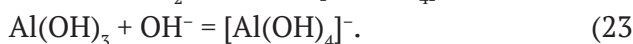
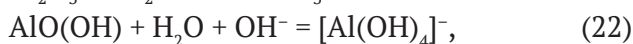
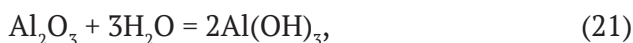
Now, a number of literary sources [112 – 115] report that in an aqueous solution it is possible to generate isomeric forms of the HOOH molecule, in particular, the oxywater molecule $[\text{H}_2\text{O}^+\text{O}^-]$ in the form of a zwitterion. The latter heterolytically dissociates with the release of a water molecule and a singlet oxygen atom $\text{O}([\uparrow\downarrow][\uparrow\downarrow])$ or ^1D -oxene $\text{O}([\uparrow\downarrow][\uparrow\downarrow][_])$, which exhibit high oxidising properties and mediate the decomposition of hydrogen peroxide itself. We do not rule out the possibility of the formation of such highly reactive molecules in the studied system. The formation of oxywater and singlet oxygen can probably be postulated in the general scheme of aluminium–ROS interactions.

In the overall process of aluminium biocorrosion, we propose to conditionally distinguish several stages [116–118]. *Aluminium biocorrosion induction stage*, during which the hydrolysis of the protective passive film occurs, leading to an impairment of its continuity and an increase in the permeability for water molecules. This becomes possible due to the presence of structural defects in the passive aluminium film that are impermeable to air oxygen, but open upon contact with liquid water, for example, due to the Rehbinder effect. Another possible reason for the destruction of the protective film is its chemical dissolution, which will occur locally in its most defective sites. This is facilitated by the formation of a liquid exudate with basic properties by micromycetes. At $\text{pH} > 7$, the

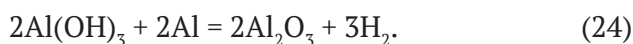
dissolution of aluminium oxide compounds occurs mainly with the formation of $[\text{Al}(\text{OH})_4]^-$ ions [119, 120] and includes oxide hydration and dissolution of the formed aluminium hydroxide according to schemes (21)–(23):



or



According to [121], when aluminium hydroxide comes into contact with metallic aluminium, the so-called “rehydrolysis” of aluminium hydroxide can occur, leading to the formation of aluminium oxide according to reaction (24):



The resulting aluminium oxide is less permeable to water molecules than aluminium hydroxide. Defects that are opened upon contact with water are closed by a newly formed oxide, which significantly inhibits the biocorrosion of the metal.

At the induction stage [77–80], the Al–O–Al structural bridges are destroyed with the formation of Al–OH bonds; at the same time, the pH of the exudate formed by micromycetes increases, the value of which can reach up to 11. With a passive aluminium film thickness of 2–4 nm [76], 5–10 aluminium oxide layers can be located above the surface of a pure metal. The passive film localised at the boundaries of crystal grains will probably have the most defective structure [79].

Hydroxyl groups are able to diffuse from the “exudate-passive film” interface to the “passive film-aluminium” interface, forming structural

hydroxides. The diffusion of OH groups is significantly accelerated with an increase in the number of defects in alumina [80]. When the OH-groups come into contact with metallic aluminium, aluminium hydroxide is “rehydrolysed” according to reaction (24). The resulting aluminium oxide will increase the thickness of the passive film and may be hydrolysed again. The intensification of the process will be facilitated by the destruction of the oxide coating.

In experiments, we noticed the formation of hydrogen and saturation of drops of liquid exudate adjacent to the surfaces of the samples with it (Fig. 9). If the rate of hydrogen formation is higher than the rate of its diffusion, the resulting hydrogen, accumulating under the oxide coating, can lead to its destruction [75]. The oxide coating is a significant obstacle to the formation of hydrogen, since the diffusion coefficient of hydrogen in the oxide is 10^{-13} – 10^{-14} cm²/s [122, 123]. In turn, the effective diffusion coefficient of OH⁻-groups in the oxide is much lower and amounts to $\sim 10^{-17}$ cm²/s [80]. The conditional end of the induction period is due to the fact that the hydrolysed passive film dissolves locally in the most defective sites, which leads to the intensification of biocorrosion.

Intensive aluminium biocorrosion stage. As the oxidation of the metal proceeds, point penetration defects and their number per unit surface increases. The resulting aluminium hydroxide covers most of the aluminium surface. In the process of aluminium oxidation, aluminium hydroxide micelles are formed in the zones of penetration defects, which do not prevent the transfer of water to the oxidising metal, fill the defect volume, and eventually emerge on the

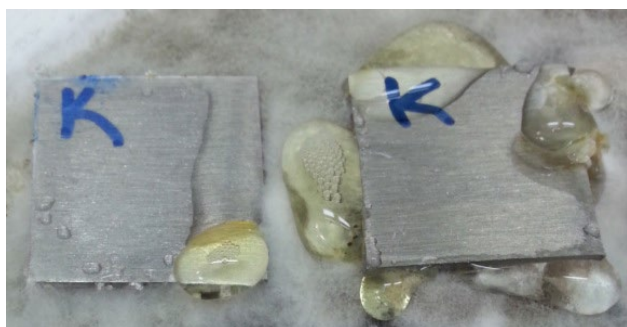


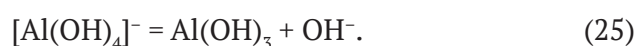
Fig. 9. The formation of hydrogen produced during the interaction of exudate with the D16T alloy at the sites of its contact with the lawn of micromycete mycelium.

aluminium surface. Further, this leads to the formation of a water-saturated gel, enveloping the corroding area of the surface of the metal sample.

The transfer of aluminium hydroxide is carried out mainly by ions $[\text{Al}(\text{OH})_4]^-$ [118]. Mass transfer prevents the rapid accumulation of solid corrosion products on the aluminium surface and promotes an increase in the rate of biocorrosion. Over time, the gel-like aluminium hydroxide, enveloping the surface of the metal, is converted into its crystalline form. Over time, the gel ages: it loses water molecules, becomes structured, compacted, and loses the ability to pass water to the surface of the oxidised metal [77]. With a lack of hydroxide ions, a decrease in water permeability occurs due to an increase in the volume of corrosion products and structuring of the freshly formed hydroxide. These processes can be represented as a diagram: *micelles $\text{Al}(\text{OH})_3 \rightarrow$ water-saturated gel \rightarrow structured gel \rightarrow crystalline corrosion products*. From this moment, a slowdown in the overall rate of aluminium biocorrosion is observed. Intensive oxidation of the metal gradually fades.

pH change of the exudate during aluminium biocorrosion. We noticed that in the studied system, the pH value of the exudate formed at the metal–micromycete consortium boundary can either increase or decrease. It is known [124] that during the hydration of aluminium oxide, which forms a passive surface film, hydroxide ions are formed, which are bound to the metal

surface in various ways. The formation of the surface charge is controlled by the adsorption of protons and hydroxide ions by active sites on the surface. The surface of aluminium hydroxide is amphoteric and, depending on the pH of the medium, can act as an acid or Bronsted base. It is known, that at a pH value less than the value corresponding to the zero charge point (ZCP), the surface is charged positively, and at a higher pH value, it is charged negatively. The ZCP value can vary from ~ 7 to ~ 10 depending on the type of aluminium oxide [124]. The decrease in exudate pH during the stage of intense biocorrosion of aluminium is associated with the dissolution of aluminium hydroxide, and the increase in pH is associated with the association of $\text{Al}(\text{OH})_3$ into chains (polymerisation) [118], accompanied by the loss of OH^- according to reaction (25):



These processes compete with each other. In turn, during the stage of biocorrosion initiation (3–5 days), the pH of the exudate can reach 8–9, which is associated with the formation of ROS by micromycete cells and their interaction with water and air oxygen. These observations were confirmed by us for a wide range of metals [125, 126].

Finishing stages of biocorrosion. The process of biocorrosion ends with the depletion of the nutrient medium and the termination of the life of micromycetes. In our experiments, after at



Fig. 10. Biocorrosion products of the alloy: gel and jelly at the sites of exudate formation (a); crystalline corrosion products (b)

least ten months of exposure, complete depletion of the nutrient medium was observed. The products of aluminium biocorrosion successively turned from a gel (Fig. 10) into multi-coloured crystalline formations of irregular shape (Fig. 11). The surface of the samples, which was in direct contact with the lawn of micromycetes, was subjected to significant damage (Fig. 12).

Assessment of corrosion damage. Corrosion damage develops according to the mechanism of pitting corrosion, turning into ulcer corrosion, and is localised at the sites of contact of aluminium with exudate produced by micromycetes. After 10 months of exposure, the entire surfaces of the samples, which were in close contact with the

mycelium of the consortium of microscopic fungi, were subject to corrosion damage. Characteristic features of the final stage of biocorrosion of aluminium alloys are deep ulcers (up to 2–3 mm) and cavities of various shapes filled with corrosion products (Figs. 11, 12).

Along with white and brown corrosion products in the form of irregularly shaped clusters, we observed an insignificant amount of light blue corrosion products characteristic of copper compounds (Fig. 13).

The results of X-ray phase analysis of the corrosion products of the D16T sample, which were collected from different parts of the surface, are shown in Table 1. During the destruction of

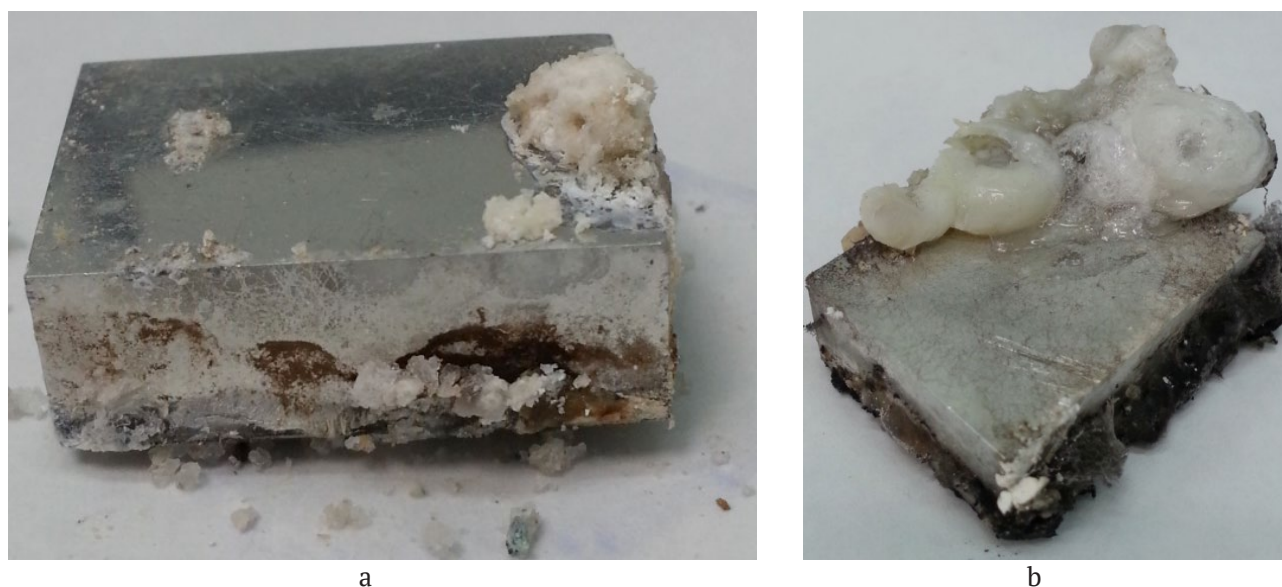


Fig. 11. Appearance of samples with corrosion products: (a) 3 months after the beginning of the experiment; (b) 10 months after the start of the experiment

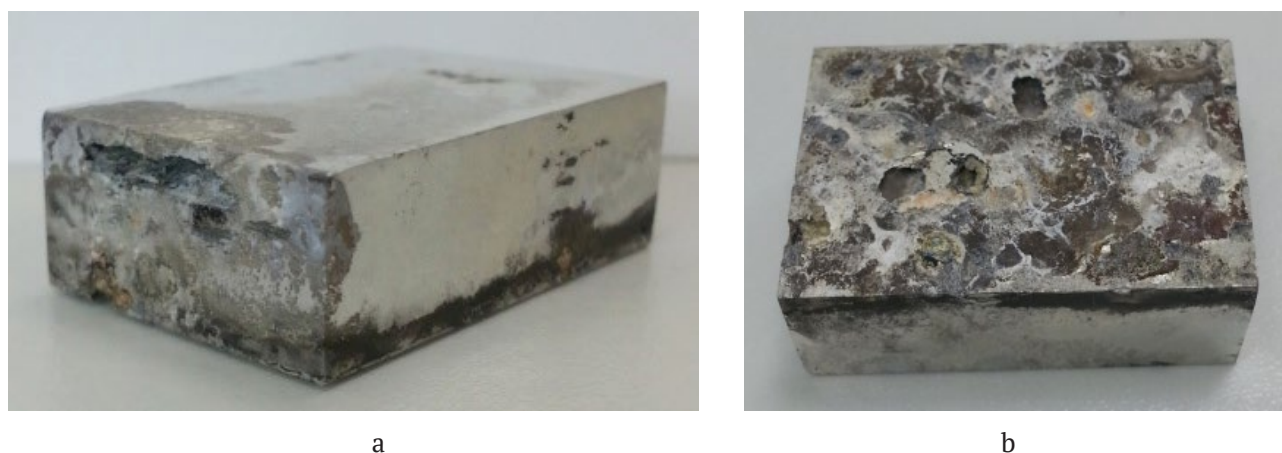


Fig. 12. Appearance of the sample without corrosion products during the final stages of the experiment (10 months): lateral edges of the sample (a) (subsurface corrosion is clearly visible); surface in direct contact with the lawn of a micromycete consortium (b)

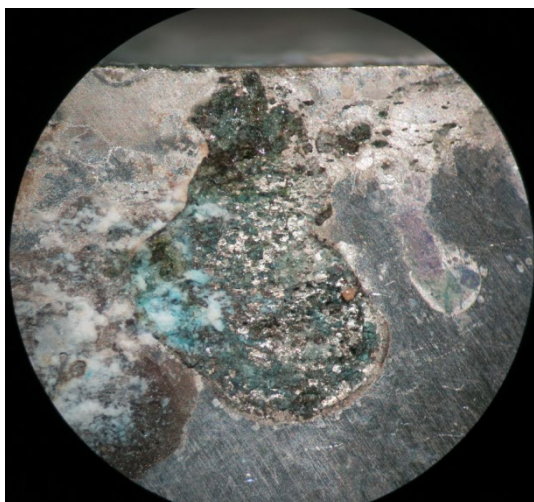


Fig. 13. Products of copper corrosion on the sample surface

the material under the influence of micromycetes, we found some oxygen compounds of aluminium in its corrosion products: $\gamma\text{-Al(OH)}_3$, $\alpha\text{-AlO(OH)}$, $5\text{Al}_2\text{O}_3 \cdot \text{H}_2\text{O}$ [120, 127, 128], copper and magnesium.

EDS analysis confirmed the presence of aluminium, copper, and magnesium oxygen compounds in the corrosion products [121, 129]. The results of the EDS analysis of the corrosion products of the D16T alloy sample collected from different parts of the sample surface are shown in Fig. 14. Phosphorus, sulphur and nitrogen

were recorded in addition to oxygen among non-metals. In our opinion, the sources of these non-metals are the remains of cells of microscopic fungi and elements of the nutrient medium.

At the initial stage, local selective corrosion is observed on a small area, which intensively spreads deep into the metal along the grain boundaries. After, local corrosion in the form of spots spreads over the surface of the samples. Observations using an electron microscope made it possible to detect the presence of centres of intergranular corrosion (Fig. 15). The depth of corrosion damage in some areas of the surface reached 1.5–2.0 mm. A corrosive medium formed as a result of the activity of microscopic fungi and containing ROS and hydroxide ions entered deep into the metal and destroyed the outer grain boundaries of the D16T alloy. There was a fragmentary destruction of the grains. In this case, the grain boundary material acted as an anode to the copper-rich grains that are the cathode regions.

Microstructural studies of the samples showed the presence of areas of biocorrosion damage under the metal’s surface. Subsurface corrosion starts at the surface of the metal and spreads deeper. The mycelium of microscopic fungi can easily penetrate into the formed cavities in the alloy, which contribute to the deepening of the process.

Table 1. Data of X-ray structural analysis of corrosion products of the D16T alloy

Location of sites (no. 1, no. 2) on the surface of the sample with corrosion products for which X-ray phase analysis was performed	Surface area number	2θ , grad	d , nm	I , %	Phase
	1	38.58	2.3336	100	Al
		40.2	2.2432	12.35	$\gamma\text{-Al(OH)}_3$
		43.54	2.0785	37.18	Al
		44.8	2.0230	58.70	$\gamma\text{-Al(OH)}_3$
		0.64	1.8025	16.97	$\gamma\text{-Al(OH)}_3$
		65.18	1.4312	15.46	Al
	2	35.22	2.5481	9.16	AlO(OH)
		36.9	2.4358	12.07	$\gamma\text{-Al(OH)}_3$
		38.69	2.3278	45.20	$5\text{Al}_2\text{O}_3 \cdot \text{H}_2\text{O}$
		40.26	2.2400	9.60	$\gamma\text{-Al(OH)}_3$
44.94		2.0170	100	Al	
50.7		1.8005	15.13	$\gamma\text{-Al(OH)}_3$	
65.28		1.4293	51.96	Al	
78.3		1.2205	22.15	Al	

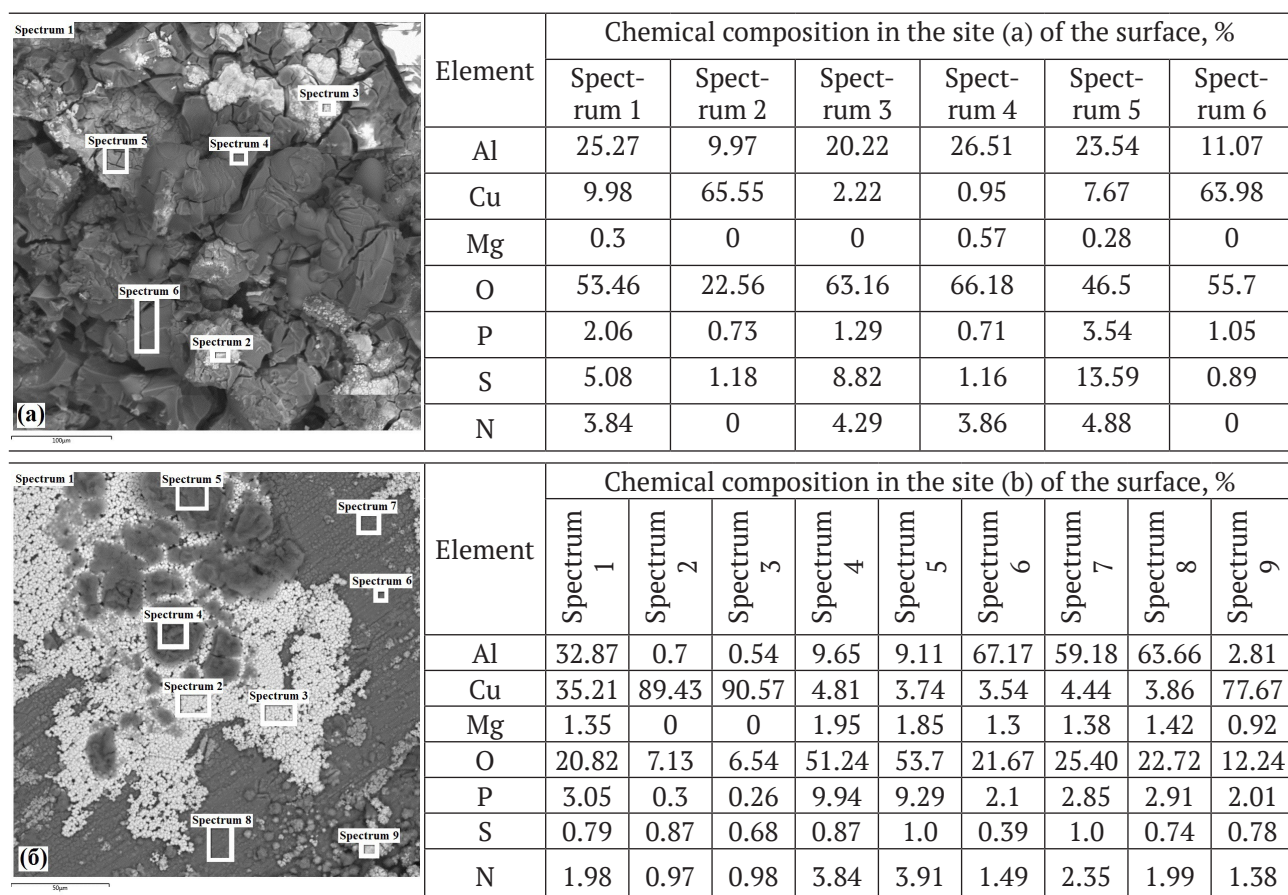
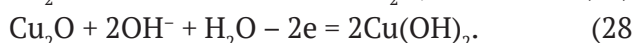
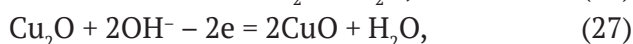
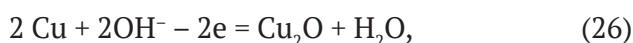


Fig. 14 Results of EDS analysis of corrosion products in sites (a) and (b) on the sample surface

The presence of copper and magnesium compounds in the biocorrosion products of the D16T alloy can be explained by component-selective corrosion of the alloy and selective etching of aluminium from its structure. A more intense destruction of aluminium occurred in the surface layers of D16T. The interaction of copper and magnesium with ROS at pH>7 is also thermodynamically possible. This was confirmed by the EDS analysis of corrosion products studied on a transverse section of the sample (Table 1).

We proposed that the oxidation of copper in an alkaline medium is realised with the formation of oxygen compounds of copper according to schemes (26)-(28):



Intergranular corrosion. The analysis of literature data shows that the driving force of the IGC is the difference in electrochemical potentials that occurs at the matrix/particle interface

(aluminium solid solution/second phase), the value of which, in the general case, is the higher, the less coherent the interface is and the larger the size particles [130].

The intensity and depth of IGC depend on the structure of the matrix, primarily on the length and structure of grain and subgrain boundaries [131]. Since the D16T alloy is located at the boundary of the ($\alpha + S$) and ($\alpha + S + \theta$) regions, two types of strengthening particles can be distinguished in it – θ (Al_2Cu) and S (Al_2MgCu), the polarisation of which is different in relation to the matrix: the θ phase is the cathode in relation to the matrix, and the S phase is the anode.

The phase of Al_2Cu intermetallic compound is distinguished by grain boundaries, which are unstable and selectively decompose due to electrochemical heterogeneity. From the intermetallic compound Al_2Cu aluminium can selectively pass into the solution and the copper forms irregularly shaped conglomerates. The surface becomes porous, cavities of various configurations and depths are formed (Figs. 15, 16).

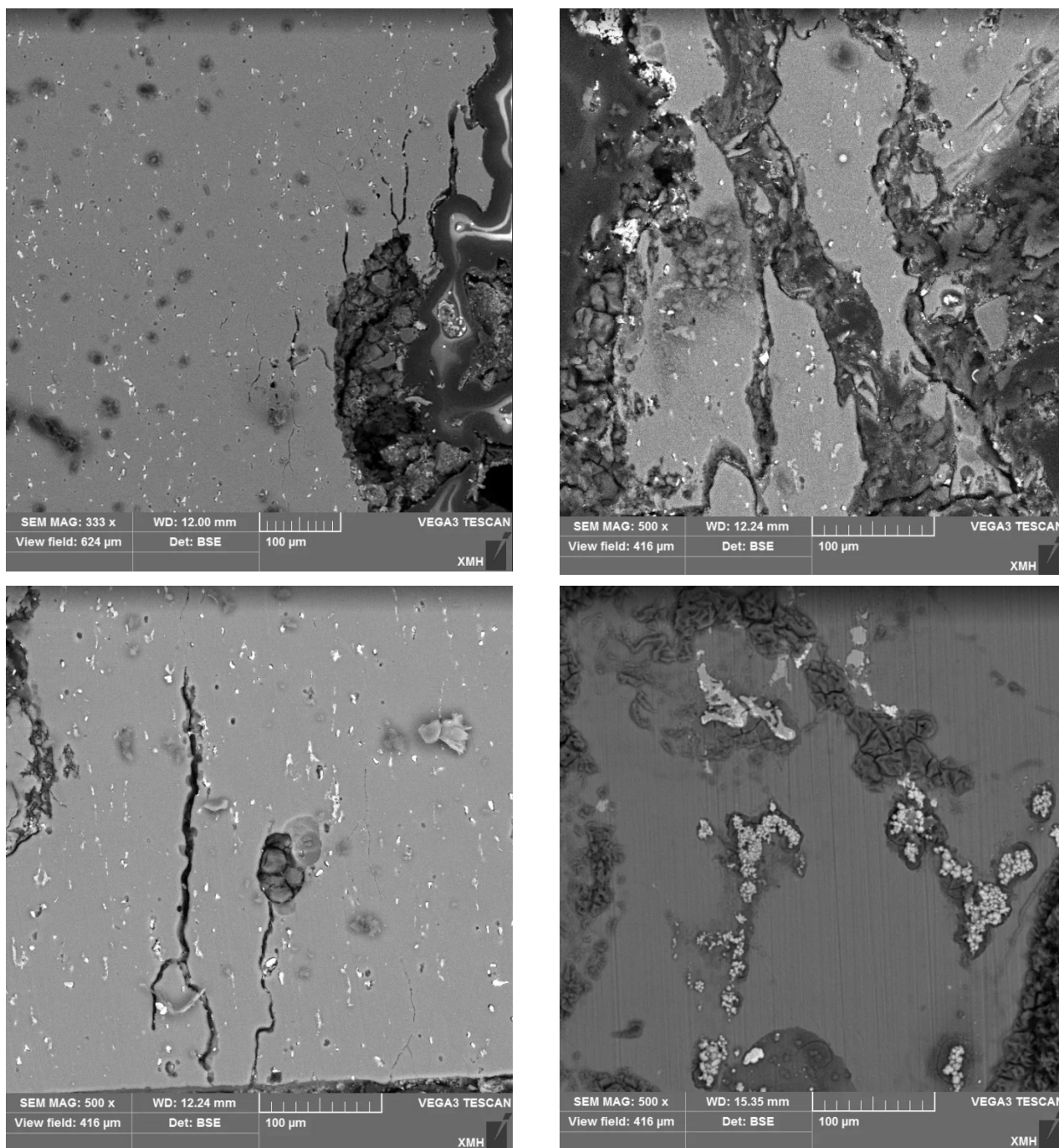


Fig. 15. Microstructures of different sections of the surface of a lateral section of a sample with foci of intergranular corrosion

Subsequently, copper also undergoes destruction, as evinced by the presence of its oxidation products.

The process of dissolution of the S phase is more complicated. First, it dissolves according to the anode mechanism, losing aluminium and magnesium ions. This leads to a change in the chemical composition of the phase, and it becomes a cathode in relation to the matrix, with

a corresponding change in the mechanism of its chipping [130].

Based on the obtained data, it can be concluded that the IGC of the D16T alloy under the influence of microscopic fungi is due to the synergistic effect of structural and phase factors. Corrosion lesions are characterised by their great depth and branching. This may be due to the separation of phases along the boundaries of subgrains and the

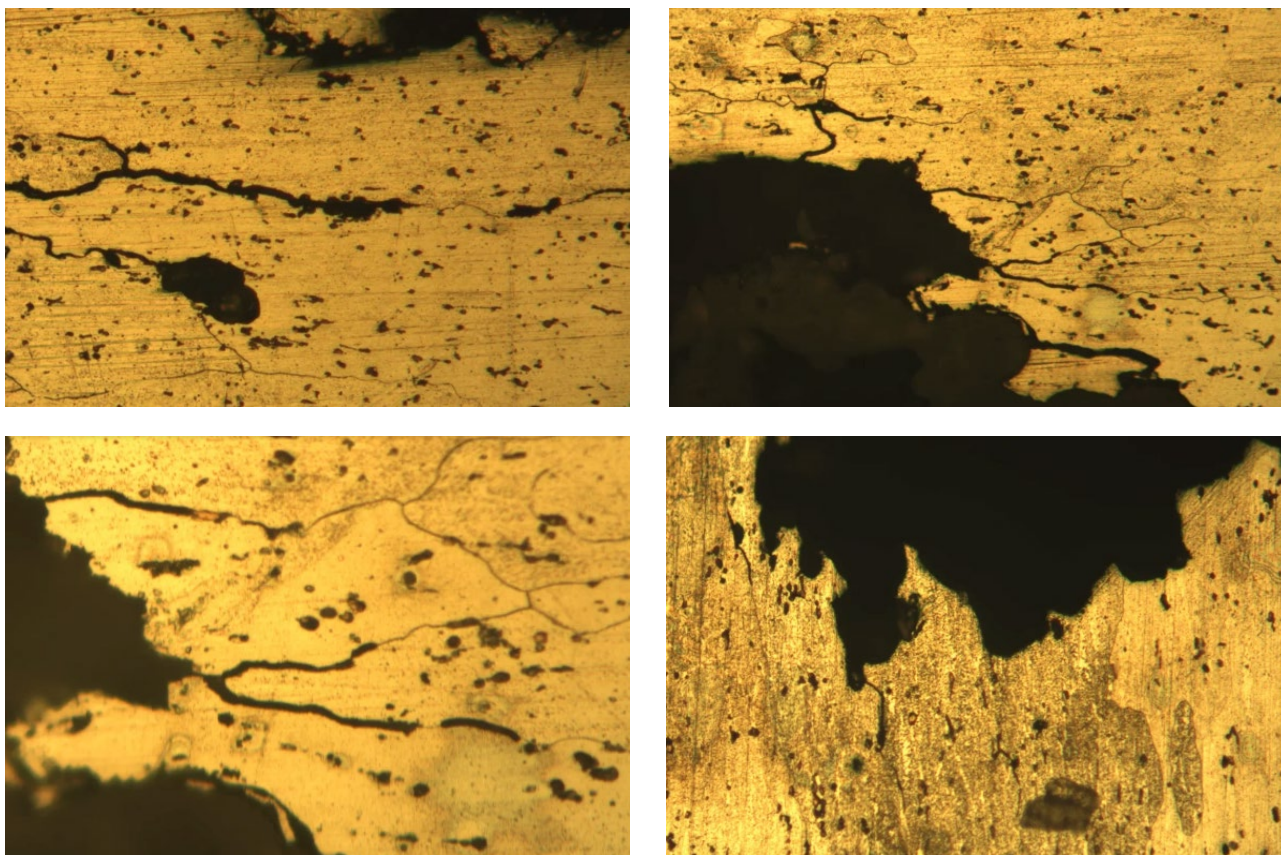


Fig. 16. Foci of intergranular corrosion of samples

emergence of a greater driving force of corrosion (difference in electrochemical potentials). Along with this, relatively narrow, but very deep channels of corrosion lesions are observed, which merge into continuous corrosion centres in the form of ulcers. This pattern may be due to the decomposition of the solid solution, which leads to the formation of large particles of stable S and θ phases in the recrystallised regions [132, 133].

Classical methods of corrosion protection, such as the use of organic inhibitors or coatings based on polymeric materials, become ineffective under conditions of microscopic fungi development. Much more often, experts offer methods of inhibiting, rather than combating biocorrosion. The tactics of combating the biocorrosion of metals under the influence of micromycetes should take into account the peculiarities of the biochemical mechanisms of the functioning of microorganisms. Only by knowing the mechanisms of interaction in the “microorganism - metal” system is it possible to create effective ways to protect metals from biocorrosion.

The formation and release of reactive oxygen species by micromycetes into the external environment is one of the factors of biocorrosion. Hyperproduction of ROS may be a consequence of oxidative stress in micromycetes. This may be caused by an impairment of the natural “redox status” of microscopic fungal cells that are in direct contact with the metal surface. The presence of water contributes to the conversion of ROS into their most stable and “long-lived” forms, which either initiate the biocorrosion of duralumin and its alloys themselves, or trigger a cascade of reactions involving hydroxide ions.

Model systems show that the surface of an aluminium alloy in contact with micromycete consortiums is subjected to global destruction, which is unacceptable when operating equipment or products under the influence of micromycetes. Based on a detailed study of the mechanism of occurrence and development of biocorrosion of duralumin under the influence of microscopic fungi, effective methods of protection against biocorrosion will be developed.

4. Conclusions

During the vital activity of microscopic fungi, reactive oxygen species that initiate the biocorrosion of the D16T alloy are formed. The initial stage of biocorrosion is due to the hydrolysis of the protective passive aluminium film. During the stage of intense biocorrosion, oxygen-containing aluminium compounds in the form of a water-saturated gel are formed. Further, this corrosion product is accumulated and its water permeability decreases. The gel undergoes “ageing” and turns into crystalline products. The conidia and hyphae of microscopic fungi adhere, mechanically attach to the surface of the metal and penetrate into the surface layers and deep into the metal, causing its corrosion damage in the form of pitting, ulcers, and cavities. The initiation of metal biocorrosion is a consequence of the hyperproduction of reactive oxygen species by micromycete cells as a result of oxidative stress. This may be their defensive strategy aimed at destroying xenobiotic material.

The development of intergranular and pitting corrosion of the D16T alloy under the action of micromycetes occurs at the sites of contact with exudate, which is locally enriched in hydroxide ions due to the cascade of reactions involving ROS. The nucleation and development of pitting on the surface of duralumin occurs in the defects of the passive oxide film due to the displacement of oxygen-containing surface compounds of aluminium and their interaction with corrosive OH⁻ anions and ROS. Hydrogen peroxide, as an intermediate product of the metabolism of micromycetes, on the surface of the D16T alloy can participate in the Fenton process or decompose heterogeneously, also provoking the development of aluminium biocorrosion.

The ultimate goal of research into the microbial corrosion of metals is the development of molecular tools aimed at diagnosing the occurrence, studying the mechanisms and rates of metal biocorrosion. This will allow the most effective strategies for protecting materials from biodegradation to be implemented. A systematic biological approach is required, including innovative methods for the isolation and characterisation of corrosive strains of microscopic fungi; conducting functional genomic studies; the investigation of the functioning

of microbial communities and dynamically developing relationships with environments; and the study of unique metabolites that are the end points of specific cellular processes.

For the determination of diagnostic signs of biocorrosion processes in metals, it is necessary to carry out a systematic study of the unique chemical and biochemical processes occurring in living cells, including the study of their low molecular weight metabolic profiles.

The study of metal corrosion mechanisms involving microbial communities will lead to new strategies for protection against biocorrosion. Our progress in understanding the mechanisms of corrosion of metals under different microbiomes is at an embryonic stage, but interdisciplinary electrochemical, microbiological and molecular tools will enable rapid progress in this area.

Author contributions

Belov D. V. – scientific leadership, research concept, methodology development, text writing, final conclusions. Belyaev S. N. – conducting experimental studies, writing a literature review and text editing.

Conflict of interests

The authors declare that they have no known competing financial interests or personal relationships that could have influenced the work reported in this paper.

References

1. Kolesnikova N. N., Lukanina Yu. K., Khvatov A. V. Biological corrosion of metal structures and protection against it. *Bulletin of the Kazan Technological University*. 2013;16(1): 170–174. (In Russ., abstract in Eng.). Available at: <https://www.elibrary.ru/item.asp?id=18726011>
2. Leckbach Y., Liu T., Li Y., Moradi M., Dou W., Xu D., Smith J. A., Lovley D. R. Microbial corrosion of metals: The corrosion microbiome. *Advances in Microbial Physiology*. 2021;78: 317–390. <https://doi.org/doi:10.1016/bs.ampbs.2021.01.002>
3. Tang H. Y., Yang C., Ueki T., Pittman C. C., Xu D., Woodard T. L., Holmes D. E., Gu T., Wang F., Lovley D. R. Stainless steel corrosion via direct iron-to-microbe electron transfer by *Geobacter* species. *The ISME Journal: Multidisciplinary Journal of Microbial Ecology*. 2021;15: 3084–3093. <https://doi.org/10.1038/s41396-021-00990-2>
4. Tang H. Y., Holmes D. E., Ueki T., Palacios P. A., Lovley D. R. Iron corrosion via direct metal-microbe

- electron transfer. *mBio*. 2019;10(3): e00303-19. <https://doi.org/10.1128/mBio.00303-19>
5. Deutzmann J. S., Sahin M., Spormann A. M. Extracellular enzymes facilitate electron uptake in biocorrosion and bioelectrosynthesis. *mBio*. 2015;6(2): e00496-15. <https://doi.org/10.1128/mbio.00496-15>
 6. Costerton J. W., Geesey G. G., Cheng K. J. How bacteria stick. *Scientific American*. 1978;238(1): 86–95. <https://doi.org/10.1038/scientificamerican0178-86>
 7. Li X., Duan J., Xiao H., Li Y., Liu H., Guan F., Zhai X. Analysis of bacterial community composition of corroded steel immersed in sanya and xiamen seawaters in China via method of illumina MiSeq Sequencing. *Frontiers in Microbiology*. 2017;8: 1737. <https://doi.org/10.3389/fmicb.2017.01737>
 8. Cetin D., Aksu M. L. Corrosion behavior of low-alloy steel in the presence of *Desulfotomaculum* sp. *Corrosion Science*. 2009;51(8): 1584–1588. <https://doi.org/10.1016/j.corsci.2009.04.001>
 9. Wikieł A. J., Datsenko I., Vera M., Sand W. Impact of *Desulfovibrio alaskensis* biofilms on corrosion behaviour of carbon steel in marine environment. *Bioelectrochemistry*. 2014;97: 52–60. <https://doi.org/10.1016/j.bioelechem.2013.09.008>
 10. Zhang P., Xu D., Li Y., Yang K., Gu T. Electron mediators accelerate the microbiologically influenced corrosion of 304 stainless steel by the *Desulfovibrio vulgaris* biofilm. *Bioelectrochemistry*. 2015;101: 14–21. <https://doi.org/10.1016/j.bioelechem.2014.06.010>
 11. McBeth J. M., Emerson D. In situ microbial community succession on mild steel in estuarine and marine environments: Exploring the role of iron-oxidizing bacteria. *Frontiers in Microbiology*. 2016; 7. <https://doi.org/10.3389/fmicb.2016.00767>
 12. Dinh H. T., Kuever J., Mußmann M., Hassel A. W., Stratmann M., Widdel F. Iron corrosion by novel anaerobic microorganisms. *Nature*. 2004;427(6977): 829–832. <https://doi.org/10.1038/nature02321>
 13. Beech I. B., Gaylarde C. C. Adhesion of *Desulfovibrio desulfuricans* and *Pseudomonas fluorescens* to mild steel surfaces. *Journal of Applied Bacteriology*. 1989;67(2): 201–207. <https://doi.org/10.1111/j.1365-2672.1989.tb03396.x>
 14. Zottola E. A. Characterization of the attachment matrix of *Pseudomonas fragi* attached to non-porous surfaces. *Journal of Bioadhesion and Biofilm Research*. 1991;5(1-2): 37–55. <https://doi.org/10.1080/08927019109378227>
 15. Siqueira V. M., Lima, N. Biofilm formation by filamentous fungi recovered from a water system. *Journal of Mycology*. 2013; Article ID 152941: 1–9. <https://doi.org/10.1155/2013/152941>
 16. Fox E. P., Singh-Babak S. D., Hartooni N., Nobile C. J. Biofilms and antifungal resistance. *Antifungals: From Genomics to Resistance and the Development of Novel Agents*. 2015; 71–90. <https://doi.org/10.21775/9781910190012.04>
 17. Müller F.-M. C., Seidler M., Beauvais A. *Aspergillus fumigatus* biofilms in the clinical setting. *Medical Mycology*. 2011;49(S1): S96–S100. <https://doi.org/10.3109/13693786.2010.502190>
 18. Reichhardt C., Ferreira J. A. G., Joubert L.-M., Clemons K. V., Stevens D. A., Cegelski L. Analysis of the *Aspergillus fumigatus* biofilm extracellular matrix by solid-state nuclear magnetic resonance spectroscopy. *ASM Journals. Eukaryotic Cell*. 2015;14(11): 1064–1072. <https://doi.org/10.1128/EC.00050-15>
 19. Donlan R. M. Biofilms: Microbial life on surfaces. *Emerging Infectious Diseases*. 2002;8(9): 881–890. <https://doi.org/10.3201/eid0809.020063>
 20. Gorbushina A. A., Panina L. K. Adhesion of micromycete conidia to polymeric materials. *Mycology and Phytopathology*. 1992;26(5): 372–377. (In Russ.)
 21. Kalinina I. G., Gumargalieva K. Z., Kuznetsova O. N., Zaikov G. E. Interrelation of adhesion of conidia of the microscopic fungus *Trichoderma viride* with the electrochemical properties of metals. *Bulletin of the Kazan Technological University*. 2012;15(12): 115–118. (In Russ., abstract in Eng.). Available at: <https://www.elibrary.ru/item.asp?id=17846266>
 22. Joubert L.-M., Ferreira J. A., Stevens D. A., Nazik H., Cegelski L. Visualization of *Aspergillus fumigatus* biofilms with scanning electron microscopy and variable pressure-scanning electron microscopy: A comparison of processing techniques. *Journal of Microbiological Methods*. 2017;132: 46–55. <https://doi.org/10.1016/j.mimet.2016.11.002>
 23. González-Ramírez A.I., Ramírez-Granillo A., Medina-Canales M. G., Rodríguez-Tovar A. V., Martínez-Rivera M. A. Analysis and description of the stages of *Aspergillus fumigatus* biofilm formation using scanning electron microscopy. *BMC Microbiology*. 2016;16, 243. <https://doi.org/10.1186/s12866-016-0859-4>
 24. Villena G. K., Fujikawa T., Tsuyumu S., Gutiérrez-Correa M. Structural analysis of biofilms and pellets of *Aspergillus niger* by confocal laser scanning microscopy and cryo scanning electron microscopy. *Bioresource Technology*. 2010;101(6): 1920–1926. <https://doi.org/10.1016/j.biortech.2009.10.036>
 25. Denkhaus E., Meisen S., Telgheder U., Wingender J. Chemical and physical methods for characterisation of biofilms. *Microchimica Acta*. 2007;158(1-2): 1–27. <https://doi.org/10.1007/s00604-006-0688-5>
 26. Beech I. B., Sunner J. A., Hiraoka K. Microbe-surface interactions in biofouling and biocorrosion processes. *International Microbiology*. 2005;8: 157–168. PMID: 16200494. <https://doi.org/10.2436/IM.V8I3.9522>

27. Beech I. B., Sunner J. Biocorrosion: towards understanding interactions between biofilms and metals. *Current Opinion in Biotechnology*. 2004;15(3): 181–186. <https://doi.org/10.1016/j.copbio.2004.05.001>
28. Yang S. L., Chung K. R. The NADPH-oxidase-mediated production of hydrogen peroxide (H₂O₂) and resistance to oxidative stress in the necrotrophic pathogen *Alternaria alternata* of citrus. *Molecular Plant Pathology*. 2012;13(8): 900–914. <https://doi.org/10.1111/j.1364-3703.2012.00799.x>
29. Gessler N. N., Averyanov A. A., Belozerskaya T. A. Reactive oxygen species in the regulation of fungal development (Review). *Biochemistry*. 2007;72(10): 1091–1109. <https://doi.org/10.1134/S0006297907100070>
30. Gamaley I. L., Klyubin N. N. The role of hydrogen peroxide as a second messenger. *Tsitologiya*. 1996;38(12): 1242–1247. Available at: <https://www.elibrary.ru/item.asp?id=14933936>
31. Barsukova M. E., Veselova I. A., Shekhovtsova T. N. Main methods and approaches to the determination of markers of oxidative stress - organic peroxide compounds and hydrogen peroxide. *Journal of Analytical Chemistry*. 2019;74(5): 425–436. <https://doi.org/10.1134/S1061934819020035>
32. Hansberg W., Aguirre J. Hyperoxidant states cause microbial cell differentiation by cell isolation from dioxygen. *Journal of Theoretical Biology*. 1990;142(2): 201–221. PMID: 2352433. [https://doi.org/10.1016/S0022-5193\(05\)80222-x](https://doi.org/10.1016/S0022-5193(05)80222-x)
33. Sideri M., Georgiou C. D. Differentiation and hydrogen peroxide production in *Sclerotium rolfsii* are induced by the oxidizing growth factors, light and iron. *Mycologia*. 2000;92(6): 1033–1042. <https://doi.org/10.2307/3761468>
34. Tkachuk V. A., Tyurin-Kuzmin P. A., Belousov V. V., Vorotnikov A. V. Hydrogen peroxide as a new secondary Messenger. *Biological Membranes*. 2012;29(1–2): 21–37. (In Russ., abstract in Eng.). Available at: <https://istina.msu.ru/media/publications/articles/300/3a4/1513469/BMM0021.pdf>
35. Zúñiga-Silva J. R., Chan-Cupul W., Kuschk P., Loera O., Aguilar-López R., Rodríguez-Vázquez R. Effect of Cd²⁺ on phosphate solubilizing abilities and hydrogen peroxide production of soil-borne micromycetes isolated from *Phragmites australis*-rhizosphere. *Ecotoxicology*. 2015;25(2): 367–379. <https://doi.org/10.1007/s10646-015-1595-5>
36. Zhang J., Miao Y., Rahimi M. J., Zhu H., Steindorff A., Schiessler S., Cai F., Pang G., Chenthamara K., Xu Y., Kubicek C. P., Shen Q., Druzhinina I. S. Guttation capsules containing hydrogen peroxide: an evolutionarily conserved NADPH oxidase gains a role in wars between related fungi. *Environmental Microbiology*. 2019;21(8): 2644–2658 <https://doi.org/10.1111/1462-2920.14575>
37. Stosz S. K., Fravel D. R., Roberts D. P. In vitro analysis of the role of glucose oxidase from *Talaromyces flavus* in biocontrol of the plant pathogen *Verticillium dahliae*. *Applied and Environmental Microbiology*. 1996;62(9): 3183–3186. <https://doi.org/10.1128/aem.62.9.3183-3186.1996>
38. Murray F. R., Llewellyn D. J., Peacock W. J., Dennis E. S. Isolation of the glucose oxidase gene from *Talaromyces flavus* and characterisation of its role in the biocontrol of *Verticillium dahliae*. *Current Genetics*. 1997;32(5): 367–375. <https://doi.org/10.1007/s002940050290>
39. Yang C.-A., Cheng C.-H., Lo C.-T., Liu S.-Y., Lee J.-W., Peng K.-C. A Novel Amino Acid Oxidase from *Trichoderma harzianum* ETS 323 Associated with Antagonism of *Rhizoctonia solani*. *Journal of Agricultural and Food Chemistry*. 2011;59(9): 4519–4526. <https://doi.org/10.1021/jf104603w>
40. Smirnova I. P., Karimova E. V., Shneider Y. A. Antibacterial Activity of L-Lysine- α -Oxidase from the Trichoderma. *Bulletin of Experimental Biology and Medicine*. 2017;163(6): 777–779. <https://doi.org/10.1007/s10517-017-3901-0>
41. Heller J., Tudzynski P. Reactive oxygen species in phytopathogenic fungi: signaling, development, and disease. *Annual Review of Phytopathology*. 2011;49(1): 369–390. <https://doi.org/10.1146/annurev-phyto-072910-095355>
42. Mentges M., Bormann J. Real-time imaging of hydrogen peroxide dynamics in vegetative and pathogenic hyphae of *Fusarium graminearum*. *Scientific Reports*. 2015;5(1), 14980: 1–10. <https://doi.org/10.1038/srep14980>
43. Eichlerová I., Homolka L., Lisá L., Nerud F. The influence of extracellular H₂O₂ production on decolorization ability in fungi. *Journal of Basic Microbiology*. 2006;46(6): 449–455. <https://doi.org/10.1002/jobm.200610064>
44. Zhao J., Janse B. J. H. Comparison of H₂O₂-producing enzymes in selected white rot fungi. *FEMS Microbiology Letters*. 1996;139(2-3): 215–221. <https://doi.org/10.1111/j.1574-6968.1996.tb08205.x>
45. Wiberth C.-C., Casandra A.-Z. C., Zhiliang F., Gabriela H. Oxidative enzymes activity and hydrogen peroxide production in white-rot fungi and soil-borne micromycetes co-cultures. *Annals of Microbiology*. 2019;69: 171–181. <https://doi.org/10.1007/s13213-018-1413-4>
46. Zhao Y., Li J., Chen Y., Hang H. Response to oxidative stress of *Coriolus versicolor* induced by exogenous hydrogen peroxide and paraquat. *Annals of Microbiology*. 2009;59(2): 221–227. <https://doi.org/10.1007/bf03178320>
47. Hansel C. M., Zeiner C. A., Santelli C. M., Webb S. M. Mn(II) oxidation by an ascomycete fungus is linked to superoxide production during asexual

- reproduction. *Proceedings of the National Academy of Sciences*. 2012;109(31): 12621–12625. <https://doi.org/10.1073/pnas.1203885109>
48. Hayyan M., Hashim M. A., AlNashef I. M. Superoxide Ion: Generation and Chemical Implications. *Chemical Reviews*. 2016;116(5): 3029–3085. <https://doi.org/10.1021/acs.chemrev.5b00407>
49. Winterbourn C. C. Biological chemistry of superoxide radicals. *ChemTexts (The Textbook Journal of Chemistry)*. 2020;6(1): 7. <https://doi.org/10.1007/s40828-019-0101-8>
50. Janik I., Tripathi G. N. R. The nature of the superoxide radical anion in water. *The Journal of Chemical Physics*. 2013;139(1): 014302-1–014302-7. <https://doi.org/10.1063/1.4811697>
51. Belov D. V., Chelnokova M. V., Kalinina A. A., Sokolova T. N., Smirnov V. F., Kartashov V. R. Active oxygen species in metal corrosion. *Corrosion: Materials, Protection*. 2011;3: 19–26. (In Russ.). Available at: <https://www.elibrary.ru/item.asp?id=16317997>
52. Belov D. V., Chelnokova M. V., Sokolova T. N., Smirnov V. F., Kalinina A. A., Kartashov V. R. Generation of superoxide radical anion by micromycetes and its role in metal corrosion. *ChemChemTech*. 2011;54(10): 133–136. (In Russ.). Available at: <https://www.elibrary.ru/item.asp?id=16547211>
53. De Grey A. D. N. J. HO₂[•]: The Forgotten Radical. *DNA and Cell Biology*. 2002;21(4): 251–257. <https://doi.org/10.1089/104454902753759672>
54. Bielski B. H. J., Allen A. O. Mechanism of the disproportionation of superoxide radicals. *Journal of Physical Chemistry*. 1977;81(11): 1048–1050. <https://doi.org/10.1021/j100526a005>
55. Xu W., Yu F., Yang L., Zhang B., Hou B., Li Y. Accelerated corrosion of 316L stainless steel in simulated body fluids in the presence of H₂O₂ and albumin. *Materials Science and Engineering: C*. 2018;92: 11–19. <https://doi.org/10.1016/j.msec.2018.06.023>
56. Yu F., Addison O., Davenport A. J. A synergistic effect of albumin and H₂O₂ accelerates corrosion of Ti6Al4V. *Acta Biomaterialia*. 2015;26: 355–365. <https://doi.org/10.1016/j.actbio.2015.07.046>
57. Miyazawa T., Terachi T., Uchida S., Satoh T., Tsukada T., Satoh Y., Wada Y., Hosokawa H. Effects of hydrogen peroxide on corrosion of stainless steel, (V) characterization of oxide film with multilateral surface analyses. *Journal of Nuclear Science and Technology*. 2006;43(8): 884–895. <https://doi.org/10.1080/18811248.2006.9711173>
58. Dong C., Yuan C., Bai X., Li J., Qin H., Yan X. Coupling mechanism between wear and oxidation processes of 304 stainless steel in hydrogen peroxide environments. *Scientific Reports*. 2017;7(1): 2327. <https://doi.org/10.1038/s41598-017-02530-5>
59. Singh A., Chaudhary V., Sharma A. Electrochemical studies of stainless steel corrosion in peroxide solutions. *Portugaliae Electrochimica Acta*. 2012;30(2): 99–109. <https://doi.org/10.4152/pea.201202099>
60. Mabillean G., Bourdon S., Joly-Guillou M. L., Filmon R., Baslé M. F., Chappard D. Influence of fluoride, hydrogen peroxide and lactic acid on the corrosion resistance of commercially pure titanium. *Acta Biomaterialia*. 2006;2(1): 121–129. <https://doi.org/10.1016/j.actbio.2005.09.004>
61. Furiya-Sato S., Fukushima A., Mayanagi G., Sasaki K., Takahashi N. Electrochemical evaluation of the hydrogen peroxide- and fluoride-induced corrosive property and its recovery on the titanium surface. *Journal of Prosthodontic Research*. 2020;64(3): 307–312. <https://doi.org/10.1016/j.jpjor.2019.09.002>
62. Yu F., Addison O., Davenport A. J. A synergistic effect of albumin and H₂O₂ accelerates corrosion of Ti6Al4V. *Acta Biomaterialia*. 2015;26: 355–365. <https://doi.org/10.1016/j.actbio.2015.07.046>
63. Been J., Tromans D. Titanium corrosion in alkaline hydrogen peroxide. *Corrosion*. 2000;56(8): 809–818. <https://doi.org/10.5006/1.3280584>
64. *Handbook of electrochemistry*. A. M. Sukhotin (Ed.). Leningrad: Chemistry Publ.; 1981. 488 p. (In Russ.)
65. Antonchenko V. Ya., Davydov A. S., Ilyin V. V. *Fundamentals of water physics*. AN Ukrainian SSR. Institute of Theoretical Physics. Kyiv: Naukova dumka Publ.; 1991. 672 p. (In Russ.)
66. *Handbook. Structure and corrosion of metals and alloys*: Atlas. Moscow: Metallurgy Publ.; 1989. 400 p.
67. Moon S.-M., Pyun S.-I. The formation and dissolution of anodic oxide films on pure aluminum in alkaline solution. *Electrochimica Acta*. 1999;44: 2445–2454. [https://doi.org/10.1016/S0013-4686\(98\)00368-5](https://doi.org/10.1016/S0013-4686(98)00368-5)
68. Davis G. D., Moshier W. C., Long G. G., Black D. R. Passive film structure of supersaturated Al-Mo alloys. *Journal of the Electrochemical Society*. 1991;138(11): 3194–3198. <https://doi.org/10.1149/1.2085392>
69. Nguyen L., Hashimoto T., Zakharov D. N., Stach E. A., Rooney A. P., Berkels B., Burnett T. L. Atomic-scale insights into the oxidation of aluminum. *ACS Applied Materials & Interfaces*. 2018;10(3): 2230–2235. <https://doi.org/10.1021/acsami.7b17224>
70. Hunter M. S., Fowle P. Natural and thermally formed oxide films on aluminum. *Journal of the Electrochemical Society*. 1956;103(9): 482–485. <https://doi.org/10.1149/1.2430389>
71. Gulbransen Earl A., Wysong W. S. Thin Oxide Films on Aluminum. *Journal of Physical Chemistry*. 1947;51(5): 1087–1103. <https://doi.org/10.1021/j150455a004>
72. Vargel C. *Corrosion of aluminium*. Hardbound: Elsevier; 2004. 700 p.

73. Gromov A. A., Il'in A. P., Foerter-Barth U., Teipel U. D. Effect of the passivating coating type, particle size, and storage time on oxidation and nitridation of aluminum powders. *Combustion, Explosion and Shock Waves*. 2006;42(2): 177–184. <https://doi.org/10.1007/S10573-006-0036-4>
74. Larichev M. N., Laricheva O. O., Leipunsky I. O., Pshechenkov P. A., Zhigach A. N., Kuskov M. L., Sedoy V. S. New “reactive” coatings for passivation surfaces of nanosized Al particles intended for energy use. *Khimicheskaya fizika*. 2006;25(10): 72–79. (In Russ.). Available at: <https://www.elibrary.ru/item.asp?id=9295873>
75. Deng Z. Y., Ferreira J. M. F., Tanaka Y., Ye J. Physicochemical mechanism for the continuous reaction of γ -Al₂O₃ modified Al powder with water. *Journal of the American Ceramic Society*. 2007;90(5): 1521–1526. <https://doi.org/10.1111/j.1551-2916.2007.01546.x>
76. Fernandez A., Sanchez-Lopez J. C., Caballero A. Characterization of nanophase Al-oxide/Al powders by electron energy-loss spectroscopy. *Journal of Microscopy*. 1998;191: 212–220. <https://doi.org/10.1046/j.1365-2818.1998.00355.x>
77. Razavi-Tousi S. S., Szpunar J. A. Mechanism of corrosion of activated aluminum particles by hot water. *Electrochimica Acta*. 2014;127: 95–105. <https://doi.org/10.1016/j.electacta.2014.02.024>
78. Lozhkomoev A. S., Glazkova E. A., Bakina O. V., Lerner M. I., Gotman I., Gutmanas E. Y., Kazantsev S. O., Psakhie S. G. Synthesis of core-shell AlOOH hollow nanospheres by reacting Al nanoparticles with water. *Nanotechnology*. 2016;27(20): 205603 (7 pp). <https://doi.org/10.1088/0957-4484/27/20/205603>
79. Kanehira S., Kanamori S., Nagashima K., Saeki T., Visbal H., Fukui T. Controllable hydrogen release via aluminum powder corrosion in calcium hydroxide solutions. *Journal of Asian Ceramic Societies*. 2013;1: 296–303. <https://doi.org/10.1016/j.jascer.2013.08.001>
80. Bunker B. C., Nelson G. C., Zavadil K. R., Barbour J. C., Wall F. D., Sullivan J. P., Windisch C. F., Engelhardt M. H., Baer D. R. Hydration of passive oxide films on aluminum. *The Journal of Physical Chemistry B*. 2002;18(106): 4705–4713. <https://doi.org/10.1021/jp013246e>
81. Fateev Yu. F., Vrzhosek G. G., Antropov L. I. On the corrosion of aluminum in alkali solutions. *Bulletin of the Kiev Polytechnic Institute. Series: Chemical Engineering and Technology*. 1979;16: 60–63. (In Russ.). Available at: <https://www.elibrary.ru/item.asp?id=17937682>
82. Grigor'eva I. O., Dresvyannikov A. F. Corrosion and electrochemical behavior of aluminum in solutions of potassium and lithium hydroxides. *Bulletin of the Kazan Technological University*. 2012;15(14): 199–202. (In Russ., abstract in Eng.). Available at: <https://www.elibrary.ru/item.asp?id=17937682>
83. Grigoryeva I. O., Dresvyannikov A. F., Masnik O. Yu., Zakirov R. A. Electrochemical behavior of aluminum in solutions of ammonium hydroxide and sodium hydroxide. *Bulletin of the Kazan Technological University*. 2011;6: 72–78. (In Russ., abstract in Eng.). Available at: <https://www.elibrary.ru/item.asp?id=16147047>
84. Pyun S. I., Moon S. M. Corrosion mechanism of pure aluminium in aqueous alkaline solution. *Journal of Solid State Electrochemistry*. 2000;5(4): 267–272. <https://doi.org/10.1007/s100080050203>
85. Bryan J. M. *Aluminium and aluminium alloys in the food industry with special reference to corrosion and its prevention*. Department of Science and Industrial Research. Food Investigation Special Report. London: H. M. Stationery Office; 1948;50: p. 153.
86. Laptev A. B., Lutsenko A. N., Kurs M. G., Bukharev G. M. Experience studies of bio-corrosion of metals. *Theory and Practice of Corrosion Protection*. 2016;2(80): 36–57. (In Russ., abstract in Eng.). Available at: <https://www.elibrary.ru/item.asp?id=29311937>
87. Nardy K., Johannes A.V. The dual role of microbes in corrosion. *The ISME Journal*. 2015;9(3): 542–551. <https://doi.org/10.1038/ismej.2014.169>
88. Smirnov V. F., Belov D. V., Sokolova T. N., Kuzina O. V., Kartashov V. R. Microbiological corrosion of aluminum alloys. *Applied Biochemistry and Microbiology*. 2008;44: 192–196. <https://doi.org/10.1134/S0003683808020117>
89. Belov D. V., Belyaev S. N., Maksimov M. V., Gevorgyan G. A. Research of corrosion fracture of D16T and AMg6 aluminum alloys exposed to microscopic fungi. *Voprosy Materialovedeniya*. 2021;3(107): 163–183. <https://doi.org/10.22349/1994-6716-2021-107-3-163-183>
90. Belov D. V., Chelnokova M. V., Sokolova T. N., Smirnov V. F., Kartashov V. R. On the role of reactive oxygen species in the initiation of corrosion of metals by microscopic fungi. *Korroziya: Materialy, Zashchita*. 2009;11: 43–48. (In Russ.). Available at: <https://www.elibrary.ru/item.asp?id=13032869>
91. Koval E. Z., Sidorenko L. P. *Microdestructors of industrial materials*. Kyiv: Naukova Dumka Publ.; 1989. 192 p. (In Russ.)
92. Sutton D. A., Fothergill A. W., Rinaldi M. G. *Guide to clinically significant fungi*. Baltimore: Williams & Wilkins; 1997. 471 p.
93. Berridge M. V., Herst P. M., Tan A. S. Tetrazolium dyes as tools in cell biology: New insights into their cellular reduction. *Biotechnology Annual Review*. 2005;11: 127–152. [https://doi.org/10.1016/s1387-2656\(05\)11004-7](https://doi.org/10.1016/s1387-2656(05)11004-7)
94. Seidler E. The tetrazolium-fomazan system: design and histochemistry. *Progress in Histochemistry*

- and *Cytochemistry*. 1991;24(1): 1–79. [https://doi.org/10.1016/s0079-6336\(11\)80060-4](https://doi.org/10.1016/s0079-6336(11)80060-4)
95. Altman F. P. Tetrazolium salts and formazans. *Progress in Histochemistry and Cytochemistry*. 1976;9(3): 3–51. [https://doi.org/10.1016/s0079-6336\(76\)80015-0](https://doi.org/10.1016/s0079-6336(76)80015-0)
96. Rotilio G., Bray R. C., Fielden E. M. A pulse radiolysis study of superoxide dismutase. *Biochimica et Biophysica Acta (BBA) - Enzymology*. 1972;268(2): 605–609. [https://doi.org/10.1016/0005-2744\(72\)90359-2](https://doi.org/10.1016/0005-2744(72)90359-2)
97. Fridovich I. Superoxide Radical and Superoxide Dismutases. *Annual Review of Biochemistry*. 1995;64(1): 97–112. <https://doi.org/10.1146/annurev.bi.64.070195.000525>
98. Fielden E. M., Roberts P. B., Bray R. C., Lowe D. J., Mautner G. N., Rotilio G., Calabrese L. The mechanism of action of superoxide dismutase from pulse radiolysis and electron paramagnetic resonance. Evidence that only half the active sites function in catalysis. *Biochemical Journal*. 1974;139(1): 49–60. <https://doi.org/10.1042/bj1390049>
99. Kalinina A. A., Belov D. V., Chelnokova M. V., Sokolova T. N., Moskvichev A. N., Razov E. N., Kartashov V. R. Electron acceptor compounds in the study of biocorrosion phenomena. *Korroziya: Materialy, Zashchita*. 2011;12:29–32. (In Russ.). Available at: <https://elibrary.ru/item.asp?id=17241858>
100. Sirota T. V. A Chain reaction of adrenaline autoxidation is a model of quinoid oxidation of catecholamines. *Biophysica*. 2020;65(4): 548–556. <https://doi.org/10.1134/S0006350920040223>
101. Misra H. P., Fridovich I. The univalent reduction of oxygen by reduced flavins and quinones. *Journal of Biological Chemistry*. 1972;247(1): 188–192. [https://doi.org/10.1016/s0021-9258\(19\)45773-6](https://doi.org/10.1016/s0021-9258(19)45773-6)
102. Misra H. P., Fridovich I. The role of superoxide anion in the autoxidation of epinephrine and a simple assay for superoxide dismutase. *Journal of Biological Chemistry*. 1972;247(10): 3170–3175. [https://doi.org/10.1016/s0021-9258\(19\)45228-9](https://doi.org/10.1016/s0021-9258(19)45228-9)
103. Bors W., Michel C., Saran M., Lengfelder E. Kinetic investigations of the autoxidation of adrenalin. *Zeitschrift Für Naturforschung C*. 1978;33(11-12): 891–896. <https://doi.org/10.1515/znc-1978-11-1215>
104. Burns J. M., Cooper W. J., Ferry J. L., King D. W., DiMento B. P., McNeill K., Miller C. J., Miller W. L., Peake B. M., Rusak S. A., Rose A. L., Waite T. D. Methods for reactive oxygen species (ROS) detection in aqueous environments. *Aquatic Sciences*. 2012;74(4): 683–734. <https://doi.org/10.1007/s00027-012-0251-x>
105. MacNevin W. M., Urone P. F. Separation of hydrogen peroxide from organic hydroperoxides. *Analytical Chemistry*. 1953;25(11): 1760–1761. <https://doi.org/10.1021/ac60083a052>
106. Pobiner H. Determination of hydroperoxides in hydrocarbon by conversion to hydrogen peroxide and measurement by titanium complexing. *Analytical Chemistry*. 1961;33(10): 1423–1426. <https://doi.org/10.1021/ac60178a045>
107. Bunker B. C., Nelson G. C., Zavadil K. R., Barbour J. C., Wall F. D., Sullivan J. P., Windisch C. F., Engelhardt M. H., Baer D. R. Hydration of passive oxide films on aluminum. *Journal of Physical Chemistry B*. 2002;106(18): 4705–4713. <https://doi.org/10.1021/jp013246e>
108. Belitskus D. Reaction of aluminum with sodium hydroxide solution as a source of hydrogen. *Journal of the Electrochemical Society*. 1970;117: 1097–1099. <https://doi.org/10.1149/1.2407730>
109. Heusler K. E., Allgaier W. Die kinetik der auflösung von aluminium in alkalischen losungen. *Werkstoffe und Korrosion*. 1971;22(4): 297–302. <https://doi.org/10.1002/mac0.19710220405>
110. Ribeiro T., Motta A., Marcus P., Gaigeot M.-P., Lopez X., Costa D. Formation of the OOH radical at steps of the boehmite surface and its inhibition by gallic acid: A theoretical study including DFT-based dynamics. *Journal of Inorganic Biochemistry*. 2013;128: 164–173. <https://doi.org/10.1016/j.jinorgbio.2013.07.024>
111. Ren T., Yang S., Jiang Y., Sun X., Zhang Y. Enhancing surface corrosion of zero-valent aluminum (ZVAL) and electron transfer process for the degradation of trichloroethylene with the presence of persulfate. *Chemical Engineering Journal*. 2018;348: 350–360. <https://doi.org/10.1016/j.cej.2018.04.216>
112. Meredith C., Hamilton T. P., Schaefer H. F. Oxywater (water oxide): new evidence for the existence of a structural isomer of hydrogen peroxide. *The Journal of Physical Chemistry*. 1992;96(23): 9250–9254. <https://doi.org/10.1021/j100202a034>
113. Jursic B. S. Density functional theory and *ab initio* study of oxywater isomerization into hydrogen peroxide. *Journal of Molecular Structure: THEOCHEM*. 1997;417(1-2): 81–88. [https://doi.org/10.1016/s0166-1280\(97\)00059-6](https://doi.org/10.1016/s0166-1280(97)00059-6)
114. Franz J., Francisco J. S., Peyerimhoff S. D. Production of singlet oxygen atoms by photodissociation of oxywater. *The Journal of Chemical Physics*. 2009;130(8): 084304. <https://doi.org/10.1063/1.3080808>
115. Chumakov A. A., Kotelnikov O. A., Slizhov Yu. G., Minakova T. S. Substantiation of the generation of oxywater zwitterions and singlet oxygen atoms from hydrogen peroxide molecules in aqueous solutions. *Bulletin of the South Ural State University. Series "Chemistry"*. 2018;10(4): 44–59. (In Russ., abstract in Eng.). <https://doi.org/10.14529/chem180405>
116. Shaitura N. S., Laricheva O. O., Larichev M. N. Study of the mechanism of low-temperature oxidation of micro-sized aluminum powder with water. *Chemical*

Physics. 2019;38(3): 9–23. (In Russ.). <https://doi.org/10.1134/S0207401X19030087>

117. Larichev M. N. Reaction of aluminum powders with liquid water and steam. In: (2014). *Metal Nanopowders*. Gromov A., Teipel U. (Eds.). Weinheim, Germany: Wiley-VCH Verlag GmbH & Co. KGaA. W.; 2014. p. 163. <https://doi.org/10.1002/9783527680696.ch8>

118. Larichev M. N., Laricheva O. O., Leipunsky I. O., Pshechenkov P. A. The reaction of aluminum particles with liquid water and water vapor is a promising source of hydrogen for the needs of hydrogen energy. *Proceedings of the Russian Academy of Sciences. Energy*. 2007;5: 125–139. (In Russ.). Available at: <https://elibrary.ru/item.asp?id=9584641>

119. Zang J., Klasky M., Letellier B. C. The aluminum chemistry and corrosion in alkaline solutions. *Journal of Nuclear Materials*. 2009;384(2): 175–189. <https://doi.org/10.1016/j.jnucmat.2008.11.009>

120. Deng Z.-Y., Ferreira J. M. F., Tanaka Y., Ye J. Physicochemical mechanism for the continuous reaction of γ -Al₂O₃-modified aluminum powder with water. *Journal of the American Ceramic Society*. 2007;90(5): 1521–1526. <https://doi.org/10.1111/j.1551-2916.2007.01546.x>

121. Rosliza R., Izman S. SEM-EDS characterization of natural products on corrosion inhibition of Al-Mg-Si alloy. *Protection of Metals and Physical Chemistry of Surfaces*. 2011;47: 395–401. <https://doi.org/10.1134/S2070205111030129>

122. Song W., Du J., Xu Y., Long B. A study of hydrogen permeation in aluminum alloy treated by various oxidation processes. *Journal of Nuclear Materials*. 1997; 246(2–3): 139–143. [https://doi.org/10.1016/S0022-3115\(97\)00146-3](https://doi.org/10.1016/S0022-3115(97)00146-3)

123. Ulanovskiy I. B. Hydrogen diffusion and porosity formation in aluminium. I. B. Ulanovskiy (Ed.). Moscow: Izdatelskiy Dom 'MISIS' Publ., 2015. p. 122.

124. Kaspzyk-Hordern B. Chemistry of alumina, reactions in aqueous solution and its application in water treatment. *Advances in Colloid and Interface Science*. 2004;110(1–2): 19–48. <https://doi.org/10.1016/j.cis.2004.02.002>

125. Belov D. V., Sokolova T. N., Smirnov V. F., Kuzina O. V., Kostyukova L. V., Kartashov V. R. Corrosion of aluminum and its alloys under the effect of microscopic fungi. *Protection of Metals and Physical Chemistry of Surfaces*. 2008;44: 737–742. <https://doi.org/10.1134/S0033173208070151>

126. Belov D. V., Belyaev S. N., Maksimov M. V., Gevorgyan G. A. On mechanism of biocorrosion of aluminum alloys D16T and AMg6 (Review). *Korroziya: Materialy, Zashchita*. 2021;10: 1–10. (In Russ.). <https://doi.org/10.31044/1813-7016-2021-0-10-1-22>

127. Lee S., Shin J. H., Choi M. Y. Watching the growth of aluminum hydroxide nanoparticles from aluminum nanoparticles synthesized by pulsed laser ablation in aqueous surfactant solution. *Journal of Nanoparticle Research*. 2013;15: 1473–1480. <https://doi.org/10.1007/s11051-013-1473-0>

128. Wefers K., Misra C., Bridenbaugh P. *Oxides and hydroxides of aluminum*. Alcoa Laboratories. 1987. 92 p.

129. Ahmed M., Qi Y., Zhang L., Yang Y., Abas A., Liang J., Cao B. Influence of Cu²⁺ ions on the corrosion resistance of AZ31 magnesium alloy with microarc oxidation. *Materials*. 2020;13(11): 2647. <https://doi.org/10.3390/ma13112647>

130. Sinyavsky V. S., Valkov V. D., Kalinin V. D. *Corrosion and protection of aluminum alloys*. Moscow: Metallurgiya Publ.; 1986. 386 p. (In Russ.)

131. Beaunier L. Corrosion of grain boundaries: initiation processes and testing. *Journal of Physique Colloques*. 1982;43(C6): 271–282. <https://doi.org/10.1051/jphyscol:1982624>

132. Krymsky S. V., Ilyasov R. R., Avtokratova E. V., Sidikov O. Sh., Markushe M. V. Intergranular corrosion of cryorolled and aged aluminum alloy D16. *Protection of Metals and Physical Chemistry of Surfaces*. 2017;53: 1091–1099. <https://doi.org/10.1134/S2070205117060144>

133. Abramova M. G., Goncharov A. A. Intergranular corrosion of wrought aluminum alloys during full-scale and full-scale accelerated climatic tests. *Proceedings of VIAM*. 2019;11(83): 85–94. (In Russ., abstract in Eng.). <https://doi.org/10.18577/2307-6046-2019-0-11-85-94>

Author information

Denis V. Belov, Cand. Sci. (Chem.), Associate Professor, Senior Research Fellow, Federal Research Centre Institute of Applied Physics of the Russian Academy of Sciences (Nizhny Novgorod, Russian Federation).

<https://orcid.org/0000-0001-7190-0477>

belov.denbel2013@yandex.ru

Sergey N. Belyaev, Cand. Sci. (Chem.), Researcher, Federal Research Centre Institute of Applied Physics of the Russian Academy of Sciences (Nizhny Novgorod Russian Federation).

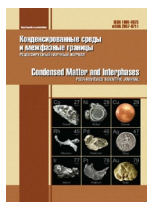
<https://orcid.org/0000-0003-2346-9103>

serg_belyaev@bk.ru

Received 29.12.2021; approved after reviewing 11.04.2022; accepted for publication 15.04.2022; published online 25.06.2022.

Translated by Valentina Mittova

Edited and proofread by Simon Cox



Original articles

Research article

<https://doi.org/10.17308/kcmf.2022.24/9257>

The quasi-binary $\text{Cu}_3\text{In}_5\text{S}_9$ – FeIn_2S_4 section

Sh. S. Abdullaeva[✉], I. B. Bakhtiyarly, R. J. Kurbanova, Z. M. Mukhtarova

Institute of Catalysis and Inorganic Chemistry named after M. Nagiev of the Azerbaijan National Academy of Sciences, 113 H. Javid ave., Baku Az1143, Azerbaijan

Abstract

The $\text{Cu}_3\text{In}_5\text{S}_9$ – FeIn_2S_4 section was studied by methods of physicochemical analysis; differential thermal (DTA), X-ray phase (XRD), microstructural (MSA) and microhardness measurement. Based on the results of the obtained data, a phase diagram of the $\text{Cu}_3\text{In}_5\text{S}_9$ – FeIn_2S_4 section of the Cu_2S – In_2S_3 – FeS ternary system was constructed. It was established that the $\text{Cu}_3\text{In}_5\text{S}_9$ – FeIn_2S_4 section is a quasi-binary section of the ternary Cu_2S – In_2S_3 – FeS systems and is eutectic by type with limited solubility based on both initial components. The liquidus of the system consists of two branches of primary crystallization of σ_1 (solid solution based on $\text{Cu}_3\text{In}_5\text{S}_9$) and σ (solid solution based on FeIn_2S_4) phases. The eutectic point has coordinates: 1150 K temperature and composition 42 mol% FeIn_2S_4 . The boundaries of the solid solutions were also determined. The region of solid solutions based on $\text{Cu}_3\text{In}_5\text{S}_9$ extends to 3 mol. % FeIn_2S_4 , the region of solid solutions based on FeIn_2S_4 extends to 5 mol. % $\text{Cu}_3\text{In}_5\text{S}_9$ at room temperature.

Keywords: Microhardness, Phase diagram, System, section, Quasi-binary, Eutectic, Solid solution

For citation: Abdullaeva Sh. S., Bakhtiyarly I. B., Kurbanova R. J., Mukhtarova Z. M. Quasi-binary section $\text{Cu}_3\text{In}_5\text{S}_9$ – FeIn_2S_4 . *Condensed Matter and Interphases*. 2022;24(2): 182–186. <https://doi.org/10.17308/kcmf.2022.24/9257>

Для цитирования: Абдуллаева Ш. С., Бахтиярлы И. Б., Курбанова Р. Дж., Мухтарова З. М. Квазибинарный разрез $\text{Cu}_3\text{In}_5\text{S}_9$ – FeIn_2S_4 . *Конденсированные среды и межфазные границы*. 2022;24(2): 182–186. <https://doi.org/10.17308/kcmf.2022.24/9257>

✉ Abdullaeva Shahri Seyfaly, e-mail: sehri.abdullayeva.83@mail.ru

© Abdullaeva Sh. S., Bakhtiyarly I. B., Kurbanova R. J., Mukhtarova Z. M., 2022



The content is available under Creative Commons Attribution 4.0 License.

1. Introduction

The study of systems based on heavy metal chalcogenides is of interest due to the relevance of the development of new semiconductor materials with different functional properties. These include systems based on compounds of groups I, III and VI (where I is Cu, Ag; III is Al, Ga, In; VI is S, Te) [1–8]. Ternary compound FeIn_2S_4 is a dilute magnetic semiconductor. This group of semiconductors attract attention due to the potential for their use in spintronics [9–12] for the production of Schottky diodes, switches, and lasers controlled by a magnetic field, light modulators, and other devices [13–16].

This study is a continuation of our research on the ternary Cu_2S – In_2S_3 – FeS system along the $\text{Cu}_3\text{In}_5\text{S}_9$ – FeIn_2S_4 section. The study was carried out in order to clarify the nature of the chemical interaction in the ternary Cu_2S – In_2S_3 – FeS system in regions with a high content of In_2S_3 and the determination of the phase formation in $\text{Cu}_3\text{In}_5\text{S}_9$ – In_2S_3 – FeIn_2S_4 and $\text{CuFeIn}_3\text{S}_6$ – $\text{Cu}_3\text{In}_5\text{S}_9$ – FeIn_2S_4 systems [17].

The initial components of the $\text{Cu}_3\text{In}_5\text{S}_9$ and FeIn_2S_4 section are formed in the corresponding binary Cu_2S – In_2S_3 and In_2S_3 – FeS systems which are quasi-binary sections of the ternary Cu_2S – In_2S_3 – FeS system [18–20].

The compound with the composition of $\text{Cu}_3\text{In}_5\text{S}_9$ melts congruently at a temperature of 1085 °C and crystallizes in a monoclinic system with lattice parameters: $a = 0.660$ nm, $b = 0.691$ nm, $c = 0.812$ nm, $\beta = 89^\circ$, $Z = 1$ [17, 18, 21]. The compound with the composition of FeIn_2S_4 melts congruently at a temperature of 1125 °C and crystallizes in a cubic lattice with parameters: $a = 1.053$ nm [20, 24, 25].

The purpose of this study was the investigation of the nature of the chemical interaction between the $\text{Cu}_3\text{In}_5\text{S}_9$ and FeIn_2S_4 compounds.

2. Experimental

Samples for the study were synthesized from preliminarily obtained Cu_2S , In_2S_3 , and FeS in evacuated quartz ampoules (1.33 Pa) with a length of 15–18 cm, a diameter of 15 cm, at temperatures of 1370–1400 K. After completion of the reaction the ampoules were kept under the regime for 1.5–2 h. After that, the ampoules were cooled to 900 K and long-term

homogenizing annealing was carried out at the same temperature.

The alloys were studied by methods of physicochemical analysis: differential thermal DTA, microstructural MSA, X-ray phase XRD analyses; microhardness measurement. DTA was carried using a Jupiter STA 449 F3 thermal analyser (NETZSCH, Germany) at a heating rate of 10 deg/min using a Pt–Pt/Rh thermocouple. The device was operated under control of the Proteus software.

XRD of the samples was carried using a D2 Phaser X-ray diffractometer (Bruker, Germany) using $\text{CuK}\alpha$ -radiation (Ni-filter). The microhardness of the alloys was measured using a PMT-3 microhardness tester under loads of 0.1 and 0.2 N. The MSA of the alloys of the system was studied using an MIM-8 metallographic microscope on pre-etched sections polished with paste. An etchant of the composition NH_4NO_3 (3–8 wt %) + $\text{K}_2\text{Cr}_2\text{O}_7$ (0.02–0.5 wt %) + concentrated H_2SO_4 during the study of the microstructure of the alloys with the etching time of 20 s.

3. Results and discussion

The interaction between $\text{Cu}_3\text{In}_5\text{S}_9$ and FeIn_2S_4 was studied using 15 samples, the compositions of which are presented in the Table. Based on the DTA data, it can be assumed that the nature of the interaction between these compounds is simple, since the samples have two effects on the thermograms.

Table 1. Composition and DTA results of alloys of the $\text{Cu}_3\text{In}_5\text{S}_9$ – FeIn_2S_4 system

Composition mol. %		Thermal effects T , K
$\text{Cu}_3\text{In}_5\text{S}_9$	FeIn_2S_4	
100	–	1360
95	5	1350, 1275
90	10	1340, 1215
80	20	1300, 1150
70	30	1240, 1150
60	40	1148, 1170
50	50	1150, 1200
40	60	1150, 1250
30	70	1300, 1155
20	80	1350, 1150
10	90	1370, 1150
5	95	1390, 1150
–	100	1400

MSA studies, carried out on ground polished surfaces of alloys, showed that samples up to 5 mol % FeIn_2S_4 and 7 mol % $\text{Cu}_3\text{In}_5\text{S}_9$ were homogeneous, and with an increase in the content of the second component, two-phase mechanical mixtures consisting of solid solutions based on the initial components ($\sigma_1 + \sigma$) were formed.

Microhardness was measured under a load of 0.1 N. When measuring the microhardness, the values for $\text{Cu}_3\text{In}_5\text{S}_9$ of 2900 MPa and for FeIn_2S_4 of

3300 MPa were stably obtained (Fig. 1.) As can be seen from the Figure, the microhardness values of alloys rich in $\text{Cu}_3\text{In}_5\text{S}_9$ and FeIn_2S_4 , increased significantly from 2700 to 2900 MPa and from 3150 to 3300 MPa with the formation of solid solutions.

Samples containing 0, 30, 50, 70, and 100 mol % FeIn_2S_4 were studied by the XRD method.

Samples of 30, 50, 70 mol % FeIn_2S_4 turned out to be two-phase (Fig. 2).

The results of DTA are presented in the Table 1.

Based on the obtained results, the phase diagram of the $\text{Cu}_3\text{In}_5\text{S}_9 - \text{FeIn}_2\text{S}_4$ section was constructed. The phase diagram provides an idea about the nature of the chemical interaction between the initial components (Fig. 3)

The section is a quasi-binary section of the ternary $\text{Cu}_2\text{S} - \text{In}_2\text{S}_3 - \text{FeS}$ system.

The liquidus of the system consists of two branches of primary crystallization of the σ_1 (solid solution based on $\text{Cu}_3\text{In}_5\text{S}_9$) and σ_2 (solid solution based on FeIn_2S_4) phases.

The co-crystallization of σ_1 and σ_2 phases occurs at a composition of 42 mol % FeIn_2S_4 and a temperature of 1150 K:

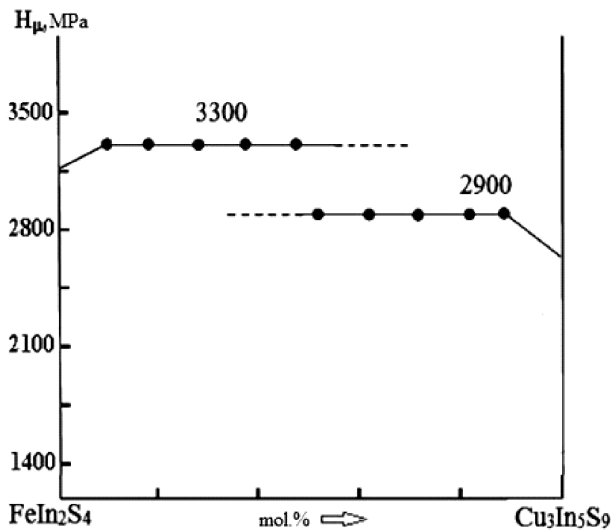
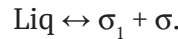


Fig. 1. H_{μ} -x diagrams of the $\text{Cu}_3\text{In}_5\text{S}_9 - \text{FeIn}_2\text{S}_4$ system

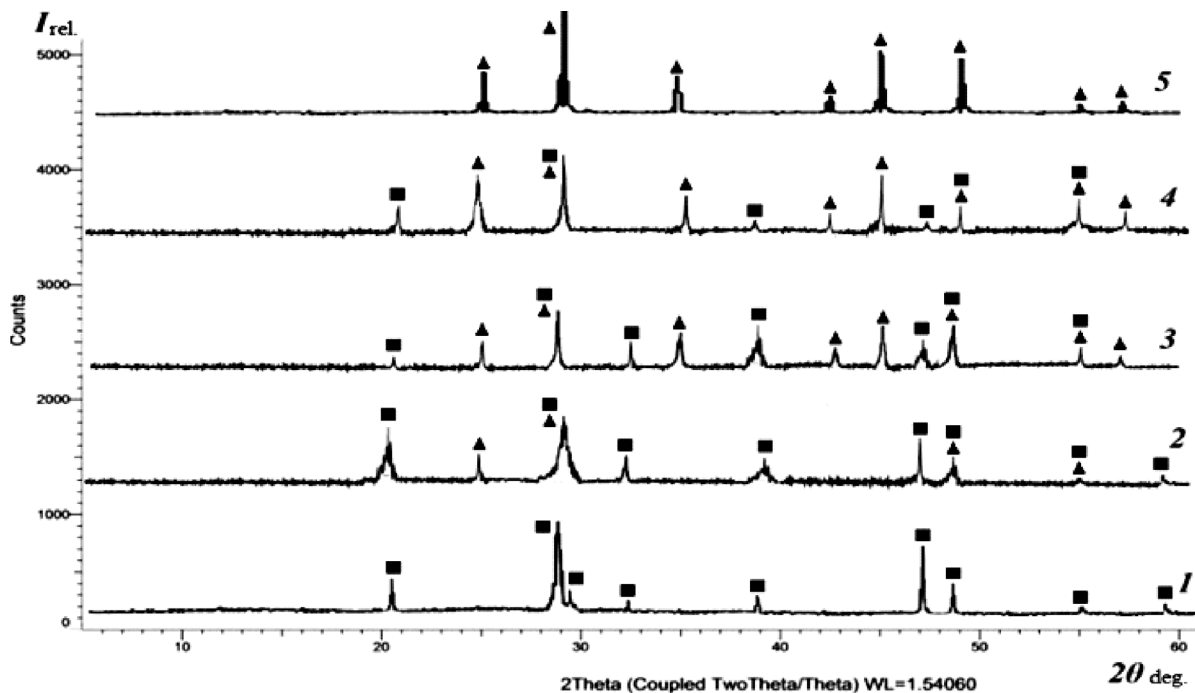


Fig. 2. Powder X-ray diffraction patterns of alloys of the $\text{Cu}_3\text{In}_5\text{S}_9 - \text{FeIn}_2\text{S}_4$ system: 1 – $\text{Cu}_3\text{In}_5\text{S}_9$; 2 – 30 mol % FeIn_2S_4 ; 3 – 50 mol % FeIn_2S_4 ; 4 – 70 mol % FeIn_2S_4 ; 5 – FeIn_2S_4 (▲ – FeIn_2S_4 ; ■ – $\text{Cu}_3\text{In}_5\text{S}_9$)

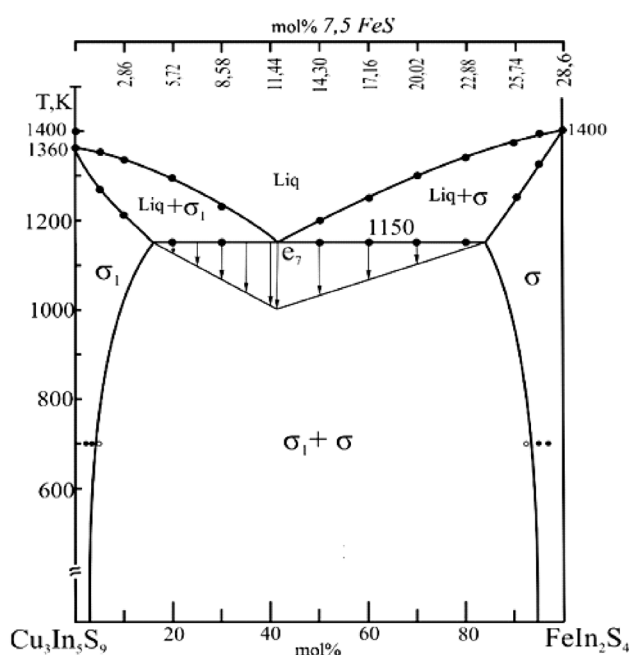


Fig. 3. Phase diagram of the $\text{Cu}_3\text{In}_5\text{S}_9$ – FeIn_2S_4 system

The composition of the eutectic was also confirmed by the plotting of the Tamman's triangle using a graphical method. As can be seen from the Figure, there are solid solution areas on the bases of the components.

To determine the limits of the regions of the solid solutions, alloys with the following compositions were additionally synthesized: 2.0; 3.0; 5.0 mol % FeIn_2S_4 and 3.0; 5.0; 8.0; mol % $\text{Cu}_3\text{In}_5\text{S}_9$. The samples were annealed at 700 K for 150 h and then quenched in iced water. After heat treatment, the microstructures of these samples were carefully studied. It was established that at a temperature of 700 K the mutual solubility of the components reached 5 mol % based on $\text{Cu}_3\text{In}_5\text{S}_9$ and 7 mol % based on FeIn_2S_4 . At room temperature the mutual solubility was 3 mol % based on $\text{Cu}_3\text{In}_5\text{S}_9$ and 5 mol % based on FeIn_2S_4 .

4. Conclusion

The phase diagram of the $\text{Cu}_3\text{In}_5\text{S}_9$ – FeIn_2S_4 system was constructed. It has been established that the section is a quasi-binary section of the ternary Cu_2S – In_2S_3 – FeS system and is eutectic. The mutual solubility of the components at a temperature of 700 K reaches 5 mol % based on $\text{Cu}_3\text{In}_5\text{S}_9$ and 7 mol % based on FeIn_2S_4 .

Author contributions

All authors made an equivalent contribution to the preparation of the publication.

Conflict of interests

The authors declare that they have no known competing financial interests or personal relationships that could have influenced the work reported in this paper.

References

1. Babanly M. B., Yusibov Yu. A., Abishev V. T. *Three-component chalcogenides based on copper and silver*. Baku: BSU Publ.; 1993. 342 p. (In Russ.)
2. Isika M., Nasser H., Ahmedova F., Guseinov A., Gasanly N. M. Optical properties of $\text{Cu}_3\text{In}_5\text{S}_9$ single crystals by spectroscopic ellipsometry. *Optik*. 2018;171: 77–82. <https://doi.org/10.1016/j.ijleo.2018.06.056>
3. Gasanly N. M. Combined low-temperature photoluminescence and thermally stimulated current studies in $\text{Cu}_3\text{In}_5\text{S}_9$ layered single crystals. *Optik*. 2016;127(12): 5148–5151. <https://doi.org/10.1016/j.ijleo.2016.03.0064>.
4. Babaeva B. K. In: *Triple semiconductors and their application*. Kishinev: Shtiintsa Publ.; 1976. 96 p. (In Russ.)
5. Berends A. C., Mangnus M. J. J., Xia C., Rabouw F. T., de Mello Donega C. Optoelectronic properties of ternary I–III–VI₂ semiconductor nanocrystals: Bright prospects with elusive Origins. *The Journal of Physical Chemistry Letters*. 2019;10(7): 1600–1616. <https://doi.org/10.1021/acs.jpcllett.8b03653>
6. Guseinov A. G., Kyazimzade A. G., Salmanov V. M., Mamedov R. M., Salmanova A. A., Gasanova L. G., Mahammadov A. Z. Features of laser-induced luminescence and photoconductivity of layered $\text{Cu}_3\text{In}_5\text{S}_9$ crystals. *Optics and Spectroscopy*. 2016;121(6): 897–900. <https://doi.org/10.1134/s0030400x16120134>
7. Parlak M., Ercelebi C., Gunal I., Ozkan H., Gasanly N. M., Culfaz A. Crystal data, electrical resistivity and mobility in $\text{Cu}_3\text{In}_5\text{S}_9$ and $\text{Cu}_3\text{In}_2\text{Te}_9$ single crystals. *Crystal Research and Technology*. 1997;32(3): 395–400. <https://doi.org/10.1002/crat.2170320305>
8. Tomashik V. Cu–In–S (Copper–Indium–Sulfur). In: *Non-Ferrous Metal Systems. Part 1*. Landolt–Börnstein – Group IV Physical Chemistry. 2006; 300–318. https://doi.org/10.1007/10915981_24
9. Niftiev N. N. Thermostimulated currents in single crystals MnIn_2S_4 . *Fizika i tekhnika poluprovodnikov*. 2002;36(7): 836–837. (In Russ.). Available at: <https://www.elibrary.ru/item.asp?id=21323814>
10. Myoung B. R., Lim J. T., Kim C. S. Investigation of magnetic properties on spin-ordering effects of FeGa_2S_4 and FeIn_2S_4 . *Journal of Magnetism and Magnetic Materials*. 2017;438: 121–125. <https://doi.org/10.1016/j.jmmm.2017.04.056>
11. Niftiev N. N., Tagiev O. B., Mamedov F. M., Muradov M. B. Electrical properties of FeIn_2S_4 on

alternating current. *Zhurnal tekhnicheskoi fiziki*. 2012;82(4): 147–149. (In Russ.). Available at: <https://www.elibrary.ru/item.asp?id=20325563>

12. Bodnar I. V., Pavlyukovets S. A., Rud V. Yu., Rud Yu. V. Growing FeIn_2S_4 single crystals and fabrication of photosensitive structures on their basis. *Semiconductors*. 2009;43(11): 1510–1513, <https://doi.org/10.1134/s1063782609110190>

13. Mammadov F. M., Babanly D. M., Amiraslanov I. R., Tagiyev D. B., Babanly M. B. $\text{FeS-Ga}_2\text{S}_3\text{-In}_2\text{S}_3$ system *Russian Journal of Inorganic Chemistry*. 2021;66(10): 1533–1543. <https://doi.org/10.1134/S0036023621100090>

14. Hwang Y., Choi J., Ha Y., Cho S., Park H. Electronic and optical properties of layered chalcogenide FeIn_2Se_4 . *Current Applied Physics*. 2020;20(1): 212–218. <https://doi.org/10.1016/j.cap.2019.11.005>

15. Niftiyev N. N., Mammadov F. M., Muradov M. B. AC electrical conductivity of FeGaInSe_4 . *Semiconductors*. 2020;54(6): 627–629. <https://doi.org/10.1134/s1063782620060123>

16. Guseinov A. G., Salmanov V. M., Mamedov R. M., Magomedov A. Z. Specific features of photoluminescence and nanosecond relaxation of photocurrent in CuIn_5S_8 crystals upon strong optical excitation. *Optics and Spectroscopy*. 2020;128(12): 1978–1982. <https://doi.org/10.1134/s0030400x20120905>

17. Bakhtiyarly I. B., Kurbanova R. J., Abdullaeva Sh. S., Mukhtarova Z. M., Mammadova F. M. Liquidus surface of the quasi-ternary system $\text{Cu}_2\text{S-In}_2\text{S}_3\text{-FeS}$. *Kondensirovannye sredy i mezhfaznye granitsy = Condensed Matter and Interphases*. 2021;23(1): 16–24. <https://doi.org/10.17308/kcmf.2021.23/3293>

18. Binsma J. J. M., Giling L. J., Bloem J. Phase relations in the system $\text{Cu}_2\text{S-In}_2\text{S}_3$. *Journal of Crystal Growth*. 1980;50(20): 429–436. [https://doi.org/10.1016/0022-0248\(80\)90090-1](https://doi.org/10.1016/0022-0248(80)90090-1)

19. Womes M., Olivier-Fourcade J., Jumas J.-C., Aubertin F., Gonser U. Characterization of the single phase region with spinel structure in the ternary system $\text{In}_2\text{S}_3\text{-FeS-FeS}_2$. *Journal of Solid State Chemistry*. 1992;97(2): 249–256. [https://doi.org/10.1016/0022-4596\(92\)90032-q](https://doi.org/10.1016/0022-4596(92)90032-q)

20. Mammadov F. M., Niftiyev N. N., Mammadov F. I. Synthesis and crystal structure of the FeGaInS_4 compound. *Azerbaijan Chemical Journal*. 2017;2: 56–59. Available at: <https://akj.az/en/journals/211>

21. Abdullaeva Sh. S., Mammadov F. M., Bakhtiyarly I. B. Quasi-binary section $\text{CuInS}_2\text{-FeIn}_2\text{S}_4$. *Russian Journal of Inorganic Chemistry*. 2020;65(1): 100–105. <https://doi.org/10.1134/s0036023619110020>

22. Bakhtiyarly I. B., Abdullaeva Sh. S., Gurbanova R. J., Mammadova F. M., Guseynova Sh. B. Study of interactions in the $\text{CuInS}_2\text{-FeS}$ system. *Russian Journal of General Chemistry*. 2019;89(8): 1659–1661. <https://doi.org/10.1134/s1070363219080188>

23. Novikova M. A. Optical properties of solid solutions $(\text{FeIn}_2\text{S}_4)_{1-x}(\text{In}_2\text{S}_3)_x$. *Doklady BGUIR*. 2014;(3): 22–26. (In Russ., abstract in Eng.). Available at: <https://doklady.bsuir.by/jour/article/view/301>

24. Bodnar I. V., Zhafar M. A., Kasyuk Y. V., Fedotova Y. A. Single crystals of $(\text{FeIn}_2\text{S}_4)_x(\text{CuIn}_5\text{S}_8)_{1-x}$ alloys: Crystal structure, nuclear gamma resonance spectra, and thermal expansion. *Semiconductors*. 2017;51: 279–284. <https://doi.org/10.1134/S106378261703006X>

25. Allakhverdiev K. R., Bedalova S. A., Gasanova L. G., Magomedov A. Z. Raman scattering in $\text{Cu}_3\text{In}_5\text{S}_9$ crystals. *Physica Status Solidi (b)*. 1991;167: K75–K77. <https://doi.org/10.1002/pssb.2221670157>

Information about the authors

Abdullaeva Shahri Seyfaly, PhD student, Researcher, Institute of Catalysis and Inorganic Chemistry named after M. Nagiev of the Azerbaijan National Academy of Sciences (Baku, Azerbaijan).

<https://orcid.org/0000-0003-17232783>
sehri.abdullaeva.83@mail.ru

Bakhtiyarly Ikhtiyar Bahram oglu, Dr. Sci. in Chemistry, Professor, Institute of Catalysis and Inorganic Chemistry named after M. Nagiev of the Azerbaijan National Academy of Sciences (Baku, Azerbaijan).

<https://orcid.org/0000-0002-7765-0672>
ibakhtiyarli@mail.ru

Kurbanova Ruksana Jalal, PhD in Chemistry, Associate Professor, Institute of Catalysis and Inorganic Chemistry named after M. Nagiev of the Azerbaijan National Academy of Sciences (Baku, Azerbaijan).

<https://orcid.org/0000-0001-6467-0079>
kurbanova.48@inbox.ru

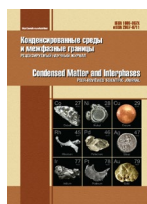
Mukhtarova Ziyafat Mamed, PhD in Chemistry, Associate Professor, Institute of Catalysis and Inorganic Chemistry named after M. Nagiev of the Azerbaijan National Academy of Sciences (Baku, Azerbaijan).

<https://orcid.org/0000-0003-1222-969X>
ziyafatmuxtarova@mail.ru

Received 13.01.2022; approved after reviewing 04.03.2022; accepted for publication 15.05.2022; published online 25.06.2022.

Translated by Valentina Mittova

Edited and proofread by Simon Cox



Original articles

Research article

<https://doi.org/10.17308/kcmf.2022.24/9258>**Calorimetric determination of phase transitions of Ag_8BX_6 (B = Ge, Sn; X = S, Se) compounds**

U. R. Bayramova, A. N. Poladova, L. F. Mashadiyeva, M. B. Babanly✉

*M. Nagiev Institute of Catalysis and Inorganic Chemistry of the Azerbaijan National Academy of Sciences, 113, H. Javid pr., Baku Az1143, Azerbaijan***Abstract**

Differential scanning calorimetry (DSC) was used to study ternary Ag_8GeS_6 , Ag_8GeSe_6 , Ag_8SnS_6 , and Ag_8SnSe_6 compounds which undergo polymorphic transformations at relatively low temperatures. Two samples of each compound with different masses in the range of 20–40 mg were examined and three DSC heating curves were taken for each sample. The DSC curve data were used to determine the temperatures and enthalpies of the phase transitions of the studied compounds from a low-temperature rhombic modification to a high-temperature cubic modification. The difference in the DSC data between all samples and all heating curves did not exceed 2%. The obtained data were used to calculate the entropies of phase transitions. It was shown that these values are abnormally high. The study also involved a comparative analysis of the obtained thermodynamic data for the Ag_8GeSe_6 and Ag_8SnSe_6 compounds and the results obtained by the method of electromotive forces.

Keywords: Ag_8GeS_6 , Ag_8GeSe_6 , Ag_8SnS_6 , Ag_8SnSe_6 , phase transition, thermodynamic functions, enthalpy, entropy, differential scanning calorimetry

Funding: The study was supported by the Science Development Foundation under the President of the Republic of Azerbaijan within the grant EIF-BGM-4-RFTF-1/2017- 21/11/ 4-M-12.

For citation: Bayramova U. R., Poladova A. N., Mashadiyeva L. F., Babanly M. B. Calorimetric determination of phase transitions of Ag_8BX_6 (B = Ge, Sn; X = S, Se) compounds. *Condensed Matter and Interphases*. 2022;24(2): 187–195. <https://doi.org/10.17308/kcmf.2022.24/9258>

Для цитирования: Байрамова У. Р., Поладова А. Н., Машадиева Л. Ф., Бабанлы М. Б. Калориметрическое определение фазовых переходов соединений Ag_8BX_6 (B = Ge, Sn; X = S, Se). *Конденсированные среды и межфазные границы*. 2022;24(2): 187–195. <https://doi.org/10.17308/kcmf.2022.24/9258>

✉ Mahammad Babanly, email: babanlymb@gmail.com

© Bayramova U. R., Poladova A. N., Mashadiyeva L. F., Babanly M. B., 2022



1. Introduction

The argyrodite family compounds with the general formula $\text{A}_8\text{B}^{\text{IV}}\text{X}_6$ (where A – Cu, Ag; B^{IV} – Si, Ge, Sn; X – S, Se, Te) have a number of valuable functional properties and have been studied by many research teams [1–3]. These compounds are attracting more and more attention as promising candidates for thermoelectric materials due to their excellent transport properties, relatively low thermal conductivity [4–13]. Moreover, their components are widely common and low-toxic. Many of these compounds undergo phase transitions at relatively low temperatures (310–520 K). Typically, high-temperature modifications crystallise in a cubic structure, and low-temperature phases have lower symmetry. Most of the high-temperature phases of these compounds, due to the peculiarities of their crystal structure, have mixed electron-ion conductivity and demonstrate high values of cationic conductivity and ionic diffusion for solids due to the high mobility of copper (or silver) ions in the “liquid-like” ion sublattice [14–20]. This makes them promising materials for ion-selective electrodes and solid electrolytes when developing various types of electric batteries, sensors, etc. [14–22].

The purpose of this work was to determine the thermodynamic functions of phase transitions of Ag_8GeS_6 , Ag_8GeSe_6 , Ag_8SnS_6 , and Ag_8SnSe_6 compounds by differential scanning calorimetry

(DSC). This method is considered to be one of the most advanced and highly sensitive methods of phase analysis. What is more, modern DSC devices have a wide range of capabilities that can be used to determine not only the temperature and enthalpy of phase transformations, heat capacity, and its dependence on thermodynamic parameters, but also the kinetic characteristics of physicochemical processes under the conditions of linear temperature change [23].

The nature of melting and the crystalline structures of the objects of our study have been examined in detail. The silver-germanium chalcogenides Ag_8GeS_6 and Ag_8GeSe_6 melt congruently at 1.228 K and 1.175 K and undergo polymorphic transformations at 493 K and 321 K, respectively [24–26]. The Ag_8SnS_6 and Ag_8SnSe_6 compounds also melt congruently at 1,112 K and 1,015 K and undergo polymorphic transformations at 445 K and 356 K, respectively [24, 27]. Low-temperature modifications (LT) of all studied compounds have rhombic structures, while their high-temperature (HT) modifications have cubic structures [24, 28–32]. More detailed information on the parameters of the crystal lattice of the above-mentioned compounds is given in Table 1.

The thermodynamic properties of the studied compounds have been investigated in a number of papers [33–37]. In [33–35], the EMF method with a glassy Ag^+ conductive electrolyte in the

Table 1. Crystallographic data for the Ag_8GeS_6 , Ag_8GeSe_6 , Ag_8SnS_6 , and Ag_8SnSe_6 compounds

Compound	Phase Transition Temperature, K	Crystallographic data
Ag_8GeS_6	493	HT rhombic phase; space group: $Pna2_1$; $a = 15.149 \text{ \AA}$; $b = 7.476 \text{ \AA}$; $c = 10.589 \text{ \AA}$ [28]
		HT cubic phase; space group: $F-43m$; $a = 10.70 \text{ \AA}$ [24]
Ag_8GeSe_6	321	HT rhombic phase; space group: $Pmn2_1$; $a = 7.823 \text{ \AA}$, $b = 7.712 \text{ \AA}$, $c = 10.885 \text{ \AA}$ [29]
		HT cubic phase; space group: $F-43m$; $a = 10.99 \text{ \AA}$ [24]
Ag_8SnS_6	445	HT rhombic phase; space group: $Pna2_1$; $a = 15.2993(9) \text{ \AA}$; $b = 7.5479(4) \text{ \AA}$; $c = 10.7045(6) \text{ \AA}$ [31]
		HT cubic phase; space group: $F-43m$; $a = 10.85 \text{ \AA}$ [24]
Ag_8SnSe_6	356	HT rhombic phase; space group: $Pmn2_1$; $a = 7.89052(6) \text{ \AA}$; $b = 7.78976(6) \text{ \AA}$; $c = 11.02717(8) \text{ \AA}$ [2]
		HT cubic phase; space group: $F-43m$; $a = 11.12 \text{ \AA}$ [24, 32]

temperature range of 400–520 K was used to study the Ag-Ge-Se and Ag-Sn-Se systems and to determine the thermodynamic functions of the formation of high-temperature modifications of the Ag_8GeSe_6 and Ag_8SnSe_6 compounds. Later, we studied these systems [36, 37] in a lower temperature region (390–450 K) by the EMF method with a solid Ag_4RbI_5 electrolyte. These EMF data were used to calculate the standard integral thermodynamic functions of the formation of both crystalline modifications of the Ag_8GeSe_6 and Ag_8SnSe_6 compounds. Thermodynamic functions of their polymorphic transitions were calculated by combining the obtained data.

2. Experimental

2.1. Synthesis

The Ag_8GeS_6 , Ag_8GeSe_6 , Ag_8SnS_6 , and Ag_8SnSe_6 compounds were synthesised for the study by direct fusion of elementary components of high purity in evacuated ($\sim 10^{-2}$ Pa) and sealed quartz ampoules. High-purity elementary components manufactured by Evochem Advanced Materials GmbH (Germany) were used for the synthesis: silver granules (Ag-00047; 99.999 %), germanium pieces (Ge-00003; 99.999 %), tin granules (Sn-00005; 99.999 %), sulphur pieces (S-00001; 99.999 %), and selenium granules (Se-00002; 99.999 %). Due to the high vapour pressure of sulphur and selenium at the melting temperatures of the synthesised compounds, the synthesis was carried out in a dual-zone mode. The temperature regime for the synthesis of each compound was selected with due account of their melting points and phase transformations. The ampoule with the reaction mixture was heated in an inclined tubular furnace to the temperature which exceeded by $\sim 50^\circ$ the melting point of the synthesised compound (“hot” zone). A part of the ampoule (~ 8 cm) was located outside the furnace and was cooled with water to control the pressure of sulphur or selenium vapours and prevent the ampoule from exploding (“cold” zone). To accelerate the interaction, the ampoule was rotated around the longitudinal axis and subjected to vibration. When the bulk of sulphur or selenium had reacted, the ampoule was introduced into the furnace completely and held in the hot zone for 1 hour. Further, the ampoule was cooled (very slowly in the region of the

polymorphic transformation temperature), and then subjected to thermal annealing just below these temperatures for 10–15 hours. This was done to ensure a complete transition of the high-temperature phase to the low-temperature phase in order to minimise the error in the enthalpy calculations. High-temperature modifications for each compound were also obtained by heating the samples in evacuated and sealed ampoules to 350°C . Then they were quenched by plunging them into ice water.

The synthesised compounds were identified by X-ray diffraction analysis (XRD). The XRD of the samples was carried out on a D8 ADVANCE powder diffractometer from Bruker (Germany) with $\text{CuK}\alpha_1$ radiation. The powder diffraction patterns presented in Fig. 1 show that the diffraction patterns of compounds which were cooled slowly after synthesis completely coincide with the XRD data (red lines in the online version) of the low-temperature rhombic modifications from the crystallographic database. The powder diffraction patterns of the quenched samples had diffraction patterns that were completely indexed in the cubic structure. Fig. 2 shows an example of a diffraction pattern of a quenched Ag_8GeS_6 sample. Thus, the XRD results of the synthesised samples confirmed their single-phase nature.

2.2. Experimental

The temperatures and the heat of the phase transitions of the studied compounds were determined by the DSC method. The principle of this method is based on the measurement of the temperature dependence of the difference in heat flows in the substance and the reference material exposed to a temperature programme. The DSC method determines heat by the heat flow, a heat derivative with respect to time. Differential scanning calorimeters have two measuring cells: one is for the studied sample while in the other, the reference cell, an empty crucible is normally placed. The measured value is the temperature difference between the sample and the reference cells at any moment of time. As a good approximation, it can be assumed that the heat exchange between the various elements of the measuring system is only carried out by the mechanism of thermal conductivity. According to the thermal conductivity equation, the

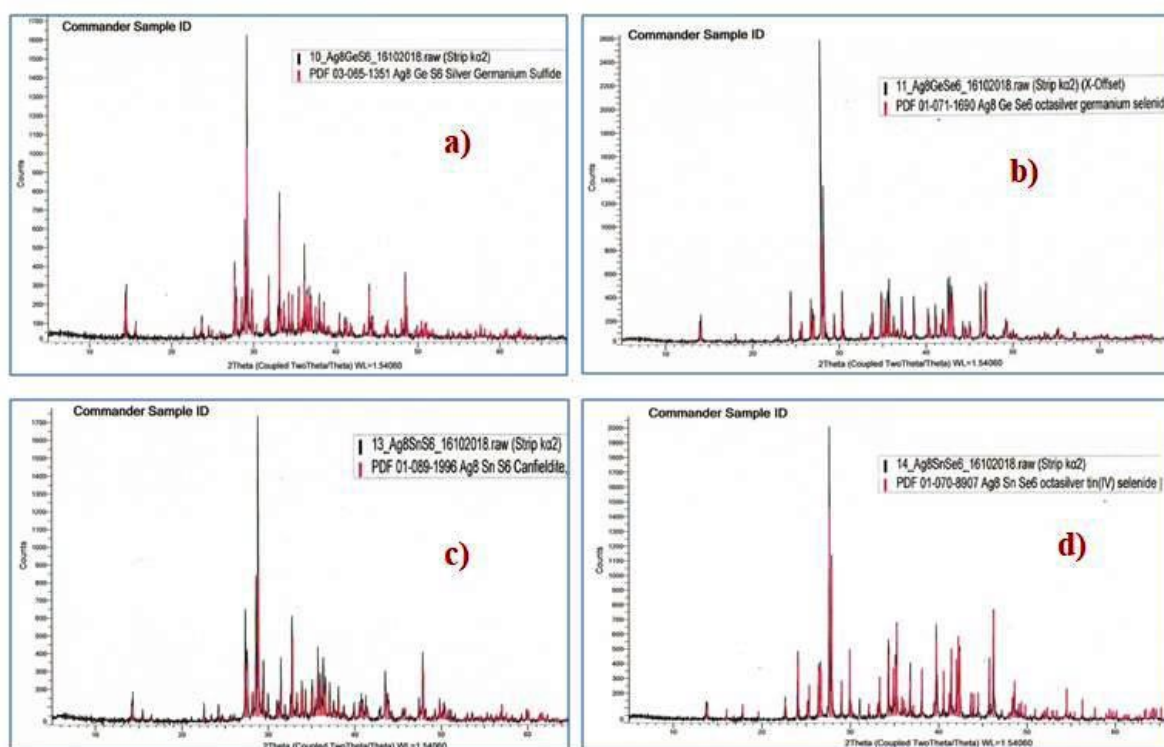


Fig. 1. Powder diffraction patterns of low-temperature modifications of the Ag_8GeSe_6 (a), Ag_8GeSe_6 (b), Ag_8SnS_6 (c), and Ag_8SnSe_6 (d) compounds

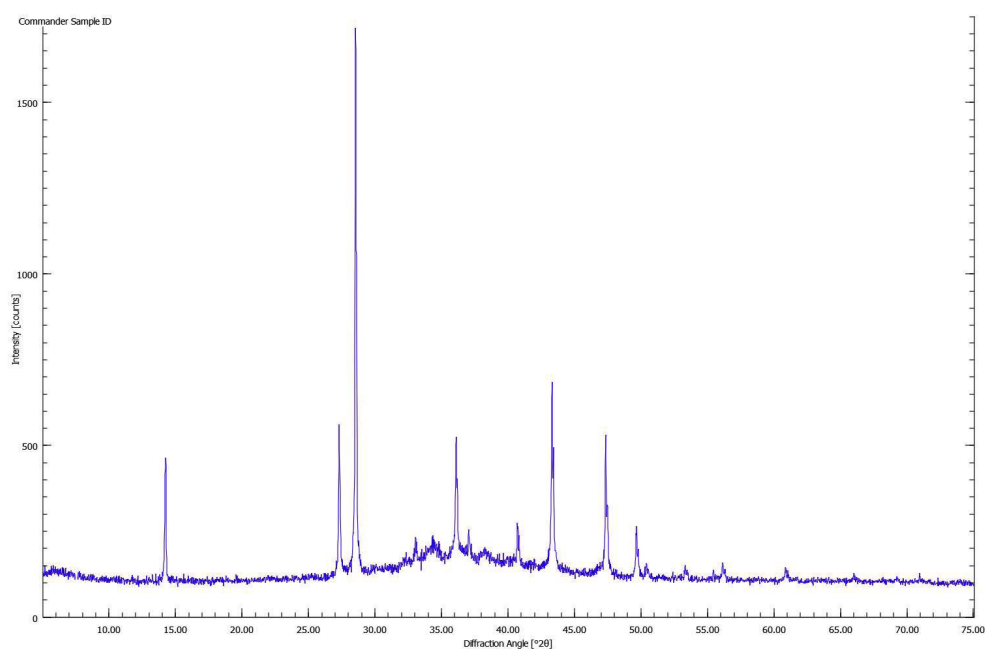


Fig. 2. Powder diffraction pattern of the Ag_8GeSe_6 sample, quenched from 350 °C

temperature difference measured at two points at the same moment of time is proportional to the value of the heat flow between them. The differential signal is displayed as a reference line. Effects, such as phase transitions of the first order, can be observed in the form of a peak. The area of the peak is the amount of enthalpy, and the

direction of the peak indicates the direction of heat flow, endothermic or exothermic [23].

Three characteristic temperatures can be used to describe the peak on the DSC curve: T_{onset} , T_{peak} , and T_{end} (Fig. 3). The initial and final temperatures correspond to the intersection of the reference line extrapolated to the peak region

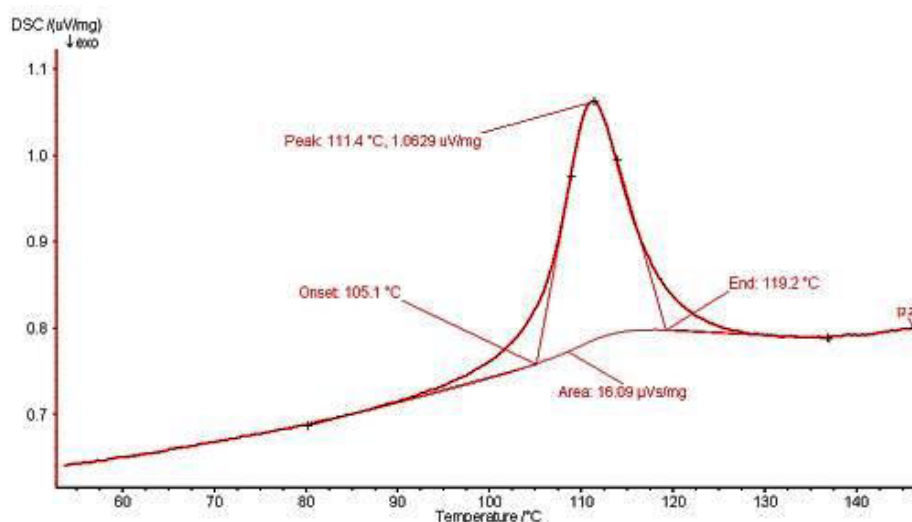


Fig. 3. Characteristics of the peak on the DSC curve

and the tangents drawn through the point of inflexion. The reference line is a virtual line drawn through the interval in which a reaction or phase transition occurs under the assumption that the heat of the process is zero.

Our experiments were carried out on a DSC400 differential scanning calorimeter manufactured by Linseis (Germany), which had the following specifications:

- Temperature range of the platinum furnace: from room temperature to 1,600 °C.
- Temperature scanning speed: in the range from 0.01 to 100 °C/min.
- Thermocouples: platinum-platinum-rhodium.
- Temperature accuracy: 0.01°.
- DSC resolution: 1 mW.
- Calorimetric sensitivity: 17.6 µW.
- Heat accuracy: ±1 %.

The measurements were taken using the Linseis TA V 2.3.1 software. The calorimeter had been pre-calibrated. Since our studies were carried out at low temperatures (300–550 K), relatively low-melting metals were used as references for the calibration of our device: indium, tin, bismuth, and zinc provided by Linseis for this purpose, with appropriate certificates. The calibration temperature for each substance was selected in accordance with the recommendations given in the manual.

The DSC of the compounds and references was performed using an aluminium crucible with a lid. Given that the studied compounds

were solid polycrystalline samples, they were preliminarily ground to a powdery state prior to the measurement in order to ensure the maximum contact area between the studied sample and the crucible bottom. Due to the fact that the amount of the sample tested by the DSC method was very small (about several tens of mg), a greater weighing error could lead to a very noticeable relative error in determining the extensive values. Therefore, to weigh the samples, we used accurate (first class of accuracy according to GOST) Radwag electronic analytical balance (Poland), AS220 series, with a range from 1 mg to 220 g and a measurement accuracy of 0.01/0.1 mg. The DSC study mode was selected based on the phase transition temperature of the studied compound. The heating rate was 3 °/min. The measurements were carried out in a flow of argon.

3. Results and Discussion

To determine the temperatures and enthalpies of the phase transitions of the Ag_8GeS_6 , Ag_8GeSe_6 , Ag_8SnS_6 , and Ag_8SnSe_6 compounds, we took DSC heating curves for the samples. Two samples of each compound with different masses in the range of 20–40 mg were selected and three DSC heating curves were taken for each sample. Thus, 6 DSC curves were taken for each compound. The DSC curves were then processed using the Linseis TA Evaluation V2.3.1 software and the temperatures of the beginning and the end of the peak and the enthalpy of the phase transition for 1 mole of substance were obtained. These values were

almost identical in the DSC curves for all samples and the difference did not exceed 2%. According to [38], in such cases, the error in determining the thermal effects is not more than $\pm 4\%$.

Below, as an example, we present the study and calculation procedure for the Ag_8SnSe_6 compound. We selected two samples of this compound with masses of 25.56 and 33.72 mg. Given that the phase transition temperature for the Ag_8SnSe_6 compound is 356 K [24], the DSC study was carried out in a dynamic mode of

heating from room temperature to 400 K. The DSC heating curve obtained for the Ag_8SnSe_6 sample with a mass of 25.56 mg is shown in Fig. 4. The following average values of phase transition enthalpies were obtained: $\Delta H_{p.t.} = 19.63$ kJ/mol (25.56 mg); $\Delta H_{p.t.} = 19.71$ kJ/mol (33.72 mg). The average for these values was taken as the final value of $\Delta H_{p.t.}$ for the Ag_8SnSe_6 compound (Table 2).

Table 2 also shows the temperatures and average values for phase transition enthalpies for

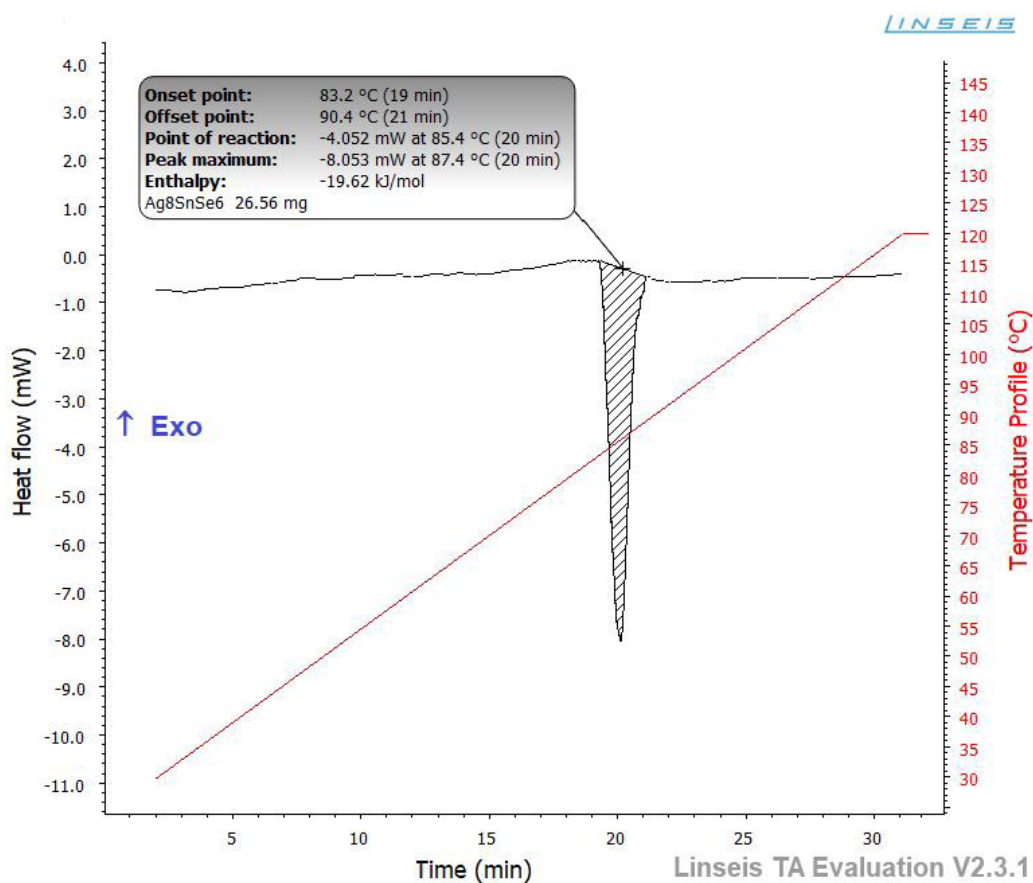


Fig. 4. DSC heating curve of the Ag_8SnSe_6 compounds with a mass of 26.56 mg

Table 2. Thermodynamic data for phase transitions of the Ag_8GeS_6 , Ag_8GeSe_6 , Ag_8SnS_6 , and Ag_8SnSe_6 compounds

Compound	Phase Transition Temperature, K	$\Delta H_{p.t.}$, kJ/mol	$\Delta S_{p.t.}$, J/(mol×K)
Ag_8GeS_6	495	9.46 ± 0.38	19.11 ± 0.76
Ag_8GeSe_6	321	16.95 ± 0.68	52.80 ± 2.11
		15.0 ± 4.7 [36]	46.9 ± 14.8 [36]
Ag_8SnS_6	446	8.77 ± 0.35	19.66 ± 0.79
Ag_8SnSe_6	355	19.67 ± 0.6	55.41 ± 2.22
		15.4 ± 4.3 [37]	43.4 ± 12.1 [37]

the rest of the studied compounds. The obtained values of enthalpies and temperatures (T_{onset}) of phase transitions were used to calculate entropies of phase transitions (Table 2) by the formula:

$$\Delta S_{\text{p.t.}} = \Delta H_{\text{p.t.}} / T_{\text{p.t.}}$$

As shown in Table 2, the entropy values of the phase transitions of the two sulphide compounds are very close. Apparently, this is due to the fact that these values refer to the same type of change in the crystal structure during the phase transition (from a rhombic lattice to a cubic lattice). In other words, the degree of disordering at the phase transition is approximately the same for both compounds. A similar pattern was also observed for selenides. It should be noted that selenides had much higher values of $\Delta S_{\text{p.t.}}$ than sulphides. This indirectly indicates a greater disordering of silver ions in the cubic lattice of selenides as compared to sulphides.

It should be noted that the values of $\Delta H_{\text{p.t.}}$ for the Ag_8GeSe_6 and Ag_8SnSe_6 compounds [36, 37] obtained by the EMF method differ from the results of this work by up to 22%, which is within the error of the data obtained by the EMF method (Table 2). It is obvious that the calorimetric data are more accurate, since the EMF method determines the heat of the phase transition from the differences in the slopes of the lines of the direct EMF temperature dependencies for the two modifications [39, 40].

The analysis of the published data on thermodynamic functions of phase transitions of chalcogenides [41] showed that the values of such functions for our research objects are quite high compared to the values of thermodynamic functions of phase transitions of the first kind. Apparently, this is due to a higher degree of disordering in their structure during phase transformation. During the transition to the high-temperature modification of the argyrodite-type $\text{Ag}_8\text{B}^{\text{IV}}\text{X}_6$ compounds, many empty positions are formed in the rigid anionic framework, which makes silver cations mobile [14, 24]. This leads to an additional growth in entropy.

4. Conclusions

We provided new data on the thermodynamic functions of phase transitions of Ag_8GeS_6 , Ag_8GeSe_6 , Ag_8SnS_6 , and Ag_8SnSe_6 compounds,

members of the argyrodite family, obtained by DSC. The abnormally high entropy values for the phase transitions characteristic of these compounds can be explained by strong disordering in the cationic sublattice of high-temperature cubic modifications, which is accompanied by an increased mobility of silver ions.

Author contributions

M. B. Babanly: scientific supervision, research concept, and conclusions. L. F. Mashadiyeva: research concept, writing of the article, discussion of the results. U. R. Bayramova, A. N. Poladova: synthesis of the compounds, research.

Conflict of interests

The authors declare that they have no known competing financial interests or personal relationships that could have influenced the work reported in this paper.

References

1. Babanly M. B., Yusibov Yu. A., Abishov V. T. *Ternary chalcogenides based on copper and silver*. Baku: BQU Publ.; 1993. 342 p. (In Russ.)
2. Semkiv I., Ilchuk H., Pawlowski M., Kusnezh V. Ag_8SnSe_6 argyrodite synthesis and optical properties. *Opto-Electronics Review*. 2017;25(1): 37–40. <https://doi.org/10.1016/j.opelre.2017.04.002>
3. Studenyak I. P., Pogodin A. I., Studenyak V. I., Izai V. Y., Filep M. J., Kokhan O. P., Kúš P. Electrical properties of copper- and silver-containing superionic $(\text{Cu}_{1-x}\text{Ag}_x)_7\text{SiS}_5\text{I}$ mixed crystals with argyrodite structure. *Solid State Ionics*. 2020;345: 115183. <https://doi.org/10.1016/j.ssi.2019.115183>
4. Lin S., Li W., Pei Y. Thermally insulative thermoelectric argyrodites. *Materials Today*. 2021;48:198–213. <https://doi.org/10.1016/j.mattod.2021.01.007>
5. Shen X., Yang C., Liu Y., Wang G., Tan H. A High temperature structural and thermoelectric study of argyrodite Ag_8GeSe_6 . *ACS Applied Materials & Interfaces*. 2019;11(2): 2168–2176. <https://doi.org/10.1021/acsami.8b19819>
6. Jin M., Lin S., Li W., Chen Z., Li R., Wang X. Pei Y. Fabrication and thermoelectric properties of single-crystal argyrodite Ag_8SnSe_6 . *Chemistry of Materials*. 2019;31(7): 2603–2610. <https://doi.org/10.1021/acs.chemmater.9b00393>
7. Jiang B., Qiu P., Eikeland E., Chen H., Song Q., Ren D., Chen L. Cu_8GeSe_6 -based thermoelectric materials with an argyrodite structure. *Journal of Materials Chemistry C*. 2017;5(4): 943–952. <https://doi.org/10.1039/C6TC05068A>

8. Jiang Q., Li S., Luo Y., Xin J., Li S., Li W., Yang J. Ecofriendly highly robust Ag_8SiSe_6 -based thermoelectric composites with excellent performance near room temperature. *ACS Applied Materials & Interfaces*. 2020;12(49): 54653–54661. <https://doi.org/10.1021/acsami.0c15877>
9. Fan Y., Wang G., Wang R., Zhang B., Shen X., Jiang P., Zhang X., Gu H., Lu X., Zhou X. Enhanced thermoelectric properties of *p*-type argyrodites Cu_8GeS_6 through Cu vacancy. *Journal of Alloys and Compounds*. 2020;822: 153665. <https://doi.org/10.1016/j.jallcom.2020.153665>
10. Yang C., Luo, Y., Li X., Cui J. N-type thermoelectric Ag_8SnSe_6 with extremely low lattice thermal conductivity by replacing Ag with Cu. *RSC Advances*. 2021;11: 3732–3739. <https://doi.org/10.1039/D0RA10454J>
11. Li W., Lin S., Ge B., Yang J., Zhang W., Pei Y. Low sound velocity contributing to the high thermoelectric performance of Ag_8SnSe_6 . *Advanced Sciences*. 2016;3(11): 1600196–1600212. <https://doi.org/10.1002/advs.201600196>
12. Ghrib T., Al-Otaibi A. L., Almessiere M. A., Assaker I. B., Chtourou R. High thermoelectric figure of merit of Ag_8SnS_6 component prepared by electrodeposition technique. *Chinese Physics Letters*. 2015;32(12): <https://doi.org/10.1088/0256-307X/32/12/127402>
13. Namiki H., Yahisa D., Kobayashi M., Shono A., Hayashi H. Enhancement and manipulation of the thermoelectric properties of n-type argyrodite Ag_8SnSe_6 with ultralow thermal conductivity by controlling the carrier concentration through Ta doping. *AIP Advances*. 2021; 11: 075125. <https://doi.org/10.1063/5.0056533>
14. Ivanov-Shits A. K., Murin I. V. *Solid state ionics, v. 1*. Saint Peterburg: SPU Publ.; 2000. 616 p. (In Russ.)
15. Berezin V. M., Vyatkin Q. P. *Superionic semiconducting chalcogenides*. Celyabinsk: Yu.Ur.Qu. Publ.; 2001. 135 p. (In Russ.)
16. Liu H., Shi X., Xu F. et al. Copper ion liquid-like thermoelectrics. *Nature Materials*. 2012;11(5): 422–425. <https://doi.org/10.1038/nmat3273>
17. Heep B. K., Weldert K. S., Krysiak Y., Day T. W., Zeier W. G., Kolb U., Snyder G. J., Tremel W. High electron mobility and disorder induced by silver ion migration lead to good thermoelectric performance in the argyrodite Ag_8SiSe_6 . *Chemistry of Materials*. 2017;29(11): 4833–4839. <https://doi.org/10.1021/acs.chemmater.7b00767>
18. Lin Y., Fang S., Su D., Brinkman K. S. Enhancing grain boundary ionic conductivity in mixed ionic–electronic conductors. *Nature Communications*. 2015;6(1): 1–9. <https://doi.org/10.1038/ncomms7824>
19. Boucher F., Evain M., Brec R. Distribution and ionic diffusion path of silver in $\gamma\text{-Ag}_8\text{GeTe}_6$: A temperature dependent anharmonic single crystal structure study. *Journal of Solid State Chemistry*. 1993;107(2): 332–346. <https://doi.org/10.1006/jssc.1993.1356>
20. Heep B. K., Weldert K. S., Krysiak Y., Day T. W., Zeier W. G., Kolb U., Snyder G. J., Tremel W. High electron mobility and disorder induced by silver ion migration lead to good thermoelectric performance in the argyrodite Ag_8SiSe_6 . *Chemistry of Materials*. 2017;29(11): 4833–4839. <https://doi.org/10.1021/acs.chemmater.7b00767>
21. Babanly M. B., Yusibov Yu. A., Babanly N. B. The EMF method with solid-state electrolyte in the thermodynamic investigation of ternary copper and silver chalcogenides. Electromotive force and measurement in several systems. *Electromotive Force and Measurement in Several Systems*. 2011;57–78: <https://doi.org/10.5772/28934>
22. Babanly M. B., Mashadiyeva L. F., Babanly D. M. et al. Some aspects of complex investigation of the phase equilibria and thermodynamic properties of the ternary chalcogenid systems involving EMF Measurements (Review). *Russian Journal of Inorganic Chemistry*. 2019;64(13): 1649–1671. <https://doi.org/10.1134/s0036023619130035>
23. Menczel J., Grebowicz J. *The handbook of differential scanning calorimetry: Techniques and low molecular mass materials*. Elsevier Science; 2022. 858 p.
24. Gorochov O. Les composés Ag_8MX_6 (M = Si, Ge, Sn et X = S, Se, Te). *Bulletin de la Société chimique de France*. 1968; 2263–2275.
25. Prince A., *Silver–germanium–selenium, in Ternary Alloys: A Comprehensive Compendium of Evaluated Constitutional Data and Phase Diagrams*. Stuttgart: Max Plank Inst.; 1992. 492 p.
26. Yusibov Y. A., Alverdiev I. D., Ibragimova F. S., Mamedov A. N., Tagiev D. B., Babanly M. B. Study and 3d modeling of the phase diagram of the Ag–Ge–Se system. *Russian Journal of Inorganic Chemistry*. 2017;62(9): 1223–1233. <https://doi.org/10.1134/S0036023617090182>
27. Yusibov Y. A., Alverdiev I. D., Mashadiyeva L. F., Babanly D. M., Mamedov A. N., Babanly M. B. Experimental study and 3d modeling of the phase diagram of the Ag–Sn–Se System. *Russian Journal of Inorganic Chemistry*. 2018;63(12): 1622–1635. <https://doi.org/10.1134/S0036023618120227>
28. Eulenberger G. Die kristallstruktur der tieftemperaturmodifikation von Ag_8GeS_6 . *Monatshefte Fur Chemie*. 1977;108(4): 901–913. <https://doi.org/10.1007/bf00898056>
29. Carré D., Ollitrault Fichet R., Flahaut J. Structure de Ag_8GeSe_6 . *Acta Crystallographica Section B Structural Crystallography and Crystal Chemistry*. 1980;36(2): 245–249. <https://doi.org/10.1107/S0567740880003032>

30. Wang N. New data for Ag_8SnS_6 (canfeildite) and Ag_8GeS_6 (argyrodite). *Neues Jahrb. Mineral., Monatsch.*; 1978; 269–272.
31. Slade T. J., Gvozdetzkyi V., Wilde J. M., Kreyssig A., Gati E., Wang L., Mudryk Y., Ribeiro R. A., Pecharsky V. K., Zaikina J. V., Bud'ko S. L., Canfield P. C. A low-temperature structural transition in canfieldite, Ag_8SnS_6 , single crystals. *Inorganic Chemistry*. 2021;60(24): 19345–19355. <https://doi.org/10.1021/acs.inorgchem.1c03158>
32. Gulay L. D., Olekseyuk I. D., Parasyuk O. V. Crystal structure of β - Ag_8SnSe_6 . *Journal of Alloys and Compounds*. 2002; 339(1): 113–117. [https://doi.org/10.1016/s0925-8388\(01\)01970-3](https://doi.org/10.1016/s0925-8388(01)01970-3)
33. Moroz M. V., Prokhorenko M. V. Determination of thermodynamic properties of saturated solid solutions of the Ag–Ge–Se system using EMF technique. *Russian Journal of Electrochemistry*. 2015;51(7): 697–702. <https://doi.org/10.1134/S1023193515070046>
34. Moroz M. V., Prokhorenko M. V. Measurement of the thermodynamic properties of saturated solid solutions of compounds in the Ag–Sn–Se system by the EMF method. *Russian Journal of Physical Chemistry A*. 2015;89(8): 1325–1329. <https://doi.org/10.1134/s0036024415080221>
35. Moroz M. V., Prokhorenko M. V., Demchenko P. Yu., Reshetnyak O. V. Thermodynamic properties of saturated solid solutions of Ag_7SnSe_5Br and Ag_8SnSe_6 compounds in the Ag–Sn–Se–Br system measured by the EMF method. *The Journal of Chemical Thermodynamics*. 2017;106; 228–231. <https://doi.org/10.1016/j.jct.2016.12.004>
36. Alverdiev I. D., Yusibov Y. A., Bagkheri S. M., Imamalieva S. Z., Babanly M. B. Thermodynamic study of Ag_8GeSe_6 by EMF with an Ag_4RbI_5 solid electrolyte *Russian Journal of Electrochemistry*. 2017;53(5): 551–554. <https://doi.org/10.1134/S1023193517050032>
37. Alverdiev I. D., Yusibov Y. A., Imamalieva S. Z., Babanly D. M., Tagiev D. B., Babanly M. B. Thermodynamic study of silver-tin selenides by the EMF method with Ag_4RbI_5 solid electrolyte. *Russian Journal of Electrochemistry*. 2019;55(5): 467–474. <https://doi.org/10.1134/s1023193519050021>
38. Hohne G. W. H., Hemminger W. F., Flammersheim H. J. *Differential Scanning Calorimetry*. Second Edition. Berlin: Springer; 2003. 300 p. https://doi.org/10.1007/978-3-662-06710-9_3
39. Morachevskiy A. Q., Voronin Q. F., Qeyderikh V. A., Kutsenok I. B. *Electrochemical research methods in thermodynamics of metallic systems*. Moscow: ISK «Akademkniga» Publ.; 2003. 334 p. (In Russ.)
40. Babanly M. B., Yusibov Yu. A., Babanly M. B., Yusibov Yu. A. *Electrochemical methods in thermodynamics of inorganic systems*. Baku: Elm Publ.; 2011. 306 p. (In Russ.)
41. *Physical and chemical properties of semiconductor substances*. Handbook. Novoselova A. V. and Lazereva V. B. (Eds.). Moscow: Nauka Publ.; 1976. 339 p. (In Russ.)

Information about authors

Ulviya R. Bayramova, PhD student, Institute of Catalysis and Inorganic Chemistry of the Azerbaijan National Academy of Sciences (Baku, Azerbaijan). <https://orcid.org/0000-0001-5096-2513>

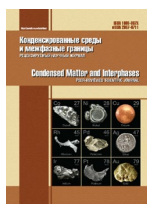
Albina N. Poladova, Junior Scientific Fellow, Institute of Catalysis and Inorganic Chemistry of Azerbaijan National Academy of Sciences (Baku, Azerbaijan). <https://orcid.org/0000-0001-9653-6675>

Leyla F. Mashadiyeva, Ph.D. (Chem.), Associate Professor, Senior Scientific Fellow, Institute of Catalysis and Inorganic Chemistry of Azerbaijan National Academy of Sciences (Baku, Azerbaijan). <https://orcid.org/0000-0003-2357-6195>

Mahammad B. Babanly, Dr. Sci. (Chem.), Professor, Associate Member of the Azerbaijan National Academy of Sciences, Executive Director of the Institute of Catalysis and Inorganic Chemistry, Azerbaijan National Academy of Sciences (Baku, Azerbaijan). <https://orcid.org/0000-0001-5962-3710>
babanlymb@gmail.com

Received 03.03.2022; approved after reviewing 18.03.2022; accepted for publication 15.04.2022; published online 25.06.2022.

Translated by Irina Charychanskaya
Edited and proofread by Simon Cox



Original articles

Research article

<https://doi.org/10.17308/kcmf.2022.24/9259>

Sorption of 3-glucosides of six common natural anthocyanidins on anatase

V. I. Deineka✉, Ya. Yu. Salasina, L. A. Deineka

Belgorod State University,
85 Pobedi str., Belgorod 308015 Russian Federation

Abstract

In this study, the sorption of 3-glucosides of six common natural aglicones: delphinidin, cyanidin, petunidin, pelargonidin, peonidin and malvidin, on the surface of anatase was studied in comparison with sorption on the surface of silica gel, as a result, a different order of change in the sorption activity of anthocyanins depending on their structure was found. The structure of the (001) face of the surface layer of anatase crystals due to the olation and oxolation of the initial $[\text{Ti}(\text{OH})_4(\text{H}_2\text{O})_2]$ octahedra upon condensation into three-dimensional grids was proposed.

The mechanisms of sorption of anthocyanins on the surface of sorbents are proposed. Delphinidin derivatives have the highest sorption activity on anatase.

Keywords: Anthocyanins, Sorption, Sorption mechanisms, Anatase, Surface layer structure, Silica gel

For citation: Deineka V.I., Salasina Ya. Yu., Deineka L. A. Sorption of 3-glucosides of six common natural anthocyanidins on anatase. *Condensed Matter and Interphases*. 2022;24(2): 196–203. <https://doi.org/10.17308/kcmf.2022.24/9259>

Для цитирования: Дейнека В. И., Саласина Я. Ю., Дейнека Л. А. Сорбция 3-глюкозидов шести основных природных антоцианидов на анатазе. *Конденсированные среды и межфазные границы*. 2022;24(2): 196–203. <https://doi.org/10.17308/kcmf.2022.24/9259>

✉ Viktor Deineka, e-mail: deineka@bsu.edu.ru

© Deineka V.I., Salasina Ya. Yu., Deineka L. A., 2022



The content is available under Creative Commons Attribution 4.0 License.

1. Introduction

Dye sensitised solar cells (DSSC) became the focus of attention after the work of Swiss researchers [1], who created a solar battery by a combination of nanostructured electrodes and a dye capable of efficient charge transfer. The use of sintered mesoporous titanium dioxide turned out to be a breakthrough idea that made it possible to lay the foundations for the design of DSSC, raising the efficiency of converting light energy into electrical energy from 1% (for batteries with non-porous TiO_2) up to 7% [2]. The principle of operation of DSSC is as follows [2]:

1) at the anode, the dye captures a light quantum, transiting into an excited electronic state:



2) the dye in the excited state transfers an electron to the semiconductor (TiO_2), transforming into the corresponding cation:



3) the dye returns to its original state, oxidizing the iodide ion from the electrolyte:



4) the electrolyte is regenerated at the cathode (Pt):



Various natural dyes, including anthocyanins, have been studied as sensitizers for the production of cheap and environmentally friendly DSSC [2–5]. For efficient electron transfer from a dye to a semiconductor, direct chemical bonding between anthocyanins and titanium atoms is required. Two variants of differing schemes were proposed for such binding, shown in Fig. 1. In the first

variant, the quinonoid [3], and in the second variant, the flavylum [4] form of anthocyanins are adsorbed, but in both cases the interaction occurs through the B-ring of anthocyanins. At the same time, due to differences in the structure of anthocyanins, the structure of the B-ring should have a decisive influence on binding, and in the case of pelargonidin derivatives, only one-point interaction is possible due to the presence of only one hydroxyl (or keto-group in the quinonoid form) group in the B-ring.

The efficiency of sorption of anthocyanins based on various aglycones on titanium dioxide has not been investigated in any of the studies known to us.

The purpose of this study was the comparison of the sorption of 3-glucosides of six common anthocyanidins (pelargonidin, cyanidin, peonidin, delphinidin, petunidin, and malvidin) on anatase, which is one of the three natural crystalline modifications of TiO_2 used as a semiconductor in solar cells and the comparison with the sorption of the same substances on silica gel.

2. Experimental

Anthocyanins were obtained by extraction with a 0.1 M HCl aqueous solution from plant materials, specifically the leaves of eastern redbud (*Cercis canadensis*) and fruits of common barberry (*Berberis vulgaris*). The resulting extracts were purified by solid-phase extraction using DIAPAC C18 syringe cartridges [5]. Re-extracts were obtained by eluting anthocyanins from the cartridges with a mixture of ethanol and 0.1 M HCl aqueous solution. Ethanol was removed using a vacuum rotary evaporator. The solutions were mixed to obtain a complete set of 3-glucosides of cyanidin, peonidin, delphinidin, petunidin,

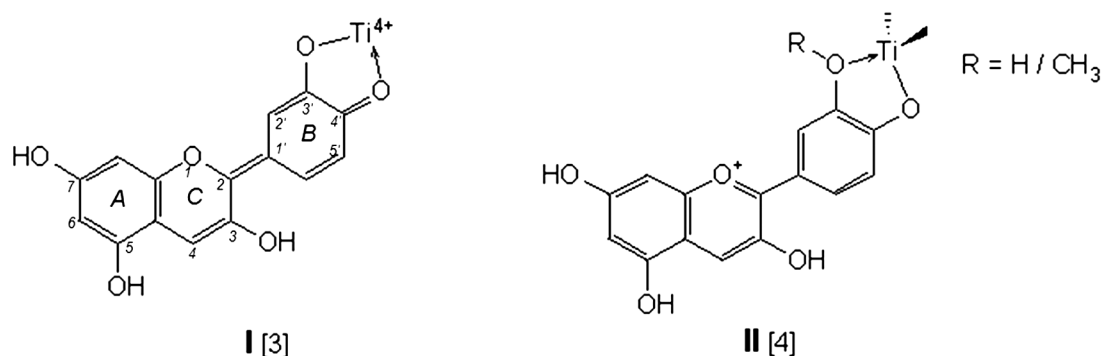


Fig. 1. Anthocyanins bonding with surface Ti atoms according to studies [3] and [4]

and malvidin from eastern redbud leaves [7] and pelargonidin 3-glucoside from barberry fruits [8] in comparable amounts.

For the sorption of anthocyanins by anatase and silica gel, the same purified extracts or their mixtures were used. Accurate weighed quantities of anatase or silica gel in the amount from 0.2 g to 1.0 g with a step of 0.2 g were added to 10 ml of extracts with a reduced (i.e., taking into account dilution before spectrophotometry) optical density at an absorption maximum of about 2–3. The resulting mixtures were vigorously shaken for at least 2 h, followed by centrifugation for 10 min at 2700 rpm. The mother solution was separated by decantation, and its composition, as well as the composition of the initial extract, was analysed by HPLC [9].

3. Results and discussion

It should be noted that the schemes of interaction between anthocyanins and anatase surface, proposed in the scientific literature and presented in Fig. 1, are not substantiated. Thus, scheme 1 in Fig. 1 suggests the formation of chelate complexes with the participation of the quinonoid structure, although the electronic absorption spectra of anthocyanins in the sorbed state presented in the cited article correspond to the flavylium form. Structure II includes titanium with an oxidation state of +3 with a tetrahedral environment and the flavylium form of anthocyanins in the form of a chelate complex. Pelargonidin derivatives cannot form such complexes, but their inefficiency does not follow from the known literature data (see review [2]).

On the other hand, it is known [10, 11] that the structures of anatase, rutile, and brookite are composed of distorted octahedra, and

the only difference is in the joining of these octahedra and in their arrangement in space. At the same time, in [12], a scheme of ololation and oxolation for the joining of $[\text{Ti}(\text{OH})_4(\text{H}_2\text{O})_2]$ or $[\text{Ti}(\text{OH})_5(\text{H}_2\text{O})_3]^+$ octahedra into bulk crystal structures was proposed. During the ololation of two such octahedra along the edges gives rise to two bridging hydroxide ions OH^- , and as a result of further oxolation, an oxygen atom with a trigonal environment of titanium atoms arises. Thus, the coordination number of titanium inside the crystals is 6, and the coordination number of oxygen atoms is 3.

A study comparing the sorption propensity of anthocyanins on the surface of anatase was performed in comparison with sorption on the surface of silica gel. The mixture was composed in such a way that the structure of anthocyanins differed in the number of hydrogen bond donors (OH-groups) and hydrogen bond acceptors (as well as electron pair donors for donor-acceptor interaction, OH^- and/or OCH_3 -groups) in the B-ring. For this, a solution containing 3-glucosides of six main natural anthocyanins: delphinidin (Dp3Glu, three OH groups in the B-ring), cyanidin (Cy3Glu, two OH groups in the B-ring), petunidin (Pt3Glu, two OH groups and one OCH_3 -group in the B-ring), peonidin (Pn3Glu, one OH group and one OCH_3 -group in the B-ring) and malvidin (Mv3Glu, one OH group and two OCH_3 -groups in the B-ring), and pelargonidin (Pg3Glu, only one OH group in the B-ring) was prepared. The results obtained for anatase and silica gel are presented in Table 1 and Table 2.

The tables show the degree of sorption of each of the anthocyanins (α), relative values of the degree of sorption, calculated using the formula:

Table 1. Parameters of sorption activity of anthocyanins on anatase

No	Anthocyanin	Experiment No. 1			Experiment No. 2			Mean value $\bar{\beta}$
		α	$\alpha(\text{rel.})$	β	α	$\alpha(\text{rel.})$	β	
1	Dp3G	0.57	11	24.5	0.74	8.81	31.5	28.0
2	Cy3G	0.28	5.43	7.19	0.45	5.31	8.83	8.01
3	Pt3G	0.37	7.01	10.5	0.55	6.5	13.2	11.8
4	Pg3G	0.05	1	1	0.08	1	1	1
5	Pn3G	0.14	2.65	2.92	0.21	2.53	2.94	2.93
6	Mv3G	0.18	3.38	3.88	0.26	3.11	3.86	3.87

α - absorption degree of the anthocyanin, $\alpha(\text{rel.})$ - ratio to the parameter for Pg3Glu, $\bar{\beta}$ - mean value.

Table 2. Parameters of sorption activity of anthocyanins on silica

No	Anthocyanin	Experiment No. 1			Experiment No. 2			Mean value $\bar{\beta}$
		α	$\alpha(\text{rel.})$	β	α	$\alpha(\text{rel.})$	β	
1	Dp3G	0.42	0.92	0.86	0.47	0.94	0.88	0.87
2	Cy3G	0.43	0.94	0.90	0.47	0.93	0.87	0.89
3	Pt3G	0.45	0.98	0.97	0.51	1.01	1.03	1
4	Pg3G	0.46	1	1	0.5	1	1	1
5	Pn3G	0.5	1.09	1.19	0.55	1.1	1.22	1.2
6	Mv3G	0.51	1.11	1.23	0.59	1.17	1.41	1.32

α - absorption degree of the anthocyanin, $\alpha(\text{rel.})$ – ratio to the parameter for Pg3Glu, $\bar{\beta}$ – mean value.

$$\alpha(\text{rel.}) = \frac{\alpha(i)}{\alpha(\text{Pg3Glu})}, \quad (5)$$

and β – sorption parameter calculated using the formula [13]:

$$\beta(i) = \frac{\frac{1}{\alpha(A)} - 1}{\frac{1}{\alpha(B)} - 1} = \frac{b(B)}{b(A)}. \quad (6)$$

On silica gel, silanol (Si-OH) groups are active and accessible, while siloxane groups are more sterically hindered and are of secondary importance in sorption. The acidity of the surface silanol groups enables their involvement in the formation of hydrogen bonds with the sorbate as proton donors. In this case, the difference in the acceptor capacity (during the formation of a hydrogen bond) of OH- and OCH₃-groups should not be high, with some preference for groups with oxygen atoms with the highest charge.

For the estimation of the charge state of oxygen atoms in anthocyanins, we calculated the distribution of electron density in model 3-methylglycones using the semi-empirical PM3 method (Table 3).

When 3-glucosides are adsorbed on the acid sites of silica gel, their functional groups can

participate in the formation of a hydrogen bond as acceptors for oxygen atoms of the B-ring or A-ring. Based on the comparison of the charges on oxygen atoms, shown in Table 3, it can be assumed that for derivatives of cyanidin, petunidin, peonidin, and malvidin, the hydrogen bond (as an acceptor) should be formed by the oxygen atom of the hydroxyl group in position 4' and in the case of delphinidin it should be formed by the oxygen atom of the hydroxyl group in position 3'.

In the case of a pelargonidin derivative, sorption at position 7 (i.e., in the A-ring) is preferable to sorption at other positions. However, the close values of the parameters of sorption activity of all six anthocyanins (Table 2) on silica gel cannot be explained by the different orientation of anthocyanins relative to the silica gel surface. Obviously, for more stable sorption of anthocyanins, the formation of two hydrogen bonds is necessary. In this case, all six anthocyanins have in common the presence of hydroxyl groups in positions 5 and 7, which have only small differences in charges for all six anthocyanins. In this case, the geometric parameters also turn out to be favourable: the distance between neighbouring silanol groups on the silica gel surface (0.526 nm [13]) is consistent with the distance between the oxygen

Table 3. Distribution of electron density between oxygen atoms in 3-methoxyanthocyanidins

Anthocyanin	The charge on the oxygen atom in position:				
	5	7	3'	4'	5'
3MeDp	-0.181	-0.185	-0.223	-0.203	-0.202
3MeCy	-0.183	-0.186	-0.209	-0.203	-
3MePg	-0.184	-0.187	-	-0.182	-
3MePt	-0.182	-0.187	-0.195	-0.204	-0.202
3MePn	-0.184	-0.188	-0.196	-0.179	-
3MeMv	-0.182	-0.187	-0.195	-0.204	-0.202

atoms of hydroxyl groups in positions 5 and 7 in anthocyanins (0.476 nm, calculated by the PM3 method); the existing small differences are levelled by the flexibility of the orientation of hydrogen bonds, and the interaction scheme is shown in Fig. 2. Moreover, the anthocyanin plane can be tilted towards the interior of the pattern in a way that the steric effect of the glycosidic substituent at position 3 can be neglected.

A significant difference in the sorption of anthocyanins on silica gel and on anatase becomes apparent when analysing the data in Table 1. The greatest increase in sorption activity is observed with an increase in the number of hydroxyl groups in the sorbate (in the series of pelargonidin - cyanidin - delphinidin derivatives), and also, even though to a lesser extent, in the series of pelargonidin - peonidin - malvidin derivatives.

For the prediction of the possible mechanism of anthocyanin sorption on anatase, it is necessary to know the surface structure of TiO_2 , the elementary crystal lattice of which is shown in Fig. 3.

The outer planar octahedral layer of the titanium-oxygen octahedra of the [001] face can be obtained by olation (i.e., combining by a bridging OH group) of $[\text{Ti}(\text{OH})_4(\text{H}_2\text{O})_2]$ octahedra at which all water molecules are removed, and

adjacent octahedra are connected by equatorial bridging OH groups, forming a solid plane, Fig. 4a. In this case, all titanium atoms must contain two axial OH groups to maintain the octahedral coordination:

a) the first octahedral layer (A) after the olation of monomeric octahedra; b) association of two layers of octahedra (A and B) with partial oxolation; c) structure after partial dehydration.

Oxolation during the formation of a three-dimensional grid can occur due to the combination of the upper layer of octahedra (A) with another similar layer (B), Fig. 4b. In this case, based on the elementary crystal cell, the oxo group is formed during the condensation of the bridging (equatorial) OH group of layer A from below with the upper axial OH group of the lower layer B. Similarly (since the octahedra of layers A and B are combined along adjacent opposite edges), additionally oxolation occurs (i.e., the formation of bridging oxo groups) of the lower axial OH groups of layer A with half of the equatorial OH groups of layer B. This leads to distortion of the octahedra due to the displacement of the oxo groups of layer A downwards, while for steric reasons another pair of *trans*-hydroxyl (before oxolation) groups of the upper layer should rise up from the plane. This allows the completion of

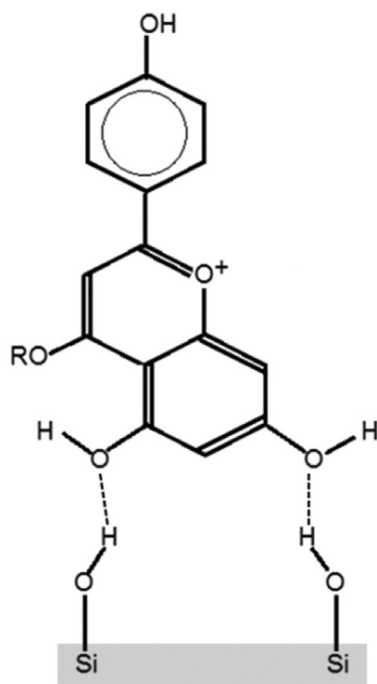


Fig. 2. Two-point anthocyanin adsorption on the silica surface

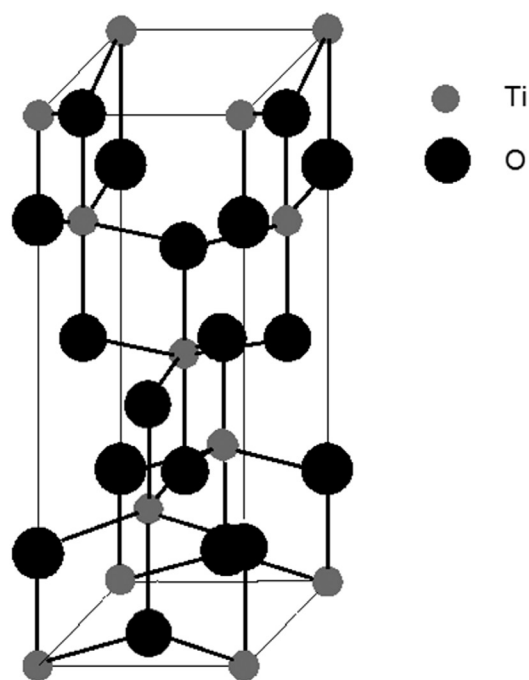


Fig. 3. Anatase unit cell

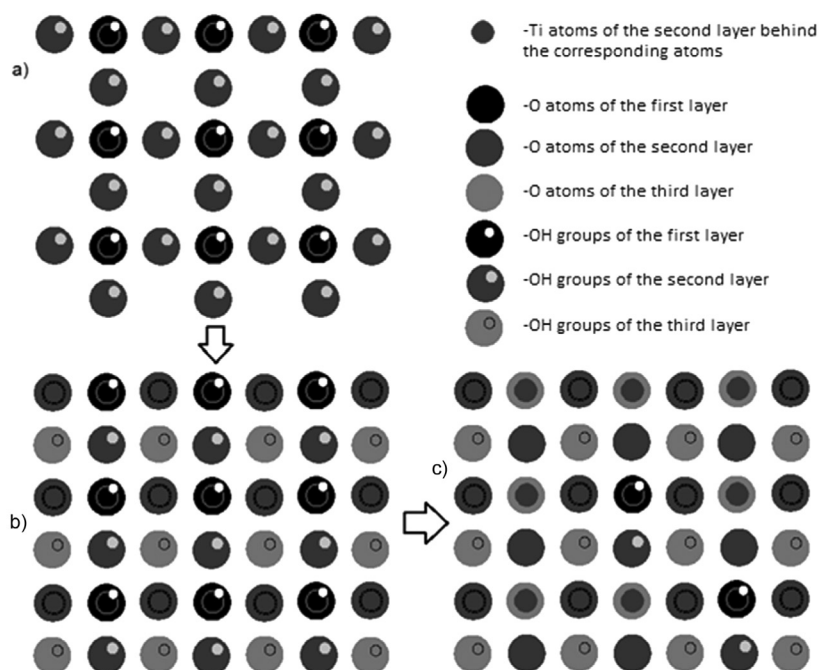


Fig. 4. Formation of the surface layers of the anatase (001) face

the oxolation of layer A from above with the third layer (B) in the formation of a three-dimensional structure.

Without this oxolation, the surface of the [001] face will be represented by titanium atoms containing axial OH groups, ribbons of coordinatively saturated oxo groups shifted downward due to oxolation, and ribbons of OH groups shifted upward and are accessible for sorption with molecules of potential sorbates, Fig. 4b. Due to the steric effect of the inner layers (with complete oxolation and with a shortened distance between titanium atoms), dehydration of the outer layer is possible with the replacement of equatorial OH groups by coordinatively unsaturated oxo groups and with the formation of an axial vacancy in the coordination sphere of the titanium atom, Fig. 4c. Such dehydration and its reverse hydration are reversible, which follows from the data of [14] on the study of X-ray photoelectron spectra of annealed titanium dioxide nanopowder before and after hydration. Indeed, in non-hydrated titanium dioxide, the main band has the lowest energy of 534.0 eV; it is attributed to internal (fully oxolated) oxygen atoms. The oxygen atoms with an energy of about 555.5 eV, which are attributed to oxygen from the surface OH groups, are also quite noticeable.

Their energies noticeably differ from the energy of oxygen atoms of sorbed water molecules with a photon energy of about 537.5 eV. During the hydration of the nanopowder, the concentration of surface hydroxyl groups increased approximately three to four times, confirming the reversibility of hydration-dehydration. However, to obtain effective DSSC, a direct donor–acceptor bond between the coordinatively unsaturated titanium atom on the surface and the oxygen atom of the auxochromic hydroxy or methoxy group of the anthocyanin molecule is desirable. Probably, the formation of an axial vacancy of the titanium atom on the surface is possible during annealing of the initial TiO_2 and explains the need for such a procedure.

As can be seen from the data in Table 1, there is a significant difference in the sorption capacity of anthocyanins depending on the structure of the B-ring. Therefore, it can be assumed that the B-ring with significantly different structure among the six anthocyanins used is responsible for the sorption of anthocyanins on anatase. Moreover, two-point sorption (i.e., the presence of two substituents in the B-ring) is preferable to one-point sorption.

Based on the values of the charges on the oxygen atoms of functional groups, it can be

assumed that an increase in the charge of the oxygen atom (i.e., its donor properties during the formation of a donor-acceptor bond) enhances sorption in the series of substituted pelargonidin (substitution of the OH group in the 4' position with a charge on the oxygen atom -0.182) < cyanidin (substitution of the OH group in position 3' with a charge on the oxygen atom -0.209) < delphinidin (substitution of the OH group in position 3' with a charge on the oxygen atom -0.223) with the possibility of two-point sorption in the last two cases. Two-point sorption is also possible for petunidin, peonidin, and malvidin derivatives. However, the substitution of the OH group by the OCH_3 -group does not contribute to the enhancement of sorption, since the increase of the charge on the oxygen atoms and OH- and OCH_3 -groups was practically not observed in the case of the peonidin and malvidin derivatives.

Therefore, delphinidin, petunidin, or cyanidin glycosides can be proposed as being the most effective anthocyanins for the sorption modification of the anatase surface, and the sorption interaction of anthocyanin with the surface can be represented by the diagrams shown in Fig. 5.

In the proposed scheme, the titanium atom completes the coordination sphere with an octahedron due to the donor-acceptor bond with the lone pair of electrons of the OH group in position 3' (Scheme I), or the OH group in

position 4'. It is this bond that is likely to be the main link in the transfer of an electron from anthocyanin to titanium dioxide in solar cells. Additionally, the oxygen atom on the anatase surface forms a hydrogen bond with the hydroxyl group in position 4' (Scheme I). For the sorption of methoxy derivatives, the donor-acceptor bond with the titanium atom must be performed by the oxygen atom of the OH groups in the 4' position (Scheme II), and the methoxy groups can enhance sorption due to the formation of a hydrogen bond with bridging hydroxyl groups on the surface. The number of hydroxyl groups is not high, which explains only a moderate increase in the sorption capacity in the case of substituted peonidin and malvidin (compared to pelargonidin derivatives).

3. Conclusions

Thus, the nature of the sorption of 3-glucosides of the six common anthocyanins on anatase is fundamentally different from the sorption on silica gel. In the first case, sorption is determined by the functional groups of the B-ring, while in the second case, it is determined by the hydroxyl groups of the A-ring. Based on the results of the experiments performed, it can be assumed that delphinidin derivatives should have the highest efficiency as anatase sensitizers.

Author contributions

All authors participated in all stages of the study, preparation and discussion of the results.

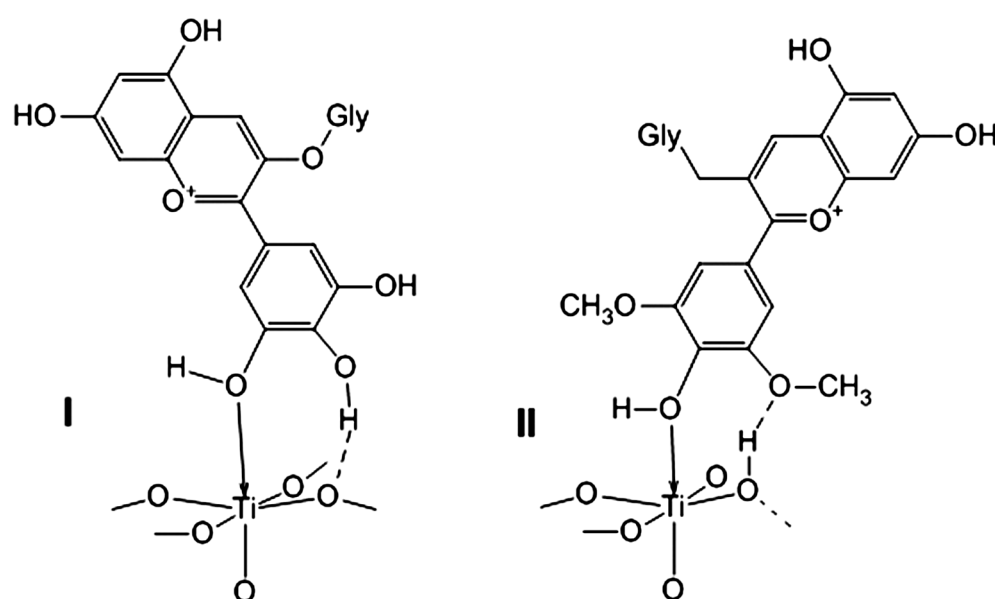


Fig. 5. Schemes of two-point sorption of anthocyanins on the anatase surface

Conflict of interests

The authors declare that they have no conflict of interest.

References

- O'Regan B., Grätzel M. A low-cost, high-efficiency solar cell based on dye-sensitized colloidal TiO₂ films. *Nature*. 1991;353: 737–740. <https://doi.org/10.1038/353737a0>
- Narayan M. R. Review: Dye sensitized solar cells based on natural photosensitizers. *Renewable and Sustainable Energy Reviews*. 2012;16(1): 208–215. <https://doi.org/10.1016/j.rser.2011.07.148>
- Fernando J. M. R. C., Senadeera G. K. R. Natural anthocyanins as photosensitizers for dye-sensitized solar devices. *Current Science*. 2008;95: 663–666.
- Buraidah M. H., Teo L. P., Yusuf S. N. F., ... Arof A. K. TiO₂/chitosan-NH₄I(+I₂)-BMII-based dye-sensitized solar cells with anthocyanin dyes extracted from black rice and red cabbage *International Journal of Photoenergy*. 2011; 1–11. <https://doi.org/10.1155/2011/273683>
- Gokilamani N., Muthukumarasamy N., Thambidurai M., Ranjitha A., Velauthapillai D. Utilization of natural anthocyanin pigments as photosensitizers for dye-sensitized solar cells. *Journal of Sol-Gel Science and Technology*. 2013;66(2): 212–219. <http://doi.org/10.1007/s10971-013-2994-9>
- Deineka V. I., Deineka L. A., Sidorov A. N., Saenko I. I., Kostenko O. M. The evaluation of the properties of the solid-phase extraction cartridge sorbents: the role of the “gallery” pores. *Sorbcionnye i hromatograficheskie processy = Sorption and chromatography processes*. 2016;16(5): 624–630. (In Russ., abstract in Eng.). Available at: <https://elibrary.ru/item.asp?id=26687004>
- Doronin A., Deineka V., Deineka L., Tretiakov M., Tokhtar V., Chulkov A. Peculiarities of use of bentonite clay at solid-phase purification of anthocyanins and flavonoids from leaves of plants. *Proceedings of the 1st International Symposium Innovations in Life Sciences (ISILS 2019)*. 2019;7: 90–93. <https://doi.org/10.2991/isils-19.2019.21>
- Sorokopudov V. N., Hlebnikov V. A., Deineka V. I. *Khimija Rastitel'nogo Syr'ja = Chemistry of Plant Raw Material*. 2005;4: 57–60. (In Russ.). Available at: <https://elibrary.ru/item.asp?id=9428605>
- Deineka V. I., Grigor'ev A. M. Determination of anthocyanins by high-performance liquid chromatography: regularities of retention. *Journal of Analytical Chemistry*. 2004;59(3): 270–274. <https://doi.org/10.1023/b:janc.0000018972.54587.ce>
- Hanaor D. A. H., Sorrell C. C. Review of the anatase to rutile phase transformation. *Journal of Materials Science*. 2011;46(4): 855–874. <http://doi.org/10.1007/s10853-010-5113-0>
- Oi L. E., Choo M.-Y., Lee H. V., Ong H. C., Hamid S. B. A., Juan J. C. Recent advances of titanium dioxide (TiO₂) for green organic synthesis. *RSC Advances*. 2016;6: 108741. <http://doi.org/10.1039/c6ra22894a>
- Zhang J., Sun P., Jiang P., Guo Z., Liu W., Lu Q., Cao W. The formation mechanism of TiO₂ polymorphs under hydrothermal conditions based on the structural evolution of [Ti(OH)h(H₂O)_{6-h}]^{4-h} monomers. *Journal of Materials Chemistry C*. 2019;7(19): 5764–5771. <http://doi.org/10.1039/C9TC00662A>
- Deineka V. I., Nguyen Van Anh, Deineka L. A. Model of a reversed phase grafted on silica gel. *Russian Journal of Physical Chemistry A*. 2019;93: 2490–2493. <https://doi.org/10.1134/S0036024419120057>
- Benkoula S., Sublemontier O., Patanen M., Nicolas C., Sirotti F., Naitabdi A., ... Miron C. Water adsorption on TiO₂ surfaces probed by soft X-ray spectroscopies: bulk materials vs. isolated nanoparticles. *Scientific Reports*. 2015;5(1): 15088. <https://doi.org/10.1038/srep15088>

Information about the authors:

Victor I. Deineka, Dr. Sci. (Chem.), Professor, Belgorod State University (Belgorod, Russian Federation).

<https://orcid.org/0000-0002-3971-2246>
deineka@bsu.edu.ru

Yaroslava Yu. Salasina, PhD student, Belgorod State University (Belgorod, Russian Federation).

<https://orcid.org/0000-0002-4118-9941>

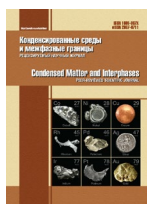
Ludmila A. Deineka, Cand. Sci. (Chem.), Associate Professor, Belgorod State University (Belgorod, Russian Federation).

<https://orcid.org/0000-0002-4101-2468>

Received 23.12.2021; approved after reviewing 28.01.2022; accepted for publication 15.04.2022; published online 25.06.2022.

Translated by Valentina Mittova

Edited and proofread by Simon Cox



Original articles

Research article

<https://doi.org/10.17308/kcmf.2022.24/9260>**Surface-active and chemical properties of alkylbenzenesulfonic acid – nitric acid – water composites**S. A. Zabolotnykh¹✉, A. D. Solovyev², A. S. Sofronov², M. G. Shcherban²¹*Institute of Technical Chemistry of the Ural Branch of the Russian Academy of Sciences, 3 ul. Akademika Koroleva, Perm 614013, Russian Federation*²*Perm State National Research University, 10 ul. Bukireva, Perm 614068, Russian Federation***Abstract**

Industrially produced anionic surfactant alkylbenzenesulfonic acid is proposed as a reagent for the ionic flotation of metals from acidic media. To establish the possibility of its application using this method, it is necessary to study the surface-active (surface tension, adsorption, cross-sectional area of a molecule in the adsorption layer) and colloidal (particle size, critical micelle concentration, solubilisation) properties of its aqueous and nitric acid solutions.

In this study, a series of solutions with various concentrations of alkylbenzenesulfonic acid and containing various amounts of nitric acid (from 1 to 10 wt%) were prepared. The surface tension of the obtained solutions was determined by the hanging drop method using a DSA 25E tensiometer. The introduction of HNO₃ led to a decrease in the surface tension of alkylbenzenesulfonic acid solutions and in its CMC value in comparison with aqueous solutions. On surface tension isotherms with a nitric acid content of 5 and 10 wt%, the presence of several inflections was found, which indicates a stepwise micelle formation. The values of surface activity and Gibbs energies of micelle formation of alkylbenzenesulfonic acid in aqueous and nitric acid solutions were calculated. Adsorption isotherms were constructed from the results of processing the curves of the surface tension of alkylbenzenesulfonic acid solutions. With small amounts of HNO₃ (1 and 2%), the limiting adsorption value of the anionic surfactant significantly increased as compared to the aqueous solution. A further increase in the acidity of the medium led to a decrease in the maximum on the adsorption isotherm. In the presence of an inorganic acid, the monomolecular layer of the surfactant first significantly loosened and then gradually became denser with an increase in acidity. The values of the limiting adsorptions, the adsorption equilibrium constants and the Gibbs energies of adsorption at the liquid-gas interface were calculated using the obtained isotherms. The solubilising ability of alkylbenzenesulfonic acid in relation to the Sudan I dye was determined photometrically using a UNICO 1201 spectrophotometer. With an increase in the solution acidity and the surfactants content the amount of solubilised dye increased.

Keywords: Alkylbenzenesulfonic acid, Surfactant properties, Nitric acid, Adsorption, Solubilisation**Funding** This work was performed in accordance with the state task, state registration No. AAAA-A18-118032790022-7.**Acknowledgements:** This work was carried out using the equipment of the Core Facilities Centre “Research of materials and matter” of Perm Federal Research Centre of the Ural Branch of the Russian Academy of Sciences (PFRC UB RAS).**For citation:** Zabolotnykh S. A., Solovyev A. D., Sofronov S. A., Scherban M. G. Surface-active and chemical properties of alkylbenzenesulfonic acid – nitric acid – water composites. *Condensed Matter and Interphases*. 2022;24(2): 204–210. <https://doi.org/10.17308/kcmf.2022.24/9260>**Для цитирования:** Заболотных С. А., Соловьев А. Д., Софронов А. С., Щербань М. Г. Поверхностно-активные и химические свойства композиций алкилбензолсульфокислота – азотная кислота – вода. *Конденсированные среды и межфазные границы*. 2022;24(2): 204–210. <https://doi.org/10.17308/kcmf.2022.24/9260>✉ Svetlana A. Zabolotnykh, zabolotsveta@mail.ru

© Zabolotnykh S. A., Solovyev A. D., Sofronov S. A., Scherban M. G., 2022



The content is available under Creative Commons Attribution 4.0 License.

1. Introduction

Solutions of surfactants are widely used in various industries: the production of detergents and cosmetics, food products and dyes, oil production and refining technology, various chemical, biochemical and pharmaceutical industries, where surfactants can be used to influence the speed and direction of processes, to synthesize mesoporous materials, etc.

A feature of surfactants is the ability to spontaneously form structured aggregates (micelles) in solution, which determines the particular practical importance of such systems. The size and shape of surfactant aggregates in solution is determined by the balance of interactions between the hydrophilic and hydrophobic parts of surfactant molecules. While hydrophobic interactions of surfactant molecules promote the growth of micelles, the repulsion between hydrophilic groups on the micelle surface limits their growth. The addition of low molecular weight inorganic compounds (salts, acids), ions of which shield the electrostatic repulsion of surfactant hydrophilic groups on the micelle surface, increases surface activity and enhances surfactant adsorption at the interphase boundary. In addition, inorganic electrolytes affect the entire complex of colloid-chemical properties of surfactants, increase their micelle-forming ability, solubilising effect, wetting, and promote, in particular, the transition of spherical micelles to cylindrical ones. If cylindrical micelles already exist in the solution, then the addition of an inorganic low molecular weight salt can lead to an increase in their length. In this case, the effect is determined not only by the amount of salt added to the surfactant solution, but also by the chemical structure of the ions formed during its dissociation. Thus, since the structure of surfactant micelles is highly sensitive to the type and amount of the inorganic low molecular weight salt added to the solution [1–3], for the control of the surface active and rheological properties of surfactant solutions electrolytes are used [4].

The anionic surfactant alkylbenzenesulfonic acid (ABSA) was proposed as a reagent for ionic flotation. ABSA mixes well with water, forms a stable foam, forms precipitates with metal ions, and it is also a fairly accessible reagent.

To establish the possibility of using ABSA as a flotation agent in acidic solutions, it is necessary to study the effect of the concentration of inorganic acids on the surfactant and micellar properties of ABSA solutions [5]. Previously, the effect of hydrochloric acid on the colloidal properties of alkylbenzenesulfonic acid was studied [6]. This study is devoted to the investigation of the colloidal properties of aqueous solutions containing ABSA and nitric acid.

2. Experimental

Reagents. Anionic surfactant alkylbenzenesulfonic acid (general formula $C_nH_{2n+1}C_6H_4SO_3H$, where $n = 10–14$, the content of the main substance is 96.8%, the average molecular weight is 320.9 g/mol, OOO KINEF). The initial ABSA solution was prepared by dissolving an accurate weighed quantity in distilled water. Solutions with lower concentrations were prepared by appropriate dilution. Sudan I dye (1-(phenylazo)-2-naphthol, chemically pure reagent, Sigma-Aldrich). Nitric acid, concentrated ($\rho = 1.49 \text{ g/cm}^3$, chemically pure reagent, RM Engineering). HNO_3 content of 1, 2, 5, and 10% in mixtures were created by introducing the calculated amount of concentrated acid.

All experiments were performed at a temperature of 25 °C.

Devices. The surface tension of ABSA – HNO_3 – H_2O systems at the liquid-gas interface was determined by the hanging drop method using a DSA 25E tensiometer manufactured by KRUSS.

The critical micelle concentration (CMC) of ABSA at different HNO_3 content was determined based on surface tension isotherms: the content of surfactant, at which the curvilinear section of the graph become straight line parallel to the abscissa axis was determined in semilogarithmic coordinates [7, 8]. The surface tension value at the water-air boundary at a given temperature was taken from the reference book [9]. All data presented in the study were obtained by averaging the results of three measurements. Surface activity was calculated as the slope of the initial section of the surface tension isotherm:

$$g = -\lim_{c \rightarrow 0} \frac{d\gamma}{dc}, \quad (1)$$

C is the concentration of the ABSA solution (kg/m^3); γ is the surface tension of the solution (N/m).

Based on the CMC values obtained, the Gibbs energies of micelle formation were calculated using the formula:

$$\Delta_m G = RT \ln \text{CMC}, \quad (2)$$

$R = 8.314 \text{ J}/\text{mol}\cdot\text{K}$ is the universal gas constant; $T = 298 \text{ K}$ is the absolute temperature; CMC is the critical micelle concentration (mol/m^3).

Adsorption G ($\mu\text{mol}/\text{m}^2$) of ABSA at the liquid-gas boundary was calculated based on the surface tension isotherms according to the equation:

$$G = -\frac{1}{RT} \frac{d\gamma}{d \ln C}, \quad (3)$$

C is the concentration of the ABS solution (kg/m^3); $R = 8.314 \text{ J}/\text{mol}\cdot\text{K}$ is the universal gas constant; $T = 298 \text{ K}$ is the absolute temperature; γ is the surface tension of the solution (N/m).

Based on the obtained adsorption data, the C/G values were calculated and the dependence $C/G - f(C)$ was plotted. According to the graph, the values of the limiting adsorption G_m (as the slope α) and adsorption equilibrium constant K (m^3/mol), as the Y-interception is equal to $1/(G_m K)$ were determined. The determination of limiting adsorption value allows to calculate the parameters of the monomolecular layer: the cross-sectional area of a molecule S (nm^2) and axial length d (nm) of the molecule according to the following formulas:

$$S = \frac{1}{G_m N_A}, \quad (4)$$

$$\delta = \frac{G_m M}{\rho}, \quad (5)$$

G_m is the limiting Gibbs adsorption (mol/m^2); $N_A = 6.02 \cdot 10^{23} \text{ mol}^{-1}$ is the Avogadro number; M is the molar mass of the surfactant (kg/mol); ρ is the surfactant density (kg/m^3).

The Gibbs energies $\Delta_{\text{ads}} G$ of adsorption at the liquid-gas interface were calculated based on the values of the adsorption equilibrium constants K according to the equation:

$$\Delta_{\text{ads}} G = -RT \ln K, \quad (6)$$

$R = 8.314 \text{ J}/\text{mol}\cdot\text{K}$ is the universal gas constant; $T = 298 \text{ K}$ is the absolute temperature; K is the adsorption equilibrium constant (m^3/mol).

The solubilising ability S (mg/dm^3) of ABSA – HNO_3 – H_2O compositions was studied by absorption photometry in relation to the oleophilic dye Sudan I [10, 11], which is insoluble in water but soluble in the hydrophobic part of micelles. The dye content in the solution was determined by measuring the optical density of the solution in 0.5 cm cuvettes using a UNICO 1201 spectrophotometer at $\lambda = 400 \text{ nm}$. In prepared solutions of surfactant compositions with a volume of 20 cm^3 dye (20 mg) was added. The flasks were stoppered, mixed using Millab Unimax 1010 shaker for 60 min until equilibrated, then the contents were filtered through filter paper. According to the calibration chart ($A = 0.0147 \cdot C$ (mg/dm^3), $R^2 = 0.9983$) [6] the amount of solubilised dye per unit volume of the solution was determined.

Molar solubilising ability S_m (mg/g) was calculated as the ratio of the obtained value of S to the ABSA concentration (c , g/dm^3) [12]:

$$S_m = \frac{S}{c}. \quad (7)$$

3. Results and discussion

3.1. Surface tension and micellization

The introduction of alkylbenzenesulfonic acid leads to a sharp decrease in the surface tension of both water and aqueous solutions of nitric acid (Fig. 1). The decrease in the value of γ reflects the process of filling the surface layer with surfactant molecules and reaching the

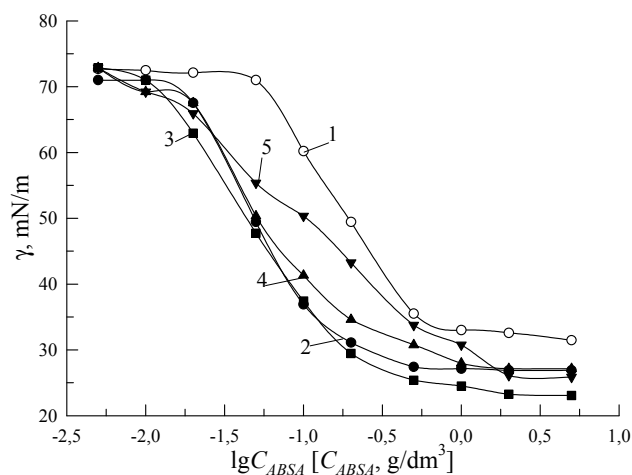


Fig. 1. Surface tension isotherms of ABSA acid compositions: 1 – without acid; 2 – 1% HNO_3 ; 3 – 2% HNO_3 ; 4 – 5% HNO_3 ; 5 – 10% HNO_3

limiting value of adsorption. After the critical micelle concentration is reached, the decrease in surface tension with an increase in the ABSA content slows down, which is associated with the formation of micelles in the solution [13].

In the presence of an inorganic acid, the decrease in surface tension is more significant than in pure water. The introduction of nitric acid at concentrations of 1 and 2 wt. % led to an increase in micelle-forming ability, expressed in a decrease in CMC values and surface tension during CMC, which was caused by dehydration of the polar groups of surface-active ions in the presence of an electrolyte. Also, with an increase in the concentration of inorganic acid, a decrease in the surface tension of the solution started at a lower content of ABSA.

An increase in the content of HNO_3 up to 5 and 10% led to the appearance of two inflections on the surface tension curves (Fig. 1, curves 4 and 5). Probably, with an increase in the concentration of the inorganic acid, the dissociation of ABSA, as a weaker acid, is suppressed ($pK_a = 2.17$ [14]), as a result it behaves similarly to a nonionic surfactant and forms pre-micellar structures at lower concentration regions [15]. With an increase in the surfactant content, the amount of ABSA anions increased, and mixed micelles were formed. This formation was accompanied by the appearance of another step on the surface tension isotherm. The obtained CMC_1 values and values of the surface activity and Gibbs energy of micellization calculated using formulas (1) and (2) depending on the ionic strength of the medium are presented in Table 1. Negative values of the Gibbs energy indicated the spontaneity of the micelle formation process. The introduction of HNO_3 led to a sharp increase in the surface activity of ABSA,

the negative value of $\Delta_m G$ slightly increased in absolute value with increasing acidity.

3.2. Adsorption at the liquid-gas interface

The increase in the acidity of the medium in the transition from water to 10 wt% HNO_3 changed the conditions for the formation of a monomolecular layer, compared with an aqueous solution, which was expressed as the change in the height and position of the maximum of adsorption isotherms, calculated based on surface tension isotherms (Fig. 2). The initial increase in acidity sharply increased the value of the limiting adsorption, however, a subsequent increase in the acid content lowered the value of G_m .

The introduction of nitric acid at concentrations of 1 and 2% led to a “loosening” of the monomolecular layer, which was expressed by an increase in the area occupied by one surfactant molecule (Table 2). In this case, the adsorption equilibrium constants (K) and the absolute values of the Gibbs energies

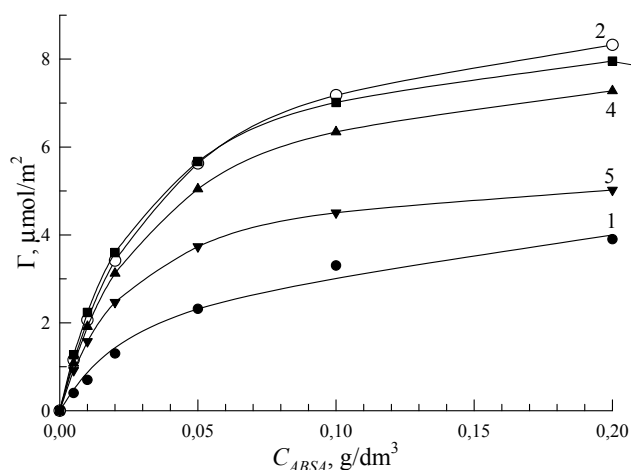


Fig. 2. ABSA adsorption isotherms at the liquid-gas interface: 1 – without acid; 2 – 1% HNO_3 ; 3 – 2% HNO_3 ; 4 – 5% HNO_3 ; 5 – 10% HNO_3

Table 1. Influence of the ionic strength of the solution on the surface-active characteristics of ABSA – HNO_3 – water compositions

C_{HNO_3} , %	I , mol/dm ³	CMC, g/dm ³	γ , mN·m ² /kg	$\Delta_m G$, kJ/mol
0.00	0.00	0.50	74.72	-33.17
1.00	0.16	0.15	252.83	-36.15
2.00	0.32	0.20	217.05	-35.44
5.00	0.79	0.20 ($\text{CMC}_2 = 0.80$)	217.05	-35.44
10.00	1.59	0.02 ($\text{CMC}_2 = 0.1$)	347.00	-41.11

Table 2. Influence of the ionic strength of the solution on the parameters of the ABSA monomolecular layer at the liquid-gas interface

$C_{\text{HNO}_3}, \%$	$I, \text{mol/dm}^3$	$G_m, \text{mmol/m}^2$	$K, \text{m}^3/\text{mol}$	$\Delta_{\text{ads}} G, \text{kJ/mol}$	S, nm^2	δ, nm
0.00	0.00	5.09	9.65	-5.62	1.96	1.58
1.00	0.29	9.90	26.31	-8.10	1.01	3.07
2.00	0.58	9.19	32.17	-8.60	1.09	2.85
5.00	1.45	8.54	28.89	-8.33	1.17	2.65
10.00	2.92	5.67	38.49	-9.04	1.76	1.76

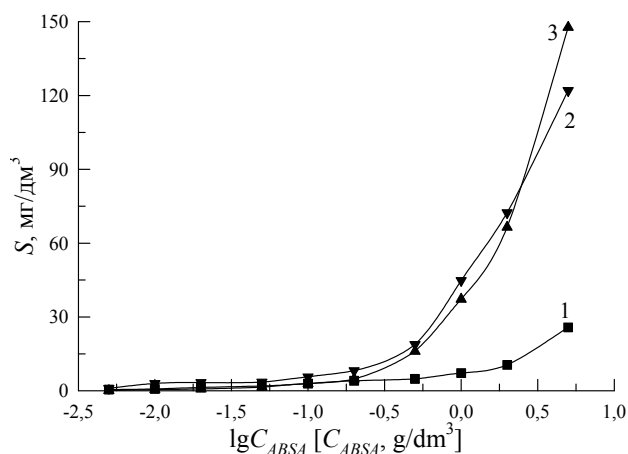
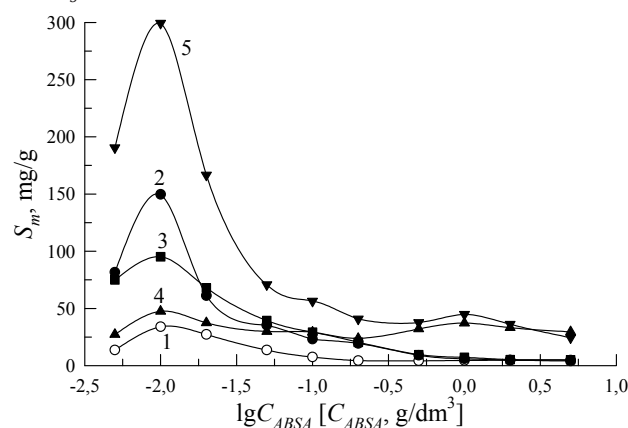
of adsorption, which characterize the adsorption, increased. With an increase in the content of inorganic acid, the transfer of 1 mol of surfactant from the solution to the surface layer requires less energy than in an aqueous solution.

3.3. Solubilisation

The mechanism of solubilisation is largely determined by the nature of the surfactant. In the case of ionic surfactants, an oleophilic dye containing polar groups is introduced into the surface layer of micelles, where its molecules are located between surfactant molecules, orienting parallel to them and turning polar groups into the aqueous phase. In this case, the solubilisate can dissolve both in the core and in the hydrophilic shell of micelles [16].

In the initial section, the amount of solubilised dye slowly increased with increasing surfactant concentration. Solubilisation isotherms in aqueous solution and in the presence of 1 and 2% HNO_3 almost coincided (Fig. 3). In a medium with 5 and 10% inorganic acid, the solubilisation of the dye increased abruptly with an increase in the ABSA content, which was probably due to the transition from one type of micelles to another.

At high concentrations of nitric acid, an increase in the solubilising capacity was also observed, which was probably due to the protonation of the dye and the formation of an ion associate with the ABSA anion. Various additives especially affect colloidal dissolution, contributing to the enlargement of micelles due to their hydrophobization (i.e., lowering the effective degree of dissociation and hydration). The molar solubilisation curves of Sudan I have maxima at an ABSA content of 0.01 g/dm^3 , only the degree of the manifestation of the maximum changed with increasing acidity (Fig. 4). With a further increase in the concentration of ABSA, the

**Fig. 3.** Effect of nitric acid concentration on the solubilisation of the Sudan I dye in ABSA solutions: 1 – without acid, 1 and 2% HNO_3 ; 2 – 5% HNO_3 ; 3 – 10% HNO_3 **Fig. 4.** Effect of nitric acid concentration on the molar solubilisation of the Sudan I dye in ABSA solutions: 1 – without acid; 2 – 1% HNO_3 ; 3 – 2% HNO_3 ; 4 – 5% HNO_3 ; 5 – 10% HNO_3

number of moles of solubilised dye per 1 mole of surfactant remained constant.

4. Conclusions

The introduction of nitric acid into aqueous solutions of alkylbenzenesulfonic acid changed the structure of surfactant monomolecular layers

and led to an increase in the surface activity of ABSA, expressed in a decrease in the CMC value. In more concentrated nitric acid solutions (5 and 10%), micelle formation proceeded in several stages. The processes of micellization and adsorption of surfactants at the liquid-gas interface proceeded spontaneously, while with an increase in the acidity of the medium, absolute values of Gibbs energies of these processes increased. The introduction of nitric acid had a positive effect on the solubilising ability of ABSA aqueous solutions in relation to the oleophilic dye Sudan I, which can be caused by the protonation of the dye and the formation of an ion associate of the solubilisate with the ABSA anion.

Author contributions

All authors made an equivalent contribution to the preparation of the publication.

Conflict of interests

The authors declare that they have no known competing financial interests or personal relationships that could have influenced the work reported in this paper.

References

1. Rusanov A. I. *Micellization in surfactant solutions*. Leningrad: Khimiya Publ.; 1992. 280 p. (In Russ.)
2. Nagarajan R. Molecular Packing Parameter and Surfactant Self-Assembly: The Neglected Role of the Surfactant Tail. *Langmuir*. 2002;18: 31–38. <https://doi.org/10.1021/la010831y>
3. Hoffmann H. Viscoelastic surfactant solutions. In: *Structure and flow in surfactant solutions*. Washington: ACS; 1994. pp. 2–31. <https://doi.org/10.1021/bk-1994-0578.ch001>
4. Ismagilov I. F., Kuryashov D. A., Vagapov B. R., Bashkirtseva N. Yu. Effect of electrolyte on micellization and rheological properties of aqueous solutions of sodium oleyl methyl taurate. *Bulletin of the Technological University Vestnik*. 2014;17(18): 46–50. (In Russ.). Available at: <https://www.elibrary.ru/item.asp?id=22480138>
5. Radushev A. V., Koltashev D. V., Nasrtdinova T. Yu., Shcherban M. G., Chekanova L. G., Plotnikova M. D. Physical and chemical properties of N-(2-Hydroxyethyl) alkylamines. *Journal of Applied Chemistry*. 2010;83(8): 1475–1479. <https://doi.org/10.1134/S107042721008029X>
6. Zabolotnykh S. A., Shcherban M. G., Solovyev A. D. Effect of the hydrochloric acid concentration on the surface-active and functional characteristics of linear alkylbenzenesulfonic acid. *Bulletin of the Karaganda University. CHEMISTRY series*. 2020;99(3): 72–79. <https://doi.org/10.31489/2020Ch3/72-79>
7. Emello G. G., Bondarenko Zh. V., Grukhalova Ye. V., Firsova L. D. Colloidal-chemical properties of technical preparations of surfactants used in the cosmetic industry. *Proceedings of BSTU*. 2012;151(4): 20–24. (In Russ.). Available at: <https://www.elibrary.ru/item.asp?id=44192982>
8. Aivazov B. V. *Workshop on the chemistry of surface phenomena and adsorption*. Moscow: Vysshaya Shkola Publ.; 1973. 206 p. (In Russ.)
9. Ravdel A. A., Ponomareva A. M. *Brief reference book of physical and chemical quantities*. Leningrad: Khimiya Publ.; 1983. 232 p. (In Russ.)
10. Demyantseva E. Yu., Kopnina R. A. *Solubilization in solutions of surfactants: educational and methodical manual*. StPb.: SPbGTURP Publ.; 2015. 31 p. (In Russ.)
11. Vasilieva E. A., Valeeva F. G., Yeliseeva O. E., Lukashenko S. S., Saifutdinova M. N., Zakharov V. M., Gavrilova E. L., Zakharova L. Ya. Supramolecular nanocontainers based on hydrophobized calix[4]resorcinol: Modification by gemini surfactants and polyelectrolyte. *Macroheterocycles*. 2017;10(2): 182–189. <https://doi.org/10.6060/mhc170509v>
12. Stas I. E., Shipunov B. P., Repeykova L. Yu., Mikhaylova O. P. The influence of the electromagnetic field in the radio-frequency band on pigment sudan III solubilization by micelles of sodium dodecylsulfate and cetylpyridinium chloride in aqueous solutions. *The News of Altai State University*. 2012;75(3-1): 194–198. (In Russ., abstract in Eng.). Available at: <https://www.elibrary.ru/item.asp?id=17877681>
13. Holmberg K., Jonsson B., Kronberg B., Lindman B. *Surfactants and polymers in aqueous solution*. 2nd Edn. John Wiley & Sons; 2002. 562 p.
14. Zabolotnykh S. A., Zhelnina V. O., Denisova S. A., Elokhov A. M., Lesnov A. E. The water – antipyrine – alkyl benzene sulfonic acid stratifying system to extract metal ions. *Journal of the Siberian Federal University. Chemistry*. 2017;10(4): 536–544. (In Russ., abstract in Eng.). <https://doi.org/10.17516/1998-2836-0047>
15. Neudachina L. K., Petrova Yu. S. *Application of surfactants in analysis: A Study Guide*. Ekaterinburg: UrFU Publ.; 2017. 76 p. (In Russ.)
16. Smit R. A., Demiantseva E. Yu., Andranovich O. S., Filippov A. P. Features of solubilizing effect of amphiphilic compounds during pulp deresination. *Bulletin of Higher Educational Institutions. Russian Forestry Journal*. 2021;379(1): 180–191. (In Russ., abstract in Eng.). <https://doi.org/10.37482/0536-1036-2021-1-180-191>

Information about the authors

Svetlana A. Zabolotnykh, Cand. Sci. (Chem.),
Researcher, Laboratory of Organic Complexing
Reagents, Institute of Technical Chemistry Ural Branch
of RAS (Perm, Russian Federation).

<https://orcid.org/0000-0001-8307-0386>
zabolotsveta@mail.ru

Aleksandr D. Solovyev, student, Faculty of
Chemistry, Perm State National Research University
(Perm, Russian Federation).

<https://orcid.org/0000-0002-7852-3683>
solovev_s92@mail.ru

Aleksey S. Sofronov, student, Faculty of Chemistry,
Perm State National Research University (Perm,
Russian Federation).

sofronov_alexey@mail.ru

Marina G. Scherban, Cand. Sci. (Chem.), Associate
Professor, Physical Chemistry Department, Perm State
National Research University (Perm, Russian
Federation).

<https://orcid.org/0000-0002-6905-6622>
ma-sher74@mail.ru

*Received 20.01.2022; approved after reviewing
28.01.2022; accepted for publication 15.04.2022;
published online 25.06.2022.*

Translated by Valentina Mittova

Edited and proofread by Simon Cox



Original articles

Research article

<https://doi.org/10.17308/kcmf.2022.24/9261>

Substances and the transformations they undergo: basic concepts

V. P. Zlomanov✉, P. E. Kazin, A. V. Yatsenko

Lomonosov Moscow State University,
1 Leninskie Gory, Moscow 119991, Russian Federation

Abstract

We formulated the specific features for the notions of substances and transformation of substances. A substance is a set of interacting particles characterised by the following parameters 1) composition, or the type and ratio of amounts of particles that form the substances, 2) the energy of their interactions, 3) their structure and, finally, 4) the size of particles (dispersion). Transformations of substances occur when these properties change. Such processes are called chemical reactions. To control the transformation of a substance from the thermodynamic point of view, we need to evaluate: 1. The possibility of spontaneous processes (without energy consumption). 2. The thermal effect of the chemical reaction. 3. The equilibrium composition of the reaction medium.

We solved these problems using a mathematical model based on the improved notions (substance, energy, work, supersaturation) and the known laws of thermodynamics.

Keywords: Substances, Transformation of substances, Thermodynamics, Energy, Work, Chemical reactions, Chemical equilibrium, Spontaneous process, Thermochemistry, Supersaturation

For citation: Zlomanov V. P., Kazin P. E., Yatsenko A. V. Substances and the transformations they undergo: basic concepts. *Condensed Matter and Interphases*. 2022;24(2): 211–219. <https://doi.org/10.17308/kcmf.2022.24/9261>

Для цитирования: Зломанов В. П., Казин П. Е., Яценко А. В. Вещество и его превращения: основные понятия. *Конденсированные среды и межфазные границы*. 2022;24(2): 211–219. <https://doi.org/10.17308/kcmf.2022.24/9261>

✉ Vladimir P. Zlomanov, e-mail: zlomanov1@mail.ru

© Zlomanov V. P., Kazin P. E., Yatsenko A. V., 2022



The content is available under Creative Commons Attribution 4.0 License.

1. Introduction

A notion is a set of specific properties and relations between the subjects under consideration that exists in our thinking as a thought. Words and phrases that describe notions are called terms. Like notes in music and words in people's conversations, notions form the basis of science. As new data are accumulated, sometimes we need to generalise scientific facts, improve the old ones, and introduce new notions. According to the decision of the "Third national meeting of heads of departments of inorganic chemistry" that took place between 9 and 12 October 2016 in Ivanovo, professors V. Zlomanov, P. Kazin, and A. Yatsenko of Lomonosov Moscow State University, and professor E. Rumyantsev of Ivanovo State University of Chemistry and Technology, were given the task of improving the basic notions of chemistry. The results of their work are presented in a brief glossary [1]. It does not replace the information in existing textbooks but complements them and expands knowledge in the field of chemistry. The glossary includes the most important notions at the modern level of comprehension of chemistry that allow defining the conditions required to control the transformation of substances based on thermodynamics. We will analyse the specifics of some notions related to substances and their transformations.

2. Chemistry and substance

Chemistry holds an important place among natural sciences. It is also of economic significance and it generally has an impact in our everyday life. Chemistry does not come to the fore in our lives. However, without chemistry, it would have been impossible to achieve many great things in this field and create new substances that are necessary for human life, such as materials for the production and transformation of energy, for creating vehicles, communication systems, food, medicines, clothing, etc. As chemistry is present everywhere, people often forget about it and underestimate some of its important notions. Chemistry is the science that deals with substances and the transformations they undergo. However, there is no clearly understanding of what substances actually are and what transformations they undergo. According to the

philosophical definition of a substance as a form of matter or physical essence, it objectively exists but this definition does not allow the conditions required to control the composition, structure, and, consequently, the properties of substances to be determined. The notion of a substance can be specified based on the atomic structure model. **We will define substances (chemical) as a set of interacting particles that are characterised by four features: 1) composition, or the type and ratio of amounts of particles forming the substance (atoms, molecules, ions), 2) energy of their interaction, 3) structure and, finally, 4) dispersion or, in other words, the size of particles.** The specified features determine the physical and chemical properties of substance. It should be noted that the suggested definition of substances is newer and clearer as compared to those existing in academic and scientific papers.

3. Transformation of substances

When changes occur in the composition, structure, interaction energy, and size of particles of substances and, as a result, in their physical and chemical properties, these processes are called chemical reactions. Sometimes the processes of electron density redistribution between atomic nuclei are called chemical reactions, which is not really correct since the changes of all substance properties are not taken into account. Unlike nuclear reactions, in chemical reactions the atomic nuclei of substances do not change, although electrons and nuclei are redistributed.

First, we will analyse the specifics of substance properties, and then we will consider the thermodynamics of the transformation processes they undergo.

4. Substance features

Composition is a type and qualitative ratio of the particles of atoms, molecules, ions, etc., that substances are made of.

When characterising the composition, it is important to decide which substances should be considered pure. Pure substances are a relative notion which is associated with the functional applications of substances. For example, the properties of semiconductors are determined by the concentration of charge carriers, such as electrons and holes, and their mobility. The

criterion of purity of semiconductors is the ratio between the required functional concentration of charge carriers and that determined by the properties of substances. For instance, when using a $\text{Hg}_{1-x}\text{Cd}_x\text{Te}$ solid solution to detect infra-red radiation, the concentration of uncompensated carriers should not exceed 10^{16} cm^{-3} . Therefore, only substances with a total concentration of carriers due to impurities, nonstoichiometry, etc. of less than 10^{16} cm^{-3} , or 10^{-4} at. % can be considered as pure.

Energy of the interaction of particles that form substances is a quantitative measure of the movement and interaction between particles in a system that determines its ability to operate is the most important notion in all natural sciences. An **interaction** is a form of energy exchange that occurs when systems (substances) come into contact. There are electrical, magnetic, gravitational, weak, and strong interactions. Chemistry is limited by the analysis of electrostatic (and in some cases, magnetic) interactions between nuclei and electrons, atoms, and molecules. The energy of such interactions can be described using the Gibbs energy function $G = f(T, p, n_i)$, as its arguments or such natural variables as temperature T , pressure p , and the amount of moles of the components n_i can be measured and recorded in order to control chemical transformations. The change of Gibbs

energy (ΔG) includes the enthalpy (ΔH) and the entropy (ΔS) components: $\Delta G = \Delta H - T\Delta S$. The first of them (ΔH) describes the common chemical bond which occurs due to the electrostatic interaction between electrons and atomic nuclei. Depending on the distribution of electron density, there are different types of chemical bonds, including ionic, covalent, and metallic. The type of chemical bond determines the physical and chemical properties of substances. The significant role of the entropy component can be seen in complex cyclic compounds “without” chemical bonds, for example, in catenanes and rotaxanes. The molecules of these compounds consist of two or more cycles that put one through the other like chain links (Fig. 1). The interaction between atoms in cycles is determined by the covalent bond, that is by the value ΔH . The interaction between the same cycles is due to the entropy component ΔS . The molecules of the studied compounds undergo structural changes under the action of light and start rotating like a wind turbine blade in a strictly defined direction. Based on this effect, Jean-Pierre Sauvage (France), James Fraser Stoddart (USA), and Bernard Feringa (Netherlands) designed and manufactured molecular machines and received the 108th Nobel Prize for their work.

Molecular Borromean rings and cyclic DNAs are also examples of other compounds “without” chemical bonds.

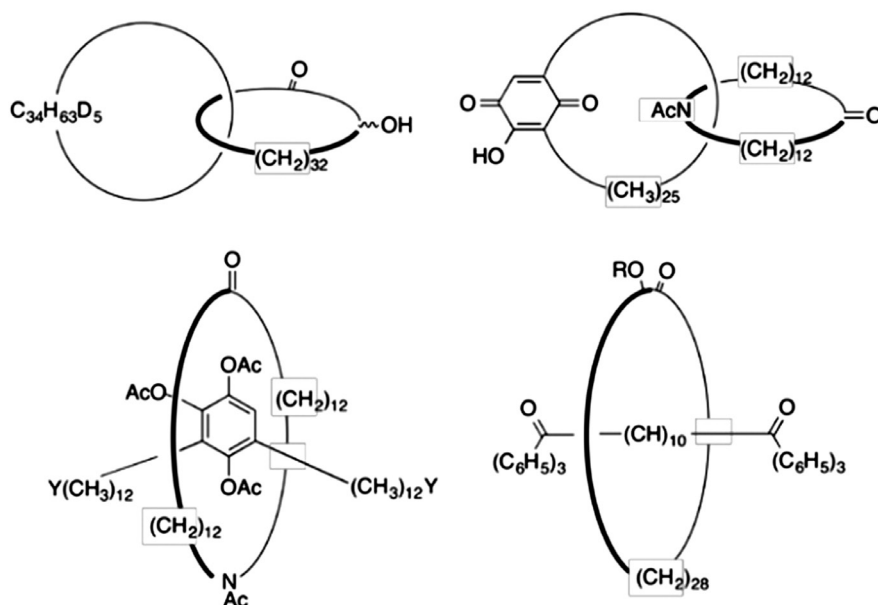


Fig. 1. The scheme of the structure of catenanes (top) and rotaxanes (bottom). Shill G. Catenanes, Rotaxanes, and Knots: transl. from English. M.: Mir, 1973. 211 p. (ill.: p. 202-208)

The interaction between particles in substances leads to the formation of a structure of short-range and long-range order in their spatial distribution.

Chemical and crystal chemical structure is a well-ordered spatial arrangement of particles that form substances. The properties of a crystal, such as the energy of the crystal lattice, as well as electrical, optical, chemical, and other properties, are determined by the composition and structure of the crystal. Different arrangement of the same particles in space, for example, of carbon atoms in diamonds and graphites, results in different properties, including the energy of the crystal lattice that determines the melting and boiling points, hardness, etc.

Size, or the linear (geometric) size of the particles of substances, influences the ratio of the surface and volume energies. Substance particles with a size of 1–100 nm are called **nanoparticles**. Their surface and volume energies are compatible. This leads to the emergence of essentially new properties.

5. Thermodynamics of substance transformation

We study chemistry as a science in order to understand how to synthesise substances with the required functional properties. We can find the solution to this problem in chemical thermodynamics (we will call it thermodynamics from now on in this paper). The transformations themselves are determined by the kinetics of processes. **Thermodynamics** (from Greek θερμη meaning “warmth” and δυναμις meaning “strength”) studies the methods of transformation (and transmission) of energy. Thermodynamics has some special features because it focuses only on the macroscopic properties relating to a rather great amount of substances. What’s more, it studies only equilibrium processes and it does not study processes over the course of time. The issues of non-equilibrium thermodynamics have been considered in [3].

What do we teachers have to know and what do we have to teach our students in order to control the transformation of substances? Thermodynamics provides the following answer to this question. We need to know how to evaluate the following:

1. The possibility of spontaneous occurrence of processes (without any ambient energy consumption).

2. The sign and value of the thermal effect of a chemical reaction.

3. The equilibrium composition of the reaction medium.

The answers to these questions can be given using a mathematical model based on the notions and laws of thermodynamics. Therefore, at first we will consider the basic concepts and laws of thermodynamics.

6. Basic concepts of thermodynamics

Thermodynamics is a study of **systems**. Everything that is outside a system is called the **environment**. The system and the environment can exchange energy and substances. A system that can exchange both substances and energy with the environment is called an **open system**. If it is impossible for the system to exchange substances with the environment, such a system is called a **closed system**. In **isolated** systems there is no exchange of substances or energy with the environment.

The state of the system is determined by several variables. They are all interconnected. To make the construction of mathematical models easier, they are provisionally divided into independent variables and their functions. Similar to mathematics, the former are called *arguments* or *state coordinates*. There are two types of variables: *intensive* and *extensive*. Intensive parameters, such as temperature and pressure, reflect the individual properties of substances and do not depend on the quantity of substances. Extensive parameters describe a particular sample of substances and are proportional to their quantity. To determine their values, for example, volume or weight, we need to totalise them in all parts of the system. To determine the state of the system, we need at least one extensive variable among the coordinates (parameters).

The variables that describe the quantitative composition of the system take a special place among the coordinates that determine the state of the system. The minimal set of substances that are enough to characterise the composition of the system is called the **components**. To perform a definite qualitative and quantitative

characterisation of the composition, they must satisfy the following requirements [2]: a) they must be independent, which means that it is impossible to obtain certain components from others, b) the concentration dependence of the substance properties must be fully described, c) the conditions of electrical neutrality and material balance in the system must be maintained.

Work is the form (method) of transmission of energy. For the work to be performed, the resistance of the external force F must be overcome. If the system is not affected by external forces, it does not perform work. The value of work δW is represented as the product of the overcome force F on the change of dX of the corresponding coordinate X : $\delta W = FdX$. The symbol of variation δ stands for infinitely small amounts of work W . There are different types of work, such as mechanical, thermal, “chemical”, and so on. It should be noted that unlike internal energy, work is not a function of state, it depends on the course of the process. Work is measured in the same units as energy U . In the SI this unit is the joule (J). Sometimes the values of U and W are expressed in calories (cal). $1 \text{ cal} = 4.1840 \text{ J}$.

Heat is a form (method) of transmission of energy from a more heated system to a less heated one through heat exchange, i.e. as a result of a chaotic collision of particles. Unlike thermodynamics, in thermochemistry heat is considered positive if it is released into the environment and negative if it is absorbed. If we consider temperature (T) as a force (measure of effect) and entropy (S) (the definition of which will be given in article 7) as a coordinate, then the product $TdS = \delta W_{\text{heat}}$ can be considered as **heat work**, or the amount of transmitted heat.

“**Chemical work**”^{*} $\delta W_{\text{chem}} = \sum_i \mu_i dn_i$, W_{chem} is performed upon the transformation (**chemical reaction**) of a certain amount of moles (n_1) of one substance into n_2 moles of another substance. In this case, the chemical potential μ_i acts as force F (see article 6.), while a change of the amount of moles (dn_i) acts as the change of coordinate X .

Chemical potential μ_i describes the “rate” of change in the internal energy U (enthalpy H ,

* We use this notion with quotation marks to show that it is a relatively conditional notion since the transformation of substances includes not only chemical work but also heat and mechanical work.

Helmholtz energy F , and Gibbs energy G) of the system that occurs when one mole of the i^{th} component is added to it (see article 6.) while the values of other arguments remain the same.

$$\mu_i = \left(\frac{\partial U}{\partial n_i} \right)_{S,V,k \neq i} . \quad (1)$$

7. Basic laws of thermodynamics

The logic of the structure of notions and definitions of thermodynamics may seem difficult at first but it can be explained if we see how it works, for example, when solving the main problem of chemistry, which is predicting the result of the transformation of initial substances into products when the substances are provided in a certain ratio and placed under certain conditions. The mathematical model that allows solving the basic problems of thermodynamics can be constructed using the basic laws of thermodynamics.

The first law of thermodynamics is usually represented as follows:

$$dU = \delta Q + \delta W . \quad (2)$$

According to this law, the internal energy U of the isolated system is constant. In a non-isolated system it may change due to the fact that the environment performs work dW upon the system and transmits heat δQ to it. It should be noted that according to IUPAC, those** changes that increase the internal energy of the system are considered to be positive.

As it was mentioned previously, **heat** is a form (method) of transmission of energy through heat exchange, and the product of $TdS = \delta W_{\text{heat}}$ can be considered as **heat work** δW_{heat} or the amount of transmitted heat. Therefore, the first law concerning the constant internal energy of the system can be expressed as follows:

$$dU = \sum W_i , \quad (3)$$

i. e., due to changes in internal energy dU , the system can perform various types of work W_i .

As for the open systems, the first law of thermodynamics is represented as an equation (4):

$$dU = \delta Q + \delta W_{\text{mech}} + \sum \mu_i dn_i , \quad (4)$$

** Sometimes another system of signs is used. For instance, if work is considered positive, it is performed by the system upon the environment.

where the latter sum is called “chemical work” (see article 6.). It describes the process of the transmission of substances between the system and its environment.

The first law of thermodynamics shows that processes may occur but it does not mention anything about their direction or which of the processes occur spontaneously. These issues are explained by the **second law of thermodynamics**. For this purpose, a new variable, **entropy** S , is introduced. It is used as one of the parameters (coordinates) that determine the state of the system. It changes dS in case of a revertable process can be expressed as the ratio of heat effect δQ of the process to temperature T , and according to the recommendation of IUPAC, the value δQ is considered to be positive if the system obtains heat from the environment:

$$dS = \frac{\delta Q}{T}. \quad (5)$$

In SI, entropy (energy divided by temperature) is expressed as follows: $\text{J}\cdot\text{K}^{-1}$. The sign and the value of entropy change determine the direction of the process. If the entropy increases $dS > 0$ in an isolated system, the process occurs spontaneously, which means that it is irreversible. The maximum of entropy and its constant state show that the system is in equilibrium.

What does **entropy** mean? We can answer this question using statistical thermodynamics. **Thermodynamic probability** w is used to evaluate the measure (value) of probability of a particular state. Its value equals the number of ways in which N particles can be placed in available microstates $N_1, N_2, N_3, \dots, N_i^*$:

$$w = \frac{N!}{N_1!N_2!\dots N_i!}, \quad (6)$$

where the factorial sign stands for the product $N! = 1 \cdot 2 \cdot 3 \cdot \dots \cdot N$ and $0! = 1$. To illustrate the notion of thermodynamic probability w , we will consider two macrostates** of a system consisting of six particles ($N = 6$) that can be distributed by

* Microstate is the state of the system that is determined by the simultaneous specification of three coordinates x, y, z and three impulses p , or three products of mass m by the velocity vector: $\vec{p}_x = m\vec{v}_x$, $\vec{p}_y = m\vec{v}_y$, $\vec{p}_z = m\vec{v}_z$ of all the particles comprising the system.

** Macrostate is a state of the system consisting of a large number of particles.

three ($i = 3$) microstates (cells). Let us consider the first macrostate with all six particles in one cell. It is a case of thermodynamic probability

$$w_1 = \frac{6!}{6!0!0!} = 1.$$

In the second macrostate, all six particles will be distributed evenly by three cells. The probability of the second macrostate equals

$$w_2 = \frac{6!}{2!2!2!} = 90.$$

It is obvious that the probability of an even distribution is 90 times higher as compared to an uneven distribution. According to L. Boltzmann, spontaneous processes occur when the final state is more probable than the initial one, in other words, when the final macrostate can be achieved with a larger number of microstates. Let us remember that a spontaneous process in an isolated system is characterised by increased entropy $dS > 0$.

Thermodynamic probability w is associated with entropy S in the following ratio (7):

$$S = k \ln w, \quad (7)$$

where k is the Boltzmann constant. Thus, we have explained the physical sense of entropy. Similar to thermodynamic probability, it is a **measure** of the system’s tendency towards equilibrium. Increased entropy corresponds to the system’s transformation into the most probable state.

As opposed to internal energy U , we can find an absolute value for entropy. It becomes possible when we use **the third law of thermodynamics**, which is formulated as follows: at 0 K the entropy of an ideal crystal (the one without any structural violations or defects) is zero.

To construct a mathematical model that allows solving the main problems of thermodynamics, we need to choose the state function and the arguments that determine it, for example, $G = f(T, p, \text{composition})$. Then, we must analyse its form and determine its extremum coordinates (minimum and maximum values), and thus solve the specified problems. To choose the required function, we combined equations (J. Gibbs) (2), (4), and (5), representing the first and the second laws, into one fundamental equation (8).

$$dU = TdS - pdV + \sum \mu_i dn_i. \quad (8)$$

Equation (8) has two important features.

1. Energy change dU is expressed through the sum of uniformly constructed products of forces F , represented by T, p, μ_i , by the changes of coordinates dS, dV , and dn_i . Each product represents work: the product of $TdS = W_{\text{heat}}$ represents heat work, the product of $pdV = W_{\text{mech}}$ represents mechanical work, and the product of $\sum \mu_i dn_i = W_{\text{chem}}$ represents “chemical” work. Thus, the first law of thermodynamics as the law of conservation of energy can be formulated as follows: internal energy U of the system is constant and it can be transformed into thermal, mechanical, chemical, and other types of work:

$$U = \sum W_i. \quad (3)$$

2. In equation (8) internal energy U acts as the function of arguments, such as entropy S , volume V , and number n_i of moles of the components. However, some of the arguments are not convenient to work with in practice. For example, it is impossible to measure and control entropy S , therefore, in order to use the arguments that can be measured and recorded as well as to solve practical problems, we introduced new functions that are related to internal energy:

$$\text{enthalpy } H = U + pV, \quad (9)$$

$$\text{Helmholtz energy } F = U - TS, \quad (10)$$

$$\text{and Gibbs energy } G = H - TS. \quad (11).$$

Once the equations (9)–(11) were differentiated and dU changed with the expression (8) in the obtained ratios, we obtained new state functions $H = f(S, p, n_i)$, $F = f(T, V, n_i)$, and $G = f(T, p, n_i)$:

$$dH = TdS + Vdp + \sum \mu_i dn_i, \quad (12)$$

$$dF = -SdT - pdV + \sum \mu_i dn_i, \quad (13)$$

$$dG = -SdT + Vdp + \sum \mu_i dn_i. \quad (14)$$

The Gibbs energy function $G = f(T, p, n_i)$ is important for practical thermodynamic calculations, as its arguments, or natural variables, T, p, n_i in equation (14) can be measured and recorded in order to control chemical transformations.

Next, we will consider the application of equations (11)–(14) in the solution of three main problems of thermodynamics. Let us start with the first problem.

8. Possibility of spontaneous process flow (without consumption of any external energy)

If we change equation (8) so that entropy S becomes a state function and internal energy U , volume V , and the amount of moles of n_i components become arguments, that is, if $S = f(U, V, n_i)$, then the first sufficient condition for the spontaneous flow of the process is formulated as follows: if the entropy of an isolated system increases $(dS)_{U,V,n_i} > 0$, the process may occur spontaneously. In the state of equilibrium this function reaches its maximum and remains constant $(dS)_{U,V,n_i} = 0$.

The Gibbs energy function $G = f(T, p, n_i)$ can be used to evaluate the probability of a spontaneous process, as its arguments (or natural variables), such as temperature T , pressure p , and the amount of moles n_i , can be measured and recorded in order to control chemical transformations. Why does it happen? It happens due to the fact that spontaneous processes are those that can perform work W . If it is impossible, equilibrium $\Delta G = 0$ occurs. But when $\Delta G < 0$ with constant T, p, n_i , the system may perform “chemical” work of transformation of n_1 moles of initial substances into n_2 moles of final substances: $(\Delta G)_{p,T} = (W_{\text{chem}})_{p,T}^{\text{max}} = \sum \mu_i dn_i$, and the process occurs spontaneously, $dn_2 > 0$. As the process occurs and the system reaches the equilibrium, its “performance” decreases.

9. Thermal effect of a chemical reaction. Thermochemistry

Since internal energies of products and initial substances are different, changes in energy occur during chemical transformations (chemical reactions). It may happen as a release or absorption of heat δQ and the performance of heat work. There is considerable heat in the reaction (see article 6), so it can be measured. **Thermochemistry** deals with the study of the heat of chemical reactions. The issues of thermochemistry are considered in detail in [3–5].

10. Calculation of equilibrium composition of the reaction medium. Chemical equilibrium

The most important task in chemistry is to determine the composition of an equilibrium

mixture during the transformation of one substance into another. We will consider its solution at a constant temperature $T = \text{const}$ based on the example of the interaction of ideal gases (reaction (15))*:



To solve this problem, let us assess the dependence of the change of Gibbs energy $\Delta_r G$ of reaction (15) on real conditions, including partial pressures p_i^* (composition), general pressure p , and temperature T . With the assumptions made, the chemical potential of each participant of reaction (15) can be expressed by equation (16):

$$\mu_i(p, T) = \mu_i^0(T) + RT \ln p_i^*, \quad (16)$$

where p_i^* is the specified pressure: $p_i^* = \frac{p_i}{p^0}$, where

p^0 is 1 bar. Then the change of Gibbs energy $\Delta_r G$ of process (15) will be expressed as follows (17):

$$\begin{aligned} \Delta_r G &= c\mu_c + d\mu_d - a\mu_a - b\mu_b = \\ &= c\mu_c^0 + d\mu_d^0 - a\mu_a^0 - b\mu_b^0 + RT \ln \frac{p_c^c p_d^d}{p_a^a p_b^b} = \\ &= \Delta_r G^0 + RT \ln \frac{p_c^c p_d^d}{p_a^a p_b^b}. \end{aligned} \quad (17)$$

Expression (17) is called an **isotherm reaction equation**. The term isotherm stands for the equality of the temperatures during the initial and final states of the process. However, the temperature may change when the system transits from one state to another. The first summand in equation (17) is the change of standard Gibbs energy of reaction (15). With equilibrium $\Delta_r G = 0$, we determine that:

$$\Delta_r G^0 = -RT \ln \frac{p_c^c p_d^d}{p_a^a p_b^b}. \quad (18)$$

The symbol of the logarithm in the last expression is the ratio of the products of the equilibrium partial pressures of final and initial substances in reaction (15). This value is called the **equilibrium constant** of a reaction in the gaseous phase. It describes the depth of the process flow. If $K_p > 1$, then equilibrium (15) is shifted towards the products of the reaction

and, vice versa, if $K_p < 1$, it is shifted towards the initial substances. The introduction of the K_p equilibrium constant allows changing equations (18) and (17) as follows:

$$\Delta_r G^0 = -RT \ln K_p, \quad (19)$$

$$\Delta_r G = -RT \ln K_p + RT \ln \frac{p_c^c p_d^d}{p_a^a p_b^b}. \quad (20)$$

The specified ratios are important for the solution of practical problems of thermodynamics, such as:

(1) Assessing the direction of the transformation process.

(2) Determining the equilibrium composition.

(3) Changing the composition of the equilibrium reaction mixture with variations in external conditions, including temperature, pressure, and the ratio of interacting substances.

These problems are solved in the following way:

1. The direction of the process can be assessed by the sign of $\Delta_r G$, if we know the equilibrium constant (or the standard thermodynamic properties of the process participants) and the partial pressures of the initial substances upon their mixing.

2. Without an experiment, we can determine the equilibrium composition of the mixture if there are reference thermodynamic data for the calculation of $\Delta_r G$.

3. The sign of the logarithm in expressions (17) and (20) stands for the ratio of the products of the current partial pressures that are recorded and controlled by the experimenter. Taking this into account as well as the known temperature and baric dependences of the equilibrium constants, it should be noted that equation (20) allows controlling the composition of the reaction mixture using external conditions.

Equation (20) has two important features:

a) If we change the ratio of the current partial pressures, we can evaluate the temperature when the sign changes from $\Delta_r G > 0$ to the condition of $\Delta_r G < 0$, i. e., when a non-spontaneous process becomes a spontaneous one.

b) The difference between the summands in equations (17) and (20) shows that the system deviates from equilibrium and it can be considered as **supersaturation**. It is a very important

* Due to the amounts of substances A, B, C, and D, the decrease and the formation of different substances do not change the composition and the conditions of the system's existence.

feature, since a connection is established between thermodynamics and kinetics. For example, supersaturation values can help in assessing the rate of formation and growth of nuclei of a new phase, which is required for the synthesis of materials with the specified composition and properties.

Depending on the conditions of the process, the equilibrium constant can be expressed not only through partial pressures (activities) but also through other variables, for instance, through the mole fraction or molarity, which is studied in [3].

As it was mentioned before, the equilibrium of the process of substance transformation corresponds to the minimum of the Gibbs energy of the system, which corresponds to the condition of $\Delta_r G = 0$. Modern computational programs allow finding the minimum of the Gibbs energy of the system and, correspondingly, assessing the composition of the equilibrium reaction mixture for a large number of variables. This allows calculating chemical equilibria in general. To do this, we only need to specify the elemental composition of the system and indicate all possible substances that can be formed from the specified elements [3].

Author contributions

All authors made an equivalent contribution to the preparation of the publication.

Conflict of interests

The authors declare that they have no known competing financial interests or personal relationships that could have influenced the work reported in this paper.

References

1. Zlomanov V. P., Kazin P. E., Yatsenko A. A., Rumyantsev E. V. *Brief Dictionary of Basic Chemical Concepts*. St. Petersburg: Lan' Publ.; 2020. 52 p. (In Russ.)
2. Voronin G. F. *Fundamentals of thermodynamics*. Moscow: Moscow State University Publ.; 1987. 192 p. (In Russ.)
3. Eremin V. V., Kargov S. I., Uspenskaya I. A., Kuzmenko N. E., Lunin V. V. *Fundamentals of physical chemistry; Textbook Part 1. Theory. 2nd ed. revised and additional*. Moscow: BINOM Publ.; 2013. 320 p. (In Russ.)
4. Gorshkov V. I., Kuznetsov I. A. *Fundamentals of physical chemistry. 3rd ed. revised and additional*. Moscow: BINOM. Publ.; 2006. 407 p. (In Russ.)
5. Tamm M. E., Tretyakov Yu. D. *Inorganic chemistry. T. 1. Physical and chemical foundations of inorganic chemistry*. Moscow: Akademiya Publ.; 2012. 240 p. (In Russ.)

Information about the authors

Vladimir P. Zlomanov, Dr. Sci. (Chem.), Professor, Department of Inorganic Chemistry of the Faculty of Chemistry, Lomonosov Moscow State University (Moscow, Russian Federation).

<https://orcid.org/0000-0002-0327-4715>
zlomanov1@mail.ru

Pavel E. Kazin, Dr. Sci. (Chem.), Professor, Department of Inorganic Chemistry of the Faculty of Chemistry, Lomonosov Moscow State University (Moscow, Russian Federation).

<https://orcid.org/0000-0002-1415-2190>

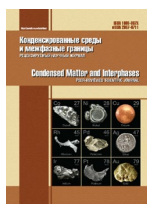
Alexander V. Yatsenko, Dr. Sci. (Chem.), Professor, Department of General Chemistry of the Faculty of Chemistry, Lomonosov Moscow State University (Moscow, Russian Federation).

<https://orcid.org/0000-0001-8742-8779>

Received 02.02.2022; approved after reviewing 03.03.2022; accepted for publication 15.04.2022; published online 25.06.2022.

Translated by Marina Strepetova

Edited and proofread by Simon Cox



Original articles

Research article

<https://doi.org/10.17308/kcmf.2022.24/9262>

Electrocrystallisation of Cu-Sn-TiO₂ composite coatings in sulphuric acid electrolytes

A. A. Kasach¹✉, D. S. Kharytonau², I. M. Zharskii¹, I. I. Kurilo¹

¹Belarusian State Technological University
13a Sverdlova st., Minsk 220006, Belarus

²Jerzy Haber Institute of Catalysis and Surface Chemistry, Polish Academy of Sciences,
8 Niezapominajek, Krakow 30-239, Poland

Abstract

The aim of the article is to determine the peculiarities of electrochemical production of Cu-Sn-TiO₂ composite coatings in sulphuric acid electrolytes with intermittent agitation under stationary and pulsed modes of electrolysis.

Linear voltammetry and static and pulsed chronopotentiometry were used to study the kinetic features of electrocrystallisation of Cu-Sn-TiO₂ composite coatings in a sulphuric acid electrolyte with intermittent agitation. When the electrolyte was stirred, the cathodic potential shifted towards electropositive values. It was shown that after switching the agitation off, the value of the cathodic potential at which the copper-tin alloy forms at a cathodic current density of -0.013 A/cm^2 was reached within 70 s and when using pulsed electrolysis, it was reached within 80 s. Scanning electron microscopy established that the most homogeneous and uniform Cu-Sn-TiO₂ coatings were formed when pulsed electrolysis was used.

Intermittent agitation of the sulphuric acid electrolytes led to the formation of ordered multilayer structures consisting of microlayers of the Cu-Sn alloy and copper due to the intermittent elimination of diffusion limitations for the discharge of copper(II) ions when agitation was switched on, which resulted in suppression of the process of the underpotential deposition of tin.

Keywords: Electrocrystallisation, Formation of alloys, Composite coating, Pulsed electrolysis, Structure

Funding: This research was funded by the Ministry of Education of the Republic of Belarus as part of the State Research Programme “Mechanics, metallurgy, and diagnostics in machinery construction” (2016–2020), subprogramme “Electroplating”, order No. 4.1.28 “Electrochemical composite coatings based on tin alloys with photocatalytic properties” (2019–2020, state registration number 20212333).

For citation: Kasach A. A., Kharytonau D. S., Zharskii I. M., Kurilo I. I. Electrocrystallisation of Cu-Sn-TiO₂ composite coatings in sulphuric acid electrolytes. *Condensed Matter and Interphases*. 2022;24(2): 220–226. <https://doi.org/10.17308/kcmf.2022.24/9262>

Для цитирования: Касач А. А., Харитонов Д. С., Жарский И. М., Курило, И. И. Электрокристаллизация композиционных покрытий Cu-Sn-TiO₂ в сернокислых электролитах. *Конденсированные среды и межфазные границы*. 2022;24(2): 220–226. <https://doi.org/10.17308/kcmf.2022.24/9262>

✉ Aliaksandr A. Kasach, e-mail: kasach2018@bk.ru

© Kasach A. A., Kharytonau D. S., Zharskii I. M., Kurilo I. I., 2022



The content is available under Creative Commons Attribution 4.0 License.

1. Introduction

Electrochemical copper and tin alloys are characterised by high hardness, wear resistance, and corrosion resistance [1, 2]. Alloys containing up to 20 wt% of Sn (yellow bronzes) are used as protective and decorative coatings, as well as a sublayer before chrome plating [3, 4]. Recently, these alloys have attracted a wide attention due to their antibacterial activity against many Gram positive and Gram negative bacteria [5–8]. Unlike copper coatings, which are characterised by low wear resistance, fade quickly in the air, and lose their decorative appearance, copper-tin alloys are less susceptible to wear and corrosion [9, 10].

Sulphuric acid electrolytes can be used for electrochemical production of yellow bronzes [11–13]. This type of electrolyte is characterised by low toxicity. What is more, wastewater generated as a result of their application is easily regenerated and disposed. In sulphuric acid electrolytes, the process of alloy formation can occur at potentials with higher positive values than those of the standard electrode potential of the Sn²⁺|Sn⁰ system (–0.136 V) [13, 14]. In order to obtain homogeneous and fine-grained coatings, special organic additives are added to sulphuric acid electrolytes: thiourea [14], quaternary ammonium salts [15], gelatin [16], synthanol, etc. [17]. Among the disadvantages of sulphuric acid electrolytes used for the deposition of Cu-Sn alloys are their low covering and scattering power, as well as narrow intervals of cathodic current densities providing for homogeneous and shiny coatings [15]. In [15], it was found that pulsed electrolysis with a relative current pulse duration of 1.5 and a frequency of 66.7 Hz allows expanding the working range of cathodic current densities, at which semi-shiny yellow bronze coatings are formed, almost by four times. The formation of copper and tin alloys in sulphuric acid electrolytes occurs if the duration of the cathodic current pulse exceeds the value of the transition time of the discharge process of copper(II) ions. The modification of the Cu-Sn matrix by TiO₂ nanoparticles hardens it and improves the antibacterial properties of coatings [18]. In [19] it was shown that the introduction of TiO₂ nanoparticles in the amount of 1 to 10 g/dm³ into the sulphuric acid electrolyte at a deposition potential of –0.05 V leads to the production

of composite electrochemical coatings (CECs) containing between 0.17 and 1.72 wt% of TiO₂. The potentiostatic electrolysis ensures the formation of coatings with homogeneous distribution of the alloy components. In industry, galvanostatic electrolysis is mainly used for electrochemical deposition of metals and alloys since using potentiostatic modes on an industrial scale is difficult. In the case of galvanostatic electrolysis, electrolyte stirring significantly influences cathodic polarisation, which, in turn, can affect the quantitative composition of the formed Cu-Sn alloy.

The aim of the work was to determine the peculiarities of the electrochemical production of Cu-Sn-TiO₂ composite coatings in sulphuric acid electrolytes with intermittent agitation under the stationary and pulsed modes of electrolysis.

2. Experimental

An electrolyte of the following composition was used for the electrochemical deposition of Cu-Sn coatings, g/dm³: CuSO₄·5H₂O – 40; SnSO₄ – 40; CS(NH₂)₂ (thiourea) – 0.005; H₂SO₄ – 100. The electrolysis was carried out without agitation of the electrolyte at a cathodic current density of 0.013 A/cm². When obtaining the Cu-Sn-TiO₂ CEC, TiO₂ nanoparticles (Degussa aeroxide P25) in the amount of 5 g/dm³ were introduced into the basic composition. In order to deagglomerate the particles in the electrolyte for the CEC application, it was sonicated for 20 min using a UP 200 Ht homogenizer (Hielscher Ultrasonics GmbH, Teltow, Germany). To maintain the TiO₂ particles in suspension, during the precipitation process of the CEC the electrolyte was agitated intermittently with a magnetic stirrer every 5 min for 10 s (stirring rate of 400 rpm). The electrolysis was carried out using both stationary and pulsed modes. When using stationary electrolysis, the cathodic current density was 0.013 A/cm². The parameters of pulsed electrolysis: relative pulse duration – 1.5; pulse frequency – 66.7 Hz; cathodic density of the pulse current – 0.0225 A/cm². The parameters of stationary and pulsed modes of electrolysis used in the work were selected based on the results of previous studies [15] and provided high-quality and homogeneous yellow bronze coatings. The cathodes were pieces of copper-foiled dielectric. M0 copper was used for

the anodes. The dimension of the working surface of the electrodes was 6 cm².

Cathodic polarisation curves and chronopotentiograms of copper electrode in electrolytes used for the application of the Cu-Sn alloy and CECs based on it were taken in a standard three-electrode cell using an Elins P40X potentiostat/galvanostat (Electrochemical Instruments, Russia). The polarisation curves of the copper electrode were taken at a linear potential sweep rate of 1 mV/s. A saturated silver/silver chloride electrode was used as the reference and a M0 copper plate was used as the counter electrode. The values of electrode potentials were recalculated in the scale of the standard hydrogen electrode. To obtain reliable results, all electrochemical studies were carried out at least three times.

The morphology, qualitative, and quantitative compositions of the formed coatings were studied using a JSM-5610 LV scanning electron microscope (Jeol Ltd.) equipped with a JED-2201 energy dispersion X-ray (EDX) analyser. The accelerating voltage for surface imaging and elemental analysis was 20 kV.

3. Results and Discussion

To assess the effect of electrolyte mixing on the kinetic features of electrodeposition of coatings, polarisation curves of the copper electrode in electrolytes used for the application of Cu-Sn (Fig. 1, curve 1) and Cu-Sn-TiO₂ (Fig. 1, curves 2, 3) were obtained. In the used electrolytes, the process of copper and tin codeposition could occur in the range of cathodic potentials from 0.0 to -0.136 V, i.e., at potentials corresponding to the process of underpotential deposition of Sn [14]. When 5 g/dm³ of TiO₂ was introduced into the studied electrolyte within the potential range of -0.01–(-0.06) V, the cathodic polarisation curves of the copper electrode shifted towards negative values and the cathodic current density decreased and reached 4±1.5 mA/cm² at a potential of -0.04 V, which indicated the inhibition of the process of the reduction of copper(II) ions. The agitation of the electrolyte used to deposit Cu-Sn-TiO₂ had a depolarising effect (Fig. 1, curve 3) due to a decrease in the diffusion limitations for the discharge of copper(II) ions. Codeposition of tin and copper was possible when the discharge of

copper(II) ions occurred at the limiting diffusion current [14]. Mechanical mixing of the electrolyte helped to remove the diffusion limitations for the discharge of copper(II) ions, however, it did not provide a uniform mass transfer over the volume of the cell and the area of the cathode [19]. This, in turn, led to the formation of either copper coatings or Cu-Sn coatings with a low tin content. Thus, constant agitation of electrolyte prevented the formation of Cu-Sn coatings corresponding to the composition of yellow bronze. Therefore, the electrolyte should be agitated intermittently to obtain Cu-Sn-TiO₂ CECs.

Fig. 2 shows the chronopotentiograms of the copper electrode during the deposition of the Cu-Sn alloy (Fig. 2a, curve 1) and the Cu-Sn-TiO₂ CEC (Fig. 2a, curve 2). The introduction of TiO₂ particles of the modifying phase into the electrolyte led to a slight shift of the *E*-*t*-dependency towards the electronegative values. The authors of [19] suggested that the increase in electrode polarisation during the deposition of the Cu-Sn-TiO₂ CEC may be due to the adsorption of the modifying phase particles on the surface of the growing precipitate, which, in turn, may reduce the active area of electrode involved in the electrochemical reaction. When the agitation of the electrolyte was switched on (*t* = 300 s), the cathodic potential shifted towards positive values from -0.07 to 0.07–0.10 V. After the magnetic stirrer was turned off (*t* = 310 s),

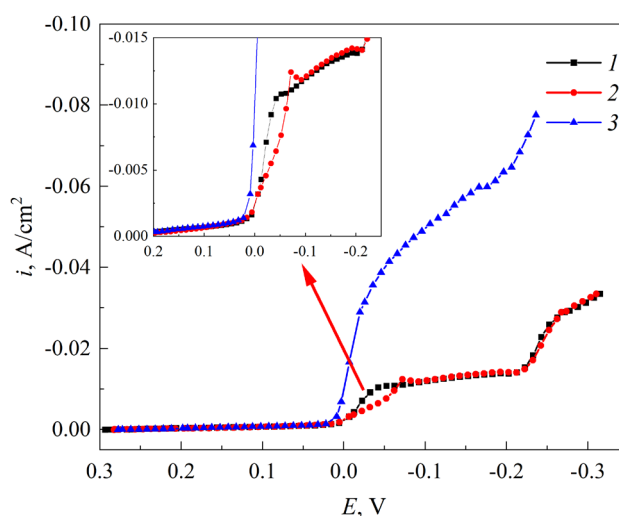


Fig. 1. Cathodic polarisation curves of the copper electrode in electrolytes used for the application of Cu-Sn (curve 1) and Cu-Sn-TiO₂ (curve 2, 3); 1, 2 – without stirring the electrolyte; 3 – mechanical stirring

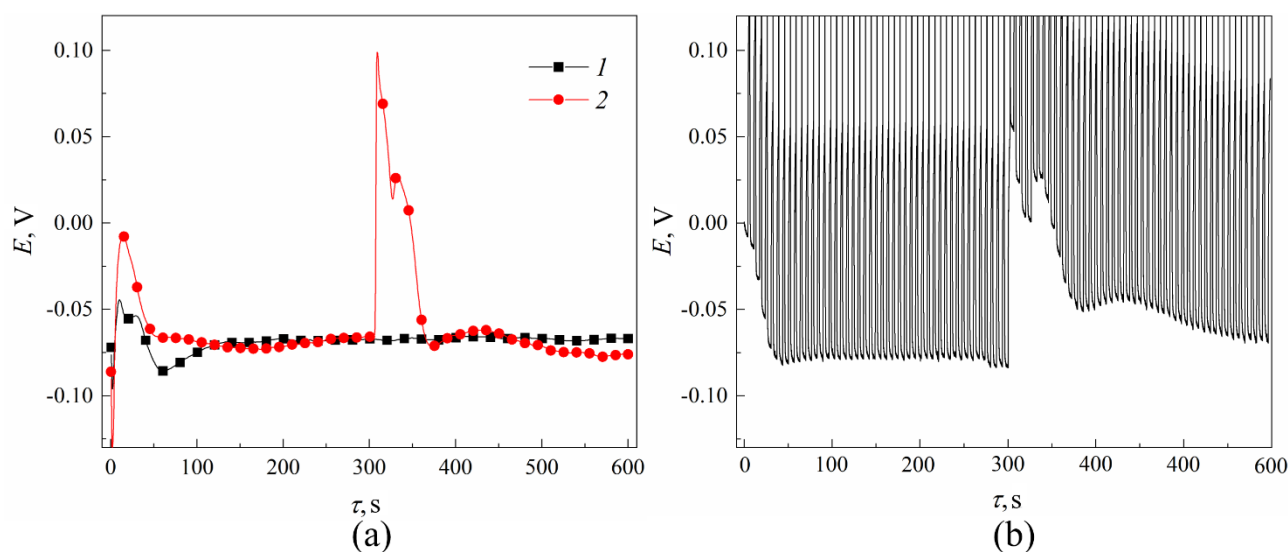


Fig. 2. Chronopotentiograms of the copper electrode in electrolytes used for the application of Cu-Sn (*a*, curve 1) and Cu-Sn-TiO₂ (*a*, curve 2; *b*). Electrolysis mode: *a* – stationary; *b* – pulsed

there was a gradual increase in the cathodic polarisation of the electrode, which was due to the contribution of the diffusion overvoltage. The value of the cathodic potential corresponding to the formation of the Cu-Sn alloy was reached 60 seconds after the magnetic stirrer was turned off. When using pulsed electrolysis (Fig. 2b), it took longer for the constant value of the cathodic potential to be reached (70–80 s) after mixing was switched off, which was due to the relaxational effect of the pause.

Fig. 3 shows micrographs of the obtained Cu-Sn and Cu-Sn-TiO₂ coatings. Under stationary conditions, at a cathodic current density of 0.013 A/cm² (Fig. 3a), fine-grained and homogeneous Cu-Sn coatings were formed. The introduction of TiO₂ nanoparticles into the electrolyte led to the formation of rough and less uniform coatings (Fig. 3b, c). The surface of the Cu-Sn-TiO₂ CEC included globules whose size

varied between 5 and 20 μm. Coatings obtained by pulsed electrolysis (Fig. 3c) were characterised by a more uniform and smoother structure.

The table presents data on the elemental composition of the obtained coatings. The cathodic current density of 0.013 A/cm² and stationary conditions resulted in the formation of Cu-Sn coatings containing up to 10.9 wt% of Sn. The introduction of TiO₂ nanoparticles in the amount of 5 g/dm³ in the composition of the electrolyte led to an increase in the content of tin in the coating to 12.6 wt%, which was due to an increase in cathodic polarisation during the formation of the alloy (Fig. 1, curve 2). The obtained coating contained 0.8 wt% of Ti which was present due to the integration of TiO₂ nanoparticles into the metal Cu-Sn matrix.

The pulsed mode of electrolysis allowed obtaining coatings of the following composition, wt.%: Cu – 87.2; Sn – 12.1; Ti – 0.7. It should be

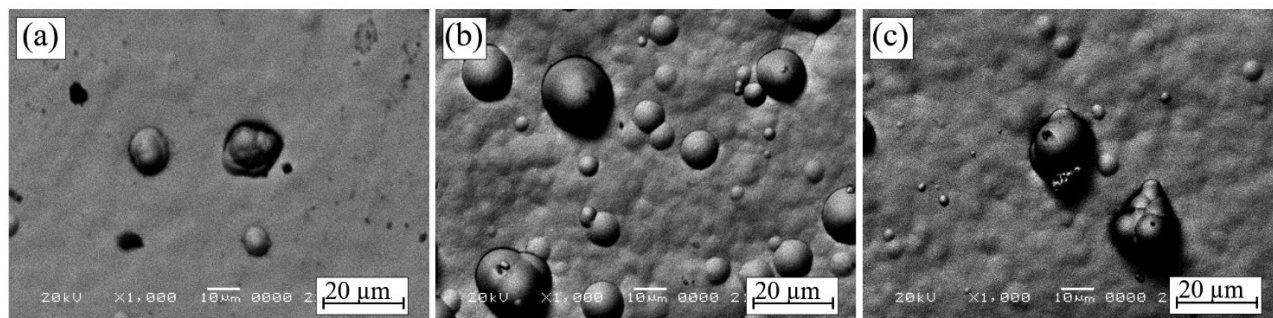


Fig. 3. Micrographs of the surface of Cu-Sn (*a*) and Cu-Sn-TiO₂ (*b*, *c*) coatings. Electrolysis mode: *a*, *b* – stationary; *c* – pulsed

Table. Elemental composition of the surface of Cu-Sn and Cu-Sn-TiO₂ coatings (scanning area of 50×50 μm)

Coating	Current density, A/cm ²	Pulse frequency, Hz	Content in the alloy, wt%		
			Cu	Sn	Ti
Cu-Sn	0.013	–	89.1	10.9	–
Cu-Sn-TiO ₂	0.013	–	86.6	12.6	0.8
Cu-Sn-TiO ₂	0.0225	66.7	87.2	12.1	0.7

noted that the change in the electrolysis mode did not significantly affect the quantitative content of the TiO₂ particles in the alloy.

Fig. 4 shows crosscut SEM images of Cu-Sn (Fig. 4a) and Cu-Sn-TiO₂ coatings (Fig. 4b, c). The obtained coatings had a clear boundary with the substrate metal and were characterised by high adhesive power. The crosscut of the Cu-Sn-TiO₂ coating obtained by stationary electrolysis had defects in the form of globules and microcracks. The crosscuts of CuSn-TiO₂ CECs deposited by means of the pulsed electrolysis had no pronounced defects, which is probably due to the uniform microdistribution of current over the surface of the growing precipitate.

Over the entire thickness of the Cu-Sn-TiO₂ CEC, there were areas (layers) with different image contrasts, which were evenly distributed over the entire thickness of the coatings. The thickness of light sections varied from 3 to 5 μm, while that of dark sections was less than 1 μm. When using the backscattered electrons, this contrast distribution indicated a different elemental composition of these coating regions.

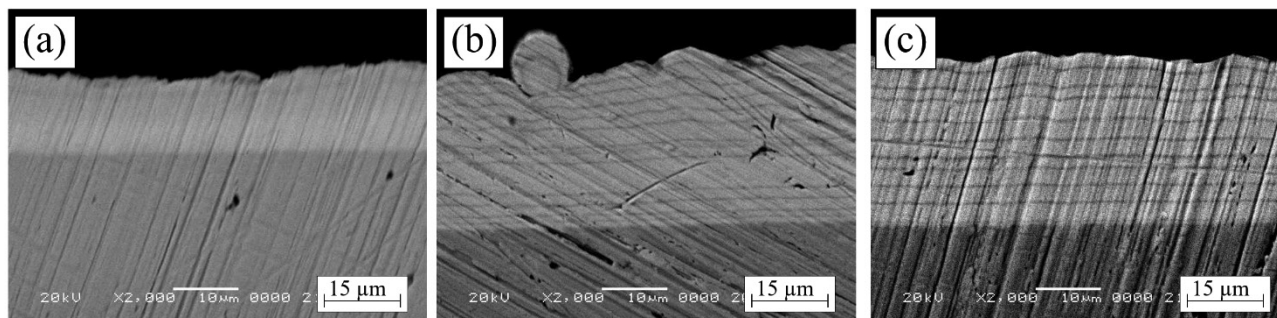
In order to establish the elemental composition and nature of areas of different contrasts, their EDX point analysis was carried out (Fig. 5).

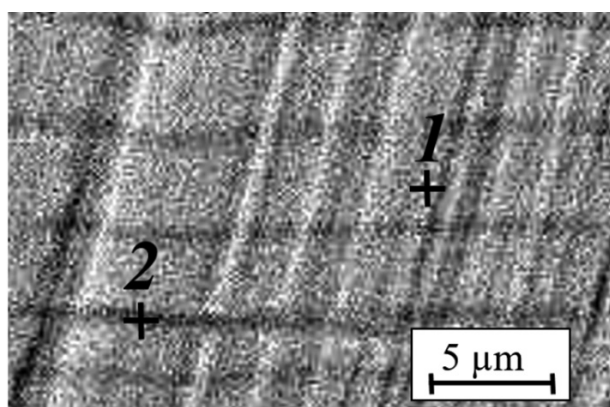
According to the obtained data, dark areas of the coatings were characterised by a lower

content of tin. The ratio of the mass content of tin in the alloy between the light and dark areas was approximately 4 : 1. Stirring of the electrolyte led to depolarisation of the electrode and removal of diffusion limitations for the discharge of copper(II) ions, which made the underpotential deposition of tin impossible to achieve. Thus, when the agitation of the electrolyte was switched on, in order to maintain TiO₂ particles in suspension, ordered alloy layers enriched in copper were formed. Codeposition of copper and tin was observed when agitation was switched off and when the transition time of the discharge of copper(II) ions was reached.

4. Conclusions

In sulphuric acid electrolytes used for the application of the Cu-Sn alloy and the Cu-Sn-TiO₂ composite coatings in the absence of agitation, copper and tin codeposition takes place at potentials corresponding to the process of underpotential deposition of Sn. Introduction of TiO₂ nanoparticles in the amount of 5 g/dm³ into the composition of the electrolyte helps to inhibit the reduction of copper(II) ions and reduces its content in the coating by ≈3 wt%. Application of pulsed electrolysis at a relative current pulse duration of 1.5, a frequency of 66.7 Hz, and cathodic current density of 0.0225 A/cm²

**Fig. 4.** Micrographs of sections of Cu-Sn (a) and Cu-Sn-TiO₂ (b, c) coatings. Electrolysis mode: a, b – stationary; c – pulsed



Point	Chemical Composition, wt. %		
	Cu	Sn	Ti
1	85.9	13.4	0.7
2	96.1	3.5	0.4

Fig. 5. Micrographs of sections and the data of the EDX point analysis for the Cu-Sn-TiO₂ coating section obtained by means of pulsed electrolysis

allows obtaining Cu-Sn-TiO₂ CECs of similar composition (≈ 0.7 – 0.8 wt% of titanium, 12.1 – 12.6 wt% tin) but more homogeneous and uniform than those formed by the stationary mode at a cathodic current density of 0.013 A/cm².

Intermittent agitation of the sulphuric acid electrolytes leads to the formation of ordered multilayer structures consisting of microlayers of the Cu-Sn and copper alloy due to the intermittent elimination of diffusion limitations for the discharge of copper(II) ions when agitation is switched on, which results in suppression of the process of the underpotential deposition of tin. When agitation is switched off, the value of the cathodic potential at which the alloy of copper and tin forms at a cathodic current density of -0.013 A/cm² is reached within 70 s and when using pulsed electrolysis, it is reached within 80 s.

Author contributions

All authors made an equivalent contribution to the preparation of the publication.

Conflicts of interest

The authors declare that they have no known competing financial interests or personal relationships that could have influenced the work reported in this paper.

References

1. Karthik M., Abhinav J., Shankar K. V. Morphological and mechanical behaviour of Cu-Sn alloys – A review. *Metals and Materials International*. 2021; 1915–1946. <https://doi.org/10.1007/s12540-020-00899-z>
2. Souissi N., Sidot E., Bousselmi L., Triki E., Robbiola L. Corrosion behaviour of Cu-10Sn bronze in aerated NaCl aqueous media - Electrochemical investigation. *Corrosion Science*. 2007;49(8): 3333–3347. <https://doi.org/10.1016/j.corsci.2007.01.013>
3. Lehmann L., Höhlich D., Mehner T., Lampke T. Irregular electrodeposition of Cu-Sn alloy coatings in [emim]cl outside the glove box with large layer thickness. *Coatings*. 2021;11(3): <https://doi.org/10.3390/coatings11030310>
4. Jung M., Lee G., Choi J. Electrochemical plating of Cu-Sn alloy in non-cyanide solution to substitute for Ni undercoating layer. *Electrochimica Acta*. 2017;241: 229–236. <https://doi.org/10.1016/j.electacta.2017.04.170>
5. Wilks S. A., Michels H., Keevil C. W. The survival of escherichia coli O157 on a range of metal surfaces. *International Journal of Food Microbiology*. 2005;105(3): 445–454. <https://doi.org/10.1016/j.ijfoodmicro.2005.04.021>
6. Grass G., Rensing C., Solioz M. Metallic copper as an antimicrobial surface. *Applied and Environmental Microbiology*. 2011;77(5): 1541–1547. <https://doi.org/10.1128/AEM.02766-10>
7. Chang T., Sepati M., Herting G., Leygraf C., Rajarao G. K., Butina K., Odnevall Wallinder I. A novel methodology to study antimicrobial properties of high-touch surfaces used for indoor hygiene applications-A study on Cu metal. *PLoS One*. 2021;16(2): e0247081. <https://doi.org/10.1371/journal.pone.0247081>
8. Chang T., Babu, R. P., Zhao W., Johnson C. M., Hedström P., Odnevall I., Leygraf C. High-resolution microscopical studies of contact killing mechanisms on copper-based surfaces. *ACS Applied Materials & Interfaces*. 2021;13(41): 49402–49413. <https://doi.org/10.1021/acsami.1c11236>
9. Walsh F. C. Low C. T. J. A review of developments in the electrodeposition of tin-copper alloys. *Surface and Coatings Technology*. 2016;304: 246–262. <https://doi.org/10.1016/j.surfcoat.2016.06.065>
10. Hutchison M. J. Scully J. R. Patina enrichment with SnO₂ and its effect on soluble Cu cation release and passivity of high-purity Cu-Sn bronze in artificial perspiration. *Electrochimica Acta*. 2018;283: 806–817. <https://doi.org/10.1016/j.electacta.2018.06.125>
11. Survila A., Mockus Z., Kanapekaitė S., Bražinskienė D., Juškėnas R. Surfactant effects in Cu-Sn alloy deposition. *Journal of The Electrochemical*

Society. 2012;159(5): 296–302. <https://doi.org/10.1149/2.084205jes>

12. Juškėnas R., Mockus Z., Kanapeckaitė S., Stalnionis G., Survila A. XRD studies of the phase composition of the electrodeposited copper-rich Cu-Sn alloys. *Electrochimica Acta*. 2006;52(3): 928–935. <https://doi.org/10.1016/j.electacta.2006.06.029>

13. Survila A., Mockus Z., Kanapeckaitė S., Jasulaitienė V., Juškėnas R. Codeposition of copper and tin from acid sulphate solutions containing polyether sintanol DS-10 and benzaldehyde. *Journal of applied electrochemistry*. 2009;39(10): 2021–2026. <https://doi.org/10.1007/s10800-009-9914-2>

14. Kasach A. A., Kharitonov D. S., Makarova I. V., Wrzesińska A., Zharskii I. M., Kurilo I. I. Effect of thiourea on electrocrystallization of Cu–Sn alloys from sulphate electrolytes. *Surface and Coatings Technology*. 2020;399: 126137. <https://doi.org/10.1016/j.surfcoat.2020.126137>

15. Kasach A. A., Kharitonov D. S., Radchenko S. L., Zharskii I. M., Kurilo I. I. Effect of parameters of pulse electrolysis on electrodeposition of copper–tin alloy from sulfate electrolyte. *Russian Journal of Electrochemistry*. 2020;56(9): 744–753. <https://doi.org/10.1134/S1023193520090049>

16. Meudre C., Ricq L., Hihn J. Y., Moutarlier V., Monnin A., Heintz O. Adsorption of gelatin during electrodeposition of copper and tin-copper alloys from acid sulfate electrolyte. *Surface and Coatings Technology*. 2014;252: 93–101. <https://doi.org/10.1016/j.surfcoat.2014.04.050>

17. Nakanishi S., Sakai S. I., Nagai T., Nakato Y. Macroscopically uniform nanoperiod alloy multilayers formed by coupling of electrodeposition with current oscillations. *The Journal of Physical Chemistry B*. 2005;109(5): 1750–1755. <https://doi.org/10.1021/jp045876x>

18. Kharitonov D. S., Kasach A. A., Sergievich D. S., Wrzesińska A., Bobowska I., Darowicki K., Zielinski A.,

Ryl J., Kurilo I. I. Ultrasonic-assisted electrodeposition of Cu-Sn-TiO₂ nanocomposite coatings with enhanced antibacterial activity. *Ultrasonics Sonochemistry*. 2021;75: 1–11. <https://doi.org/10.1016/j.ultsonch.2021.105593>

19. Kasach A. A., Kharytonau D. S., Paspelau A. V., Ryl J., Sergievich D. S., Zharskii I. M., Kurilo I. I. Effect of TiO₂ concentration on microstructure and properties of composite Cu–Sn–TiO₂ coatings obtained by electrodeposition. *Materials*. 2021;14(20): 6179. <https://doi.org/10.3390/ma14206179>

Information about authors

Aliaksandr A. Kasach, Assistant at the Department of Chemistry, Technology of Electrochemical Production and Electronic Engineering Materials, Belarusian State Technological University (Minsk, Belarus).

<https://orcid.org/0000-0001-5522-2928>
kasach2018@bk.ru

Dzmitry S. Kharytonau, PhD in Chemistry, postdoctoral fellow at Jerzy Haber Institute of Catalysis and Surface Chemistry of the Polish Academy of Sciences (Krakow, Poland).

<https://orcid.org/0000-0003-2071-3975>
dmitry.kharitonov@ikifp.edu.pl

Ivan M. Zharskii, Cand. Sci. (Chem.), Associate Professor at the Department of Chemistry, Technology of Electrochemical Production and Electronic Engineering Materials, Belarusian State Technological University (Minsk, Belarus).

<https://orcid.org/0000-0002-3942-5175>

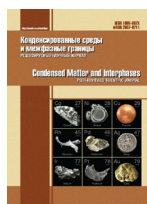
Irina I. Kurilo, Cand. Sci. (Chem.), Associate Professor at the Department of Physical, Colloid, and Analytical Chemistry, Belarusian State Technological University (Minsk, Belarus).

<https://orcid.org/0000-0002-0016-6719>
september@tut.by

Received 09.12.2021; approved after reviewing 15.02.2022; accepted for publication 15.04.2022; published online 25.06.2022.

Translated by Irina Charychanskaya

Edited and proofread by Simon Cox



Original articles

Research article

<https://doi.org/10.17308/kcmf.2022.24/9263>

Theoretical and experimental investigation on ADT organic semiconductor in different solvents

D. M. Mamand¹, H. H. Rasul¹, P. K. Omer², H. M. Qadr¹✉

¹University of Raparin, College of Science, Department of Physics, Sulaymaniyah, Iraq

²University of Raparin, College of Science, Department of Chemistry, Sulaymaniyah, Iraq

Abstract

The purpose of this work is to investigate experimental and theoretical methods for the properties of (ADTs) organic semiconductors. The effect of solvent on optical and electrical on Anthradithiophene (ADT) characteristics was investigated. The optoelectronic properties associated with experimental work consists of bandgap energy, Tauc plot, transparency, electrical and optical conductance and dielectric properties calculated. For theoretical calculations, firstly, HOMO and LUMO have been used for the computation of the bandgap energy. The average bandgap energy between HOMO and LUMO is found to be 2.84 eV by using five basis sets in gas phases. After that, the FTIR has been elucidated. In addition, to determine the functional group, and determined the important region did not take place absorption. In general, this region did not occur absorption which is around between 1650 cm⁻¹ and 3200 cm⁻¹ by using five basis sets. The UV-Vis spectroscopy was elucidated. Furthermore, to determine the energy band-gap, the average energy band gap was found to be 2.59 eV, and it was determined the correct transition type. The ADT molecule exhibited the indirect allowed transition.

Keywords: UV-visible spectroscopy, FTIR, HOMO, LUMO, HF and DFT

For citation: Mamand D. M., Rasul H. H., Omer P. K., Qadr H. M. Theoretical and experimental investigation on ADT organic semiconductor in different solvents. *Condensed Matter and Interphases*. 2022;24(2): 227–242. <https://doi.org/10.17308/kcmf.2022.24/9263>

Для цитирования: Маманд Д. М., Расул Х. Х., Омер П. К., Квадр Х. М. Теоретическое и экспериментальное исследование антрадитиофена в различных растворах. *Конденсированные среды и межфазные границы*. 2022;24(2): 227–242. <https://doi.org/10.17308/kcmf.2022.24/9263>

✉ Hiwa Mohammad Qadr, e-mail: hiwa.physics@uor.edu.krd

© Mamand D. M., Rasul H. H., Omer P. K., Qadr H. M., 2022



1. Introduction

Organic semiconductors (OS) have been investigated as different to conventional inorganic semiconductors by their low cost and ease of manufacture. Applications envisioned for OS include thin film (TF) transistors, light-emitting diodes (LED), solar cells (SC), and photo-refractive devices. Small molecular of the weight solution-processable materials that can be cast into high-performance conductive that TF has special technical significance [1–6]. Organic TF transistors formed on pentacene or oligothiophenes have reached device performance with mobilities in the range of $0.1–1 \text{ cm}^2 \text{ V}^{-1} \text{ s}^{-1}$ with large on/ off current ratios [1]. The most important material properties for the semiconductors to create thin film (TF) are high mobility, low “off” conductivity, stability and processability [7, 8].

Anthradithiophene (ADTs) showed better stability than pentacene and was lower than the experimental value by nearly 0.6 eV. The IP of ADT is calculated to be 6.15 eV and the ADT has small reorganization energy of 0.094 eV is equivalent to pentacene [9-17]. Slight chemical modifications of the side groups of both ADT and pentacene derivatives bring about considerable variations in molecular packing which affects electronic and optical properties (OP) of TF [1]. Its single crystal, alerted by H. Katz et al., which have become a common core in both small-molecule semiconductor and polymeric systems [7]. ADTs have produced materials with hole-mobility extracted from field-effect transistor

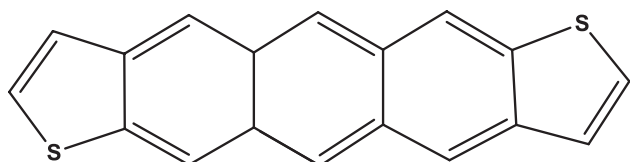


Fig. 1. Chemical structure of ADT organic semiconductor

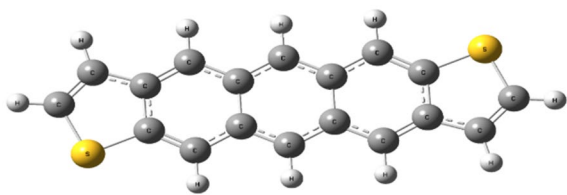


Fig. 2. Optimized ADT organic semiconductor

(FET) devices on the order of $0.1 \text{ cm}^2 \text{ V}^{-1} \text{ s}^{-1}$ [12, 13], but EFT exposed differences mobilities of $0.12 \text{ cm}^2 \text{ V}^{-1} \text{ s}^{-1}$ for anti-ADT [8]. The hole mobility in ADT single crystals nearly increases with decreasing temperature following a power law ($\mu \propto T^{-n}$) [13, 14].

O. Kwon et al. have studied ADT, the intrinsic electronic structure, the relevant intermolecular interaction, and the intramolecular vibrational modes which are very comparable to those in pentacene [15]. Also, they indicated that the first ionization of Anthra [2, 3-b: 6, 7-b'] dithiophene has an energy of vertical is around 6.6996 eV and the anti-ADT is more stable than the syn-ADT by nearly 0.02 kcal/mole. The angular ADT molecules have the low-lying HOMO level (-4.81 eV), also LUMO level is calculated to be -2.02 eV , the band-gap energy is estimated to be 2.79 eV . The ADT indicates great oxidation stability in organic field-effect transistors (OFET) devices due to the low-lying HOMO level and the implementations of OFETs [16].

Some researchers used the ADT-donor unit and aforesaid acceptor units to synthesize corresponding copolymers to explore their photovoltaic performance. ADT was manufactured as reported earlier. Thin (ten micrometres) sized platelets of ADT single crystals were grown from the vapour phase in a stream of gas [7]. J. Schön et al. [15] have been reported that the properties of the ADT is a small organic molecule and charge transport dependence of temperature, in the layered p-type, the mobility for in-plane transport displays an inverse power law temperature. The ADT was initially synthesized as a mixture of anti-isomer and syn-isomer due to complications with isomer departure [13].

This paper investigates optoelectronic properties in high-quality Anthradithiophene organic material, the chemical structure shown in Fig. 1. Moreover, the influence of molecular structure and energy reflectivity, dielectric constant and bandgap are important for this study.

2. Computational procedures

In performing the theoretical calculations, Gaussian 09 program was used [19]. In the investigation of molecule structure and quantum chemical computational calculations, many

software is possible in the literature depending on the purpose of the work, the optimized molecule structure is shown in Fig. 2. In this study, to explain the theoretical optical properties and structure of the molecule, the electrostatic potential map and UV-visible was used. The first optimized the molecule structure in the various basis set for comparison between them. Based on DFT, the HOMO has the highest occupied molecular orbital and LUMO has the lowest unoccupied molecular orbital which is calculated in various basis sets. According to bandgap energy, the comparison between theoretical and experimental results was performed. The UV-visible spectroscopy, HOMO and LUMO and electrostatic potential map calculations associated with Hartree-Fock and density functional theory were performed to compare the results, according to various basis sets such as Split-Valence Basis Sets (SVBSs) 6-31G and 6-311G. In addition, the single first polarization function is 6-311++ (d,p), the basis set 3-21G has polarization functions on second-row atoms only, and LANL2DZ (Los Alamos National Laboratory 2 double ξ) basis set represents the transition metals electrons.

2.1. Theoretical calculation of ADT molecule properties

This study obtained several properties of the ADT molecule based on the DFT and HF approximations of different basis sets. There are two important parameters which are HOMO and LUMO energy. HOMO is the highest energy-filled molecular orbital, but LUMO is the lowest energy empty molecular orbital. The tendency of molecules to give electrons or to receive electrons can be decided based on Lewis bases. For instance, HOMO means a high-energy molecule in water that has a high tendency to give out electrons, and LUMO means a high-energy molecule in water that has a high tendency to receive electrons [20].

The ionization energy can calculate based on HOMO energy. Thus, the energy was required to break an electron out of a chemical species in the gas phase or the isolated state. Theoretically, using Kopman's theorem, can interpret and estimate the ionization energies of the chemical species which are the energy required to break an electron from HOMO [21, 22]:

$$I = -E_{\text{HOMO}}. \quad (1)$$

In the gas phase or isolated state, the energy change in an electron uptake reaction of a chemical species indicates the electron affinity. The LUMO energy is related to electron affinity considering the electron to be received which will enter the lowest-energy free orbital in a basic type. According to Koopmans theory can calculate the electron affinity A , as the following equation:

$$A = -E_{\text{LUMO}}. \quad (2)$$

The difference between the HOMO and LUMO indicates the bandgap energy and can be expressed as the following:

$$\Delta E = E_{\text{LUMO}} - E_{\text{HOMO}}. \quad (3)$$

The HOMO and LUMO of molecules describe the strong ionic and covalent interaction. A strong covalent chemical interaction is expected between molecules which energy gap is close to each other. Based on the energy gap, some physical and chemical properties of the particles can be determined such as the nonlinear properties and spaced low energy particles which predict to exhibit nonlinear optical properties and exhibit photoconductivity.

Electronegativity, hardness and softness are very significant parameters to investigate the electronic properties of molecular, finite study have been performed on corrosion inhibition efficiency based on these parameters. A soft molecule refers to large and high polarized chemical species, but a hard molecule refers to small and low polarized species:

$$\eta = \frac{I - A}{2}, \quad (4)$$

$$\sigma = \frac{1}{\eta}, \quad (5)$$

where η is the hardness and σ is the softness. Based on DFT, the relationships between ionization energy and electron affinity can calculate the absolute electronegativity or Mulliken electronegativity which is the arithmetic mean of the ionization energy and electron affinity of the species. The power of a molecule to accept and donate the electron depend on the electronegativity of the molecule. More powerful electron acceptors or electrophiles indicates the molecule

which has a high electronegativity. Lower electronegativity indicates the power of the molecule to electron donors or nucleophiles:

$$\chi = \frac{A + I}{2}. \quad (6)$$

Molar Gibbs free energy and Gibbs free energy for a pure substance can be described by chemical potential. When the Gibbs free energy is low, the activity of the substance will be small. The following expression can calculate the chemical potential:

$$CP = -\chi. \quad (7)$$

Electrophilicity index ω is another significant molecule property and is a measure of energy reduction due to the maximum electron flow between the transceiver, based on the following equation:

$$\omega = \frac{(CP)^2}{2\eta}. \quad (8)$$

Electrophilicity index affects the amount of electron flux which species with a high electrophilicity index. According to the definition of the electrophilicity index, species with a high electrophilicity index have more electron flux if they are involved in a transponder interaction and lower the energy more because of this

electron flux. The results of the HF approximation calculations have no similarity or approximation with experimental results associated with different solvents as shown in Table 1. The DFT results are close agreement with experimental results as shown in Table 2. The results of the DFT can rely on explanation and investigation of the chemical property of ADT molecules because the bandgap energy difference between them is no more than 1.3 eV, especially in CHF solvent. Both HF and DFT methods are used to solve the quantum states of multi-electron systems such as molecules and crystals, each of them based on the Born–Oppenheimer approximation. The lack of the results of ADT molecule calculations in these basis sets because of the Hartree-Fock method assumes that the many-electron wave function takes the form of a determinant of single-electron wave functions which is called a Slater determinant. The problem with this assumption has a problem to express a single determinant and is that a general many-electron wavefunction cannot be expressed as a single determinant. According to HF approximation, the resulting energies as calculated tend to be too high, and the disadvantaged in Hartree-Fock methods do not fully incorporate electronic correlation. The configuration reaction in this method requires finding a complete basis for the single-electron

Table 1. Quantum chemical calculation of several properties in different basis sets for ADT molecule according to HF

Basis set	HOMO	LUMO	<i>I</i>	<i>A</i>	ΔE	η	σ	χ	<i>CP</i>	<i>W</i>	μ
6-21G	-6.85	1.16	6.85	-1.16	8.01	4.005	0.249	2.845	-2.84	1.01	0.989
6-31G	-6.697	1.184	6.697	-1.18	7.881	3.94	0.253	2.756	-2.75	0.96	1.03
6-31G (d, p)	-6.503	1.33	6.503	-1.33	7.833	3.91	0.255	2.586	-2.58	0.85	1.17
6-311G	-6.825	1.015	6.825	-1.01	7.84	3.92	0.255	2.905	-2.90	1.07	0.92
LanL2DZ	-6.827	0.893	6.827	-0.89	7.72	3.86	0.259	2.967	-2.96	1.14	0.87
SDD	-6.817	0.915	6.817	-0.91	7.73	3.86	0.25	2.95	-2.95	1.12	0.88

Table 2. Quantum chemical calculation of several properties in different basis sets for ADT molecule according to DFT

Basis set	HOMO	LUMO	<i>I</i>	<i>A</i>	ΔE	η	σ	χ	<i>CP</i>	<i>W</i>	μ
6-21G	-2.103	-0.672	2.10	0.67	1.43	0.71	1.39	1.38	-1.38	1.345	0.743
6-31G	-4.969	-2.067	4.96	2.06	2.90	1.45	0.68	3.51	-3.51	4.264	0.234
6-31G (d, p)	-4.809	-2.024	4.80	2.02	2.78	1.39	0.71	3.41	-3.41	4.191	0.238
6-311G	-5.189	-2.299	5.18	2.29	2.89	1.44	0.69	3.74	-3.74	4.85	0.206
LanL2DZ	-5.113	-2.284	5.11	2.28	2.829	1.414	0.70	3.69	-3.69	4.835	0.206
SDD	-5.095	-2.271	5.09	2.27	2.824	1.412	0.708	3.68	-3.68	4.803	0.208

wave functions. Then for these wave functions, the exact wave function of many electrons can be expressed as a linear set of all possible determinants. In the density functional theory (DFT), the wave function of many electrons is passed exactly in favour of the electron density associated with the Hohenberg-Kohn Theorems [21, 22]. The DFT mechanism for the total energy related to the ground state energy of the system is uniquely dependent on the electron density and total energy being a function of the electron density. Thus, regarding the electron density, to minimize energy, one can implement the anisotropy principle. It can not know what the energy function is, which is the problem of the DFT method. Keeping track of the spatial and spin coordinates of all N electrons requires in HF calculations. But according to DFT calculations, DFT offers the potential advantage of trading with only a single function of a single spatial coordinate. During this purpose, the applicant of DFT has been regularly growing in prevalence. Fig. 3 shows the visualization of HOMO and LUMO for ADT $C_{18}H_{10}S_2$.

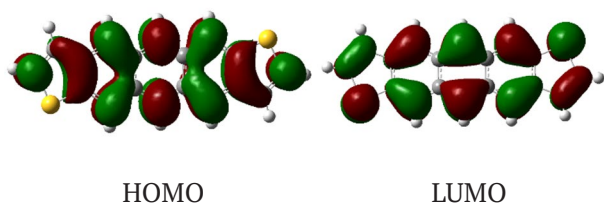


Fig. 3. The HOMO and LUMO of ADT $C_{18}H_{10}S_2$

3. The FTIR studies of the ADT organic semiconductor for different solvents

The harmonic vibrational frequency of the ADT semiconductor for different basis sets have been calculated based on the HF and DFT. In this study to investigate in depth the functional groups of the molecule, vibrational band assignments were generated using Gauss-View molecular visualization software and compared with the experimental results. Fig. 4 a and b show the correspondence between the theoretical and experimental calculations. The chemical structure of ADT is anthracene which is isoelectronic to pentacene, with five linearly-bonded aromatic rings from C = C-C in benzene rings and C-H ring which is related to vibrations. The presence of one or more aromatic rings in a structure is usually readily determined. The ADT molecular has four bounds as carbon-carbon single bond (C-C), carbon-carbon double bond (C=C), carbon-hydrogen bond (C-H) and carbon-sulfur single bond (C-S) as shown in Table 3. The advantage domain in infrared absorption is to determine the functional groups. There are two types, in which vibrations can take place, for example, bending and stretching. The bending is much lesser for the same bond since there is less resistance.

Fig. 4 b shows the FT-IR spectra of the ADT molecule for dichloromethane (DCM), chloroform (CHF) and Dimethylacetamide (DMAC) solvents. The FT-IR spectrum of the bands at about 2355 cm^{-1} for these solvents gives a strong peak

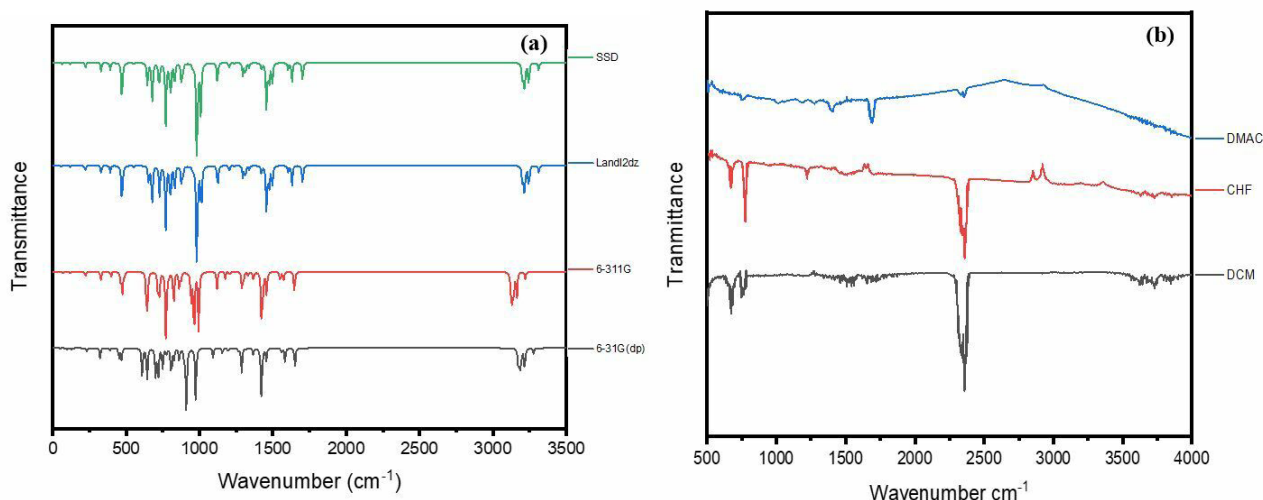


Fig. 4. FTIR absorbance spectra of the ADT organic semiconductor for CHF, DCM and DMAC solvent: (a) Theoretical, (b) Experimental

Table. 3. Characteristic IR absorption frequencies of organic functional groups

Groups	Absorption (cm ⁻¹)	Groups	Absorption (cm ⁻¹)
C=C Bending	1700–1500	C-H Bending	1650–2000
C=C Stretched	1400–1600	C-S Stretch	690–685
C-C Stretch in ring	1585–1600	C-H Bending out of the plane	900–675
C-H Stretch	3000–3300	C-H Bending weak overtone	1650–2000

which shows the strong C-H stretching. The IR spectrum band at 1693 cm⁻¹ for DMAC solvent corresponds to hydrogen bonding. The IR spectrum band at 1402 cm⁻¹ for DMAC solvent shows the δ C-H₃. The IR spectrum band at 1219 cm⁻¹ for CHF solvent indicates the CH₂ and CH₃ groups. The IR spectrum band at 772 cm⁻¹ for CHF solvent indicates the strong C-C stretching. The IR spectrum band at about 750 cm⁻¹ for CHF and DCM solvents shows the C-H bending. The IR spectrum band at about 668 cm⁻¹ for CHF and DCM solvents shows the C-S stretching.

3.1. UV-visible spectra

Organic semiconductor materials have a wide range of applications and owe their semiconducting properties to the presence of conjugated double bonds in their molecular structure. The hybridization of carbon atoms is sp^2 of conjugated double bonds and causes a rise in π and σ bonds. The energy levels consist of two split regions which have the lower energy level as the highest occupied molecular orbital (HOMO) and the higher energy level as the lowest unoccupied molecular orbital (LUMO) [25–27]. Because of some significant properties, the organic dyes have attracted attention as novel materials in high-density optical data recording media due to their low heat conduction, diversity of optical characteristics and chemical stability. The broad and narrow bandgap energy of the semiconductor are a significant characteristic of fabrication devices. Controlling the particle size and the overall photoactivity can greatly expand the hybrid semiconductor system causing the optical absorbance of narrow-band semiconductors which can incrementally tune to the absorption in the visible region [28].

The bandgap energy of Anthra [2, 3-b: 6, 7-b'] Dithiophene (ADT) molecule calculated is associated with the UV-visible spectrum as

shown in Fig. 5a and b for DCM, CHF and DMAC solvents. They investigate the UV-Vis spectra of the ADT molecule for the solvents of DCM, CHF, and DMAC. Absorbance is important for optoelectronic applications. The ADT molecule exhibits the maximum peaks at 296, 297 and 295 nm, respectively. As can be seen from the relevant curves, the ADT molecule dissolved in the DCM solution shows the largest and most stable spectrum. The ADT molecule is much more dominant in the near-ultraviolet region. The bandgap energy of the ADT molecule for CHF solvent is 4.92, 4.17 eV, whereas it is observed 4.9 and 4.18 eV for DCM, and DMAC is 4.2 and 4.59 eV. In the calculation concerning each maximum absorption, the bandgap energies are very close.

The crucial properties of semiconductor material are the absorption of light. There are two terms of absorption coefficient α and $h\nu$ exhibits light absorption. From the following expression can calculate the forbidden bandwidth of optical transitions or optical bandgap of semiconductors E_g [27]:

$$\alpha = \frac{2 \cdot 303A}{L} \quad (9)$$

$$k = \frac{\alpha\lambda}{4\pi} \quad (10)$$

Where α is absorption coefficient, A is absorbance, L is thickness (1 cm in my case).

$$(\alpha h\nu) = A^* (h\nu - E_g)^m \quad (11)$$

Here, A^* is a constant and m is the parameter related to the measuring type of band gaps. The crystal momentum conservation and energy conservation for any transition to take place have to be satisfied. The bandgap of a semiconductor includes two types which direct and indirect bandgap in semiconductor physics. In the valence band maximal-energy state and the

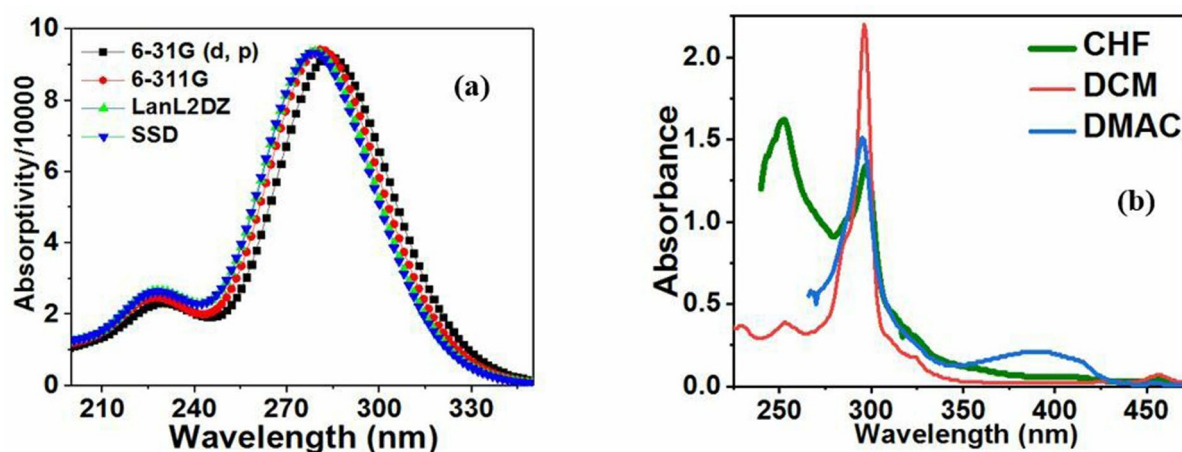


Fig. 5. UV-visible spectra of ADT molecule: (a) Theoretical in the various basis set and (b) experimental in different solvent

Table 4. Maximum absorption and bandgap energy of ADT in various solvents with the comparison between experimental and theoretical

Experimental	DCM		CHF		DMAC			
λ_{max} , nm	253	296	252	297	265	295		
E_g , eV)	4.92	4.17	4.9	4.18	4.2	4.59		
Theoretical	631G (d. P)		6311G		LanL2DZ		SSD	
λ_{max} , nm	228	284	226.5	280	226	277	228	277.6
E_g , eV)	5.44	4.37	5.48	4.43	5.49	4.49	4.30	4.47

conduction band, the minimal energy state in the Brillouin zone is characteristically identified by a certain crystal momentum. If the crystal momentum of electrons and holes are different in both the conduction band and the valence band which are called the indirect bandgap. The electron momentum of the top of the valence band and the bottom of the conduction band is not always the same. The top of the valence band and the bottom of the bandgap in a direct bandgap semiconductor have the same momentum value. By the comparison between the UV-visible bandgap energy and the Tauc plot, the method obtained the type of bandgap energy of ADT compound is indirect. The value of m is dependent on the type of semiconductor bandgap energy and include four various value which is $3/2$ for forbidden transition, 3 for forbidden indirect transition, 2 for allowing indirect transition.

Fig. 6 shows Tauc plot of ADT molecule for three different solvents. The allowed direct bandgap was obtained from the linear region. The optical band gap E_g value for all solvents is 4.058

and 4.07 eV. For CHF solvent, E_g has the same value, but for DAMC E_g is 4.07 eV. The E_g of semiconductor material is significant to operate the solar cells at this range because the devices can operate at high voltage and temperature. The change of solvents from DAMC to ADT as illustrated in Figures 5 and 6, enables more electrons to enter the conduction band by longer photon wavelengths. When the absorbance increased, the allows more electrons to be conduction band consequently increasing the efficiency of devices.

3.2. Refractive index

In recent decades, the application of semiconductor materials has been attracted to optical designers due to their use in the fabrication of electronic, optoelectronic and optoelectronic properties such as photodetectors (PD), heterogeneous lasers, light-emitting diodes (LEDs), and photonic modulators that operate in regions of Mid-infrared (2–5 μm) and integrated circuits. The refractive index and bandgap energy are two main important properties of semiconductor ma-

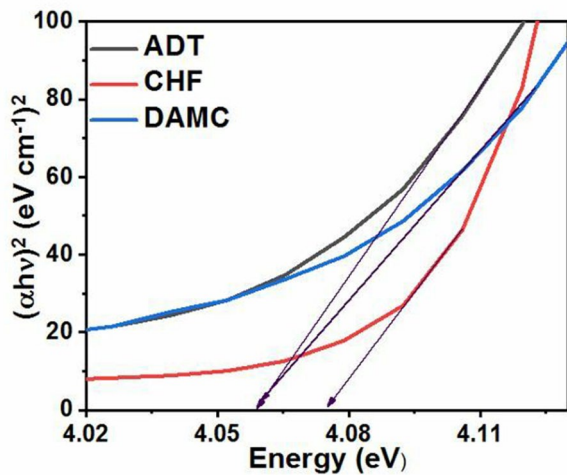


Fig. 6. Tauc plot of ADT molecule for various solvent

materials, and the fundamental properties can decide on these two properties [30, 31]. The refractive index is related to the structure of materials and is a measure of transparency to the incident photon. The threshold of photon absorption of a semiconductor determines the energy gap.

The following equation can calculate the refractive index. Fig. 7 shows that the refractive index decreased with increased bandgap energy. The refractive index of ADT molecule in DMAC solvent has the highest value at the lowest E_g after 2.55 eV decreased up to 2.67 eV and interpreted the ADT solvent line of refractive index. Fig. 8 illustrates the effect of solvent in the refractive index of the ADT material. The refractive index of ADT for DMAC solvent at low E_g differs from other solvents, but after 2.67 eV is similar to another solvent:

$$n = \left\{ \left[\frac{4R}{(R-1)^2} - k^2 \right]^{\frac{1}{2}} - \frac{R+1}{R-1} \right\}. \tag{12}$$

The refractive index of semiconductor material can determine by using many relations such as Ravindra, Moss, Kumar and Singh, Herve and Vandame. These relations depend on bandgap energy, and these relations are extensively used to determine the n of semiconductors [32]:

Reddy relation:

$$n^4 (E_g - 0.365) = 154. \tag{13}$$

Moss relationship:

$$n^4 E_g = 95 \text{ eV}. \tag{14}$$

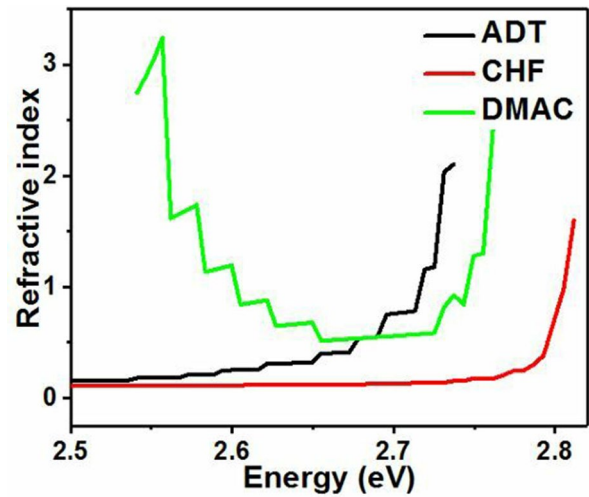


Fig. 7. Refractive index against energy bandgap of ADT molecule in various solvent

Kumar and Singh relation:

$$n = KE_g^c. \tag{15}$$

Where K and C are constants and K is 3.3668 and C is -0.32234 .

Herve-Vandamme relationship:

$$n^2 = 1 + \left(\frac{A}{E_g + B} \right)^2. \tag{16}$$

Ravindra relationship:

$$n = 4.084 - 0.62E_g. \tag{17}$$

3.3. Transmittance

The optical transmission spectra for ADT of different solvents are shown in Fig. 9. The transmission spectra at low E_g is high and depends on the type of solvent. The solvent DCM and DMAC at the lowest level have the highest transmission. But for the CHF solvent, the light transmission in the UV visible range is low, compared to other solvents.

The transparent material has poor electrical conductivity and high reflectivity. The ADT molecule at the 3.75 eV for all solvents exhibits the lowest transparency and highest reflectivity. Generally, the transmittance gradually decreases by increasing bandgap energy.

3.4. Normal dispersion region

For investigating the physical properties of materials such as light bending and how light bends at each specific wavelength, should consider the dispersion parameter. Designers

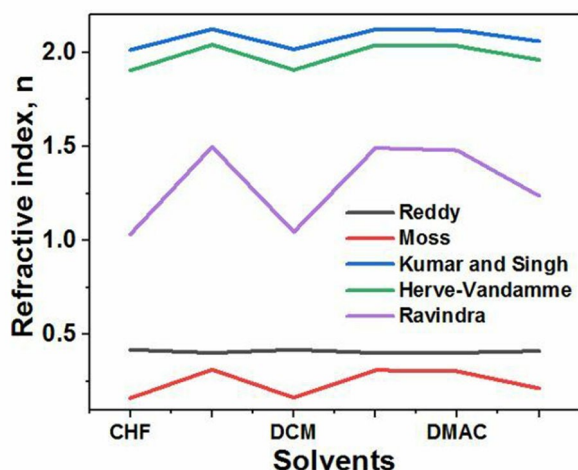


Fig. 8. The refractive index plots of the ADT semiconductor for the various solvents

make materials into optical pigments, and the scattering area is an important property. The scattering area depends on the refractive index of the material. When the angular frequency increases, the refractive index can fluctuate and then increase the scattering area.

In the construction of optical instruments, material dispersion can be a desirable or undesirable effect in optical applications. Allowing more accurate discrimination of wavelengths when using light scattering by glass prisms to create spectroradiometers, spectrometers and stereo grids. The frequency change with the refractive index is called dispersion. The refractive of light decreases at a lower frequency. The angular frequency band of ADT in the CHF solvent has the highest band, and the normal scattering area is 5.6 PHz. In the DMAC solvent, the frequency range is the lowest, and the scattering region is 4.51 PHz. The normal scattering region is 5.4 PHz for ADT molecule in DMAC solvent as shown in Fig. 10.

3.5. Reflectivity and reflection loss

The optical response of the surface of a material can be estimated using the reflectivity coefficient. Reflectivity coefficient is the ratio of the reflected power to the incident power which is important for the optical properties of materials. The relation between the extinction coefficient and refractive index can calculate the reflectivity as the following expression [33, 34].

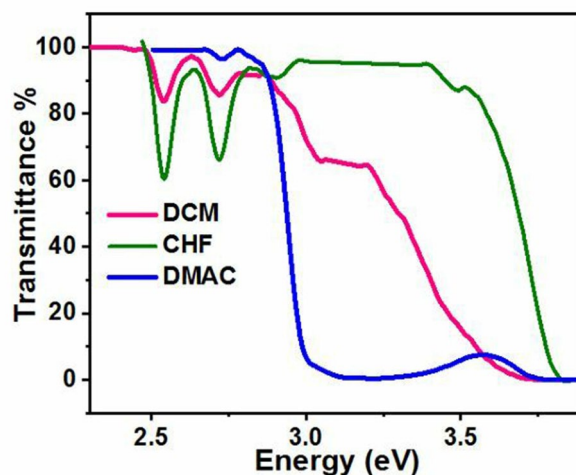


Fig. 9. Eg against transmittance of ADT semiconductor for various solvents

$$R = \frac{(n-1)^2 + k^2}{(n+1)^2 + k^2}, \quad (18)$$

where k is the frequency-dependent extinction coefficient calculated from equation (10), for a weak absorber k can be considered too small and at the high frequency it vanishes. The following expression can calculate the reflectivity at a higher frequency:

$$R = \left(\frac{n-1}{n+1} \right)^2, \quad (19)$$

where n is a refractive index, obtained in equation (12).

The relation between reflectivity and reflection coefficient can determine the reflection coefficient according to the following equation:

$$r = \sqrt{R}. \quad (20)$$

The absorption technique is a significant property, because of the relation between electrical and optical properties through the conductivity tensor. Good electrical conductor material indicates a high reflection, but the transparent materials are expected reasonably poor electrical conductivity. The reflectivity of the ADT molecule associated with the UV visible spectra is well-matched with each other, since the reflectivity ratio depends on the bandgap energy, a large bandgap indicates low reflectance, while a small bandgap indicates high reflectivity as shown in Fig. 11.

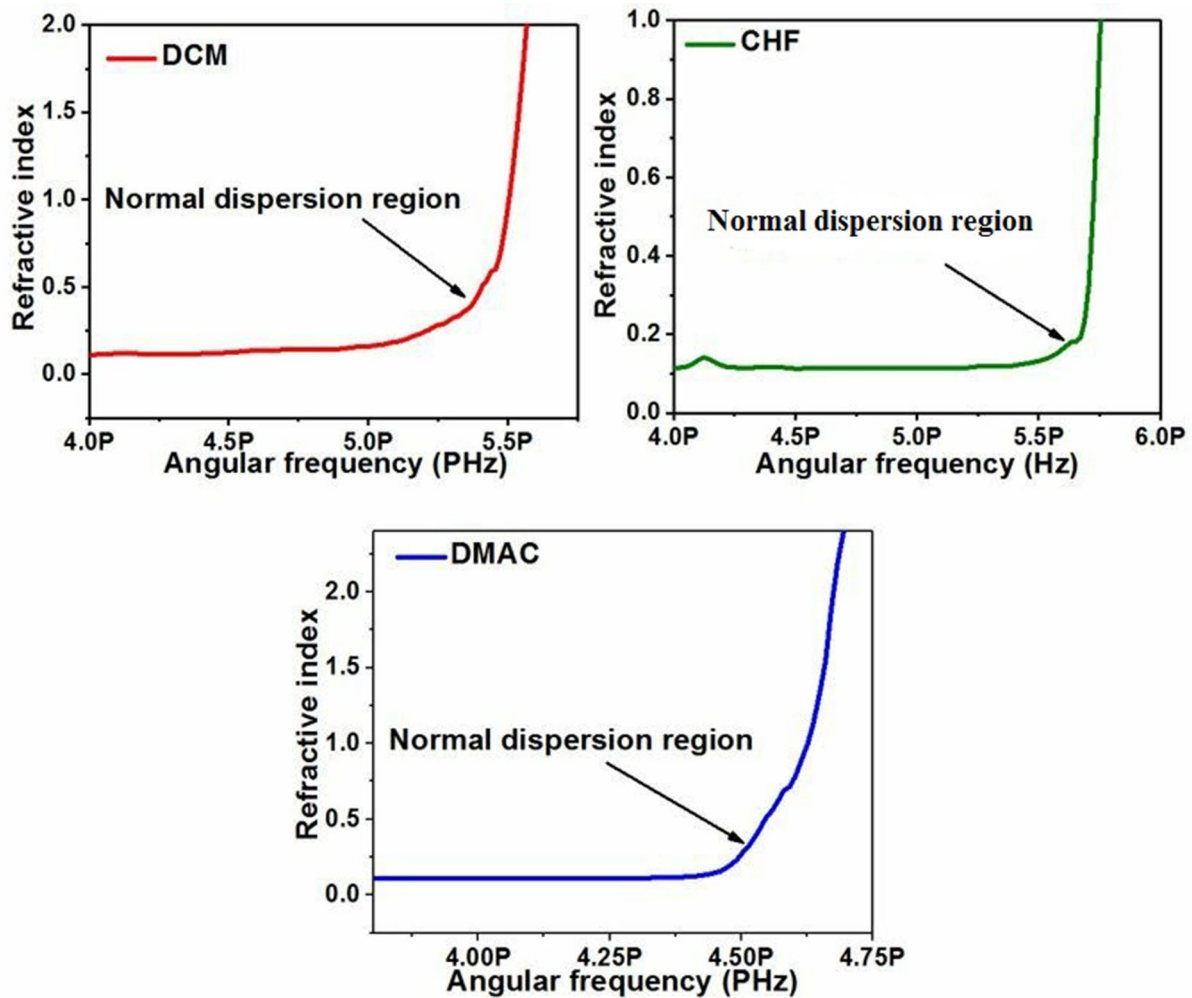


Fig. 10. Normal dispersion region calculation and plot the angular frequency against refractive index of ADT molecule

3.6. Reflection loss and transmission coefficient

The reflection loss and transmission coefficient in telecommunication are the principal characteristics. From the following equations can calculate each of them and the express presents the correlation between the reflection loss and transmission coefficient as shown in Fig. 12. It can be shown that a partial inverse proportionality between the two quantities [34, 35]:

$$R_L = \left[\frac{n-1}{n+1} \right]^2. \tag{21}$$

$$T = \frac{2n}{n^2 + 1}. \tag{22}$$

For estimates of how much of an electromagnetic wave (light) passes through

a surface or an optical element can use the transmission coefficient in the optics field. Using the transmission coefficient, the amplitude and intensity of the wave can be measured. The chemistry field can describe the transmission coefficient to a chemical reaction overcoming a potential barrier [36].

4. Electrical and optical conductivity

There are two important parameters to decide on electrical and optical behaviour which are electrical and optical conductivity based on the following parameters [36].

$$\sigma_{opt} = \frac{\alpha n c}{4\pi}. \tag{23}$$

$$\sigma_{ele} = \frac{2\lambda \sigma_{opt}}{\alpha}. \tag{24}$$

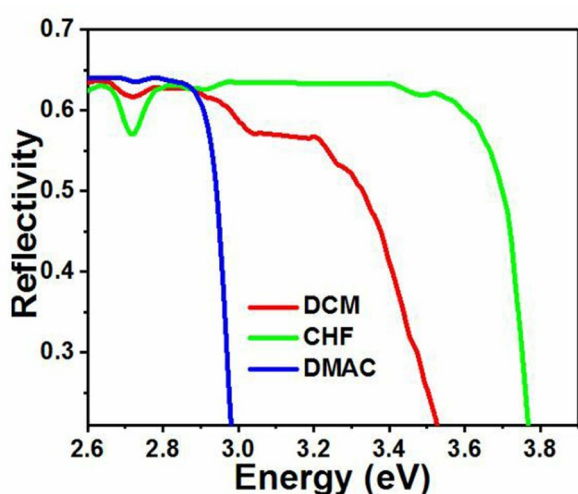


Fig. 11. Reflectivity relation of ADT molecule with energy gap in various solvent

By considering the electronic structure of materials, due to free electrons in the conduction band, the electrical conductivity of materials and semiconductor optical conductivity are the change in conductivity induced by illumination, both a decrease or an increase.

The Drude model explained the electrical conductivity of materials, and the band theory plays a significant role in explaining the concept of conductivity. The conduction band get more free electrons when the valence band and conduction band overlapped. The resistivity possesses in the material, and the scattering mechanism describes the process, and the excited electrons from the valence band to the conduction band are responsible for conduction. The dielectric constant of a material is related in this process to allowing light to propagate through the material. In the case of optical propagation, the relaxation time and plasma frequency are important [37]. Two physical quantities are playing an important role because when light energy as a photon hits the surface of the material, it drives the electron. If there is no scattering, the light gets reflected totally, and hence metals are shiny. This part is associated with the material colour.

The electrical conductance of the ADT molecule differs in various solvents. The electrical conductivity in the range 2.87 to 3.4 eV have the highest value which indicates the ADT molecule easily allows electric current to flow through it for DMAC solvent, and inversely. Electrical resistivity measures how strongly a material

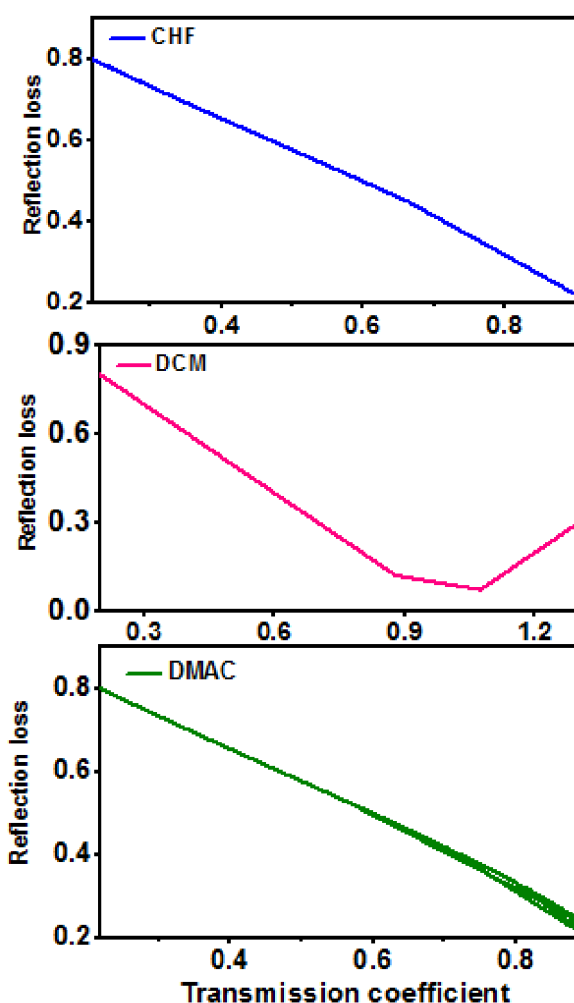


Fig. 12. Transmission coefficients against reflection loss of ADT molecule for different solvents

resists the flow of electric current. In the CHF solvent, the electrical conductivity is the lowest at 3.78 V and then has risen slightly. At the small bandgap energy, the ADT molecule in CHF solvent is not allowed the electric current to through it. Generally, the electrical conductance for each solvent rises after 3.6 eV which indicates the ADT molecule and has a wide range of bandgap energy. The type of solvent is very significant to the optoelectronic and electrical properties of molecules. The optical conductance has lower than the electrical conductance of the ADT molecule, as shown in figure 13b. The electrical and optical conductance have more similarity based on Figures 13 a and b. It can be clearly seen that energy increases and then decreases, after that both are the same according to the bandgap energy of various solvents. The

optical conductivity at the high energy gap has a high value, and the lines are more increased compared with electrical conductance. The wide bandgap and increasing optical conductance at 3.6 eV indicates the ADT molecule which has a wide bandgap and is very useful to fabrication for materials operating at high voltage and temperature such as solar cells. The increase of σ_{real} and σ_{optical} can be attributed to an increase in the absorption coefficient in this region. Whereas, a decrease of σ_{real} value after the second peak can be attributed to a decrease in the absorption coefficient within this energy region. These two peaks of the ADT molecule in DMAC in the σ_{real} show areas of deeper penetration for electromagnetic waves, and they also show high conductivity. When the photons are at these peak energy values, the high conductivity can be optimized.

4.1. Dielectric constant

For investigation about the conduction properties of materials, the dielectric constant is a significant parameter. The usage of the film for photovoltaic applications depends on the electrical properties of the materials which are a great importance in determining the usage. The various growth parameters related to the electrical properties such as rate of deposition and substrate temperature [38]. The two parameters ϵ' and ϵ'' represent the real part dielectric constant and imaginary part (dielectric loss), respectively. The complex dielectric constant can calculate from the following expression:

$$\epsilon^* = \epsilon' + j\epsilon'' \tag{25}$$

where ϵ' is represent the real part of dielectric constant, ϵ'' is represent the dielectric loss and the complex dielectric constant is ϵ^* . The dielectric spectroscopy of materials is very important because it is related to many parameters such as grain boundary, grain and insights into the structure of compounds, transport properties and charge storage capabilities of dielectric material. At the grain boundaries, potential barrier generates in the thin films or solids which cause the increase of dielectric constant with increasing frequency and is related to the presence of space charge polarization [39, 40].

The polarization concepts of ADT molecules in various solvents can rely on the relation between the dielectric loss and permittivity modalities because polarization depends on the electric field under the condition. If the relaxation time of the electric field applied and frequency is the same which indicates the occurring phase lag. On the other hand, when the frequency is slower than the relaxation of the electric field, polarization occurs. Depolarization does not occur when the relaxation time is lower than the frequency of the electric field. Fig. 14 shows the frequency variation with the real and imaginary part of the dielectric constant of ADT for different solvents.

4.2. Electrostatic potential map

This section describes a map that is called an electrostatic potential map (often called a potential map). It explains information about atomic charges which can suggest advantages of EPM [41]. The first is used for specifying the polar and nonpolar on the parts of the molecule. The second advantage can be used to compare

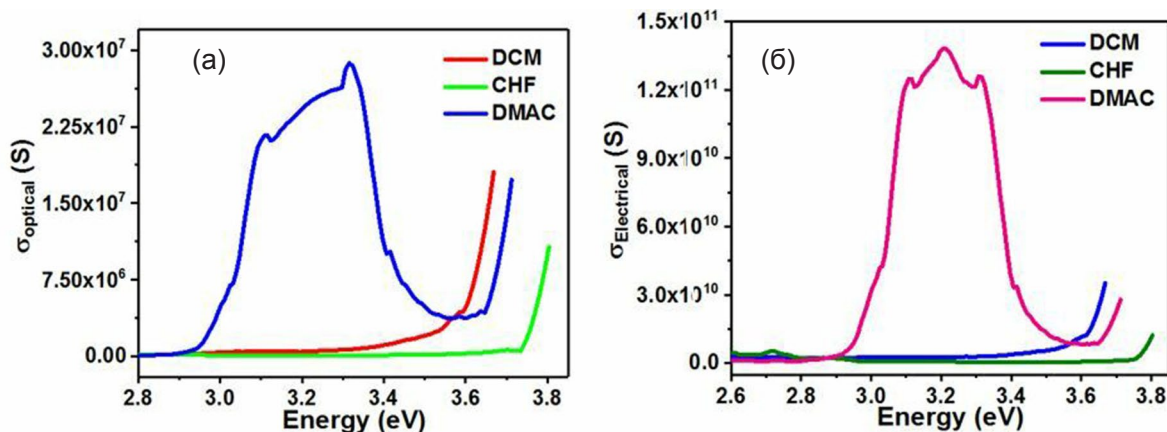


Fig. 13. Variation of optical (a) and electrical (b) conductivity of ADT molecule

the charges between one molecule with another to obtain information about the product of a chemical reaction. The third factor investigates the shape of the electron cloud of atoms and reveals an irregularity used to tell which region has the highest electron density or concentration and which area has the lowest electron density or depletion. The final advantage, according to this study is to determine which charge atoms repel or attract to the molecules. The interaction between molecules is similar to why molecules assemble and how polymer complexes are formed. These reactions are also related to a chemical reaction. The electrostatic potential map is the actual valuable three-dimensional chart of molecules. It is useful for explaining the charge distribution of charges on the surface of the molecule and investigating the properties of molecules. They permit the researcher to imagine the form and size of the molecule [42]. The electrostatic potential has very powerful for predicting the behaviour of complex molecules. Colour codes to identify charge distribution [43]. The default colour scale starts from the red area to the darker blue. The red colour tells us that the region has a higher electron density, which means that the electrostatic potential has decreased and is at its lowest. This means that the red area in Fig. 15 indicates the largest region of electronegativity. Moreover, the blue colour represents a small electronegativity. Associate with yellow and green, they have more electronegativity than blue, less than red. Yellow is more electronegative than

green. Recall that the area of lowest electrostatic potential corresponds to the region of greatest electron concentration. Around sulfur have more electronegativity comparing with another area. As well as, around of all hydrogens have less electronegativity compared with other regions. The sulfurs have the highest electronegativity value, and the hydrogens have the smallest electronegativity value. On the other hand, the sulfur would be affiliated with the red region of the EPM, and the hydrogen would be affiliated with the blue area. The sulfur has 6 valence electrons and is involved in forming chemical bonds with other elements, and hydrogen has one valence electron.

5. Conclusion

In this investigation, the optical and electrical properties of ADT molecule organic semiconductors for different solvents with theoretical and experimental methods were compared in detail. From the UV-visible spectroscopy calculated the optoelectronic properties such as bandgap energy, allowing indirect transition, refractive index, angular dispersion region, electrical and optical conductivity and dielectric properties in various solvents. The bandgap energy is condensed and determined in many ways to explain the optoelectronic properties. The experimental results in the various basis set are a good agreement with theoretical results. DFT and HF approximation are two significant theoretical methods. The calculations based on them were

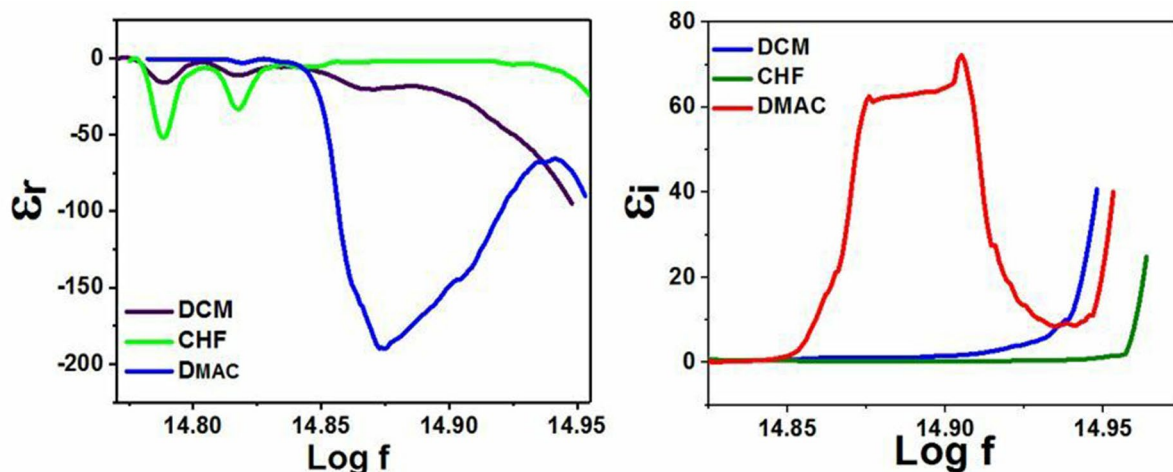


Fig. 14. Relation between the real and imaginary part of the dielectric constant of ADT molecule in three different solvents

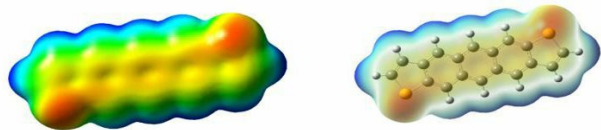


Fig. 15. The Potential Energy Surfaces (PES) of ADT molecule

performed and compared the results for the ADT molecule. The average band-gap energy between the HOMO and LUMO was found to be 2.84 eV by using five basis sets. As a result, based on DFT techniques along with B3LYP, some basis sets were utilized for optimizing the ADT. The result was shown that the electrostatic potential map (EPM) of ADT in the sulfurs have the highest electronegativity value and the hydrogens have the lowest electronegativity value. In this study, the advantages of ADT investigated optoelectronic characteristics of the ADT for various methods and conditions will provide to optoelectronic technologies due to interesting and significant results.

Author contributions

All authors made an equivalent contribution to the preparation of the publication.

Conflicts of interest:

The authors state that there is no conflict of interest in the printing of this manuscript.

References

1. Platt A. D., Day J., Subramanian S., Anthony J. E., Ostroverkhova O. 'Optical, fluorescent, and (photo) conductive properties of high-performance functionalized pentacene and anthradithiophene derivatives. *The Journal of Physical Chemistry C*. 2009;113(31): 14006–14014. <https://doi.org/10.1021/jp904021p>
2. Sekar A., Sivula K. Organic semiconductors as photoanodes for solar-driven photoelectrochemical fuel production. *CHIMIA International Journal for Chemistry*. 2021;75(3): 169–179. <https://doi.org/10.2533/chimia.2021.169>
3. Li H., Brédas J.-L. Developing molecular-level models for organic field-effect transistors. *National Science Review*. 2021;8(4): nwaal167. <https://doi.org/10.1093/nsr/nwaal167>
4. Rojas H. C., Bellani S., Fumagalli F., Tullii G., Leonardi S., Mayer M. T., Schreier M., Grätzel M., Lanzani G., Di Fonzo F. Polymer-based photocathodes with a solution-processable cuprous iodide anode layer and a polyethyleneimine protective coating. *Energy & Environmental Science*. 2016;9(12): 3710–3723. <https://doi.org/10.1039/c6ee01655c>
5. Qadr H. M. A molecular dynamics calculation to cascade damage processes. *The Annals of "Dunarea de Jos" University of Galati. Fascicle IX, Metallurgy and Materials Science*. 2020;43(4): 13–16. <https://doi.org/10.35219/mms.2020.4.02>
6. Qadr H. M. A molecular dynamics study of temperature dependence of the primary state of cascade damage processes. *Russian Journal of Non-Ferrous Metals*. 2021;62(5): 561–567. <https://doi.org/10.3103/s1067821221050096>
7. Laquindanum J. G., Katz H. E., Lovinger A. J. Synthesis, morphology, and field-effect mobility of anthradithiophenes. *Journal of the American Chemical Society*. 1998;120(4): 664–672. <https://doi.org/10.1021/ja9728381>
8. Zhu G., Sun Y., Li M., Tao C., Zhang X., Yang H., Guo L., Lin. Ionic crosslinked polymer as protective layer in electrochromic supercapacitors for improved electrochemical stability and ion transmission performance. *Electrochimica Acta*. 2021;365: 137373. <https://doi.org/10.1016/j.electacta.2020.137373>
9. Qadr H. M. Effect of ion irradiation on the mechanical properties of high and low copper. *Atom Indonesia*. 2020;46(1): 47–51. <https://doi.org/10.17146/aij.2020.923>
10. Mamada M., Minamiki T., Katagiri H., Tokito S. Synthesis, physical properties, and field-effect mobility of isomerically pure syn-/anti-anthradithiophene derivatives. *Organic Letters*. 2012;14(16): 4062–4065. <https://doi.org/10.1021/ol301626u>
11. Miao Q. (Ed.). *Polycyclic arenes and heteroarenes: synthesis, properties, and applications*. John Wiley & Sons; 2015. <https://doi.org/10.1002/9783527689545>
12. Brédas J.-L., Calbert J. P., da Silva Filho D. A., Cornil J. Organic semiconductors: A theoretical characterization of the basic parameters governing charge transport. *Proceedings of the National Academy of Sciences*. 2002;99(9): 5804–5809. <https://doi.org/10.1073/pnas.092143399>
13. Hallani R. K., Thorley K. J., Mei Y., Parkin S. R., Jurchescu O. D., Anthony J. E. Structural and electronic properties of crystalline, isomerically pure anthradithiophene derivatives. *Advanced Functional Materials*. 2016;26(14): 2341–2348. <https://doi.org/10.1002/adfm.201502440>
14. Mamada M., Katagiri H., Mizukami M., Honda K., Minamiki T., Teraoka R., Uemura T., Tokito S. Syn-/anti-anthradithiophene derivative isomer effects on semiconducting properties. *ACS Applied Materials & Interfaces*. 2013;5(19): 9670–9677. <https://doi.org/10.1021/am4027136>
15. Schön J., Kloc C., Siegrist T., Laquindanum J., Katz H. Charge transport in anthradithiophene single

crystals. *Organic Electronics*. 2001;2: 165–169. [https://doi.org/10.1016/s1566-1199\(01\)00022-2](https://doi.org/10.1016/s1566-1199(01)00022-2)

16. Qadr H. M. 'Pressure effects on stopping power of alpha particles in argon gas. *Physics of Particles and Nuclei Letters*. 2021;18(2): 185–189. <https://doi.org/10.1134/s1547477121020151>

17. Kwon O., Coropceanu V., Gruhn N., Durivage J., Laquindanum J., Katz H., Cornil J., Brédas J.-L. Characterization of the molecular parameters determining charge transport in anthradithiophene. *The Journal of Chemical Physics*. 2004;120(17): 8186–8194. <https://doi.org/10.1063/1.1689636>

18. Yang H., Locklin J., Singh B., Bao Z. Organic field-effect transistors with solution-processible thiophene/phenylene based-oligomer derivative films. *Organic Field-Effect Transistors VI, International Society for Optics and Photonics*. 2007: 66581A. <https://doi.org/10.1117/12.733953>

19. Caricato M., Frisch M. J., Hiscocks J., Frisch M. J. *Gaussian 09: IOps Reference, Citeseer*. 2009.

20. Qadr H. M., Mamand D. M. Molecular structure and density functional theory investigation corrosion inhibitors of some oxadiazoles. *Journal of Bio-and Tribo-Corrosion*. 2021;7(4): 1–8. <https://doi.org/10.1007/s40735-021-00566-9>

21. Mamand D. Determination of the band gap energy of poly benzimidazobenzophenanthroline and comparison between HF and DFT for three different basis sets. *Journal of Physical Chemistry and Functional Materials*. 2019;2(1): 32–36. Режим доступа: <https://dergipark.org.tr/en/pub/jphcfum/issue/45047/589803>

22. Mamand D. M., Qadr H. M. Comprehensive spectroscopic and optoelectronic properties of BBL organic semiconductor. *Protection of Metals and Physical Chemistry of Surfaces*. 2021;57(5): 943–953. <https://doi.org/10.1134/s207020512105018x>

23. Görling A. Density-functional theory beyond the Hohenberg-Kohn theorem. *Physical Review A*. 1999;59(5): 3359. <https://doi.org/10.1103/physreva.59.3359>

24. Gilbert T. L. Hohenberg-Kohn theorem for nonlocal external potentials. *Physical Review B*. 1975;12(6): 2111. <https://doi.org/10.1103/physrevb.12.2111>

25. Mamand D. Theoretical calculations and spectroscopic analysis of gaussian computational examination-NMR, FTIR, UV-Visible, MEP on 2, 4, 6-Nitrophenol. *Journal of Physical Chemistry and Functional Materials*. 2019;2(2): 77–86. Режим доступа: <https://dergipark.org.tr/en/pub/jphcfum/issue/50562/645745>

26. Iliev V., Tomova D., Rakovsky S., Eliyas A., Puma G. L. Enhancement of photocatalytic oxidation of oxalic acid by gold modified WO_3/TiO_2 photocatalysts under UV and visible light irradiation. *Journal of Molecular Catalysis A: Chemical*. 2010;327(1-2): 51–57. <https://doi.org/10.1016/j.molcata.2010.05.012>

27. Aceto M., Agostino A., Fenoglio G., Idone A., Gulmini M., Picollo M., Ricciardi P., Delaney J. K. Characterisation of colourants on illuminated manuscripts by portable fibre optic UV-visible-NIR reflectance spectrophotometry. *Analytical Methods*. 2014;6(5): 1488–1500. <https://doi.org/10.1039/c3ay41904e>

28. Wu J., Walukiewicz W., Shan W., Yu K., Ager W. J., Haller E. E., Lu H., Schaff W. J. Effects of the narrow band gap on the properties of InN. *Physical Review B*. 2002;66(20): 201403. <https://doi.org/10.1103/physrevb.66.201403>

29. Orek C., Gündüz B., Kaygılı O., Bulut N. Electronic, optical, and spectroscopic analysis of TBADN organic semiconductor: Experiment and theory. *Chemical Physics Letters*. 2017;678: 130–138. <https://doi.org/10.1016/j.cplett.2017.04.050>

30. Herve P., Vandamme L. K. J. General relation between refractive index and energy gap in semiconductors. *Infrared physics & technology*. 1994;35(4): 609–615. [https://doi.org/10.1016/1350-4495\(94\)90026-4](https://doi.org/10.1016/1350-4495(94)90026-4)

31. Hader J., Moloney J., Koch S. Microscopic theory of gain, absorption, and refractive index in semiconductor laser materials-influence of conduction-band nonparabolicity and coulomb-induced intersubband coupling. *IEEE Journal of Quantum Electronics*. 1999;35(12): 1878–1886. <https://doi.org/10.1109/3.806602>

32. Ravindra N., Ganapathy P., Choi J. Energy gap-refractive index relations in semiconductors—An overview. *Infrared Physics & Technology*. 2007;50(1): 21–29. <https://doi.org/10.1016/j.infrared.2006.04.001>

33. Linda D., Duclère J.-R., Hayakawa T., Dutreilh-Colas M., Cardinal T., Mirgorodsky A., Kabadou A., Thomas P. Optical properties of tellurite glasses elaborated within the $\text{TeO}_2\text{-Ti}_2\text{O-Ag}_2\text{O}$ and $\text{TeO}_2\text{-ZnO-Ag}_2\text{O}$ ternary systems. *Journal of Alloys and Compounds*. 2013;561: 151–160. <https://doi.org/10.1016/j.jallcom.2013.01.172>

34. Umar S., Halimah M., Chan K., Latif A. Polarizability, optical basicity and electric susceptibility of Er^{3+} doped silicate borotellurite glasses. *Journal of Non-Crystalline Solids*. 2017;471: 101–109. <https://doi.org/10.1016/j.jnoncrysol.2017.05.018>

35. Maheshvaran K., Linganna K., Marimuthu K. Composition dependent structural and optical properties of Sm^{3+} doped boro-tellurite glasses. *Journal of Luminescence*. 2011;131(12): 2746–2753. <https://doi.org/10.1016/j.jlumin.2011.06.047>

36. Yoshino K., Oyama S., Yoneta M. Structural, optical and electrical characterization of undoped ZnMgO film grown by spray pyrolysis method. *Journal of Materials Science: Materials in Electronics*. 2008;19(2): 203–209. <https://doi.org/10.1007/s10854-007-9333-2>

37. Jiménez-González A. E., Soto Urueta J. A., Suárez-Parra R. Optical and electrical characteristics

of aluminum-doped ZnO thin films prepared by solgel technique. *Journal of Crystal Growth*. 1998;192(3-4): 430–438. [https://doi.org/10.1016/s0022-0248\(98\)00422-9](https://doi.org/10.1016/s0022-0248(98)00422-9)

38. Sassi M., Oueslati A., Moutia N., Khirouni K., Gargouri M. A study of optical absorption and dielectric properties in lithium chromium diphosphate compound. *Ionics*. 2017;2394): 847–855. <https://doi.org/10.1007/s11581-016-1903-y>

39. Xie P., Wang Z., Zhang Z., Fan R., Cheng C., Liu H., Liu Y., Li T., Yan C., Wang N. Silica microsphere templated self-assembly of a three-dimensional carbon network with stable radio-frequency negative permittivity and low dielectric loss. *Journal of Materials Chemistry C*. 2018;6(19): 5239–5249. <https://doi.org/10.1039/c7tc05911f>

40. Yang K., Huang X., Huang Y., Xie L., Jiang P. Fluoro-polymer@ BaTiO₃ hybrid nanoparticles prepared via RAFT polymerization: toward ferroelectric polymer nanocomposites with high dielectric constant and low dielectric loss for energy storage application. *Chemistry of Materials*. 2013;25(11): 2327–2338. <https://doi.org/10.1021/cm4010486>

41. Leboeuf M., Köster A., Salahub D. Approximation of the molecular electrostatic potential in a gaussian density functional method. *Theoretical Chemistry Accounts*. 1997;96(1): 23–30. <https://doi.org/10.1007/s002140050199>

42. Ramalingam S., Babu P. D. S., Periandy S., Feyrduni E. Vibrational investigation, molecular orbital studies and molecular electrostatic potential map

analysis on 3-chlorobenzoic acid using hybrid computational calculations. *Spectrochimica Acta Part A: Molecular and Biomolecular Spectroscopy*. 2011;84(1): 210–220. <https://doi.org/10.1016/j.saa.2011.09.030>

43. Ramalingam S., Karabacak M., Periandy S., Puviarasan N., Tanuja D. Spectroscopic (infrared, Raman, UV and NMR) analysis, Gaussian hybrid computational investigation (MEP maps/HOMO and LUMO) on cyclohexanone oxime. *Spectrochimica Acta Part A: Molecular and Biomolecular Spectroscopy*. 2012;96: 207–220. <https://doi.org/10.1016/j.saa.2012.03.090>

Information about authors

Dyari Mustafa Mamand, MSc in Atomic and Molecular Physics, Department of Physics, University of Raparin, (Sulaymaniyah, Iraq).

<https://orcid.org/0000-0002-1215-7094>

dyari.mustafa@uor.edu.krd

Hazhar Hamad Rasul, MSc in Atomic and Molecular Physics, Department of Physics, University of Raparin, (Sulaymaniyah, Iraq).

hazharhrm@uor.edu.krd

Peshang Khdir Omer, MSc in Chemistry, Department of Chemistry, University of Raparin, (Sulaymaniyah, Iraq).

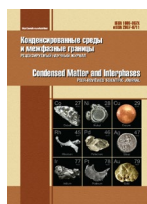
peshang.khdir@uor.edu.krd

Hiwa Mohammad Qadr, MSc in Physics, Lecture of the Department of Physics, University of Raparin, (Sulaymaniyah, Iraq).

<https://orcid.org/0000-0001-5585-3260>

hiwa.physics@uor.edu.krd

Received 10.01.2022; approved after reviewing 30.03.2022; accepted 15.05.2022; published online 25.06.2022.



Condensed Matter and Interphases

Kondensirovannye Sredy i Mezhfaznye Granitsy
<https://journals.vsu.ru/kcmf/>

Original articles

Research article

<https://doi.org/10.17308/kcmf.2022.24/9264>

Preparation and characterization of Ge-Ni-Te nanocomposite

Iman A. Mahdy¹ ✉, S. M. El Sheikh², Hosny A. Omar², P. V. Seredin³, Manal A. Mahdy⁴

¹Al-Azhar University, Physics Department, Faculty of Science (Girls),
Nasr City 11753, Cairo, Egypt

²School of Sciences and Engineering, Physics Department, American University in Cairo,
New Cairo 11835, Cairo, Egypt

³Voronezh State University, Physics Faculty,
1 Universitetskaya pl., Voronezh 394018, Russian Federation

⁴National Research Centre, Solid State Physics Department,
Dokki 12622, Giza, Egypt

Abstract

$\text{Ni}_x\text{Ge}_{50-x}\text{Te}_{50}$ with $x = 2, 4, 6, 8, 10, 15$ and 20 at% ternary nanocomposite prepared using multistage solid-state direct reaction. Nanocrystalline nature was studied by X-ray powder diffraction, results revealed that, the main phase is rhombohedral GeTe polymorph, and the second major phase is hexagonal Ni_3GeTe_2 . The calculated average crystallite size of the whole constituents in prepared samples is within the range of 47.3 – 83.8 nm. Optical properties evaluated from diffuse reflection measurements and the calculated bandgap of all samples are nonmonotonically changes with Ni content from 1.45 to 1.62 eV with the direct allowed transition.

Keywords: Ni-Ge-Te, Nanocomposite, Structural and optical properties, Diamagnetic

Funding: This work was supported by the American University in Cairo (AUC) project № SSE-PHYS-S.E.- F.Y17- F.Y18- F.Y19-RG(2)-2016-Feb-10-08+45-59 & project № SSE-PHYS-H.O- F.Y20- RG(2-19)-2018-Dec-08-03-06-32-.FZGU-2020-0036. As well as technical support from Nanomaterials Laboratory at Physics Department, Faculty of Science, Al-Azhar University (Girls Branch) and National Research Centre (Cairo, Egypt).

For citation: Mahdy I. A., El Sheikh S. M., Omar H. A., Seredin P. V., Mahdy M. A. Preparation and characterization of Ge-Ni-Te nanocomposite. *Condensed Matter and Interphases*. 2022;24(2): 243–249. <https://doi.org/10.17308/kcmf.2022.24/9264>

Для цитирования: Махди И. А., Эль Шейх С. М., Омар Х. А., Середин П. В., Махди М. А. Получение и исследования нанокомпозитов Ge-Ni-Te. *Конденсированные среды и межфазные границы*. 2022;24(2): 243–249. <https://doi.org/10.17308/kcmf.2022.24/9264>

✉ Иман А. Махди, e-mail: imanmahdy@azhar.edu.eg

© Махди И. А., Эль Шейх С. М., Омар Х. А., Середин П. В., Махди М. А., 2022



The content is available under Creative Commons Attribution 4.0 License.

1. Introduction

Diluted magnetic semiconductors (DMS) are the focus of great interest due to their exceptional potential for implementation in the spintronic industry. Their importance lies in the fact that it provides scientific information and potential technological applications of semiconductors [1–4] for tunable ferromagnetic devices [5]. Among the IV–VI semi-magnetic semiconductors, only a few compounds (PbSnMnTe, SnMnTe, GeCrTe, and GeMnTe) show the ferromagnetic (FM) ordering [6]. The interaction between magnetic Mn ions doped GeTe films is ferromagnetic although Ni-doped GeTe films are paramagnetic [7] and $\text{Ni}_{5.42}\text{GeTe}_2$, crystallized in the tetragonal system [8]. Both crystallization speed and thermal stability of GeTe are significantly increased by Ni doping. The carrier concentration in multiferroic diluted magnetic semiconductors can control its magnetic properties; which may provide some new opportunities for novel spintronic and magnetoelectronic materials and devices. The magnetic, magneto-optical, and transport properties of the DMS materials, which are recently treated as spintronic model materials, are controlled via three coupled subsystems: free carriers, lattice excitations (phonons), and magnetic ions [9]. The spin and energy transfer between these coupled systems controls spin dynamics in DMS, where the magnetic ions and free carriers (electrons and holes) have non-vanishing spins [10]. Cao L. et al., [11, 12] studied the effect of Ni-doped GeTe thin films and demonstrated the possibility of using it in high-temperature phase-change memory (PCM) applications. This is due to the distinctive characteristics of its ability to low power consumption, retain data for a long time (10- years), and consider an excellent electric switching speed of 6 ns. Due to its high crystallization temperature and good data retention ability, a short electrical pulse of up to 6 ns can achieve a reverse switch between the SET and RESET states.

The major goal of this research is to study the effect of replacing Ge with Ni in a GeTe system with various Ni concentrations (2-20%) on the structural and optical properties of GeTe, as well as their magnetic response as the Ni ratio changes.

2. Methods of production and studying of the samples

In the present work the $\text{Ni}_x\text{Ge}_{50-x}\text{Te}_{50}$ with $x = 2, 4, 6, 8, 10, 15$ and 20 at% ternary compound has been prepared in an evacuated quartz ampoule with 14 mm diameter by the conventional solid-state direct reaction by multistage preparation from high purity crystalline Ge 99.999% Ge, Ni 99.999%, and Te 99.999% grade Sigma Aldrich. Starting Ge, Te and Ni were mixed in sealed quartz ampoule evacuated under argon atmosphere for preventing oxidation, and then prepared with their direct reaction at 1000 ± 1 °C for 24 hr and then cooled at a cooling rate 2 °C/min to obtain the initial ingot. In the second stage, the obtained ingots were ground in an agate mortar and then loaded in a pressing die with 13 mm diameter at a pressure of 5 tons for 5 min, pellet samples were sealed and evacuated again. Samples were heated in a vertical furnace to reduce the temperature gradient and then thermally treated at 700 ± 1 °C for 10 days without breaking, and then cooled with a cooling rate of 2 °C/min to reach room temperature. finally, the second stage was repeated once at 1000 ± 1 °C for 150 hr. The crystalline nature of all compounds is investigated using [Bruker X-Ray Diffractometer D8] with ($\text{CuK}\alpha$) radiation over [4: 90°] angular range with a normal scan, step size 0.03 and wavelength ~ 1.54061 Å. Diffuse reflection of all compounds was measured using a (Jasco V-570) spectrophotometer. The magnetic properties of all samples were investigated using a vibrating sample magnetometer (Lakeshore 7410).

3. Results and their discussion

3.1. Structural properties of Ni-Ge -Te

Structural properties of the prepared samples are investigated using XRD, Results of the X-ray diffraction pattern depicted in Fig. 1. phase analysis shows that the $\text{Ni}_x\text{Ge}_{1-x}\text{Te}$ has a multi-phase nanocrystalline structure. The main phase of all compositions is rhombohedral GeTe modification identified by the ICDD card (No 47-1079) GeTe. The second phase which appeared in the composite is the ternary phase that was identified as a Ni_3GeTe_2 hexagonal crystal with lattice parameters: $a = 3.911$ Å, $c = 16.022$ Å – which was identified by ICDD card

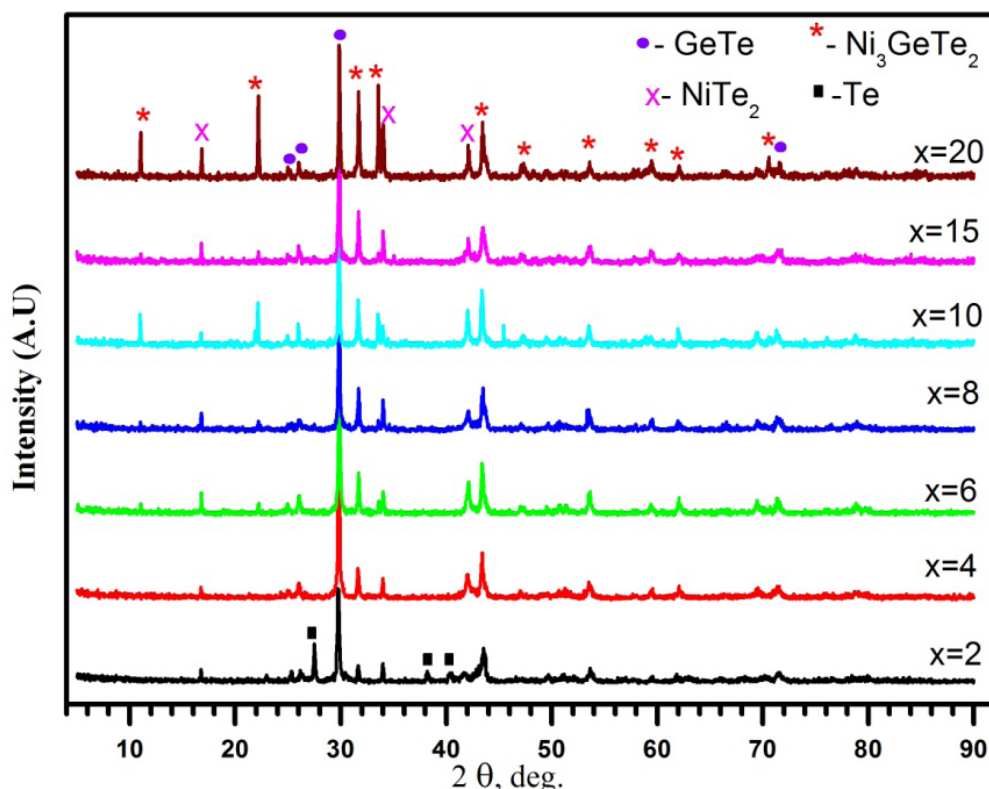


Fig. 1. X-ray diffractogram of $\text{Ni}_x\text{Ge}_{50-x}\text{Te}_{50}$ nanocomposite with different concentrations

No (01-075-5621). The additional secondary phases are identified as a NiTe_2 hexagonal system of lattice parameters: $a = 3.854 \text{ \AA}$, $c = 5.2604 \text{ \AA}$ – which was identified by ICDD card No (88-2278). But at low values of Ni content $x = 2$ at%, there is some precipitation of Te which indicated by the diffraction lines at $2\theta = 22.97, 27.50,$ and 40.34 diffraction lines, all Te peaks are disappeared at different concentrations from $x = 4$ to $x = 20$ at% as depicted in Fig. 1. The highly intensive diffraction peak of the main GeTe phase was used to determine crystallite size D using Scherrer's equation [13, 14]:

$$D = \frac{k\lambda}{\beta \cos(\theta)}, \quad (1)$$

where the shape factor $k \approx 0.9$, and β : full width at half maximum (FWHM) of the diffraction peak (radians), $\lambda = 1.5405 \text{ \AA}$ represents the wavelength of ($\text{CuK}\alpha$) radiation, θ is the Bragg angle of the XRD peaks. Moreover, the average crystallite size overall the different phases that appeared in the composite and strain ϵ established in the preparation process were evaluated using the William-

son–Hall, W–H, plot as shown in Fig. 2 using the following equation [15, 16]:

$$\beta \cos \theta = \frac{k\lambda}{D} + 4\epsilon \sin \theta. \quad (2)$$

The calculated crystallite size from both Scherrer's and W–H, plot confirms the nanocrystalline nature of the prepared composite. The obtained result of crystallite size and strain ϵ formed in nanocomposite with different compositions during the preparation process indexed in Tabl. 1.

3.2 Optical band gap calculations using Diffuse reflection

Diffuse reflection is one of the employed methods for optical characterization. The electronic transitions of solid materials can be described by using the technique of optical diffuse reflection [17]. Diffuse reflection spectra of Ge-Ni-Te samples were measured in the spectral range from 190 to 2500 nm and represented in Fig. 3. The absorption spectra can be obtained by using the following relation of Kubelka–Munk [17, 18]:

$$F(R) = (1 - R)^2 / 2R, \quad (3)$$

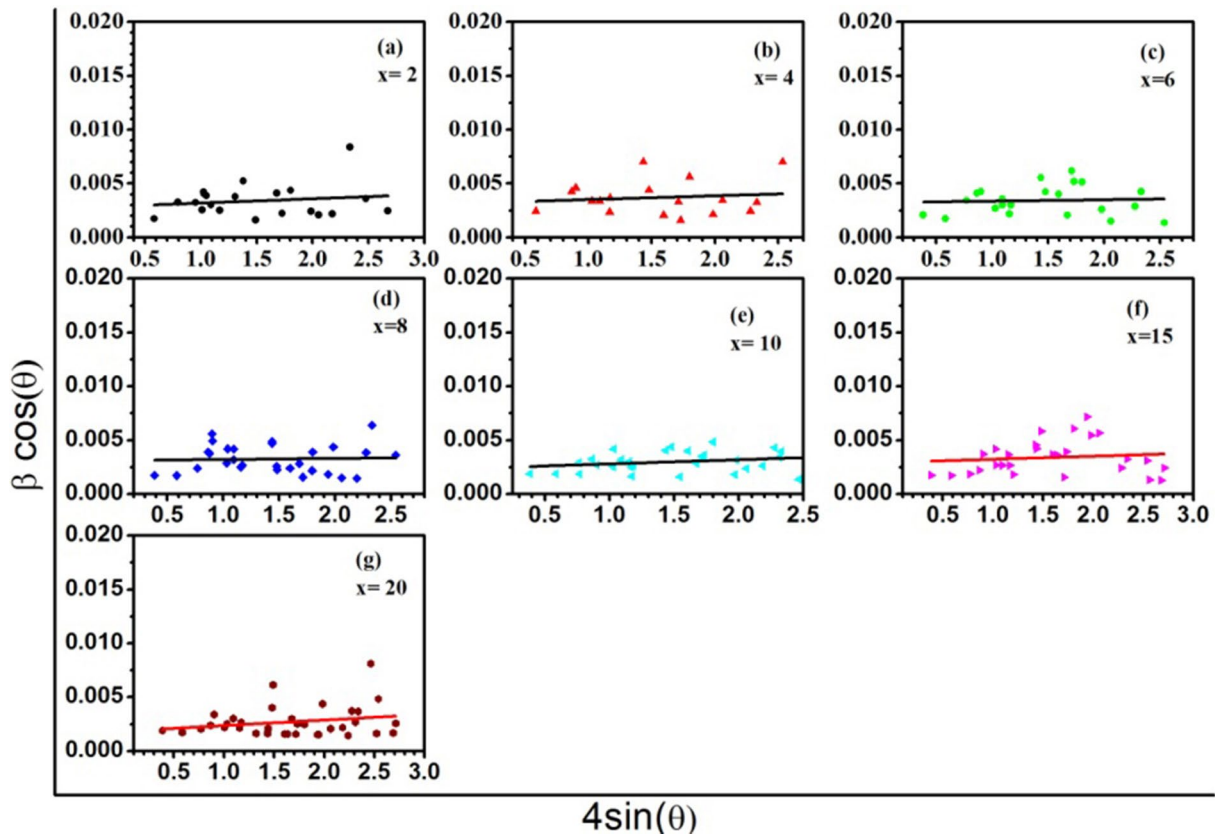


Fig. 2. Williamson–Hall plot of $Ni_xGe_{50-x}Te_{50}$ nanocomposite with different concentrations

where $F(R)$ is the Kubelka–Munk function and R represents the measured diffuse reflection. Fig. 3 represents the plot of $(F(R)*E)^2$ as a function of photon energy E [19]. The optical band gap for each composite was determined from the intercept of the linear part with the energy axis as seen in Fig. 1, the energy gap evaluated is listed in Tabl. 1. The optical band gap of all examined samples is greater than those of GeTe in microcrystal $\sim 0.73\text{--}0.95$ eV [20]. The redshift that appeared in the bandgap of nanocomposite can be attributed to the particle size of the prepared nanocomposite.

3.3. Magnetic properties of Ni-Ge-Te.

Magnetic properties of $Ni_xGe_{50-x}Te_{50}$ nanocomposite system were measured at room temperature. The resultant data of magnetic moment as a function of the applied magnetic field is depicted in Fig. 4 for different compositions. All results show that all samples have the predominant diamagnetic effect despite the presence of the paramagnetic phase Ni_3GeTe_2 [21, 22] as a secondary phase as mentioned above. That diamagnetic behavior can be attributed to the main GeTe phase which is characterized as a diamagnetic material [23].

Table 1. The evaluated crystallite size and optical gap of nanocomposite samples with different compositions

Ni at%	D nm, Scherrer	D nm, W-H plot	Strain ϵ % $\times 10^{-4}$	E_g (eV)
2	55.4	32.7	3.9	1.54
4	55.4	49.1	3.49	1.51
6	47.8	51.38	1.3	1.62
8	49.4	48.36	0.9	1.57
10	64.2	54.8	3.9	1.45
15	52.4	51.3	2.8	1.54
20	83.3	54.8	5.1	1.45

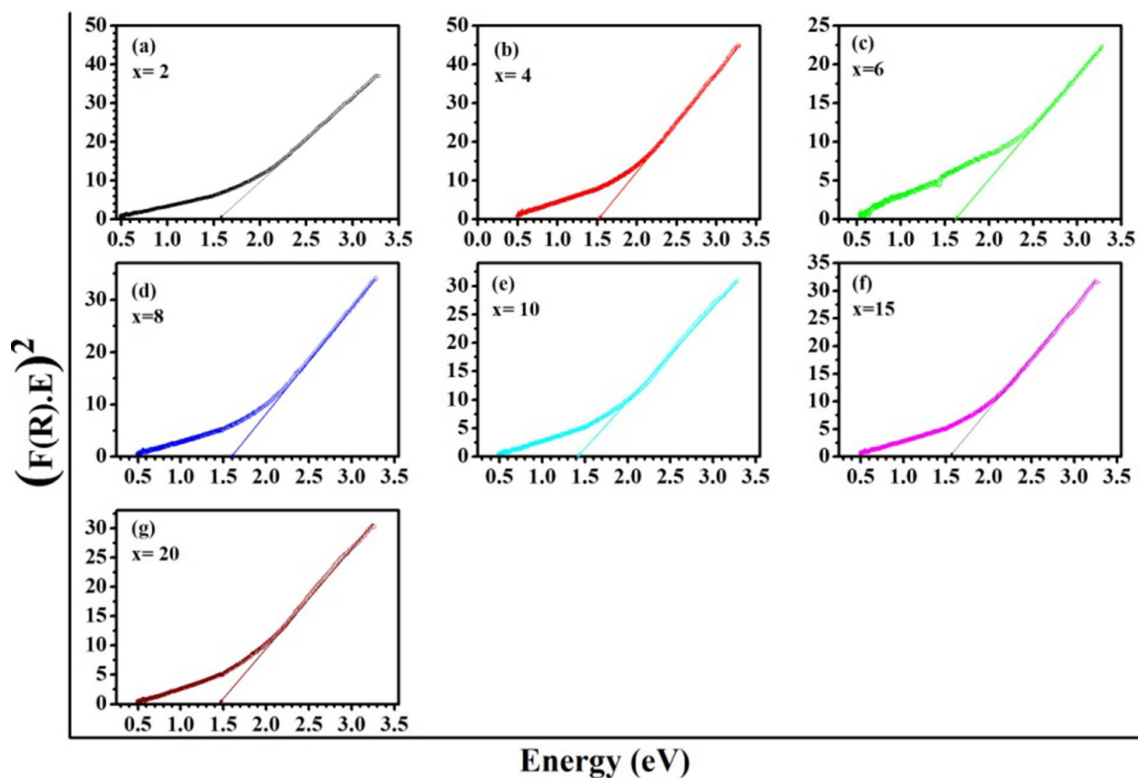


Fig. 3. Representation of $(F(R) \cdot E)^2$ as a function of photon energy E in eV of $Ni_xGe_{50-x}Te_{50}$ nanocomposite with different concentrations

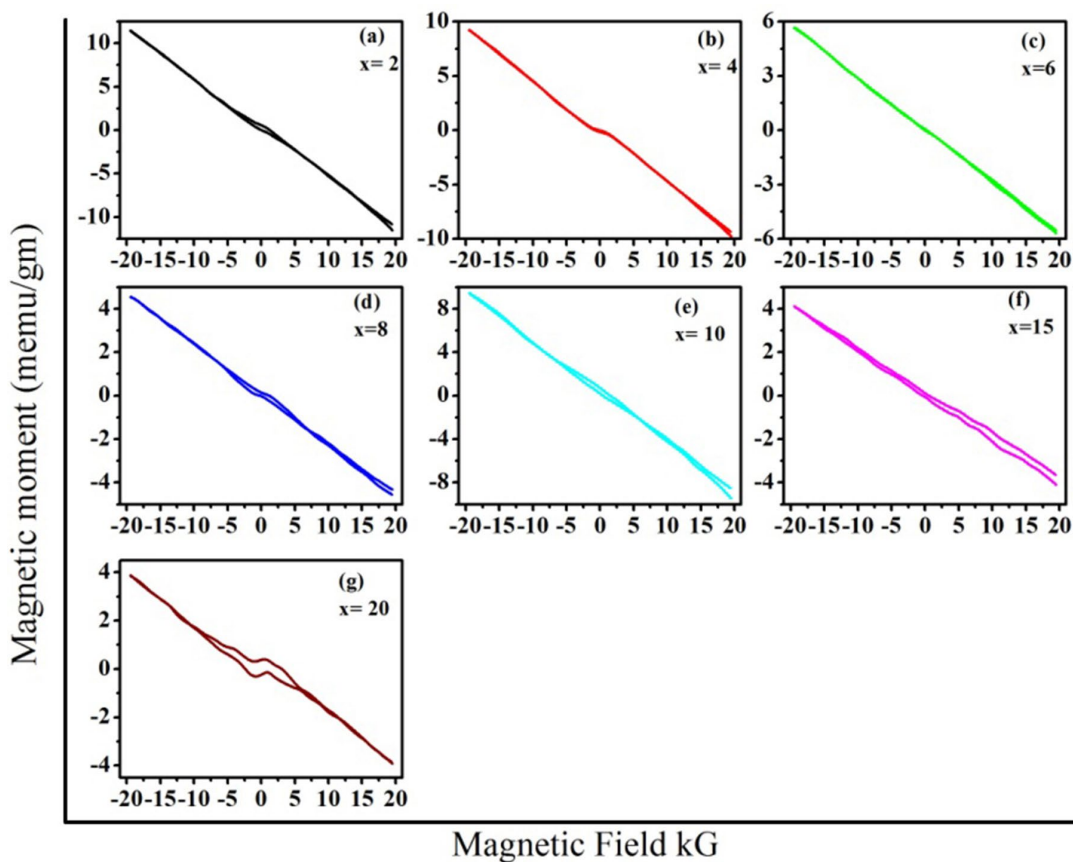


Fig. 4. Results of the magnetic moment as a function of the applied magnetic field of $Ni_xGe_{50-x}Te_{50}$ nanocomposite with different concentrations

4. Conclusions

The prepared Ni_xGe_{50-x}Te₅₀ alloy, $x = 2, 4, 6, 8, 10, 15, 20$ at% identified as a nanocomposite form with a multiphase structure of average crystallite size 47.8–83.8 nm. Optical properties of such nanocomposites show a direct allowed electronic transition with optical gap changes in the range of 1.45 to 1.62 eV with irregular change which can be attributed to the multiphase structure. Magnetic measurements confirm the diamagnetic behavior of all nanocomposite samples, which can be attributed to the predominant GeTe rhombohedral crystalline modifications.

Author Contributions

Iman A. Mahdy – conceptualization, scientific management, research concept, methodology development, formal analysis, writing – review & editing, visualization, final conclusions. S. M. El Sheikh – resources, supervision, project administration. Hosny A. Omar – resources, supervision, project administration. Pavel V. Seredin – writing the Russian version. Manal A. Mahdy – investigation, formal analysis, methodology, writing – review & editing.

Conflicts of interest

The authors declare that they have no known competing financial interests or personal relationships that could have appeared to influence the work reported in this paper.

References

- Ohno H. Making nonmagnetic semiconductors ferromagnetic. *Science*. 1998;281(5379): 951–956. <https://doi.org/10.1126/science.281.5379.951>
- Furdyna J. K. Diluted magnetic semiconductors. *Journal of Applied Physics*. 1988;64: R29–R64. <https://doi.org/10.1063/1.341700>
- Fiederling R., Keim M., Reuscher G., Ossau W., Schmidt G., Waag A., Molenkamp L.W. Injection and detection of a spin-polarized current in a light-emitting diode. *Nature*. 1999;402(6763): 787–789. <https://doi.org/10.1038/45502>
- Ohno Y., Young D. K., Beschoten B., Matsukura F., Ohno H., Awschalom D. D. Electrical spin injection in a ferromagnetic semiconductor heterostructure. *Nature*. 1999;402: 790–792. <https://doi.org/10.1038/45509>
- Koshihara S., Oiwa A., Hirasawa M., Katsumoto S., Iye Y., Urano C., Takagi H., Muneke H. Ferromagnetic order induced by photogenerated carriers in magnetic III-V semiconductor heterostructures of (In,Mn)As/GaSb. *Physical Review Letters*. 1997;78(24): 4617–4620. <https://doi.org/10.1103/physrevlett.78.4617>
- Leong T. K., Ferromagnetism in narrow gap semiconductor. In: *SYMPOSIUM D3&C2 - iumrs-icam*. 2013: Department of Electrical and Computer Engineering, National University of Singapore. 2013.
- Fukuma Y., Asada H., Miyashita J., Nishimura N., Koyanagi T., Magnetic properties of IV-VI compound GeTe based diluted magnetic semiconductors. *Journal of Applied Physics*. 2003;93(10): 7667–7669. <https://doi.org/10.1063/1.1556113>
- Isaeva A. A., Baranov A. I., Doert Th., Ruck M., Kulbachinskii V. A., Lunin R. A., Popovkine B. A. New metal rich mixed chalcogenides with an intergrowth structure: Ni_{5.68}SiSe₂, Ni_{5.46}GeSe₂, and Ni_{5.42}GeTe₂. *Russian Chemical Bulletin*. 2007;56(9): 1694–1700. <https://doi.org/10.1007/s11172-007-0263-1>
- Przybylin' Ska H., Springholz G., Lechner R. T., Hassan M., Wegscheider M., Jantsch W., Bauer G. Magnetic-field-induced ferroelectric polarization reversal in the multiferroic Ge_{1-x}Mn_xTe semiconductor. *Physical Review Letters*. 2014;112(4): 047202 1–5. <https://doi.org/10.1103/PhysRevLett.112.047202>
- Gaj J. A., Kossut J. Basic Consequences of $sp-d$ and $d-d$ interactions in DMS. In: Gaj J., Kossut J. (eds). *Introduction to the physics of diluted magnetic semiconductors. Springer series in materials science*. Berlin, Heidelberg: Springer; 2010;114. https://doi.org/10.1007/978-3-642-15856-8_1
- Cao L., Wu L., Zhu W., Ji X., Zheng Y., Song Z., Rao F., Song S., Ma Z., Xu L. High thermal stable and fast switching Ni-Ge-Te alloy for phase change memory applications. *Applied Physics Letters*. 2015;107: 242101 <https://doi.org/10.1063/1.4937603>
- Cao L. L., Wu L. C., Song Z. T., Zhu W. Q., Zheng Y. H., Cheng Y., Song S. N., Ma Z. Y., Xu L. Investigation of Ni doped Ge-Te materials for high temperature phase change memory applications. *Materials Science Forum*. 2016;848: 460–465. <https://doi.org/10.4028/www.scientific.net/MSF.848.460>
- Edward A. Elements of X-ray diffraction. *Physics Bulletin*. 1978;29(12): 572. <https://doi.org/10.1088/0031-9112/29/12/034>
- Mahdy M. A., Mahdy I. A., El Zawawi I. K. Characterization of Pb₂₄Te₇₆ quantum dot thin film synthesized by inert gas condensation. *Spectrochimica Acta Part A: Molecular and Biomolecular Spectroscopy*. 2015;134: 302–309. <https://doi.org/10.1016/j.saa.2014.06.055>
- Bahgat A. A., Heikal Sh., Mahdy I. A., Abd-Rabo A. S., Abdel Ghany A. Cyclic electrical conductivity in BaTiO₃-PbTiO₃-V₂O₅ glass-ceramic nanocomposite. *Physica B: Condensed Matter*. 2014;447: 23–29. <https://doi.org/10.1016/j.physb.2014.04.048>
- Williamson G. K., Hall W. H. X-Ray line broad-

ening from filed aluminum and wolfram. *Acta Metallurgica*. 1953;1(1):22–31. [https://doi.org/10.1016/0001-6160\(53\)90006-6](https://doi.org/10.1016/0001-6160(53)90006-6)

17. López R., Gómez R. Band-gap energy estimation from diffuse reflectance measurements on sol-gel and commercial TiO₂: a comparative study. *Journal of Sol-Gel Science and Technology*. 2012;61(1): 1–7. <https://doi.org/10.1007/s10971-011-2582-9>

18. Yeredla R. R., Xu H. An investigation of nanostructured rutile and anatase plates for improving the photosplitting of water. *Nanotechnology*. 2008;19(5): 055706. <https://doi.org/10.1088/0957-4484/19/05/055706>

19. Mahdy M. A., Kenawy S. H., Hamzawy E. M. A., El-Bassouy G. T., El Zawawi I. K. Influence of silicon carbide on structural, optical and magnetic properties of Wollastonite/Fe₂O₃ nanocomposites. *Ceramics International*. 2021;47(9): 12047–12055. <https://doi.org/10.1016/j.ceramint.2021.01.048>

20. Chopra K. L., Bahl S. K. Amorphous versus crystalline films. III. Electrical properties and band structure. *Journal of Applied Physics*. 1970;41(5): 2196–2212. <https://doi.org/10.1063/1.1659189>

21. Fukumay Y., Asada H., Miyashita J., Nishimura N., Koyanagi T. Magnetic properties of IV-VI compound GeTe based diluted magnetic semiconductors. *Journal of Applied Physics*. 2003;93(10): 7667–7669. <https://doi.org/10.1063/1.1556113>

22. Deiseroth H-Jö., Aleksandrov K., Christof R., Lorenz K., Reinhard K. K. Fe₃GeTe₂ and Ni₃GeTe₂ – two new layered transition-metal compounds: crystal structures, HRTEM investigations, and magnetic and electrical properties. *European Journal of Inorganic*

Chemistry. 2006;2006(8): 1561–1567. <https://doi.org/10.1002/ejic.200501020>

23. Domashevskaya E. P., Mahdy I. A., Grechki-na M. V. The new tetragonal phase of ternary compound CoGeTe with ferroelectric and magnetic responses. *International Journal of Advanced Information Science and Technology*. 2016;5(4): 127–131. <https://doi.org/10.15693/ijaist.2016.v5.i4.127-131>

Author information:

Iman A. Mahdy, Associate Professor, Physics Department, Faculty of Science for Girls, Al-Azhar University (Cairo, Egypt).

<https://orcid.org/0000-0002-8550-5539>
imanmahdy@azhar.edu.eg

Salah M. El Sheikh, Professor, Physics Department, School of Sciences and Engineering, the American University in Cairo (New Cairo, Cairo, Egypt).

lsheikh@aucegypt.edu

Hosny A. Omar, Professor, Physics Department, School of Sciences and Engineering, the American University in Cairo (New Cairo, Cairo, Egypt).

mhamomar@aucegypt.edu

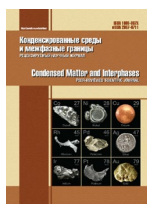
Pavel V. Seredin, Dr. Sci. (Phys.-Math.), Full Professor, Chair of department, Department of Solid State Physics and Nanostructures, Voronezh State University (Voronezh, Russian Federation).

<https://orcid.org/0000-0002-6724-0063>
paul@phys.vsu.ru

Manal A. Mahdy, associate professor, Solid State Physics Department, National Research Centre (Dokki, Giza).

<https://orcid.org/0000-0002-8210-2312>
mams411@gmail.com

Received 22.02.2022; approved after reviewing 04.03.2022; accepted for publication 15.05.2022; published online 25.06.2022



Original articles

Research article

<https://doi.org/10.17308/kcmf.2022.24/9265>

Growth of InGaAsSb/GaSb compound for infrared optoelectronic devices

Tien Dai Nguyen^{1,2✉}, J. O. Kim³, S. J. Lee^{3✉}

¹*Institute of Theoretical and Applied Research, Duy Tan University, Hanoi 100000, Vietnam*

²*Faculty of Natural Sciences, Duy Tan University, Da Nang 550000, Vietnam*

³*Metrology of Future Technology, Korea Research Institute of Standards and Science, Daejeon 34113, South Korea*

Abstract

In this study, we report on the synthesis of InGaAsSb epi-layer for optoelectronic devices in short infrared wavelengths (SWIR) at room temperature (RT).

The InGaAsSb with lattice matched to GaSb substrate was grown by the molecular beam epitaxy (MBE) using the strain engineering. The structural and optical properties of InGaAsSb layer was investigated by high resolution X-ray diffractometer (XRD), and photoluminescence (PL). Devices with a 400×400 μm of size were fabricated using traditional photolithography and inductively coupled plasma etching. The spectral response of InGaAsSb photodetector with a 90% cutoff wavelength and electroluminescence spectra of light emitting diode (LED) obtained at 2.38 μm at an applied bias of −0.1 V and 2.25 μm with $J_{ic} = 500$ mA, respectively at room temperature. Also, the spectral response of the detector indicates an increasing intensity and low noise when the temperature is high.

Keywords: InGaAsSb; MBE, Optoelectronic device, SWIR

Funding: This work was supported by the Korea Evaluation Institute of Industrial Technology (KEIT) grant 10052824 funded by the Korea government (MOTIE) and the Institute of Theoretical and Applied Research (ITAR), Duy Tan University.

For citation: Nguyen T. D., Kim J. O., Lee S. J. Growth of InGaAsSb/GaSb compound for infrared optoelectronic devices. *Condensed Matter and Interphases*. 2022;24(2): 250–255. <https://doi.org/10.17308/kcmf.2022.24/9265>

Для цитирования: Нгуен Т. Д., Ким Д. О., Ли С. Д. Выращивание соединения InGaAsSb/GaSb для инфракрасных оптоэлектронных приборов. *Конденсированные среды и межфазные границы*. 2022;24(2): 250–255. <https://doi.org/10.17308/kcmf.2022.24/9265>

✉ Nguyen Tien Dai, e-mail: nguyentien dai@duytan.edu.vn

✉ Lee S. J., e-mail: sjlee@kriss.re.kr

© Nguyen T. D., Kim J. O., Lee S. J., 2022



The content is available under Creative Commons Attribution 4.0 License.

1. Introduction

Infrared (IR) light-emitting diode (LED) and short wavelength IR detector (SWIR, 1.7–3 μm) are useful for various infrared applications (academia, industry, military, especially, atmospheric remote sensing, and gas detection) [1–7]. The antimony (Sb) material based III–V semiconductor compound is a promising candidate for the development of IR-detectors and -LED devices in short and mid wavelength IR range. Especially, the quaternary InGaAsSb compound has been interesting for the IR optoelectronic devices [8, 9]. The InGaAsSb based LED and photodetectors might be used for optical sensing (CO, CO₂, and CH₄ gas detections) due to lower noise, high sensitive, and high output power issues [3, 10]. The InGaAsSb compounds have been grown by many epitaxial systems such as metalorganic vapour phase epitaxy (MOVPE), [11] liquid phase epitaxy (LPE) [12] and molecular beam epitaxy (MBE) [13]. Among them, the MBE has several advantages such as lower growth temperature and precise control of the epi-thickness and composition. Therefore, in this study, we report on growth InGaAsSb/GaSb compound for IR detector and LED devices using MBE growth approach. The crystalline, morphological and optical properties of epi-layers (InGaAsSb and Al(Ga)AsSb) were investigated. Based on this result, we fabricated the full structure of photodetector and LED. Characterizations (spectral response, current–voltage and spectral

electroluminescence) of InGaAsSb devices are studied at room temperature.

2. Experimental

2.1. Growth of infrared photodetector

Fig. 1(a) shows the schematic of InGaAsSb photodetector with the *n* type-barrier-*n* type layer (*nBn*) structure design. This InGaAsSb composition layer was proposed to control lattice-matched on the *n*⁺-GaSb (100) substrate. Layers were grown by the molecular beam epitaxy (MBE) system (RIBER 32P) using As₂ and Sb₂ cracker sources. The stack of layers consisted of a bottom contact, *n*⁺-In_{*x*}Ga_{*1-x*}As_{*y*}Sb_{*1-y*} (2·10¹⁸ cm⁻³) with thickness of 300 nm, a 300 nm thick *n*⁺-GaSb (2·10¹⁸ cm⁻³) buffer, and a top contact of *n*⁺-GaSb (2·10¹⁸ cm⁻³), which was 200 nm thick. A 2 μm thick *n*-In_{*x*}Ga_{*1-x*}As_{*y*}Sb_{*1-y*} (2·10¹⁶ cm⁻³) active sandwich structure (*nBn*) between the top and bottom contacts consisted of InGaAsSb where the composition of indium was 17%, while composition of As was 15%, a 2 μm thick *n*-In_{*x*}Ga_{*1-x*}As_{*y*}Sb_{*1-y*} (2·10¹⁶ cm⁻³). An unipolar barrier of Al_{0.5}Ga_{0.7}Sb with 60 nm thick was grown on the active layer. The InGaAsSb layer was characterized by high resolution X-ray diffractometer (XRD). The XRD results indicated that the InGaAsSb layer was lattice matched to the GaSb substrate, as shown in Fig. 2(a) [14].

2.2. Growth of infrared light emitting diode

Fig. 1. (b) shows a detailed schematic of LED structure, which consists of three

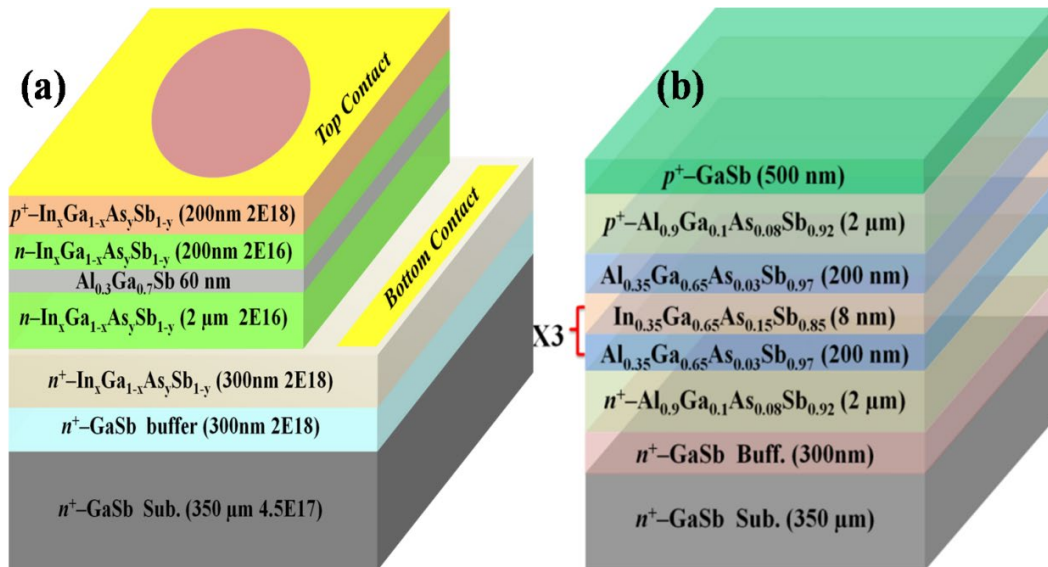


Fig. 1. (Color online) (a) Layer structure of IR–photodetector (b) Layer structure of IR–LED

$\text{In}_{0.35}\text{Ga}_{0.65}\text{As}_{0.15}\text{Sb}_{0.85}/\text{Al}_{0.35}\text{Ga}_{0.65}\text{As}_{0.05}\text{Sb}_{0.97}$ quantum wells with an 8 nm/200 nm thick, respectively. Following the $\text{In}_{0.35}\text{Ga}_{0.65}\text{As}_{0.15}\text{Sb}_{0.85}$ active layer is a 2 μm thick $n(p)\text{-Al}_{0.9}\text{Ga}_{0.1}\text{As}_{0.08}\text{Sb}_{0.92}$ ($1 \cdot 10^{18} \text{ cm}^{-3}$) cladding and capping layers. A 500 nm thick $p^+\text{-GaSb}$ ($1 \cdot 10^{18} \text{ cm}^{-3}$) was grown for top contact. The substrate temperature for growth InGaAsSb layer was at temperature of 460 °C, while that of the other layers (AlGaAsSb cladding, and barrier) was grown at temperature of 480 °C [14, 15].

2.3. Device fabrication

The photodetector device with a mesa size of $400 \times 400 \mu\text{m}$ was processed using photolithography and inductively coupled plasma etching. The ohmic contact metals with Ge/Au/Ni/Au layers were deposited by the electron beam evaporation (EBV) on the contact layer. The contacts were annealed at temperature of 200 °C using rapid thermal annealing. The detector had a circular aperture of 300 μm in each mesa, as shown in Fig. 3(a). The device was mounted on a leadless chip carrier for characteristics. Besides, the contact metals of Ti/Pt/Au were also deposited by the EBV on the $p\text{-GaSb}$ contact for LED device. The GaSb substrate was lapped and polished down to about 200 μm thick with a roughness of 12 nm. The LED die with a $400 \times 400 \mu\text{m}$ size was fabricated using photolithography, as shown in Fig. 3 (b). The top contact metals of Ge/Au/Ni/Au were deposited. After the device process, the

sample was mounted and wire-bonded onto a standard TO-18 package and a leadless chip carrier, as shown in Fig. 3 (c) [14].

3. Results and discussion

3.1. Characterizations of IR detector

In Fig. 4(a), the dark current density of detector measured at different temperatures using a Keithley 236. At the temperature range of 200–300 K, voltage–current curves exhibit an asymmetric shape that is attributed to the effect of a unipolar barrier ($\text{Al}_{0.5}\text{Ga}_{0.7}\text{Sb}$) [6]. Fig. 4 (b) shows the spectral response of a detector, which was measured by the Fourier transform infrared (FTIR-Nicolet 5700), using a white source and KBr window. The device exhibited the redshift of spectral when we carried out the increasing temperature from 100–300 K with a 90% cutoff wavelength from 1.95 to 2.38 μm . The cutoff wavelength of the device matches our calculation of $\text{In}_{0.17}\text{Ga}_{0.83}\text{As}_{0.15}\text{Sb}_{0.85}$ compound at 300 K. In order to match this cutoff wavelength, the composition of an InGaAsSb could be controlled due to both In and As concentrations [16, 17]. Also, the spectral response of the detector indicates an increasing intensity and low noise when the temperature is high. This phenomenon is attributed to the carrier blocking the effect of the AlGaSb barrier layer and re-align the band offset of the valance region. Thus, this mechanism

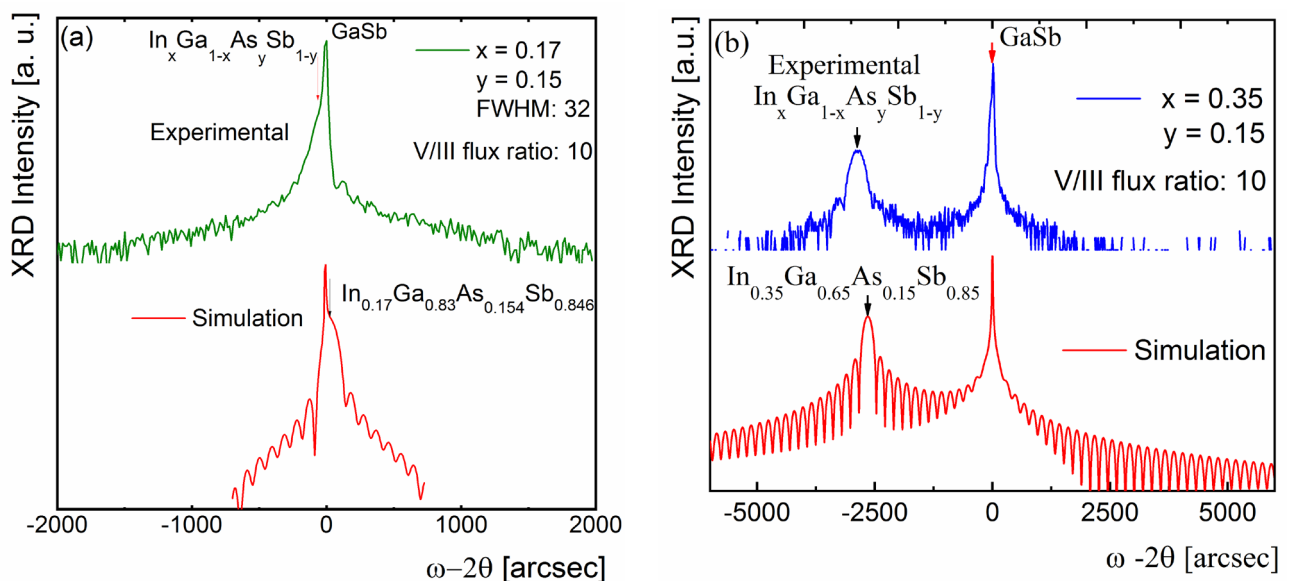


Fig. 2. (Color online) (a) X-ray diffraction rocking curve (004) planes of an $\text{In}_{0.17}\text{Ga}_{0.83}\text{As}_{0.15}\text{Sb}_{0.85}$ alloy for detector (b) optimization of $\text{In}_{0.35}\text{Ga}_{0.65}\text{As}_{0.15}\text{Sb}_{0.85}$ alloy for LED

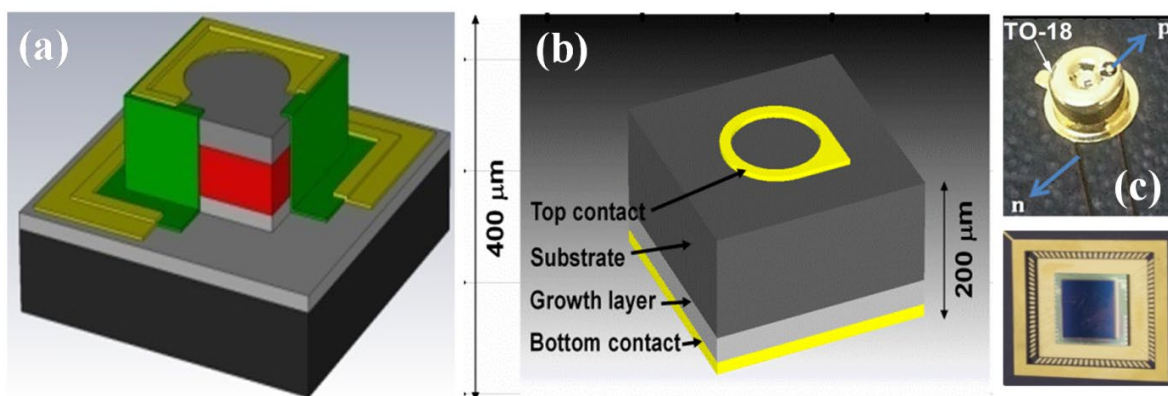


Fig. 3. (Color online) (a) Schematic view of single photodiode, (b) light emitting diode device and (c) mounted in standard TO–18 package and leadless chip carrier

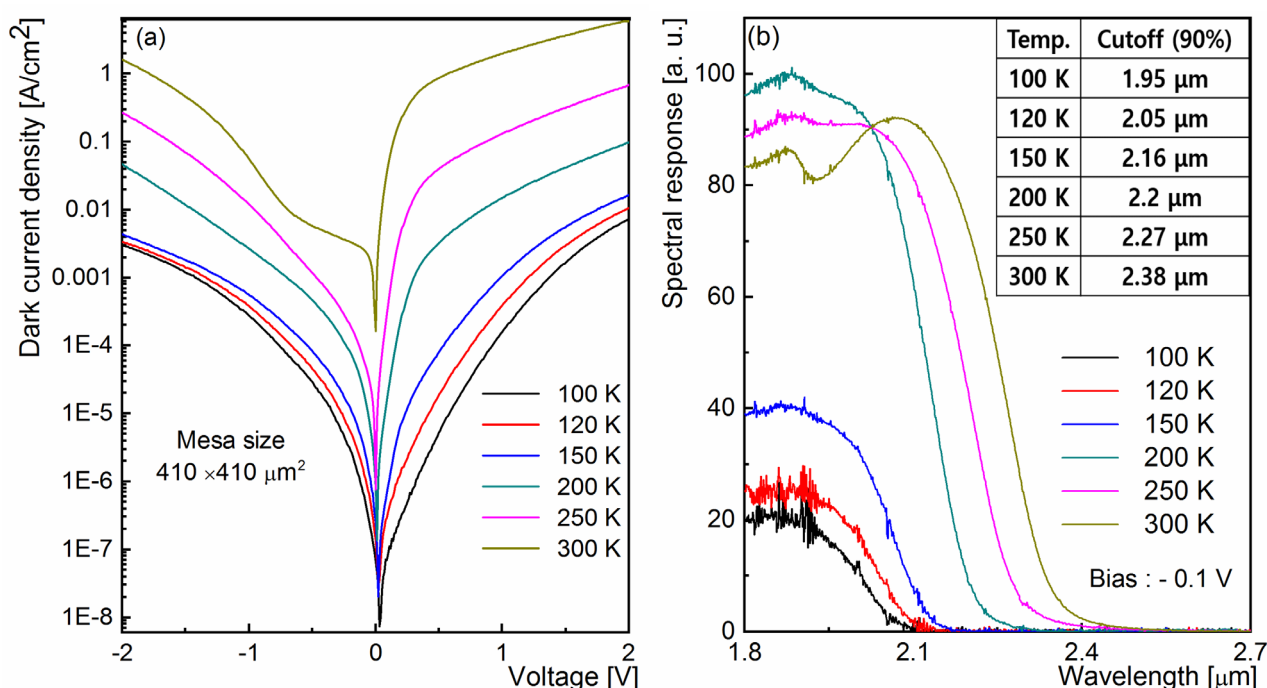


Fig. 4 (Color online) (a) The temperature depends on the dark current density of photodetector (b) Spectral response of the 90% cutoff wavelength shifts from 1.95 to 2.38 μm at temperature of 100–300 K

needs to detail the study by simulation approach.

3.2. Characterizations of light emitting diode

Fig. 5(a) is a current–voltage (I - V) of the LED at room temperature that shows a clear rectifying behavior with a turn–on voltage of about 0.35 V and an exponential increase in the forward current with increasing forward bias voltage. Due to this turn on voltage, we only supply a small potential that the photon easily emits from the active layer under suitable injection current (J_{ic}) condition. The series resistance, R_s , is 12.3 Ω, which was evaluated from the slope of I - V curve of LED device at room temperature. The small R_s value implies a well ohmic contact between GaSb

and metal layers. However, this value is still high compared to a commercial LED device (~ 3 – 5 Ω) that is the effect of the injection current on out power efficiency of the LED device.

In Fig. 5(b), the electroluminescence (EL) characteristic of IR–LED shows at room temperature. The peak of spectral EL is at 2.25 μm with 161 nm of full width haft maximum (FWHM) under injection current of 500 mA. The spectral EL is a recombination of electron–hole pairs of the first quantized level when the transmit from the conduction band to the valence band of a quantum well, as seen inserted picture in Fig. 5(b). There are two shoulder peaks at 1.96 μm

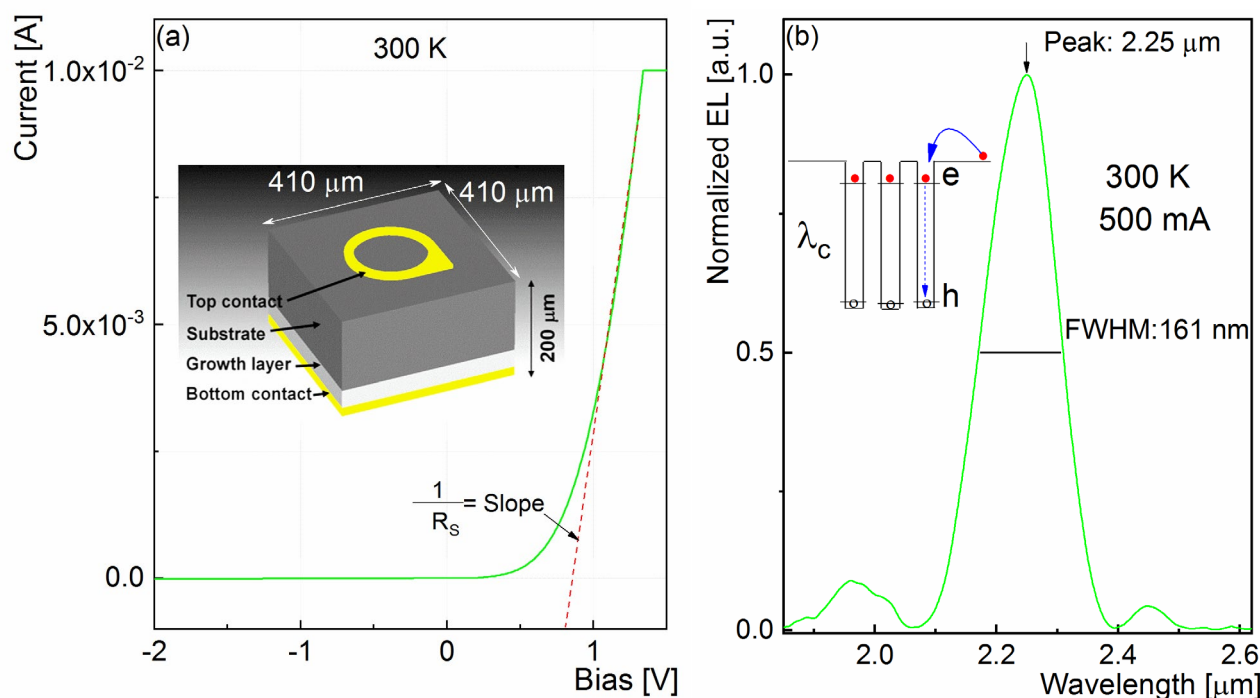


Fig. 5. (Color online) (a) Current–voltage, (b) Spectral electroluminescence characterizations of the IR light emitting diode measured at temperature of 300 K

and 2.45 μm , which is attributed to the effect of a thermal generation when LED die undergone a high injection current ($J_{ic} = 500 \text{ mA}$). As mention in above paragraph, the injection current is higher than the commercial LED (50 mA) due to the larger series resistance. This parameter should be optimized by the treatment of GaSb surface, optimized RTA condition, and change the metal contacts for improving output power efficiency.

4. Conclusions

We grew InGaAsSb epi-layer lattice matched to GaSb for infrared photodetector and light emitting diode, LED. By using the MBE approach, structural devices (nBn for photodetector and quantum well for LED) were synthesized. The photodetector obtained the spectral response at 2.38 μm , under the applied bias of -0.1 V, while LED shows spectral emission peak of 2.25 μm (FWHM = 161 nm) with injection current of 500 mA at room temperature. Based on those results, those optoelectronic devices might be served for spectrometers and with nondispersive infrared, NDIR, sensor.

Acknowledgements

This work was supported by the Korea Evaluation Institute of Industrial Technology

(KEIT) grant 10052824 funded by the Korea government (MOTIE) and the Institute of Theoretical and Applied Research (ITAR), Duy Tan University.

Conflict of interest

The authors declare that they have no known competing financial interests or personal relationships that could have influenced the work reported in this paper

References

1. Benoit J., Boulou M., Soulage G., Joullie A., Mani H. Performance evaluation of GaAlAsSb/GaInAsSb SAM-APDs for high bit rate transmissions in the 2.5 μm wavelength region. *Journal of Optical Communications*. 1988;9(2): 55. <https://doi.org/10.1515/joc.1988.9.2.55>
2. Carter B. L., Shaw E., Olesberg J. T., Chan W. K., Hasenberg T. C., Flatte M. E. High detectivity GaInAsSb pin infrared photodetector for blood glucose sensing. *Electronics Letters*. 2000;36(15): 1301–1303. <https://doi.org/10.1049/el:20000956>
3. Suchalkin S., Jung S., Kipshidze G., Shterengas L., Hosoda T., Westerfeld D., Snyder D., Belenky G. GaSb based light emitting diodes with strained InGaAsSb type I quantum well active regions. *Applied Physics Letters*. 2008;93(8): 081107. <https://doi.org/10.1063/1.2974795>

4. Gibson D., MacGregor C. A novel solid state non-dispersive infrared CO₂ gas sensor compatible with wireless and portable deployment. *Sensors*. 2013;13(6): 7079–7103. <https://doi.org/10.3390/s130607079>
5. Craig A. P., Jain M., Wicks G., Golding T., Hos-sain K., McEwan K., Howle C., Percy B., Marshall A. R. J. Short-wave infrared barricide detectors using InGaAsSb absorption material lattice matched to GaSb. *Applied Physics Letters*. 2015;106(20): 201103. <https://doi.org/10.1063/1.4921468>
6. Martyniuk P., Kopytko M., Rogalski A. Barrier infrared detectors. *Opto-Electronics Review*. 2014;22(2): 127–146. <https://doi.org/10.2478/s11772-014-0187-x>
7. Hoang A. M., Dehzangi A., Adhikary S., Razeghi M. High performance bias-selectable three-color short-wave/mid-wave/long-wave infrared photodetectors based on type-II InAs/GaSb/AlSb superlattices. *Scientific Reports*. 2016;6(1): 24144. <https://doi.org/10.1038/srep24144>
8. Scholz L., Perez A. O., Knobelspies S., Wöllenstein J., Palzer S. MID-IR LED-based, photoacoustic CO₂ sensor. *Procedia Engineering*. 2015;120: 1233–1236. <https://doi.org/10.1016/j.proeng.2015.08.837>
9. Refaat T. F., Abedin M. N., Koch G. J., Singh U. N. InGaAsSb detectors' characterization for CO₂ Lidar/DIAL applications. *NASA Langley Research Center; Hampton, VA, 23681-2199*. United States: 2003. p. 32.
10. Joullié A., Christol P. GaSb-based mid-infrared 2–5 μm laser diodes. *Comptes Rendus Physique*. 2003;4(6): 621–637. [https://doi.org/10.1016/s1631-0705\(03\)00098-7](https://doi.org/10.1016/s1631-0705(03)00098-7)
11. Cherng M. J., Jen H. R., Larsen C. A., Strigfellow G. B., Lundt H., Taylor P. C. MOVPE growth of GaInAsSb. *Journal of Crystal Growth*. 1986;77(1-3): 408–417. [https://doi.org/10.1016/0022-0248\(86\)90331-3](https://doi.org/10.1016/0022-0248(86)90331-3)
12. Gong X., Yang B., Ma Y., Gao F., Yu Y., Han W., Lui X., Xi J., Wang Z., Lin L. Liquid phase epitaxy growth and properties of GaInAsSb/AlGaAsSb/GaSb heterostructures. *Japanese Journal of Applied Physics*. 1991;30(7R): 1343–1347. <https://doi.org/10.1143/jjap.30.1343>
13. Reddy M. H. M., Olesberg J. T., Cao C., Pri-neas J. P. MBE-grown high-efficiency GaInAsSb mid-infrared detectors operating under back illumination. *Semiconductor Science and Technology*. 2006;21(3): 267–272. <https://doi.org/10.1088/0268-1242/21/3/009>
14. Kim J. O., Nguyen T. D., Ku Z., Urbas A., Kang S.-W., Lee S. J. Short wavelength infrared photodetector and light emitting diode based on InGaAsSb. *Infrared Technology and Applications XLIII*. 2017. <https://doi.org/10.1117/12.2264969>
15. Nguyen T. D., Hwang J., Kim Y., Kim E.-T., Kim J. O., Lee S. J. Dual-wavelength InGaAsSb/AlGaAsSb quantum-well light-emitting diodes. *Journal of the Korean Physical Society*. 2018;72(10): 1249–1253. <https://doi.org/10.3938/jkps.72.1249>
16. Nguyen T. D., Kim J. O., Kim Y. H., Kim E. T., Nguyen Q. L., Lee S. J. Dual-color short-wavelength infrared photodetector based on InGaAsSb/GaSb heterostructure. *AIP Advances*. 2018;8(2): 025015. <https://doi.org/10.1063/1.5020532>
17. Reddy M. H. M., Olesberg J. T., Cao C., Pri-neas J. P. MBE-grown high-efficiency GaInAsSb mid-infrared detectors operating under back illumination. *Semiconductor Science and Technology*. 2006;21(3): 267–272. <https://doi.org/10.1088/0268-1242/21/3/009>

Information about the authors

Tien Dai Nguyen, PhD in Advanced Materials Science and Engineering, Lecturer/ Research at Institute of Theoretical and Applied Research (ITAR), Duy Tan University (DTU) (Hanoi, Vietnam).

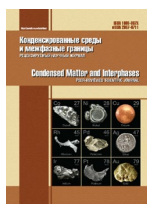
<https://orcid.org/0000-0002-9420-210X>
nguyentiendai@duytan.edu.vn

J. O. Kim, PhD in Physics; Senior Researcher, Advanced Instrumentation Institute, Korea Research Institute of Standards and Science (Yuseong-gu, Daejeon, South Korea).
jokim@kriss.re.kr

S. J. Lee, PhD in Physics, Principal Research Scientist, Korea Research Institute Standards and Science (KRISS) Associate Professor at University of Science and Technology (UST) (Yuseong-gu, Daejeon, South Korea).

sjlee@kriss.re.kr

Received 24.01.2022; approved after reviewing 04.03.2022; accepted 15.03.2022; published online 25.06.2022.



Original articles

Research article

<https://doi.org/10.17308/kcmf.2022.24/9266>Kinetics of the cathodic evolution of hydrogen on alloys of the $\text{Mo}_x\text{W}_{1-x}\text{Si}_2$ system in an alkaline electrolyteV. V. Panteleeva¹✉, G. A. Simonov¹, A. B. Shein¹, P. A. Miloserdov², V. A. Gorshkov²¹Perm State University,

15 Bukirev str., Perm 614990, Russian Federation

²Merzhanov Institute of Structural Macrokinetics and Materials Science, Russian Academy of Sciences,

8 Academician Osipyan str., Chernogolovka 142452, Russian Federation

Abstract

The kinetics and mechanism of the hydrogen evolution reaction on alloys of the $\text{Mo}_x\text{W}_{1-x}\text{Si}_2$ system ($x = 1.0; 0.68; 0.41; 0$) in a 1.0 M NaOH solution have been studied by the methods of polarization and impedance measurements. The cathodic polarization curves of silicides were characterized by the Tafel plots with constants a and b , equal to 0.47–0.49 and 0.068–0.076 V, respectively. The impedance spectra of $\text{Mo}_x\text{W}_{1-x}\text{Si}_2$ electrodes in the Tafel region are a combination of a capacitive semicircle with a displaced centre at high frequencies and an inductive arc at low frequencies. In the region of the highest frequencies on the impedance plots a straight-line section with a slope slightly higher than 45° was recorded, indicating the presence of pores in the surface layer of the electrodes.

To describe the hydrogen evolution reaction on silicides an equivalent electrical circuit was used, the Faraday impedance of which consisted of series-connected charge transfer resistance R_1 and a parallel R_2C_2 -chain (at $R_2 < 0$, $C_2 < 0$), which corresponded to the atomic hydrogen adsorption on the electrode surface. The impedance of the double layer capacitance was modelled by the constant phase element CPE₁.

The results of polarization and impedance measurements for the investigated silicides were in satisfactory agreement with the discharge – electrochemical desorption mechanism, in which both stages are irreversible and have unequal transfer coefficients. The limiting stage is the electrochemical desorption. The Langmuir isotherm for adsorbed atomic hydrogen was fulfilled. It was concluded that $\text{Mo}_x\text{W}_{1-x}\text{Si}_2$ alloys in an alkaline electrolyte are promising electrode materials that are active in the electrolytic hydrogen evolution reaction.

Keywords: Molybdenum and tungsten silicides, Hydrogen evolution reaction, Electrocatalysis, Self-propagating high-temperature synthesis

Funding: The research was supported by the Perm Research and Education Centre for Rational Use of Subsoil, 2021 and within the state assignment to Merzhanov Institute of Structural Macrokinetics and Materials Science, Russian Academy of Sciences.

For citation: Panteleeva V. V., Simonov G. A., Shein A. B., Miloserdov P. A., Gorshkov V. A. Kinetics of the cathodic evolution of hydrogen on alloys of the $\text{Mo}_x\text{W}_{1-x}\text{Si}_2$ system in an alkaline electrolyte. *Condensed Matter and Interphases*. 2022;24(2): 256–264. <https://doi.org/10.17308/kcmf.2022.24/9266>

Для цитирования: Пантелеева В. В., Симонов Г. А., Шеин А. Б., Милосердов П. А., Горшков В. А. Кинетика катодного выделения водорода на сплавах системы $\text{Mo}_x\text{W}_{1-x}\text{Si}_2$ в щелочном электролите. *Конденсированные среды и межфазные границы*. 2022;24(2): 256–264. <https://doi.org/10.17308/kcmf.2022.24/9266>

✉ Viktoria V. Panteleeva, e-mail: vikpant@mail.ru

© Panteleeva V. V., Simonov G. A., Shein A. B., Miloserdov P. A., Gorshkov V. A., 2022



The content is available under Creative Commons Attribution 4.0 License.

1. Introduction

Among the priority areas for the development of research in the hydrogen energetics, the search for efficient and inexpensive electrode materials for the electrolytic production of hydrogen occupies a leading position. In this regard, metals, alloys, intermetallic and metal-like compounds, and composite materials have been studied as catalysts for the hydrogen evolution reaction of (HER) [1–9]. The study of HER on transition metal silicides showed [1–3, 5–7, 10–14] that the electrocatalytic activity of these materials in the cathodic process depends significantly on the nature and concentration of the metal in the compound, the structure of the material, the pH, and the composition of the medium. A number of authors [2, 5, 11, 14] noted the high electrochemical activity of silicides in HER and the corrosion resistance of these compounds.

Transition metal silicides can be obtained by various methods (direct synthesis from elements, electrolysis of melts, thermal reduction of metal oxides, gas-phase synthesis, etc. [15]). One of the most high-performance and low-power-consuming methods for obtaining silicides and composite materials based on them is self-propagating high-temperature synthesis (SHS) [16]. The use of this method allows controlling the chemical and phase composition, the microstructure of the resulting material by changing the composition of the initial mixture and synthesis parameters.

The aim of this study was to establish the kinetics and mechanism of the reaction of hydrogen evolution on $\text{Mo}_x\text{W}_{1-x}\text{Si}_2$ silicides ($x = 1.0; 0.68; 0.41; 0$) synthesized by the SHS method in an alkaline electrolyte and the determination of the electrochemical activity of $\text{Mo}_x\text{W}_{1-x}\text{Si}_2$ in HER.

2. Experimental

$\text{Mo}_x\text{W}_{1-x}\text{Si}_2$ silicides ($x = 1.0; 0.68; 0.41; 0$), obtained by the SHS method from powder oxides of molybdenum and tungsten (analytical grade) and silicon KR-0 mixed with aluminium in an argon atmosphere under a gas pressure of 5 MPa. The synthesis technique and research materials are described in detail in [17].

For electrochemical measurements, the samples were placed in specially made fluoroplastic holders and filled with polymerised

epoxy resin, leaving only the working surface of the electrodes uninsulated, which was 0.8–1.4 cm². All the specific values provided in the study are presented per unit of the geometric area of the electrode surface. Before measurements, the electrode surface was polished with abrasive papers with a successive decrease in grain size, degreased with ethyl alcohol, and rinsed with a working solution.

Electrochemical measurements were carried out at a temperature of 25 °C under natural aeration conditions in an unstirred 1.0 M NaOH solution. The solution was prepared using deionized water (water resistivity, 18.2 MΩ cm, organic carbon content, 4 µg/L), obtained using a Milli-Q water purification system from Millipore (France), and NaOH (chemically pure).

The measurements were carried out using a potentiostat-galvanostat with a built-in Solartron 1280C frequency analyser (Solartron Analytical, Great Britain) in an YASE-2 electrochemical cell with cathode and anode sections separated by a porous glass diaphragm. A saturated silver chloride electrode was used as the reference electrode and a platinum electrode was used as the auxiliary electrode. The potentials in the study are presented relative to the standard hydrogen electrode.

Once the electrode was immersed in the solution, it was subjected to cathodic polarisation with a current density of 0.5 mA/cm² within 10 min; then held with an open circuit potential until a stable potential was established, which was -0.63 ± 0.02 , -0.66 ± 0.02 , -0.69 ± 0.03 and -0.80 ± 0.02 V for MoSi_2 -, $\text{Mo}_{0.68}\text{W}_{0.32}\text{Si}_2$ -, $\text{Mo}_{0.41}\text{W}_{0.59}\text{Si}_2$ -, and WSi_2 electrodes, respectively; then the impedance spectra were recorded. Before the measurement of the impedance spectra, potentiostatic polarisation of the electrode was conducted at each potential until an almost constant current value was established. After that, the impedance was measured at this value of E and lower potentials, and the potential was changed with a fixed step. Cathodic potentiostatic curves were plotted based on the obtained values of i values for a given value of E . The range of frequencies used for impedance measurements $f(\omega/2\pi)$ was from 20 kHz to 0.01 Hz (10 points per decade with a uniform distribution on a logarithmic scale), the amplitude of the alternating signal was 5–10 mV.

The value of hydrogen evolution overvoltage was determined relative to the equilibrium potential of the hydrogen electrode in a 1.0 M NaOH solution (-0.818 V).

The data were measured and processed using the programs CorrWare2, ZPlot2, and ZView2 (Scribner Associates, Inc.). Confidence intervals were calculated at a significance level of 0.05.

3. Results and discussion

The cathodic polarization curves of MoSi_2 -, $\text{Mo}_{0.68}\text{W}_{0.32}\text{Si}_2$ -, $\text{Mo}_{0.41}\text{W}_{0.59}\text{Si}_2$ -, and WSi_2 electrodes corrected for the Ohmic drop [18] in a 1.0 M NaOH solution are shown in Fig. 1.

The cathodic curves of MoSi_2 , $\text{Mo}_{0.68}\text{W}_{0.32}\text{Si}_2$, and $\text{Mo}_{0.41}\text{W}_{0.59}\text{Si}_2$ silicides had the same type and were characterized by the presence of a Tafel region in the potential range from -1.04 to -1.13 V with a slope $b \approx 0.068$ – 0.074 V and constant a equal to ~ 0.47 – 0.49 V (Table 1). The polarisation curve of the WSi_2 electrode had a linear section in the potential range from -1.0 to -1.1 V with a slope of ~ 0.076 V and $a \approx 0.48$ V (Table 1). Based on the constant values a and b in accordance with [19], it was concluded that the studied silicides in an alkaline electrolyte are materials with a low overvoltage for hydrogen evolution.

The theoretical value of the Tafel slope was ~ 0.06 V (with transfer the coefficients of $\alpha \approx 0.5$ for charge transfer stages), the values of b were

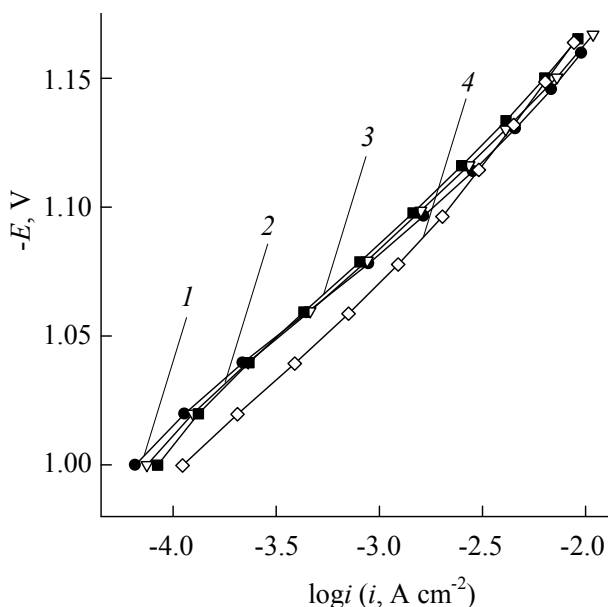


Fig. 1. Cathodic polarization curves in 1.0 M NaOH: 1 – MoSi_2 ; 2 – $\text{Mo}_{0.68}\text{W}_{0.32}\text{Si}_2$; 3 – $\text{Mo}_{0.41}\text{W}_{0.59}\text{Si}_2$; 4 – WSi_2

closest when reordered for $\text{Mo}_x\text{W}_{1-x}\text{Si}_2$ electrodes (Table 1) may have several explanations. Tafel slope ~ 0.06 V can be observed in the case of following mechanisms, assuming that the Langmuir adsorption isotherm for adsorbed atomic hydrogen H_{ads} was fulfilled: 1) delayed barrier-free discharge or delayed barrier-free electrochemical desorption [20]; 2) delayed surface diffusion of atomic hydrogen (for this mechanism, the Tafel slope is ~ 0.06 V [21] or ~ 0.079 V [22]).

The value of b of ~ 0.06 V when the logarithmic Temkin adsorption isotherm for H_{ads} was fulfilled, can be explained in the case of following mechanisms [23]: 1) discharge – recombination with a quasi-equilibrium discharge stage with non-activated hydrogen adsorption; 2) discharge – electrochemical desorption with a quasi-equilibrium discharge stage.

The observed relatively small deviations of the Tafel slope for $\text{Mo}_x\text{W}_{1-x}\text{Si}_2$ from the theoretical ~ 0.06 V can be associated with specific values of the transfer coefficients of HER stages and other factors [24].

For the clarification of the mechanism and kinetic regularities of HER on silicides, the frequency dependences of the impedance components were measured.

The impedance spectra of $\text{Mo}_x\text{W}_{1-x}\text{Si}_2$ silicides for all studied values of E were a combination of a capacitive semicircle with a centre below the axis of the real component of the impedance Z' at high frequencies (HF) and the inductive arc at low frequencies (Fig. 2). On the impedance graphs in the region of the highest frequencies, deviations from the semicircle were recorded. These deviations had the form of almost rectilinear segments with an inclination somewhat higher than 45° and, probably, indicate the presence of pores, approximately corresponding to the model of cylindrical pores in the surface layer of

Table 1. Kinetic parameters of the hydrogen evolution reaction on the alloys of the $\text{Mo}_x\text{W}_{1-x}\text{Si}_2$ system in 1.0 M NaOH

Electrode	$-b, \text{V}$	$-a, \text{V}$
MoSi_2	0.068 ± 0.001	0.47 ± 0.01
$\text{Mo}_{0.68}\text{W}_{0.32}\text{Si}_2$	0.071 ± 0.001	0.48 ± 0.01
$\text{Mo}_{0.41}\text{W}_{0.59}\text{Si}_2$	0.074 ± 0.002	0.49 ± 0.02
WSi_2	0.076 ± 0.001	0.48 ± 0.02

the electrodes [25]. The slope angle higher than 45° can be explained by the significant influence of the “flat” electrode surface around the pores [26], for which the slope Z'' , Z' -dependences in the high frequency region was lower than 90° , but significantly higher than 45° (see below the data for the CPE constant phase element). Resistance R_Ω , equal to the distance between the point obtained by extrapolation of the rectilinear section to the region of high frequencies to the intersection with the axis Z' , and the point obtained by extrapolating the capacitive semicircle into the HF-region to the intersection with the axis Z' , was 0.44 ± 0.02 , 0.46 ± 0.02 , 0.41 ± 0.03 , and $0.47 \pm 0.02 \Omega \cdot \text{cm}^2$ for MoSi_2 -, $\text{Mo}_{0.68}\text{W}_{0.32}\text{Si}_2$ -, $\text{Mo}_{0.41}\text{W}_{0.59}\text{Si}_2$ -, and WSi_2 electrodes, respectively. The low value of R_w indicated that the pores were not deep.

According to the theory of porous electrodes for the model of cylindrical pores [27]:

$$R_\Omega = \frac{\rho L}{3n\pi r^2},$$

where r is the resistivity of the electrolyte solution, r and L are the pore radius and length, respectively, n is the number of pores per 1 cm^2 of the electrode surface; $S = n\pi r^2$ is the total cross section of pores per 1 cm^2 of the surfaces. The ratio for R_Ω does not allow to determine r and L separately; only L/r^2 or L/S ratios can be determined. For 1.0 M NaOH , $r = 6.05 \Omega \cdot \text{cm}$ [28], and, for example, for the MoSi_2 electrode the L/S ratio

was 0.22 cm^{-1} ; based on the assumption that $S = 0.01 \text{ cm}^2$ we get $L = 22 \mu\text{m}$.

Let f_0 denote the frequency corresponding to the transition point from a rectilinear HF section to a capacitive semicircle. At the frequency f_0 the alternating current passes through the entire length of the pores, and at $f < f_0$ the electrode with pores behaves like a smooth electrode with a surface area equal to the total surface of the electrode, including the inner surface of the pores [26]. For the processing of the impedance spectra for the study of the kinetics and mechanism of HER, points at $f < f_0$ were selected. This allows the use of equivalent circuits normally used for smooth electrodes.

The impedance graphs of $\text{Mo}_x\text{W}_{1-x}\text{Si}_2$ electrodes indicate the staged nature of HER. At least two time constants were required for the description. The registration of the inductive impedance in the low-frequency region indicates that HER proceeded according to the discharge-electrochemical desorption path. According to [29], the inductive impedance can appear only when H_{ads} is removed via the electrochemical desorption stage and cannot appear in the case of the discharge-recombination mechanism. Thus, based on the frequency dependences of the impedance components, it can be concluded that in the studied range of potentials for the description of hydrogen evolution on the $\text{Mo}_x\text{W}_{1-x}\text{Si}_2$ silicides discharge - recombination path can be rejected.

The equivalent electrical circuits shown in Fig. 3 were used for the modelling of HER on

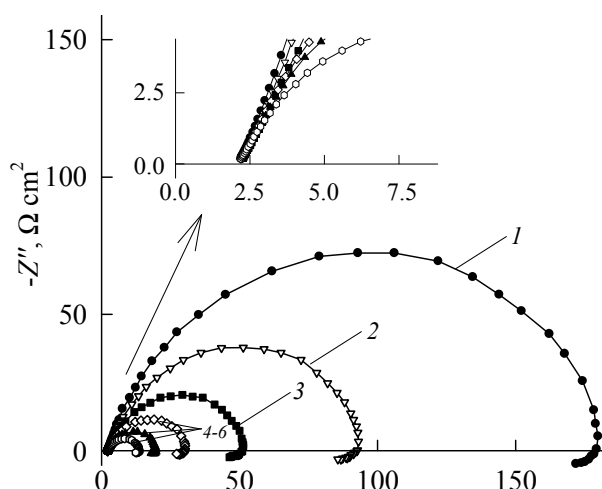


Fig. 2. Impedance spectra of MoSi_2 in 1.0 M NaOH at $E, \text{ V}$: 1 – -1.04 ; 2 – -1.06 ; 3 – -1.08 ; 4 – -1.10 ; 5 – -1.12 ; 6 – -1.14

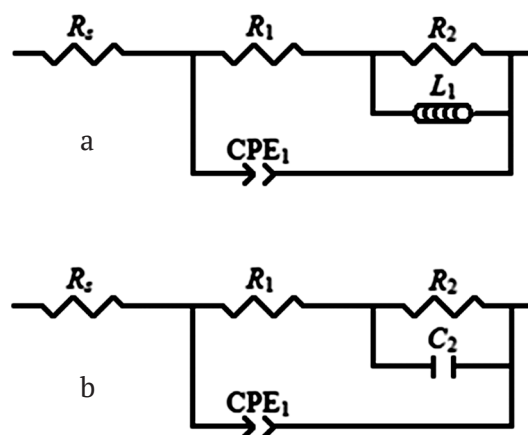


Fig. 3. Equivalent electrical circuits for the alloys of the $\text{Mo}_x\text{W}_{1-x}\text{Si}_2$ system in 1.0 M NaOH in the range of potentials of hydrogen evolution

$\text{Mo}_x\text{W}_{1-x}\text{Si}_2$ silicides. In the diagram shown in Fig. 3a: R_s is the electrolyte resistance, R_1 is the polarization resistance, resistance R_2 and inductance L_1 describe the atomic hydrogen adsorption (filling relaxation of H_{ads} when an alternating signal is applied) on the electrode surface, the CPE_1 element simulates double layer capacitance on the inhomogeneous surface of the solid electrode.

The impedance of the constant phase element is:

$$Z_{\text{CPE}} = Q^{-1}(j\omega)^{-p}.$$

In this ratio, with $p = 1 - \gamma$ the constant phase element is non-ideal capacitance; γ is the value significantly less than 1 (typically $\gamma < 0.2$) [18].

The equivalent circuit in Fig. 3b is identical to the circuit in Fig. 3a (in the scheme in Fig. 3b: R_1 is the charge transfer resistance, and the adsorption of atomic hydrogen on the electrode surface is modelled using the R_2C_2 -chain). According to [30], to describe HER on electrodes that correspond to impedance spectra with inductance in the low-frequency region, it is advisable to use the equivalent circuit in Fig. 3b with negative R_2 and C_2 . In this case, absolute values of $|R_2|$ and $|C_2|$ are used as diagnostic criteria for HER mechanisms based on the analysis of the dependence of the Faraday impedance parameters on the potential.

Experimental impedance spectra of silicides at the studied values of E were satisfactorily described by the diagram in Fig. 3b with negative values of R_2 and C_2 . The criterion χ^2 calculated by ZView2 (using statistical weights expressed via the reciprocal of the impedance module) was $(1.1\text{--}2.3) \cdot 10^{-4}$; the sum of square deviations was $(1.0\text{--}2.1) \cdot 10^{-2}$; the error in determining the values R_s , R_1 , and CPE_1 did not exceed 1–3%, and reached 8–10% for the parameters R_2 and C_2 . Parameter

values of the equivalent circuit for the MoSi_2 electrode are shown in Table 2.

The results of the determination of the numerical values of $X = R_1, |R_2|, |C_2|$ parameters of the equivalent circuit in Fig. 3b for $\text{Mo}_x\text{W}_{1-x}\text{Si}_2$ electrodes were analysed depending on the potential in semilogarithmic coordinates. $\lg X, E$ dependencies for the MoSi_2 electrode, corrected for the ohmic potential drop are shown in Fig. 4. The slopes $(\partial \lg X / \partial E)_{c_{\text{NaOH}}}$ for $\text{Mo}_x\text{W}_{1-x}\text{Si}_2$ are shown in Table 3. For all the studied silicides at the potentials of the Tafel region, a linear decrease in the values of $\lg R_1$ and $\lg |R_2|$ and a weak increase in $\lg |C_2|$ with increasing cathodic polarization were revealed.

Based on the polarization measurements, for HER on silicides was considered the mechanism of discharge–electrochemical desorption with a quasi-equilibrium stage of the discharge when

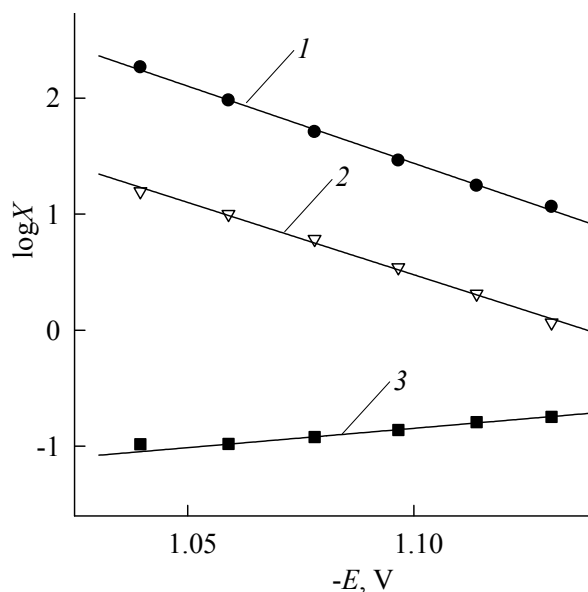


Fig. 4. Dependences of $\log X$ (X : 1 – R_1 , 2 – $|R_2|$, 3 – $|C_2|$) on the potential of MoSi_2 in 1.0 M NaOH. Values of R_1 and R_2 are in $\text{W}\cdot\text{cm}^2$, C_2 in $\text{F}\cdot\text{cm}^{-2}$

Table 2. The values of the equivalent electrical circuit (Fig. 3b) parameters for MoSi_2 in 1.0 M NaOH

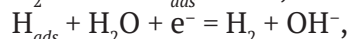
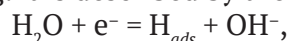
$-E, \text{V}$	$R_1, \Omega\cdot\text{cm}^2$	$R_2, \Omega\cdot\text{cm}^2$	$-C_2, \text{F}\cdot\text{cm}^{-2}$	$Q_1\cdot 10^4, \text{F}\cdot\text{cm}^{-2}\cdot\text{s}^{(p_1-1)}$	p_1
1.04	184.9	15.8	0.104	4.69	0.827
1.06	95.8	10.0	0.105	4.82	0.831
1.08	51.2	6.1	0.120	4.89	0.834
1.10	29.0	3.5	0.138	4.89	0.842
1.12	17.6	2.0	0.161	4.74	0.858
1.14	11.6	1.2	0.179	5.19	0.852

the logarithmic adsorption isotherm for H_{ads} was fulfilled. However, for this mechanism, in accordance with [30] the independence of R_1 and C_2 from the potential was noted. The significant decrease in R_1 and the small increase in $|C_2|$ with the potential (Table 2) experimentally registered for $\text{Mo}_x\text{W}_{1-x}\text{Si}_2$ silicides did not correspond to the theoretical ones for the considered HER mechanism.

The mechanism of slow surface diffusion of atomic hydrogen during hydrogen evolution on $\text{Mo}_x\text{W}_{1-x}\text{Si}_2$ silicides can be considered probable, since different atoms are present in the studied materials, and, consequently, the formation of adsorbed hydrogen atoms during the transfer of an electron to a water molecule and electrochemical desorption H_{ads} can occur on different parts of the surface (active centres) of the electrodes. The use of an equivalent circuit corresponding to this mechanism [31] for modelling the impedance spectra of silicides leads to high errors in determining the diffusion impedance parameters and capacitance values for H_{ads} on active sites to which surface diffusion occurs. Probably, the mechanism of delayed surface diffusion can also be rejected.

Parallel $\lg R_1, E$ - and $\lg |R_2|, E$ -dependencies and a slight change in $\lg |C_2|$ with decreasing potential are characteristic of the discharge – electrochemical desorption mechanism, in which both stages are irreversible and the transfer coefficients of the stages are not equal [30]. The impedance measurements were carried out at an overvoltage higher than 0.18 V, which are sufficiently high for the stages to be irreversible. According to [30], in this mechanism, with a logarithmic adsorption isotherm for H_{ads} there is no inductance on the impedance spectra. In the case of the Langmuir isotherm, inductance

can appear both in the case of a slow stage of the discharge and in the case of a slow stage of electrochemical desorption. Thus, based on the obtained dependences of the elements of the Faraday impedance of $\text{Mo}_x\text{W}_{1-x}\text{Si}_2$ electrodes from E it can be assumed that HER on silicides in the studied potential range proceeds according to the discharge - electrochemical desorption path, e.g. it is described by the sequence of reactions:



with the Langmuir adsorption isotherm for H_{ads} . Additional criteria for HER mechanisms based on dependency analysis of iR_1 , $|iR_2|$, and R_2C_2 on the electrode potential [32], also indicate the implementation of this mechanism on silicides. For MoSi_2 the electrode slopes $(\partial \lg Y / \partial E)_{c_{\text{NaOH}}}$ for $Y = iR_1, |iR_2|, R_2C_2$ were $-1.3 \pm 0.2, -1.1 \pm 0.4,$ and $9.8 \pm 0.4 \text{ V}^{-1}$ respectively.

With irreversible stages of HER there are two possible explanations for the results obtained: a) the limiting stage is the formation of H_{ads} with the transfer of an electron to a H_2O molecule $\alpha_1 > \alpha_2$; b) the limiting step is electrochemical desorption, $\alpha_1 < \alpha_2$. Here α_1 and α_2 are the transfer coefficients of the discharge and electrochemical desorption stages, respectively. Molybdenum and tungsten are metals with a very high binding energy with hydrogen $E_{\text{M-H}}$ [20]. In this case, $E_{\text{W-H}}$ was about 12 kJ/mol higher than $E_{\text{Mo-H}}$ during adsorption from the gas phase, and estimates for aqueous solutions provide close $E_{\text{M-N}}$ values for these metals. Due to the high strength of the metal-hydrogen bond, the probable mechanism of HER for Mo and W in acidic solutions is delayed electrochemical desorption (barrier-free at relatively low η and ordinary at higher η) [20]. Probably, $E_{\text{M-N}}$ on molybdenum and tungsten silicides is somewhat different from $E_{\text{M-N}}$ for pure

Table 3. The values of $(\partial \lg X / \partial E)_{c_{\text{NaOH}}}$ ($X = R_1, |R_2|, |C_2|$) slopes and transfer coefficients α_1 and α_2 for the alloys of the $\text{Mo}_x\text{W}_{1-x}\text{Si}_2$ system in 1.0 M NaOH

Electrode	$\left(\frac{\partial \lg R_1}{\partial E}\right)_{c_{\text{NaOH}}}, \text{V}^{-1}$	$\left(\frac{\partial \lg R_2 }{\partial E}\right)_{c_{\text{NaOH}}}, \text{V}^{-1}$	$\left(\frac{\partial \lg C_2 }{\partial E}\right)_{c_{\text{NaOH}}}, \text{V}^{-1}$	α_1	α_2
MoSi_2	13.3 ± 0.2	13.1 ± 0.4	-3.3 ± 0.4	0.59 ± 0.04	0.78 ± 0.02
$\text{Mo}_{0.68}\text{W}_{0.32}\text{Si}_2$	12.9 ± 0.3	12.6 ± 0.3	-3.6 ± 0.2	0.55 ± 0.02	0.76 ± 0.03
$\text{Mo}_{0.41}\text{W}_{0.59}\text{Si}_2$	12.1 ± 0.4	12.3 ± 0.5	-3.8 ± 0.4	0.49 ± 0.04	0.72 ± 0.04
WSi_2	10.5 ± 0.2	10.3 ± 0.3	-4.8 ± 0.3	0.34 ± 0.03	0.62 ± 0.02

metals. At the same time, it was shown that the electrocatalytic activity of silicides correlates with the activity of the corresponding metals, and the highest current densities were observed on platinum silicide [3]. It can be assumed that on molybdenum and tungsten silicides, as well as on Mo and W, the hydrogen adsorption energy is high. Therefore, out of the two described above variants, variant (b), which is delayed electrochemical desorption, seems to be more probable. At the same time, this stage is probably in the transition state from ordinary electrochemical desorption to barrier-free desorption, which is expressed as higher α_2 values (Table 3). The HER stage transfer coefficients on $\text{Mo}_x\text{W}_{1-x}\text{Si}_2$ were calculated based on the ratios provided in [30]: the transfer coefficient α_2 of the limiting stage was determined based on the slope of $\lg R_1, E$ -dependencies, and the difference ($\alpha_2 - \alpha_1$) was determined based on the slope of $\lg |C_2|, E$ -dependencies.

4. Conclusions

Based on polarization and impedance measurements, it was shown that the reaction of hydrogen evolution on alloys of $\text{Mo}_x\text{W}_{1-x}\text{Si}_2$ system in an alkaline electrolyte proceeds according to the discharge – electrochemical desorption path with a delayed stage of electrochemical desorption, both stages were irreversible, and the transfer coefficients of the stages were not equal. The Langmuir isotherm for adsorbed atomic hydrogen was fulfilled. It was found that alloys of the $\text{Mo}_x\text{W}_{1-x}\text{Si}_2$ system in an alkaline electrolyte are characterized by a low overvoltage of hydrogen evolution and, thus, represent promising electrode materials for the electrolytic production of hydrogen.

Author contributions

All authors made an equivalent contribution to the preparation of the publication.

Conflict of interests

The authors declare that they have no known competing financial interests or personal relationships that could have influenced the work reported in this paper.

References

1. Shamsul Huq A. K. M., Rosenberg A. J. J. Electrochemical behavior of nickel compounds: I. The

hydrogen evolution reaction on NiSi, NiAs, NiSb, NiS, NiTe₂, and their constituent elements. *Journal of The Electrochemical Society*. 1964;111(3): 270-278. <https://doi.org/10.1149/1.2426107>

2. Tilak B. V., Ramamurthy A. C., Conway B. E. High performance electrode materials for the hydrogen evolution reaction from alkaline media. *Proceedings of the Indian Academy of Sciences – Chemical Sciences volume*. 1986;97(3-4): 359–393. <https://doi.org/10.1007/BF02849200>

3. Wirth S., Harnisch F., Weinmann M., Schröder U. Comparative study of IVB–VIB transition metal compound electrocatalysts for the hydrogen evolution reaction. *Applied Catalysis B: Environmental*. 2012;126: 225–230. <https://doi.org/10.1016/j.apcatb.2012.07.023>

4. Meyer S., Nikiforov A. V., Petrushina I. M., Kohler K., Christensen E., Jensen J. O., Bjerrum N. J. Transition metal carbides (WC, Mo₂C, TaC, NbC) as potential electrocatalysts for the hydrogen evolution reaction (HER) at medium temperatures. *International Journal of Hydrogen Energy*. 2015;40(7): 2905–2911. <https://doi.org/10.1016/j.ijhydene.2014.12.076>

5. Safizadeh F., Ghali E., Houlachi G. Electrocatalysis developments for hydrogen evolution reaction in alkaline solutions – A Review. *International Journal of Hydrogen Energy*. 2015;40(1): 256–274. <https://doi.org/10.1016/j.ijhydene.2014.10.109>

6. Sapountzi F. M., Gracia J. M., Weststrate C. J., Fredriksson H. O. A., Niemantsverdriet J. W. Electrocatalysts for the generation of hydrogen, oxygen and synthesis gas. *Progress in Energy and Combustion Science*. 2017;58: 1–35. <https://doi.org/10.1016/j.peccs.2016.09.001>

7. Eftekhari A. Electrocatalysts for hydrogen evolution reaction. *International Journal of Hydrogen Energy*. 2017;42(16): 11053–11077. <https://doi.org/10.1016/j.ijhydene.2017.02.125>

8. Kichigin V. I., Shein A. B. An electrochemical study of the hydrogen evolution reaction at YNi₂Ge₂ and LaNi₂Ge₂ electrodes in alkaline solutions. *Journal of Electroanalytical Chemistry*. 2018;830-831: 72–79. <https://doi.org/10.1016/j.jelechem.2018.10.029>

9. Theerthagiri J., Lee S. J., Murthy A. P., Madhavan J., Choi M. Y. Fundamental aspects and recent advances in transition metal nitrides as electrocatalysts for hydrogen evolution reaction: A review. *Current Opinion in Solid State and Materials Science*. 2020;24(1): 100805–100827. <https://doi.org/10.1016/j.cossms.2020.100805>

10. Vijh A. K., Belanger G., Jacques R. Electrochemical activity of silicides of some transition metals for the hydrogen evolution reaction in acidic solutions. *International Journal of Hydrogen Energy*. 1990;15(11): 789–794. [https://doi.org/10.1016/0360-3199\(90\)90014-P](https://doi.org/10.1016/0360-3199(90)90014-P)

11. Vijn A. K., Belanger G., Jacques R. Electrolysis of water on silicides of some transition metals in alkaline solutions. *International Journal of Hydrogen Energy*. 1992;15(7): 479–483. [https://doi.org/10.1016/0360-3199\(92\)90146-N](https://doi.org/10.1016/0360-3199(92)90146-N)
12. Kichigin V. I., Shein A. B. Kinetics and mechanism of hydrogen evolution reaction on cobalt silicides in alkaline solutions. *Electrochimica Acta*. 2015;164: 260–266. <https://doi.org/10.1016/j.electacta.2015.02.198>
13. Panteleeva V. V., Votinov I. S., Polkovnikov I. S., Shein A. B. Kinetics of cathodic hydrogen evolution manganese monosilicide in sulfuric acid electrolyte. *Kondensirovannye sredy i mezhfaznye granitsy = Condensed Matter and Interphases*. 2019;21(3): 432–440. (In Russ., abstract in Eng.). <https://doi.org/10.17308/kcmf.2019.21/1153>
14. Kuzminykh M. M., Panteleeva V. V., Shein A. B. Cathodic hydrogen evolution on iron disilicide. I. Alkaline solution. *Izvestiya vuzov. Khimiya i khimicheskaya tekhnologiya = ChemChemTech*. 2019;62(1): 38–45. <https://doi.org/10.6060/ivkkt.20196201.5745>
15. Gurin V. N. Methods for the preparation of refractory compounds of transition metals and prospects for their development. *Uspekhi khimii = Russian Chemical Reviews*. 1972;41(4): 323–340. <https://doi.org/10.1070/RC1972v041n04ABEH002059>
16. Merzhanov A. G., Borovinskaya I. P. Self-propagating high-temperature synthesis of refractory inorganic compounds. *Doklady AN SSSR*. 1972;204(2): 366–369. (In Russ.). Available at: http://www.ism.ac.ru/handbook/1st_art.htm
17. Gorshkov V. A., Yukhvid V. I., Miloserdov P. A., Sachkova N. V. Autowave synthesis of cast Mo-W-Si silicides. *Inorganic Materials*. 2011;47(4): 375–378. <https://doi.org/10.1134/S002016851104011X>
18. Orazem M. E., Tribollet B. *Electrochemical impedance spectroscopy*. John Wiley and Sons, Hoboken; 2008. 533 p.
19. Conway B. E., Bai L., Sattar M. A. Role of the transfer coefficient in electrocatalysis: applications to the H_2 and O_2 evolution reactions and the characterization of participating adsorbed intermediates. *International Journal of Hydrogen Energy*. 1987;12(9): 607–621. [https://doi.org/10.1016/0360-3199\(87\)90002-4](https://doi.org/10.1016/0360-3199(87)90002-4)
20. Krishtalik L. I. Hydrogen overvoltage and adsorption phenomena: Part III. Effect of the adsorption energy of hydrogen on overvoltage and the mechanism of the cathodic process. In: P. Delahay (Ed.), *Advances in Electrochemistry and Electrochemical Engineering*. Vol. 7. Intersci. Publ., New York; 1970. pp. 283–340.
21. Fleischmann M., Grenness M. Electrocrystallization of Ruthenium and Electrocatalysis of Hydrogen Evolution. *Journal of the Chemical Society, Faraday Transactions 1: Physical Chemistry in Condensed Phases*. 1972;68: 3205–3215. <https://doi.org/10.1039/F19726802305>
22. Vvedenskii A. V., Gutorov I. A., Morozova N. B. The kinetics of cathodic hydrogen evolution on transition metals. I. Theoretical analysis. *Kondensirovannye sredy i mezhfaznye granitsy = Condensed Matter and Interphases*. 2010;12(3): 288–300. (In Russ., abstract in Eng.). Available at: <https://elibrary.ru/item.asp?id=15574174>
23. Thomas J. G. N. Kinetics of electrolytic hydrogen evolution and the adsorption of hydrogen by metals. *Transactions Faraday Society*. 1961;57(9): 1603–1611. <https://doi.org/10.1039/TF9615701603>
24. Frumkin A. N. *Selected proceedings: hydrogen overvoltage*. Moscow: Nauka Publ.; 1988. 240 p. (in Russ.)
25. Keiser H., Beccu K. D., Gutjahr M. A. Abschätzung der Porenstruktur porösen Elektroden aus Impedanzmessung. *Electrochimica Acta*. 1976;21(8): 539–543. [https://doi.org/10.1016/0013-4686\(76\)85147-X](https://doi.org/10.1016/0013-4686(76)85147-X)
26. Lasia A. Modeling of impedance of porous electrode. In: *Modern Aspects of Electrochemistry*. No. 43. Ed. by M. Schlesinger. Springer, New York, 2009. pp. 67–137.
27. Candy J.-P., Fouilloux P., Keddou M., Takenouti H. The characterization of porous electrodes by impedance measurements. *Electrochimica Acta*. 1981;26(8): 1029–1034. [https://doi.org/10.1016/0013-4686\(81\)85072-4](https://doi.org/10.1016/0013-4686(81)85072-4)
28. Sukhotin A. M. *Handbook of electrochemistry*. Leningrad: Khimiya Publ.; 1981. 488 p. (in Russ.)
29. Novoselskii I. M., Gudina N. N. Calculation of the mechanism and kinetics of hydrogen evolution from impedance measurements. *Elektrokhimiya = Soviet Electrochemistry*. 1969;5(6): 670–676. (In Russ.)
30. Kichigin V. I., Shein A. B. Diagnostic criteria for hydrogen evolution mechanisms in electrochemical impedance spectroscopy. *Electrochimica Acta*. 2014;138: 325–333. <https://doi.org/10.1016/j.electacta.2014.06.114>
31. Kichigin V. I., Shein A. B. The kinetics of cathodic hydrogen evolution on CeCu_2Ge_2 electrode in alkaline solution. The role of surface and bulk diffusion of atomic hydrogen. *Bulletin of Perm University. Chemistry*. 2016;23(3): 6–19. (In Russ., abstract in Eng.). Available at: <https://elibrary.ru/item.asp?id=27128572>
32. Kichigin V. I., Shein A. B. Additional criteria for the mechanism of hydrogen evolution reaction in the impedance spectroscopy method. *Bulletin of Perm University. Chemistry*. 2018;8(3): 316–324. (In Russ., abstract in Eng.). <https://doi.org/10.17072/2223-1838-2018-3-316-324>

Information about the authors

Viktoria V. Panteleeva, Cand. Sci. (Chem.), Associate Professor, Department of Physical Chemistry, Perm State University (Perm, Russian Federation).

<https://orcid.org/0000-0002-1506-6665>
vikpant@mail.ru

Grigoriy A. Simonov, Student, Department of Physical Chemistry, Perm State University (Perm, Russian Federation).

<https://orcid.org/0000-0002-9948-6797>
grisha.simonov@yandex.ru

natoliy B. Shein, Dr. Sci. (Chem.), Professor, Head of the Department of Physical Chemistry, Perm State University (Perm, Russian Federation).

<https://orcid.org/0000-0002-2102-0436>
ashein@psu.ru

Pavel A. Miloserdov, Cand. Sci. (Tech.), PhD in Technical Sciences, Senior Researcher, Laboratory for SHS melts and cast materials, Merzhanov Institute of Structural Macrokinetics and Materials Science, Russian Academy of Sciences (Chernogolovka, Russian Federation).

<https://orcid.org/0000-0002-2587-0067>
yu_group@ism.ac.ru

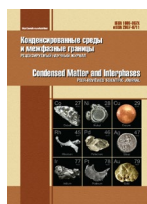
Vladimir A. Gorshkov, Dr. Sci. (Tech.), Leading Researcher, Laboratory for SHS melts and cast materials, Merzhanov Institute of Structural Macrokinetics and Materials Science, Russian Academy of Sciences (Chernogolovka, Russian Federation).

<https://orcid.org/0000-0001-8845-4717>
gorsh@ism.ac.ru

Received 20.10.2021; approved after reviewing 18.02.2022; accepted for publication 15.04.2022; published online 25.06.2022.

Translated by Valentina Mittova

Edited and proofread by Simon Cox



Original articles

Research article

<https://doi.org/10.17308/kcmf.2022.24/9267>**TEM and XPS studies of bio-nanohybrid material based on bacterial ferritin-like protein Dps**E. V. Parinova¹ ✉, S. S. Antipov^{1,2}, E. A. Belikov¹, O. A. Chuvenkova¹, I. S. Kakuliia¹, D. A. Koyuda¹, S. Yu. Trebunskikh¹, M. S. Skorobogatov¹, R. G. Chumakov³, A. M. Lebedev³, A. A. Sinelnikov¹, V. G. Artyukhov¹, O. V. Ovchinnikov¹, M. S. Smirnov¹, S. Yu. Turishchev¹¹Voronezh State University,

1 Universitetskaya pl., Voronezh 394018, Russian Federation

²Immanuel Kant Baltic Federal University,

2 Universitetskaya ul., Kaliningrad 236041, Russian Federation

³National Research Center “Kurchatov Institute”

1 Akademika Kurchatova pl., Moscow 123182, Russian Federation

Abstract

The work is related to the research of a biohybrid nanomaterial formed on the basis of protein molecules of bacterial origin recombinant ferritin Dps.

To obtain recombinant protein, *Escherichia coli* cells were used as producers, and purification was carried out chromatographically. The source of iron atoms for the formation of the biohybrid nanomaterial was the Mohr salt. The possibility of the hybrid particles formation, the shape and size of their inorganic core were studied experimentally by high-resolution transmission electron microscopy. The composition and specificity of hybrid particles inorganic core physico-chemical state were studied by X-ray photoelectron spectroscopy, including the use of focused ion etching.

It is shown that using the chosen method of nanomaterial formation, the internal cavities of protein molecules deposited inorganic nanoparticles. The sizes of these nanoparticles formed in hollow protein molecules averaged 2 nm. A complex composition of particles has been established, mainly including oxides of the iron-oxygen system. Inclusions of metallic iron are also possible.

The results obtained show the possibility of smooth properties control of the biohybrid nanomaterial through their composition. This makes it extremely attractive for the implementation of modern technologies tasks such as spintronics or targeted delivery of functional nanoparticles.

Keywords: Nanostructures, Biomolecules, Hybrid materials, Developed surface, Recombinant ferritin-like Dps protein, Transmission electron microscopy, Combination, X-ray photoelectron spectroscopy

Funding: The work is supported under scholarship of the President of Russian Federation SP-189.2021.1 for young scientists. The study was supported by the Ministry of Science and Higher Education of Russia under Agreement N 075-15-2021-1351 in part of X-ray photoelectron spectra measurements methodology.

For citation: Parinova E. V., Antipov S. S., Belikov E. A., Chuvenkova O. A., Kakuliia I. S., Koyuda D. A., Trebunskikh S. Yu., Skorobogatov M. S., Chumakov R. G., Lebedev A. M., Sinelnikov A. A., Artyukhov V. G., Ovchinnikov O. V., Smirnov M. S., Turishchev S. Yu. TEM and XPS studies of bio-nanohybrid material based on bacterial ferritin-like protein Dps. *Condensed Matter and Interphases*. 2022;24(2): 265–272. <https://doi.org/10.17308/kcmf.2022.24/9267>

✉ Elena V. Parinova, e-mail: parinova@phys.vsu.ru

© Parinova E. V., Antipov S. S., Belikov E. A., Chuvenkova O. A., Kakuliia I. S., Koyuda D. A., Trebunskikh S. Yu., Skorobogatov M. S., Chumakov R. G., Lebedev A. M., Sinelnikov A. A., Artyukhov V. G., Ovchinnikov O. V., Smirnov M. S., Turishchev S. Yu., 2022



The content is available under Creative Commons Attribution 4.0 License.

Для цитирования: Паринаова Е. В., Антипов С. С., Беликов Е. А., Чувенкова О. А., Какулия Ю. С., Коюда Д. А., Требунских С. Ю., Скоробогатов М. С., Чумаков Р. Г., Лебедев А. М., Синельников А. А., Артюхов В. Г., Овчинников О. В., Смирнов М. С., Турищев С. Ю. Исследования био- наногибридного материала на основе бактериального ферритин-подобного белка Dps методами ПЭМ и РФЭС. *Конденсированные среды и межфазные границы*. 2022;24(2): 265–272. <https://doi.org/10.17308/kcmf.2022.24/9267>

1. Introduction

Synthesis and research of new functional materials is an extremely popular task in science, engineering and technology. Nature-like technologies for the formation of functional nanomaterials attract great scientific and practical interest. This is due to such promising directions as high efficiency and reproducibility in combination with insignificant economic costs when introducing these technologies based on biosynthesis into production, compared with physical or chemical methods of nanomaterials synthesis [1–2]. A great example of such a nature-like formation technology of the functional nanomaterials can be the synthesis of inorganic nanoparticles inside a natural protein molecule. Ferritins are natural complex structures consisting of a protein shell and an inorganic (metal-oxide) core, about ten nm in size [3–4].

Ferritin-like protein Dps (DNA-binding Protein from Starved cells) has a unique set of properties, including affinity for iron, small size and the ability to form strong complexes with DNA [5–7]. The composition and structure of the Dps core is strictly dependent on the method of its isolation and purification, storage conditions, as well as methods of further modification and use [8–9]. Previously, we have shown the possibility of forming two-dimensional structures by Dps ferritin molecules [10], but there is no clear understanding about the Dps inorganic core structure specificity yet. In this work, a combination of Transmission Electron Microscopy (TEM) and X-ray Photoelectron Spectroscopy (XPS) methods was used, which provides information about the composition, morphology and physico-chemical state of the object under study.

Thus, it is actual to study the formation of hybrid nanostructures with inorganic nanoparticles – cores of ferritin Dps protein molecules. This work is devoted to the study of inorganic cores in the structure of a hybrid material based on ferritin Dps, including the analysis of their sizes and composition under conditions of equilibrium

formation of nanoparticles and stimulated one by the additional introduction of iron ions.

2. Experimental

Recombinant Dps protein was obtained using *Escherichia coli* BL21*(DE3) cells as producers. *E. coli* cells were transformed by the pGEM_dps plasmid. In [11], detailed information is provided on the preparation of recombinant protein purified from inorganic components by step hydrolysis and dialysis, its subsequent isolation and purification. The protein solution had a concentration of 1.2 mg/ml in a buffer containing 10 mM NaCl, 50mM tris-HCl (pH 7.0) and 0.1 mM EDTA. A freshly prepared solution of Mohr salt $\text{Fe}(\text{NH}_4)_2(\text{SO}_4)_2 \cdot 6\text{H}_2\text{O}$ was used as a source of iron, which was added to the protein solution until an iron ion concentration of 0.25 mM was reached and incubated for 15 minutes, after which the same portion of Mohr salt was added and incubation was repeated, the resulting sample was used in studies.

The sizes of protein molecules were controlled by Dynamic Light Scattering according to the technique described in [12]. For the TEM experiments, prepared thin carbon replicas ~ 15 nm thick were used, on which a molecular culture was placed by immersion in a solution and subsequent evacuation in the loading chamber of a Zeiss LIBRA 120 microscope. The Image J software package was used to estimate the number and size of nanoparticles.

For XPS experiments, protein molecules were deposited on the surface of formed and pre-purified silicon substrates by layering 10 μl of solution. After that, the resulting structure was dried in laboratory conditions, washed with deionized water (by pulling) in order to remove residual salts and dried again under the same conditions.

XPS studies was carried out on the NANOFES beamline ESCA module of the Kurchatov synchrotron ultrahigh vacuum experimental end-station (National Research Center Kurchatov Institute, Moscow), equipped with an electron

energy analyzer SPECS Phoibos 150 [13]. Monochromatized Al K α radiation of an X-ray tube (1486.61 eV) was used, the depth of the informative layer was ~ 2-3 nm [14]. Survey spectra in the binding energy range of 0-800 eV and data of Fe 2*p* states were recorded, for the measured data interpretation reference structures were used: iron foil covered by natural oxide, as well as commercially available powders of Fe₂O₃, Fe₃O₄ and FeO(OH) compounds produced by AlfaAesar. A standard approach to data normalization and calibration based on independent recording of the pure gold foil (Au 4f) signal was used. To register the spectral data of reference iron compounds, C1s calibration of the hydrocarbon contamination line was used [14]. To compare and analyze the main features of Fe 2*p* XPS spectra, well-known databases were used, from which the actual and most accurate (monochromatic) spectra were selected [14–16]. A focused source of surface etching with argon ions at an accelerating voltage of 1 kV with an etching duration of 30 minutes was used. The area of the etching site was selected with an excess of the surface area from which the XPS data were recorded.

3. Results and discussion

Fig. 1 presents high-resolution TEM data for a bio-nanohybrid material based on bacterial ferritin-like protein Dps and an estimate of the average sizes distribution of inorganic nanoparticles that make up the “core” of molecules and their number.

The data obtained by the Dynamic Light Scattering on the molecules sizes distribution coincide with the results [12], which indicates the successful formation of the molecular culture. The TEM data confirm the deposition of inorganic nanoparticles in the internal cavities of molecules as a result of the Mohr salt introduction into the protein culture solution. Inorganic particles have an almost identical shape, agglomeration is not observed, most likely due to the presence of protein walls of individual molecules that prevent them from sticking together. At the same time, the average particle size was about 2 nm, which is almost two times less than the data [11]. This effect can be observed for several reasons: due to the lack of iron ions in the solution to completely fill the molecules, insufficient incubation

time, the use of stepwise saturation of protein molecules. According to the evaluation results, the number of particles in the field of view was ~ 280.

Fig. 2 shows the X-ray photoelectron spectra surveys for the initial surface of the prepared sample and after half an hour etching with argon ions at an accelerating voltage of 1 kV. Note that this value referred to the “softest” effect on the surface, with an estimated removal of 1.5 Å per minute obtained for the silicon substrate.

According to the data of the initial sample photoelectron survey spectra, the main line is carbon, that is, a hybrid material. The presence

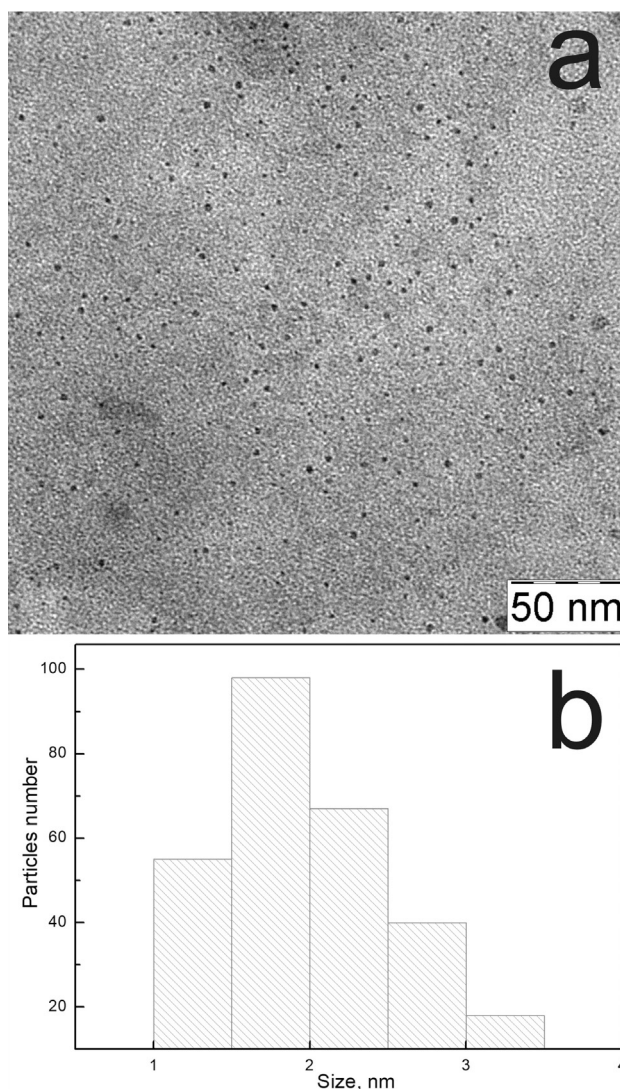


Fig. 1. TEM data of bio-nanohybrid material based on bacterial ferritin-like protein Dps (a). Estimation of inorganic nanoparticles average sizes distribution and their number (b)

of oxygen and nitrogen 1s lines noticeable in intensity confirms the enough amount of the sample itself. A relatively small amount of hybrid material makes it possible to reliably register a signal from a silicon substrate. Traces of salt of the buffer solution (lines of sodium and chlorine) are also noticeable. However, their intensity is noticeably low, which indicates a sufficient degree of the sample washing after layering. The presence of salt in the surface layers and the organic material of the sample as a whole did not lead to a variation of lines positions for the observed core levels associated with the charging of the sample surface. Finally, for the initial sample, the fact of deposited iron nanoparticles signal observation on the survey spectrum is not obvious. Nevertheless, in order to register the iron 2p core level data with a high resolution, we performed a long signal collection, which will be discussed below.

The situation changes slightly after half an hour surface treatment (etching) with argon ions. After prolonged etching, the position and relative

intensity of the carbon line practically did not change, which indicates a sufficient amount of the biohybrid sample remaining after removal. The silicon substrate lines (approximately 100 and 150 eV) began to be observed more intensively, confirming the fact of ion beam exposure and partial removal of the etched sample. At the same time, an argon line is observed, which confirms the assumption that the bio-coating of the substrates is saturated with ions during processing and is characteristic of this class of materials.

The fact that there are no core level lines of the sulfur on the survey spectra (Fig. 2) (S 2p and S 2s states at ~ 163 eV and ~ 228 eV respectively) allows us to conclude that there are no residual traces of Mohr salt. Thus, the source of iron atoms was completely used up for the molecular culture deposition. The effect of washing can be excluded, since after ion etching (in the deep part of the bio-coating), no signal from sulfur atoms was observed.

Finally, in the region of iron atoms binding energy (about 710 eV), a low-intensity feature

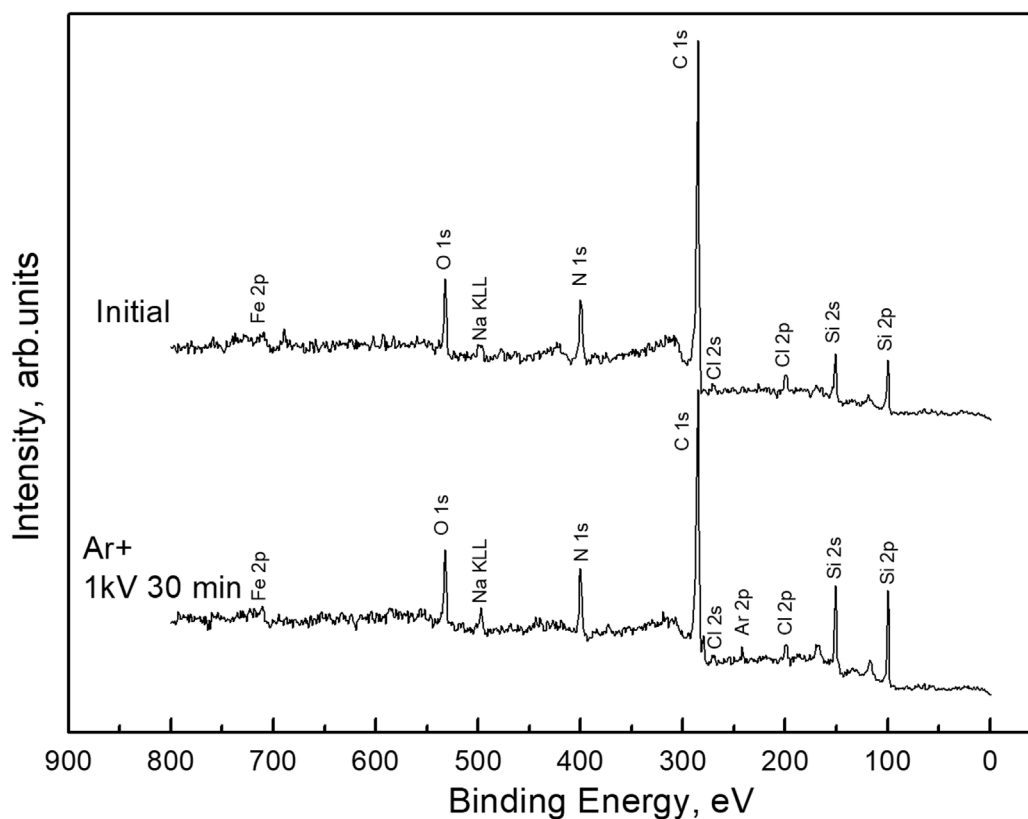


Fig. 2. XPS survey spectra of a bio-nanohybrid material sample based on bacterial ferritin-like protein Dps: the initial state of the surface (initial) and after half an hour etching with an ion beam (Ar⁺ 1 kV 30 min). The elements that make up the studied surface of the sample are designated

is observed. This fact confirmed the need for an increased collection time to record a signal from iron atoms, which we used for the initial sample.

Fig. 3 shows the Fe $2p$ data of X-ray photoelectron spectra from the prepared and processed sample together with the data of reference samples registered under the same methodological conditions (only with a significantly smaller, no more than 20, spectra scans collection number). The binding energy values for the reference structures are in full agreement with the known literature data [14–16]. The most significant uncertainty is observed in these data for FeO oxide unstable under normal conditions, for which Fig. 3 shows the range of values of the Fe $2p$ binding energy level according to the data of the sources used [14–16]. Thus, we emphasized the range of binding energies in which it is possible to observe this compound in the composition of the experimental sample surface. Earlier [12] we obtained data by the synchrotron XANES technique (X-ray Absorption Near Edge Structure), which showed the expected complex structure and composition of inorganic nanoparticles of bio-nanohybrid material.

For this reason and due to the close values of the observed components binding energies with a generally high amount of signal collection time (several hours), we carried out a qualitative assessment of the prepared sample studied surface composition. For this purpose, the fine structure of the Fe $2p$ spectra (Fig. 3) and the energy position of its features were considered.

Analysis of the XPS Fe $2p$ spectra fine structure for reference samples when compared with the data of a hybrid nano-biomaterial made it possible to carry out a qualitative assessment of inorganic nanoparticles cores composition. The position of the XPS Fe $2p$ spectra main maximum of the studied sample is almost unchanged after ion etching. Thus, we received a signal from inorganic nanoparticles of the iron-oxygen system, including from the “bulk” part of the sample (after ion etching). This signal is less noisy. In our opinion, this is due to significantly different rates of ion etching of the bio-environment and the inorganic nanoparticles themselves. It means that the increase of the etching time leads to an increase in the number of particles available for probing by the XPS technique. The

most interesting is the observation of a binding energies feature of ~ 706.7 eV corresponding to metallic iron (Fig. 3). There are two possible reasons for such an observation. Firstly, the “bulk” part of the nanoparticles may contain iron atoms unbound with oxygen. However, the weak signal of the initial spectrum at binding energies of ~ 706.7 eV does not allow us to confirm or deny this statement. Secondly, partial reduction of iron can occur as a result of prolonged exposure to argon ions. Stability of the survey spectra data (see Fig. 2) does not confirm such an assumption. We plan to further investigate this issue in further

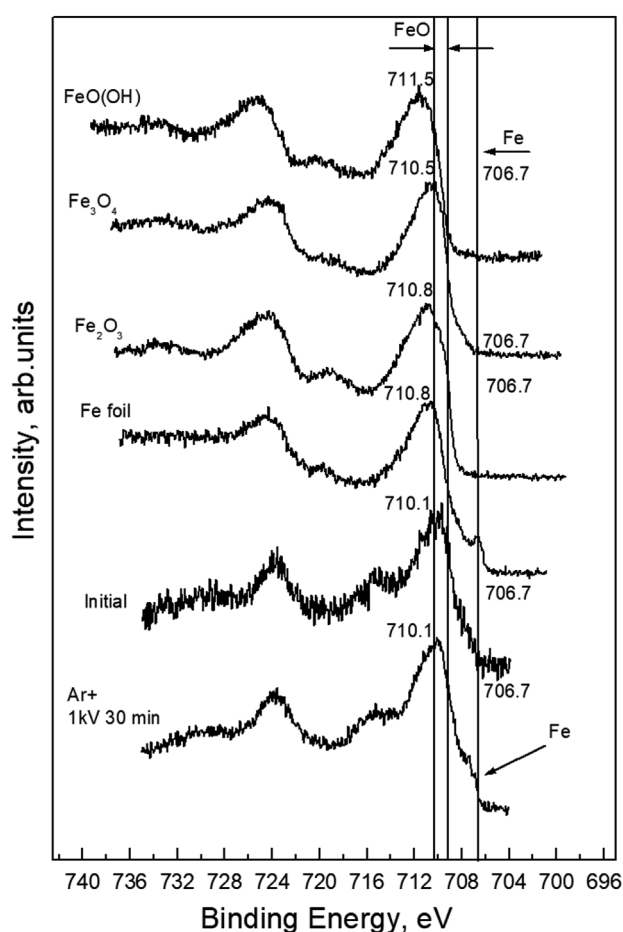


Fig. 3. Fe $2p$ high-resolution XPS spectra of a bio-nanohybrid material prepared sample based on bacterial ferritin-like protein Dps: the initial state of the surface (initial) and after half an hour etching with an ion beam (Ar+ 1 kV 30 min). The data of reference structures are given: iron foil covered with natural oxide (Fe foil), as well as Fe_2O_3 , Fe_3O_4 and FeO(OH) powders. The positions of the observed spectral curves main maxima are indicated. The range of binding energies for FeO and the metallic iron line are indicated as well

experiments, while effectively using a stepwise general etching mode.

Of all the analyzed binding energies values [14–16] for reference objects, the closest values of the main maximum position for studied hybrid nano- biomaterial sample relate to Fe_3O_4 , confirming the conclusions made earlier [12]. At the same time, the observed signal in the region of binding energies $\sim 709\text{--}710$ eV indicates the possible presence of FeO in the composition of nanoparticles, which is also in agreement with [12]. Nevertheless, since the XPS has a greater sensitivity to the surface (compared to XANES), the observation of a sufficiently wide main maximum of the initial experimental sample and one after ion etching does not exclude the presence of Fe_2O_3 and FeO(OH) in the nanoparticles composition. This indicates a complex, composition of iron-oxygen system inorganic particles in the composition of a bio-nanohybrid material based on bacterial ferritin-like protein Dps. The studied sample was reproduced by a series of control samples, all data were obtained at the same time and under identical conditions, including about three weeks of laboratory conditions storage before the XPS measurements. At the same time, a signal different from the expected Fe_2O_3 oxide (the uppermost layers of the surface, within the method probing depth) is reliably detected, which is in good agreement with synchrotron data [12] and confirms the complex, composite nature of inorganic nanoparticles of the hybrid material.

Finally, the above results of high-resolution TEM and XPS data analysis allow us to state that by variation of the samples incubation time and the concentration of iron source salts, it is possible to control the size and composition of inorganic nanoparticles of the studied bio-nanohybrid material based on bacterial ferritin-like protein Dps.

4. Conclusions

For the first time, a joint study of a bio-nanohybrid material based on bacterial ferritin-like protein Dps was carried out using TEM and XPS techniques. In molecular culture, the possibility of small inorganic particles formation of identical shape and an average size of about 2 nm has been shown. Agglomeration is not observed. The results obtained demonstrate

a complex composite nature of inorganic particles, including Fe^{2+} and Fe^{3+} oxides of the iron-oxygen system, mainly close to Fe_3O_4 . Inclusions of metallic iron have been established. Thus, it is possible to adjust the properties of nanomaterials by varying the composition and modes of formation. This makes it promising to use bio-nanohybrid structures based on bacterial ferritin-like protein Dps for targeted delivery of nanoparticles, as well as in modern technologies for surface functionalization, for example, in spintronics.

Author contributions

All authors made an equivalent contribution to the preparation of the publication.

Conflict of interests

The authors declare that they have no known competing financial interests or personal relationships that could have appeared to influence the work reported in this paper.

References

- Hikono T., Uraoka Y., Fuyuki T and Yamashita I. Novel method for making nanodot arrays using a cage-like protein. *Japanese Journal of Applied Physics*. 2003;42: L398. <https://doi.org/10.1143/JJAP.42.L398>
- Cai Y., Deng T., Pan Y., Zink J. I. Use of ferritin capped mesoporous silica nanoparticles for redox and pH triggered drug release *in vitro* and *in vivo*. *Advanced functional materials*. 2020;30(39): 2002043. <https://doi.org/10.1002/adfm.202002043>
- Harrison P. M., Arosio P. The ferritins, molecular properties, iron storage and cellular regulation. *Biochimica et Biophysica Acta*. 1996;1275(3): 161–203. [https://doi.org/10.1016/0005-2728\(96\)00022-9](https://doi.org/10.1016/0005-2728(96)00022-9)
- Kim J. W., Choi S., Lillehei P. T. Electrochemically controlled reconstitution of immobilized ferritins for bioelectronics applications. *Journal of Electroanalytical Chemistry*. 2006;601(1): 8–16. <https://doi.org/10.1016/j.jelechem.2006.10.018>
- Almiron M., Link A. J., Furlong D., Kolter R. A novel DNA-binding protein with regulatory and protective roles in starved *Escherichia coli*. *Genes & Development*. 1992;6: 2646–2654. <https://doi.org/10.1101/gad.6.12b.2646>
- Ilari A., Ceci P., Ferrari D., Rossi G. L., Chiancone E. Iron incorporation into *Escherichia coli* Dps gives rise to a ferritin-like microcrystalline core. *The Journal of Biological Chemistry*. 2002;277(40): 37619–37623. <https://doi.org/10.1074/jbc.M206186200>
- Dubrovina E. V., Dadinova L. A., Petoukhov M. V., Soshinskaya E. Yu., Mozhaev A. A., Klinov D. V., Schaffer T. E., Shtykova E. V., Batishchev O. V. Spatial

organization of Dps and DNA–Dps complexes. *Journal of Molecular Biology*. 2021;433(10): 166930. <https://doi.org/10.1016/j.jmb.2021.166930>

8. Zhang Y., Fu J., Chee S. Y., Ang E. X., Orner B. P. Rational disruption of the oligomerization of the mini-ferritin *E. coli* DPS through protein–protein interface mutation. *Protein Science*. 2011;20(11): 1907–1917. <https://doi.org/10.1002/pro.731>

9. Bessonova T. A., Shumeiko S. A., Purtov Y. A., Antipov S. S., Preobrazhenskaya E. V., M. Tutukina N., Ozoline O. N. Hexuronates influence the oligomeric form of the Dps structural protein of bacterial nucleoid and its ability to bind to linear DNA fragments. *Biophysics*. 2016;61(6): 825–832. <https://doi.org/10.1134/S0006350916060075>

10. Antipov S. S., Praslova N. V., Usoltseva D. S., Belikov E. A., Chuvenkova O. A., Artyukhov V. G., Turishchev S. Y., Preobrazhenskaya E. V., Ozoline O. N., Pichkur E. B., Presnyakov M. Y. High resolution cryogenic transmission electron microscopy study of *Escherichia coli* Dps protein: first direct observation in quasinative state. *Results in Physics*. 2018;11: 926–928. <https://doi.org/10.1016/j.rinp.2018.10.059>

11. Antipov S., Turishchev S., Purtov Yu., Shvyreva U., Sinelnikov A., Semov Yu., Preobrazhenskaya E., Berezhnoy A., Shusharina N., Novalokina N., Vakhtel V., Artyukhov V., Ozoline O. The oligomeric form of the *Escherichia coli* Dps 3 protein depends on the availability of iron ions. *Molecules*. 2017;22(11): 1904. <https://doi.org/10.3390/molecules22111904>

12. Turishchev S. Yu., Antipov S. S., Novolokina N. V., Chuvenkova O. A., Melekhov V. V., Ovsyannikov R., Senkovskii B. V., Timchenko A. A., Ozoline O. N., Domashevskaya E. P. A soft X-ray synchrotron study of the charge state of iron ions in the ferrihydrite core of the ferritin Dps protein in *Escherichia coli*. *Biophysics*. 2016;61(5): 705–710. <https://doi.org/10.1134/S0006350916050286>

13. Lebedev A. M., Menshikov K. A., Nazin V. G., Stankevich V. G., Tsetlin M. B., Chumakov R. G.. NanoPES photoelectron beamline of the Kurchatov Synchrotron Radiation Source. *Journal of Surface Investigation: X-ray, Synchrotron and Neutron Techniques*. 2021;15(5): 1039–1044. <https://doi.org/10.1134/s1027451021050335>

14. Moulder J. F. et al *Handbook of X-ray photoelectron spectroscopy*. Chastain J. (ed). Minnesota: Perkin-Elmer Corporation Physical Electronics; 1992.

15. *Handbooks of Monochromatic XPS Spectra. Vol. 1: The Elements and Native Oxide*. XPS International, Inc.; 1999.

16. *NIST X-ray Photoelectron Spectroscopy Database*. Режим доступа: <https://srdata.nist.gov/xps/>

Information about the authors

Elena V. Parinova, Cand. Sci. (Phys.–Math.), Researcher of the Joint Laboratory “Atomic and Electronic Structure of Functional Materials”, Voronezh State University (Voronezh, Russian Federation).

<https://orcid.org/0000-0003-2817-3547>
parinova@phys.vsu.ru

Sergey S. Antipov, Dr. Sci. (Biology), Associate Professor, Biophysics and Biotechnology Department, Voronezh State University (Voronezh, Russian Federation).

<https://orcid.org/0000-0003-3244-1428>
ss.antipov@gmail.com

Evgeny A. Belikov, Engineer of Joint Laboratory “Atomic and Electronic Structure of Functional Materials”, Voronezh State University Voronezh (Voronezh, Russian Federation).

<https://orcid.org/0000-0001-8336-2231>
belikov@phys.vsu.ru

Olga A. Chuvenkova, Cand. Sci. (Phys.–Math.), Researcher of the Joint Laboratory “Atomic and Electronic Structure of Functional Materials”, Voronezh State University (Voronezh, Russian Federation).

<https://orcid.org/0000-0001-5701-6909>
chuvenkova@phys.vsu.ru

Iuliia S. Kakuliia, Leading Engineer of General Physics Department, Voronezh State University (Voronezh, Russian Federation).

<https://orcid.org/0000-0002-0953-9024>
kakuliia@phys.vsu.ru

Dmitry A. Koyuda, Junior Researcher of the Joint Laboratory “Atomic and Electronic Structure of Functional Materials”, Voronezh State University (Voronezh, Russian Federation).

<https://orcid.org/0000-0001-5635-0788>
koyuda@phys.vsu.ru

Sergey Yu. Trebunskikh, Cand. Sci. (Phys.–Math.), Researcher of the Joint Laboratory “Atomic and Electronic Structure of Functional Materials”, Voronezh State University (Voronezh, Russian Federation).

<https://orcid.org/0000-0002-2481-2797>
tsu@phys.vsu.ru

Matvey S. Skorobogatov, bachelor student of the Department of Biophysics and Biotechnology, Voronezh State University (Voronezh, Russian Federation).

<https://orcid.org/0000-0002-9051-8174>
mataska7111@gmail.com

Ratibor G. Chumakov, Cand. Sci. (Phys.–Math.), Senior Researcher of the National Research Center “Kurchatov Institute” (Moscow, Russian Federation).
<https://orcid.org/0000-0002-3737-5012>
ratibor.chumakov@gmail.com

Alexei M. Lebedev, Cand. Sci. (Phys.–Math.), Senior Researcher of the National Research Center “Kurchatov Institute” (Moscow, Russian Federation).
<https://orcid.org/0000-0001-9998-8941>
lebedev.alex.m@gmail.com

Alexander A. Sinelnikov, Cand. Sci. (Phys.–Math.), Director of the Collective use Center of Scientific Equipment, Voronezh State University (Voronezh, Russian Federation).
<https://orcid.org/0000-0002-0549-4615>
tsu@phys.vsu.ru

Valerii G Artyukhov, Dr. Sci. (Biology), Professor, Head of the Biophysics and Biotechnology Department, Voronezh State University (Voronezh, Russian Federation).
<https://orcid.org/0000-0002-5872-8382>

Oleg V. Ovchinnikov, Dr. Sci. (Phys.-Math.), Professor, Head of the Optics and Spectroscopy Department, Voronezh State University (Voronezh, Russian Federation).

<https://orcid.org/0000-0001-6032-9295>
ovchinnikov_o_v@rambler.ru

Mikhail S. Smirnov, Dr. Sci. (Phys.-Math.), Associate Professor, Associate Professor of the Optics and Spectroscopy Department, Voronezh State University (Voronezh, Russian Federation).

<https://orcid.org/0000-0001-8765-0986>
smirnov_m_s@mail.ru

Sergey Yu. Turishchev, Dr. Sci. (Phys.-Math.), Associate Professor, Head of the General Physics Department, Voronezh State University (Voronezh, Russian Federation).

<https://orcid.org/0000-0003-3320-1979>
tsu@phys.vsu.ru

Received 22.03.2022; approved after reviewing 15.04.2022; accepted for publication 15.05.2022; published online 25.06.2022.

Translated by Sergey Turishchev



Original articles

Research article

<https://doi.org/10.17308/kcmf.2022.24/9268>Liquid-vapour phase equilibria of three-component systems formed by *n*-propanol, *n*-butanol, and *n*-alkylethanoatesYu. K. Suntsov¹ ✉, G. Yu. Kharchenko², N. S. Suntsova¹¹Voronezh State University,
1 Universitetskaya pl., Voronezh, 394018, Russian Federation²Voronezh State Pedagogical University,
86 ul. Lenina, Voronezh, 394043, Russian Federation

Abstract

The production of *n*-alcohols and ethanoic acid esters involves solving problems regarding the rectification of solutions of multicomponent systems. The main achievements related to the methods of calculating the phase equilibria in multicomponent systems have been associated with the development of equations based on local compositions. Equilibrium in multicomponent systems is predicted using data about the binary components of these systems. The most common local composition models are the Wilson and NRTL equations. Liquid-vapour equilibria of binary systems formed by aliphatic alcohols and esters of organic acids have been already studied. Liquid-vapour equilibria of the studied binary systems have been described by the Wilson and NRTL equations.

Boiling points (the pressure of saturated vapour) of solutions of three-component systems formed by *n*-propanol, *n*-butanol, *n*-propylethanoate, and *n*-butylethanoate were measured under various pressure values using the ebulliometric method. The activity coefficients of the solution components of the three-component systems were calculated using the Wilson and NRTL equations. The parameter values in the Wilson and NRTL equations for the binary systems were calculated by nonlinear regression methods. The results of the calculations were verified experimentally.

It was found that the values of the activity coefficient of *n*-propanol and *n*-butanol increase with a decrease in their concentrations in the solutions of the systems. Similar changes in the values of the activity coefficients of the components in the solutions of the systems were observed for the molecules of *n*-propylethanoate and *n*-butylethanoate. In the case of solutions of the *n*-butanol – *n*-propylethanoate – *n*-butylethanoate system, there is a predominance of the values of the *n*-propylethanoate activity coefficient. With an increase in the molar mass (molecular sizes) of *n*-alcohol, the values of its activity coefficient in solutions of the systems decrease. The Wilson model more accurately describes the vapour-liquid equilibrium of the solutions of the studied three-component systems. The obtained data are necessary for technological calculations and can be used to further improve the methods for calculating the liquid-vapour equilibrium of multicomponent systems.

Keywords: Liquid-vapour phase equilibria of three-component systems, Wilson and NRTL equations**For citation:** Yu. K. Suntsov, G. Yu. Kharchenko, N. S. Suntsova Liquid-vapour phase equilibria of three-component systems formed by *n*-propanol, *n*-butanol, and *n*-alkylethanoates. *Condensed Matter and Interphases*. 2022;24(2): 273–278. <https://doi.org/10.17308/kcmf.2022.24/9268>**Для цитирования:** Сунцов Ю. К., Харченко Г. Ю., Сунцова Н. С. Фазовые равновесия жидкость-пар трёхкомпонентных систем, образованных *n*-пропанолом, *n*-бутанолом и *n*-алкилэтанатами. *Конденсированные среды и межфазные границы*. 2022;24(2): 273–278. <https://doi.org/10.17308/kcmf.2022.24/9268>✉ Yuri K. Suntsov, e-mail: jsyntsov@mail.ru

© Yu. K. Suntsov, G. Yu. Kharchenko, N. S. Suntsova, 2022



The content is available under Creative Commons Attribution 4.0 License.

1. Introduction

Data on liquid-vapour phase equilibria are necessary to calculate indicators that determine the direction and speed of technological processes [1]. Solutions of three-component *n*-propanol–*n*-propylethanoate–*n*-butylethanoate and *n*-butanol–*n*-propylethanoate–*n*-butylethanoate systems are often used in the production of *n*-alcohols and ethanoic acid esters [2]. The studies of the phase equilibria of these systems have been fragmentary since they have been carried out solely for technological purposes [3]. As the number of components increases, the volume and complexity of liquid-vapour equilibrium studies increase dramatically. This fact stimulated the development of methods for the calculation of phase equilibria in multicomponent systems based on binary system data. The main achievements in the methods of calculating the phase equilibria have been associated with the development of equations based on local compositions. These equations are based on molecular models of solutions, which provides them with advantages over the polynomial Margules, Redlich–Kister, Van Laar, and Wohl equations. The advantages of the models of local composition are most clearly manifested when predicting the properties of multicomponent systems using the data about their binary components. The Wilson (1) and NRTL (2) equations (Non Random Two Liquid Equation) have been used the most commonly to calculate the vapour-liquid equilibrium of multicomponent systems [1]:

$$\ln \gamma_i = 1 - \ln \left(\sum_{j=1}^n x_j \lambda_{ij} \right) - \sum_{k=1}^n \left[x_k \lambda_{ki} / \sum_{j=1}^n x_j \lambda_{kj} \right], \quad (1)$$

where λ_{ij} and others are parameters of pair interactions.

$$\ln \gamma_i = \sum_{j=1}^n \tau_{ji} G_{ji} x_j / \sum_{k=1}^n x_k G_{ki} + \sum_{j=1}^n \left(x_j G_{ij} / \sum_{k=1}^n x_k G_{kj} \right) \left(\tau_{ij} - \sum_{l=1}^n x_l \tau_{il} G_{il} / \sum_{k=1}^n G_{kl} x_k \right), \quad (2)$$

where: $\tau_{ij} = C_{ij} / RT$; $C_{ij} = g_{ij} - g_{jj}$; $G_{ij} = \exp(-\alpha_{ij} \tau_{ij})$; $G_{ii} = G_{jj} = 1$; $g_{ij} = g_{ji}$; $\alpha_{ji} = \alpha_{ij}$ and for all *i* it is true that $a_{ii} = \tau_{ii} = C_{ii} = 0$; g_{ij} are variables characterising the energy of interaction of the *i*–*j* pairs; g_{jj} is the interaction of *j*–*j* pairs; a_{ij} is a pa-

rameter characterising the degree of ordering of the distribution of molecules in the solution. For solutions of a multicomponent system, it is only necessary to calculate the parameters of pair interactions determined by the experimental data for binary systems.

2. Experimental

During the study of liquid-vapour phase equilibria, water impurities significantly affected the results of the experiment by several hundredths of a percent. Alcohols and esters of chemically pure organic acids were dehydrated using methods [4] and distilled air-free in a laboratory rectifying column. Water in purified reagents was monitored by potentiometric titration using the Fisher reagent [5]. The water content in the reagents did not exceed 0.1%. The criteria for the purity of the purified substances were the boiling point, density, and refractive index. The boiling point of the purified substances was measured in Swietoslowski ebulliometers [1] with an accuracy of ± 0.05 K. The density of the substances was determined by Ostwald pycnometers with an accuracy of ± 0.1 kg/m³, and the refractive index n_D was measured by an IRF-25 refractometer with an accuracy of ± 0.0001 . The constants of purified substances corresponded with the data in [6]. They are given in Table 1. The pressure of saturated vapour and the boiling point of solutions are the most sensitive criteria for the accuracy of calculations of the vapour-liquid equilibrium of systems [1]. The boiling points of the solutions (*T*) at different pressure values (*P*) were measured with a platinum resistance thermometer using the eubuliometric method with an accuracy of ± 0.05 K. The pressure of saturated vapour of the solutions was measured with a mercury manometer using a V-630 cathetometer, with an accuracy of ± 6.66 Pa. Constant pressure in ebulliometers was maintained by an isodromic regulator with negative feedback with an accuracy of ± 6.66 Pa [7]. The obtained experimental data are shown in Tables 3 and 4. Liquid-vapour equilibria of binary systems formed by aliphatic alcohols and esters of organic acids had already been studied [8–24]. The parameter values in the Wilson and NRTL equations for the binary systems were calculated by the method of nonlinear regression [25]. They are presented in Table 2.

Table 1. Properties of purified substances

Substance	Experimental data			Literature data		
	ρ_4^{20}	T, K	n_D^{20}	ρ_4^{20}	T, K	n_D^{20}
<i>n</i> -propanol	0.8044	370.3	1.3854	0.8044	370.30	1.3854
<i>n</i> -butanol	0.8098	391.1	1.3993	0.8098	390.69	1.3993
<i>n</i> -propylethanoate	0.8870	374.7	1.3842	0.8870	374.75	1.3844
<i>n</i> -butylethanoate	0.8825	399.6	1.3940	0.8825	399.65	1.3941

Note: ρ is the density at 293.15 K; T is the boiling point at standard pressure, n_D is the refractive index at 298.15 K

Table 2. Coefficients of binary interaction in the Wilson and NRTL equations, calculated using data about liquid–vapour equilibria, $T = 333 K$

No	System name	Wilson		NRTL		
		λ_{12}	λ_{21}	τ_{12}	τ_{21}	τ_{12}
1	<i>n</i> -propanol - <i>n</i> -propylethanoate	0.8129	0.7116	0.2811	0.3162	0.3236
2	<i>n</i> -propanol- <i>n</i> -butylethanoate	0.554	0.6619	0.6309	0.2099	0.1843
3	<i>n</i> -butanol- <i>n</i> -propylethanoate	0.3838	1.0749	0.0313	0.5025	1.0399
4	<i>n</i> -butanol- <i>n</i> -butylethanoate	0.8417	0.7853	1.2273	0.0995	0.6437
5	<i>n</i> -propanol- <i>n</i> -butanol	1.1432	0.5018	0.2366	-0.5554	0.3835
6	<i>n</i> -propylethanoate- <i>n</i> -butylethanoate	2.3212	0.1319	-1.6022	1.5306	0.9113

The coefficients are oriented towards the first component of the binary system.

Table 3. Activity coefficients and the pressure of saturated vapour of the *n*-propanol (I)–*n*-propylethanoate (II)–*n*-butylethanoate (III) solutions calculated using the Wilson (1) and NRTL (2) model; $T = 333 K$

№	x , mole fractions			γ			P , mm Hg, Experiment	P , mm Hg, Calculated	Equation
	I	II	III	I	II	III			
1	0.9045	0.0473	0.0482	1.0073	1.4810	2.0110	165.2	157.2	(1)
				0.9973	0.8845	1.1877		148.2	(2)
2	0.8041	0.1025	0.0934	1.0284	1.3292	1.7512	156.7	160.3	(1)
				1.0159	0.7511	1.1955		145.1	(2)
3	0.7034	0.1266	0.1700	1.0650	1.2035	1.5625	153.4	158.4	(1)
				1.0586	0.5662	1.2068		139.7	(2)
4	0.6054	0.0795	0.3151	1.1268	1.0828	1.4053	150.8	149.2	(1)
				1.1315	0.2153	1.1618		132.5	(2)
5	0.5104	0.2506	0.2390	1.1638	1.0919	1.3110	156.4	158.9	(1)
				1.1125	0.6323	1.2880		134.8	(2)
6	0.4072	0.3122	0.2806	1.2370	1.0588	1.2170	159.8	156.8	(1)
				1.1467	0.6452	1.3349		131.4	(2)
7	0.3075	0.1100	0.5825	1.4529	0.9723	1.1121	133.3	131.2	(1)
				1.3723	0.1044	1.2964		118.6	(2)
8	0.1830	0.4115	0.4055	1.4801	1.0366	1.0665	146.2	144.2	(1)
				1.2569	0.6164	1.4738		119.9	(2)
9	0.1027	0.1857	0.7116	1.8600	1.0099	1.0198	114.1	111.5	(1)
				1.4795	0.1560	1.5346		108.9	(2)
10	0.1092	0.7231	0.1677	1.3969	1.0409	1.1113	163.7	164.9	(1)
				1.2156	0.8927	1.4363		147.4	(2)

x is the composition of the solution, γ is the activity coefficient; P is the pressure of the saturated vapour of the liquid. See the remaining designations in Table 2.

Table 4. Activity coefficients and the pressure of saturated vapour of solutions of the *n*-butanol (I) – *n*-propylethanoate (II) – *n*-butylethanoate (III) system calculated using the Wilson (1) and NRTL (2) model; $T = 333$ K

No	x , mole fractions			γ			P , mm Hg, Experiment	P , mm Hg, Calculated	Equation
	I	II	III	I	II	III			
1	0.9079	0.0454	0.0467	1.0037	1.5977	1.3779	73.8	70.5	(1)
				1.0126	0.7270	1.0698		63.2	(2)
2	0.8076	0.1080	0.0844	1.0162	1.4875	1.2750	84.9	83.3	(1)
				1.0258	0.7533	1.1259		69.3	(2)
3	0.6929	0.1321	0.1750	1.0414	1.3743	1.1907	90.7	88.0	(1)
				1.0772	0.5440	1.1795		70.5	(2)
4	0.5934	0.0759	0.3307	1.0711	1.2826	1.1405	82.5	80.3	(1)
				1.1981	0.1358	1.1433		69.9	(2)
5	0.5021	0.2547	0.2432	1.1133	1.2443	1.0791	104.3	105.4	(1)
				1.0590	0.7037	1.2835		83.6	(2)
6	0.4003	0.3138	0.2859	1.1704	1.1907	1.0389	113.8	112.1	(1)
				1.0499	0.7227	1.3340		90.1	(2)
7	0.3081	0.1047	0.5872	1.2166	1.1302	1.0318	84.6	84.4	(1)
				1.3229	0.0876	1.3330		79.9	(2)
8	0.2112	0.4115	0.3773	1.3235	1.1185	0.994	124.2	121.3	(1)
				1.0350	0.6998	1.4478		100.1	(2)
9	0.1106	0.1114	0.7780	1.3808	1.0672	1.0016	82.3	83.5	(1)
				1.3244	0.0557	1.4530		88.2	(2)
10	0.1025	0.7571	0.1404	1.5599	1.0557	1.0594	155.4	156.5	(1)
				0.9721	0.9434	1.3978		141.7	(2)

x is the composition of the solution, γ is the activity coefficient; P is the pressure of the saturated vapour of the liquid. See the remaining designations in Table 2.

3. Results and Discussion

The data in Table 2 and equations (1 and 2) were used to calculate the activity coefficients of the components in the solutions of the systems: *n*-propanol–*n*-propylethanoate–*n*-butylethanoate and *n*-butanol–*n*-propylethanoate–*n*-butylethanoate (Tables 3 and 4). The solutions of these systems are often used in the production of alcohols and esters of organic acids. The results of the calculations were verified experimentally. They are given in Tables 3 and 4. The analysis of the data in Tables 3 and 4 established that the Wilson equation more accurately describes the vapour-liquid equilibrium of three-component solutions of the systems. The deviation of the calculated values of the pressure of saturated vapour (P_{calc}) from the corresponding experimental values (P_{exper}) for the three-component systems was: using the Wilson equation $\approx 1.8\%$; using the NRTL equation $\approx 12\%$. The values of the activity coefficient for *n*-propanol and *n*-butanol calculated using the Wilson (1) and NRTL (2) models increased with a

decrease in their concentrations in the solutions of the systems. For example,

1) for the solutions of the *n*-propanol (I)–*n*-propylethanoate (II)–*n*-butylethanoate (III) system calculated using the Wilson equation (1), we had: at $x_1 = 0.9045$, $\gamma_1 = 1.0073$, it increased to $\gamma_1 = 1.8600$ at $x_1 = 0.1027$;

2) for the solutions of the same system calculated using the NRTL equation (2), we had: at $x_1 = 0.9045$, $\gamma_1 = 0.9973$, it increased to $\gamma_1 = 1.4795$ at $x_1 = 0.1027$;

3) for the solutions of the *n*-butanol (I)–*n*-propylethanoate (II)–*n*-butylethanoate (III) system calculated using the Wilson equation (1), we had: at $x_1 = 0.9079$, $\gamma_1 = 1.0037$, it increased to $\gamma_1 = 1.3808$ at $x_1 = 0.1106$;

2) for the solutions of the same system calculated using the NRTL equation (2), we had: at $x_1 = 0.9079$, $\gamma_1 = 1.0126$, it increased to $\gamma_1 = 1.3244$ at $x_1 = 0.1106$.

Similar changes in the values of the activity coefficients of the components in the solutions of the systems were observed for *n*-propylethanoate

and *n*-butylethanoate. When the concentration of ester in the solutions of the systems decreased, the values of their activity coefficients increased (Tables 3 and 4). It should be noted that for *n*-propanol (I) – *n*-propylethanoate (II) – *n*-butylethanoate (III) solutions containing *n*-propylethanoate (II) and *n*-butylethanoate (III) in close concentrations the values of the activity coefficient of *n*-butylethanoate prevailed (Table 3). In the case of solutions of the *n*-butanol – *n*-propylethanoate – *n*-butylethanoate system, there was a predominance of the values of the *n*-propylethanoate activity coefficient (Table 4). With an increase in the molar mass (molecular sizes) of *n*-alcohol, the values of its activity coefficient in solutions of the systems decreased:

1) for the *n*-propanol (I) – *n*-propylethanoate (II) – *n*-butylethanoate (III) system at $x_1 = 0.5104$, $\gamma_1 = 1.1638$;

2) for the *n*-butanol (I)–*n*-butylethanoate (II)–*n*-pentylethanoate (III) system at $x_1 = 0.5021$, $\gamma_1 = 1.1133$.

Spectral and radiographic studies established the presence of hydrogen bonds in *n*-alcohol molecules with an energy of ≈ 30 kJ/mol [26]. The introduction of ester molecules into *n*-propanol and *n*-butanol led to the destruction of the hydrogen bonded structure of the alcohol. For obvious reasons, the disordering effect increased with the increase in the size of ester molecules, which was associated with a decrease in the contribution of *n*-alcohol molecules to the structuring of the solutions of the systems.

4. Conclusions

The Wilson model more accurately describes the vapour-liquid equilibrium of the three-component solutions of the systems. The values of the activity coefficient for *n*-propanol and *n*-butanol calculated using the Wilson and NRTL models increase with a decrease in their concentrations in the system solutions. Similar changes in the values of the activity coefficients of the components in the solutions of the systems were observed for *n*-propylethanoate and *n*-butylethanoate. With an increase in the molar mass (molecular sizes) of *n*-alcohol, the values of its activity coefficient in the solutions of the systems decrease. The obtained data are necessary for technological calculations of rectification processes and can be used to further

improve the methods for calculating the liquid-vapour equilibrium of multicomponent systems.

Author contributions

All authors made an equivalent contribution to the preparation of the publication.

Conflict of interests

The authors declare that they have no known competing financial interests or personal relationships that could have influenced the work reported in this paper.

References

1. Walas S. *Phase equilibria in chemical technology*. Boston: Butterworth-Heinemann; 1985. 671 p.
2. Potekhin V. M., Potekhin V. V. *Fundamentals of the theory of chemical processes in the technology of organic substances and oil refining*. St. Petersburg: Izdatel'stvo Lan' Publ.; 2014. 896 p. (In Russ.).
3. DDBST – Dortmund Data Bank Software & Separation Technology GmbH. 2020. Available at: www.ddbst.com
4. Terenin V. I. et al. *Workshop on organic chemistry*. Zefirov N. S. (Ed.) Moscow: BINOM. Laboratoriya znanii Publ.; 2010. 568 p.
5. GOST R 57824-2017. *Organic solvents. Determination of water content by coulometric Karl Fischer titration*. 2018. (In Russ.). Available at: <https://docs.cntd.ru/document/555729803?marker=7D20K3>
6. *National institute of standards and technology (NIST), search for species data by chemical formula*. Available at: <http://webbook.nist.gov/chemistry/form-ser.html>
7. Suntsov Yu. K. Liquid-vapor phase equilibria and thermodynamic properties of binary solutions of *n*-alkyl benzenes. *Russian Journal of Physical Chemistry A*. 2008;8(4): 530–534. <https://doi.org/10.1007/s11504-008-4004-4>
8. Suntsov Yu. K. Liquid-vapor phase equilibria of some multicomponent systems formed by aliphatic alcohols and esters of organic acids. *Russian Journal of Physical Chemistry A*. 2008;82(2): 318–321. <https://doi.org/10.1007/s11504-008-2033-7>
9. Suntsov Yu. K., Goryunov V. A. Laws of changes in the thermodynamic properties of binary solutions of *n*-alkyl propanoates. *Proceedings of Voronezh State University. Series: Chemistry. Biology. Pharmacy*. 2009;1: 42–47. (In Russ., abstract in Eng.). Available at: <https://www.elibrary.ru/item.asp?id=12610284>
10. Suntsov Yu. K. Regularities of changes in the thermodynamic properties of binary systems formed by a common solvent and representatives of homologous series of organic substances. *Vestnik Kazanskogo tekhnologicheskogo universiteta*. 2010;2: 126–129. (In Russ.). Available at: <https://www.elibrary.ru/item.asp?id=13085794>

11. Suntsov Yu. K., Vlasov M. V. Liquid - vapor phase equilibria and thermodynamic properties of solutions *n*-propanol – dimethyl ketone, *n*-propanol – methyl ethyl ketone. *Proceedings of Voronezh State University. Series: Chemistry. Biology. Pharmacy.* 2010;2: 41–47. (In Russ., abstract in Eng.). Available at: <https://www.elibrary.ru/item.asp?id=15608641>
12. Vlasov M. V., Suntsov Yu. K. Research of phase equilibriums liquid-vapor and thermodynamic properties of solutions of isobutanol-dimethyl ketone, iso-butanol-methyl ethyl ketone. *Kondensirovannye sredy i mezhfaznye granitsy = Condensed Matter and Interphases.* 2011;13(1): 29–37. (In Russ., abstract in Eng.). Available at: <https://www.elibrary.ru/item.asp?id=16441621>
13. Suntsov Yu. K., Goryunov V. A. Boiling temperatures and excess thermodynamic functions of 2-propanol-*n*-alkyl propanoate solutions. *Russian Journal of Physical Chemistry A.* 2012;85(7): 1058–1063. <https://doi.org/10.1134/s0036024412070278>
14. Suntsov Yu. K., Vlasov M. V. Isobars of the boiling temperature and isotherms of excess thermodynamic functions of isobutanol-alkyl ketone solutions. *Russian Journal of Physical Chemistry A.* 2013;87(7): 1160–1164. <https://doi.org/10.1134/s0036024413070303>
15. Suntsov Yu. K., Goryunov V. A. Phase equilibria and thermodynamic properties of solutions of *n*-propanol – *n*-alkyl-2-methylpropanoate systems. *Proceedings of Voronezh State University. Series: Chemistry. Biology. Pharmacy.* 2013;2: 52–63. (In Russ., abstract in Eng.). Available at: <https://www.elibrary.ru/item.asp?id=20400922>
16. Suntsov Yu. K., Vlasov M. V. Volumetric and refractometric properties of binary solutions of butanol – aliphatic ketones. 2013;56:(9): 54–56. *ChemChemTech.* (In Russ.). Available at: <https://www.elibrary.ru/item.asp?id=20207137>
17. Suntsov Yu. K. New method of predicting the thermodynamic properties of solutions. *Journal of Chemistry and Chemical Engineering.* 2014;8(3): 306–314. <https://doi.org/10.17265/1934-7375/2014.03.013>
18. Suntsov Yu. K., Vlasov M. V., Chuikov A. M. Phase liquid-vapor equilibria and thermodynamic properties of solutions of *n*-propanol-aliphatic ketones. *Russian Journal of Physical Chemistry A.* 2015;89(6): 926–930. <https://doi.org/10.1134/s0036024415060291>
19. Suntsov Yu. K., Goryunov V. A., Chuikov A. M. Boiling temperatures and excess thermodynamic functions of *n*-butanol – *n*-alkyl-2-methylpropanoate solutions. 2015;58(4): 10–14. *ChemChemTech.* (In Russ.). Available at: <https://www.elibrary.ru/item.asp?id=23399307>
20. Suntsov Yu. K., Goryunov V.A., Chuikov A.M., Meshcheryakov A.V. Liquid–vapor phase equilibria of three-component systems of propanol-2–propanoic acid esters. *Russian Journal of Physical Chemistry A.* 2016;90(8): 1596–1601. <https://doi.org/10.1134/S0036024416080288>
21. Suntsov Yu. K., Goryunov V. A., Chuikov A. M. Liquid–vapor phase equilibria of three-component systems of propanol-2–propanoic acid esters. *Russian Journal of Physical Chemistry A.* 2017;91(12): 2485–2488. <https://doi.org/10.1134/s0036024417120299>
22. Suntsov Yu. K., Kharchenko G. Yu., Alferova S. I. Liquid–vapor phase equilibria in ternary systems formed by *n*-alcohols and *n*-alkyl ethanoates. *Russian Journal of Physical Chemistry A.* 2019;93(3): 594–597. <https://doi.org/10.1134/s0036024419030208>
23. Suntsov Yu. K., Suntsova N. S. Liquid–vapor phase equilibria and thermodynamic properties of solutions of toluene–*n*-alkylbenzene binary systems. *Russian Journal of Physical Chemistry A.* 2021;95(6): 1093–1100. <https://doi.org/10.1134/s003602442106025x>
24. Suntsov Yu. K., Suntsova N.S. Vapour-liquid phase equilibria and thermodynamic properties of solutions of the ethylbenzene and *n*-alkylbenzenes binary systems. *Kondensirovannye sredy i mezhfaznye granitsy = Condensed Matter and Interphases.* 2021;23(1): 81–92. <https://doi.org/10.17308/kcmf.2021.23/3307>
25. Nocedal J., Wright S. J. *Numerical optimization.* 2006. New York: Springer Series in Operations Research and Financial Engineering; 2006. <http://dx.doi.org/10.1007/978-0-387-40065-5>
26. Durov V. A., Ageev E. P. *Thermodynamic theory of solutions.* Moscow: Librokom Publ.; 2010. 248 p. (In Russ.)

Information about the authors

Yuri K. Suntsov, Dr. Sci. (Chem.), Professor at the Department of Physical Chemistry, Voronezh State University (Voronezh, Russian Federation).

<https://orcid.org/0000-0001-6408-8919>
jsyntsov@mail.ru

Galina Yu. Kharchenko, Cand. Sci. (Chem.), Associate Professor at the Department of Chemistry, Voronezh State Pedagogical University, (Voronezh, Russian Federation).

harchenko.g.u@mail.ru

Nina S. Suntsova, Engineer at the Department of Physical Chemistry, Voronezh State University (Voronezh, Russian Federation).

<https://orcid.org/0000-0002-1421-4830>
suntsova.nina@bk.ru

Received 26.10.2021; approved after reviewing 15.03.2022; accepted for publication 15.04.2022; published online 25.06.2022.

Translated by Irina Charychanskaya
Edited and proofread by Simon Cox

